Exploration and Design of DC MEMS Switches for Integrated Self-x Sensory Systems

Untersuchung und Entwurf von DC MEMS Schaltern für Integrierte Self-x Sensorsysteme

vom
Fachbereich Elektro- und Informationstechnik
der Technischen Universität Kaiserslautern
zur Verleihung des akademischen Grades

Doktorin oder Doktor der Ingenierwissenschaften (Dr.-Ing.)

genehmigte Dissertation

von
M. Sc. Muhammad Akmal bin Johar
geb. in Batu Pahat (Malaysia)

D386

Contents

Abstract

The advances in sensor technology have introduced smart electronic products with high integration of multi-sensor elements, sensor electronics and sophisticated signal processing algorithms, resulting in intelligent sensor systems with a significant level of complexity. This complexity leads to higher vulnerability in performing their respective functions in a dynamic environment. The system dependability can be improved via the implementation of self-x features in reconfigurable systems. The reconfiguration capability requires capable switching elements, typically in the form of a CMOS switch or miniaturized electromagnetic relay. The emerging DC-MEMS switch has the potential to complement the CMOS switch in System-in-Package as well as integrated circuits solutions. The aim of this thesis is to study the feasibility of using DC-MEMS switches to enable the self-x functionality at system level. The self-x implementation is also extended to the component level, in which the ISE-DC-MEMS switch is equipped with self-monitoring and self-repairing features. The MEMS electrical behavioural model generated by the design tool is inadequate, so additional electrical models have been proposed, simulated and validated. The simplification of the mechanical MEMS model has produced inaccurate simulation results that lead to the occurrence of stiction in the actual device. A stiction conformity test has been proposed, implemented, and successfully validated to compensate the inaccurate mechanical model. Four different system simulations of representative applications were carried out using the improved behavioural MEMS model, to show the aptness and the performances of the ISE-DC-MEMS switch in sensitive reconfiguration tasks in the application and to compare it with transmission gates. The current design of the ISE-DC-MEMS switch needs further optimization in terms of size, driving voltage, and the robustness of the design to guarantee high output yield in order to match the performance of commercial DC MEMS switches.

Kurzfassung in Deutscher Sprache

Motivation

Die hohe Komplexität heutiger Elektronik geht einher mit einer daraus resultierenden erhöhten Fehleranfälligkeit. Um einen hohen Zuverlässigkeitsstandard zu gewährleisten, werden Systeme mit rekonfigurierbaren Eigenschaften benötigt. Frühe Methoden der Rekonfigurierbarkeit, wie einfach gesteuerte Systemarchitekturen mit beschränkten Konfigurationsmöglichkeiten anhand fehlertoleranter und redundanter Systeme, sind hierfür unzureichend. Ein attraktives Potenzial zur Verbesserung der Systemstabilität bieten Self-x Konzepte [1, 2]. Eigenschaften wie Self-Monitoring, Self-Calibrating, Self-Trimming, Self-Repairing sowie weitere Self-x Fähigkeiten ermöglichen intelligentere Systeme, die auf im laufenden Betrieb auftretende dynamische Änderungen reagieren können. Die Herausforderung liegt darin, diese Eigenschaften auf einfache und systematische Weise zu implementieren, ohne dadurch die Zuverlässigkeit zu beeinflussen.

Um ein System rekonfigurierbar zu gestalten, werden praktikable Schaltelemente benötigt. Das Aufkommen der MEMS-Technologie hat hierbei neue Möglichkeiten geschaffen. Für Hochfrequenzanwendungen wie anpassbare Antennen, Filter und Phasenschieber werden RF-MEMS-Schalter eingesetzt. DC-MEMS-Schalter besitzen einen niedrigen Widerstand und halten hohen Leistungen stand bei nur geringer Größe. Die vorliegende Arbeit beschäftigt sich mit der Realisierbarkeit von DC-MEMS-Schaltern für die Rekonfigurierbarkeit in intelligenten Sensor-Systemen.

Das Augenmerk dieser Forschungsarbeit erstreckt sich auf zwei Gebiete. Zunächst wird die Vielzahl der Self-x Eigenschaften erforscht, welche potenziell in intelligenten Sensorsystemen implementierbar sind. Der zweite Schwerpunkt liegt in einer Machbarkeitsstudie, DC-MEMS-Schalter für die Rekonfigurierbarkeit von Sensorsystemen einzusetzen. Mithilfe der Resultate beider Teile wird anschließend ein intelligentes Sensorsystem mit Self-x Eigenschaften entwickelt.

Beiträge dieser Arbeit

Das Hauptziel dieser Arbeit ist die Realisierbarkeit von DC-MEMS-Schaltern zur Rekonfiguration von integrierten Sensorsystemen. Es wurde eine Studie durchgeführt, um Self-x Konzepte zu verstehen und deren generelle Anwendungsmöglichkeiten

zu identifizieren. Eine weitere Studie legt den Schwerpunkt auf die Anwendung im MEMS Bereich. Dies führt zu neuen Konzepten für die angestrebte Verwendung von DC-MEMS-Schaltern. Zusammenfassend wurde eine Tabelle erstellt, welche einen Überblick über die Ergebnisse der Untersuchungen gibt.

Es wurde MEMS-Technologie im Allgemeinen sowie deren Verfügbarkeit untersucht, um die am besten geeignete Technologie für DC-MEMS-Schalter zu bestimmen. Dies schließt aktuelle MEMS CAD-Software mit ein. Infolge dessen wurde die Software MEMS+ von Coventor erworben. Dieses Programm ergänzt Cadence Design Tools und erlaubt somit ein vollständiges Design und die Simulation von MEMS mit analoger oder mixed-signal Elektronik.

Die Implementierung der Self-x Eigenschaften Self-Monitoring und Self-Repairing wurde für ISE-DC-MEMS-Schaltern entworfen und optimiert. Die Schalter der Typen SPST und SPDT wurden charakterisiert und es wurde ein verbessertes elektrisches Modell vorgeschlagen, um die Genauigkeit des Modells zu erhöhen.

Nach Entwurf und Optimierung wurden zwei Arten von Schaltern in SPST und SPDT Konfiguration hergestellt. Diese Schalter werden über elektrostatische Aktoren und/oder Wärmeaktoren angesteuert. Das Self-Monitoring dient dabei zur Beobachtung der Beweglichkeit der Körpermasse. Der Zweck der Wärmeaktoren ist das Self-Repairing, um zusammenhaftende MEMS-Strukturen zu lösen.

Es wurden die elektrischen sowie die mechanischen Eigenschaften der SPST und SPDT Schalter charakterisiert. Aus der mechanischen Charakterisierung wird ersichtlich, dass das Zusammenhaften die Kammstruktur betrifft, wenn die Schalter über den elektrostatischen Aktor angesteuert werden.

Das ursprüngliche Modell aus der MEMS+ Software erwies sich sowohl im elektrischen als auch im mechanischen Bereich als ungenau. Die Ergebnisse der Charakterisierung der Prototypen wurden zur Validierung des zusätzlich vorgeschlagenen elektrischen Modells verwendet. Das verbesserte elektrische Modell für SPST Schalter wurde zur Simulation der Systemanwendung benutzt.

Im mechanischen Modell führte die Annahme eines starren Körpers bei der elektrostatischen Aktorstruktur zu ungenauen Simulationsergebnissen, welche in Folge zum Problem des Zusammenhaftens im Prototyp führten. Daher wurden Konformitätstests vorgeschlagen und implementiert, um die Ungenauigkeit des mechanischen Modells zu kompensieren.

Es wurden vier verschiedene Simulationen von Systemanwendungen durchgeführt, um die Leistungsfähigkeit der ISE-DC-MEMS-Schalter zu analysieren und mit der von CMOS-Schaltern zu vergleichen. Die Simulationsergebnisse wurden verwendet, um eine Vergleichsmatrix aufzustellen, welche es Anwendern erlaubt, den für ihre Zwecke am besten geeigneten Schalter auszuwählen. Ein Hybridsystem in einer Integration (System-in-Package), welches CMOS- und MEMS-Schalter kombiniert, bietet eine attraktive Kombination als Lösung für analoge und mixed-signal Elektronik.

4

Im Folgenden werden die Neuheiten und Errungenschaften dieser Arbeit aufgelistet:

- Verständliche Studie der Self-x Konzepte und deren Implementierung in MEMS-Vorrichtungen

- Studie und Analyse von DC-MEMS-Schaltern im Hinblick auf Herstellungstechnologie, Entwicklungswerkzeuge und Designvariationen

- Integration von Self-Monitoring und Self-Repairing Funktionen in der Hardware von ISE-DC-MEMS-Schaltern selbst

- Neuartiger Ansatz für Self-Repairing Konzepte, welcher nicht auf redundanten Subsystemen beruht, sondern auf aktiven Strukturen in Form von Wärmeaktoren

- Spezielle Struktur von Wärmeaktoren, welche die Stellbewegung im Zentrum der Balkenstruktur durchführt mit einem Minimum an Auslenkung aus der Ebene

- Verfahren zur Überprüfung der Konformität für den Entwurf elektrostatischer Aktoren zur Kompensation der mechanischen MEMS+ Modelle in ISE-DC-MEMS-Schaltern; dieses Verfahren kann während des Entwurfs des elektrostatischen Aktors mit Kammstruktur in der MEMS+ Software angewendet werden

- Self-x Implementierung auf Komponentenebene in Form von Self-Monitoring und Self-Repairing, wurde für AMR-Sensoren und ISE-DC-MEMS-Schalter gezeigt

- Self-x Implementierung auf Systemebene von AMR-Sensoren durch Überwachung der Umgebungstemperatur anhand der AMR-Sensorbrücke

- Aufbau eines Demonstrators als Machbarkeitsnachweis für die Implementierung von Self-x Eigenschaften auf System- und Komponentenebene

MEMS Switch with Self-x Structures

3D-AMR Sensor Module

V Supply   CCS

MEMS Switch

G1   G2

V out

IN AMP

V_T

$\dfrac{1}{S(V_T)}$

$\dfrac{H}{V_{Supply}}$

Reconfigurable Gain

Block Diagram of Sensor Systems

Physical system

Sensor(s)

Self-Calibration actuator(s)

Post-processed actuator signal

Error detection

Calibration Electronics

Digital calibration signal

Physical quantity

Electrical signal

Analog electronics

Pre-processed electrical signal

ADCs

DACs

Digital electronics

Dynamic deviations

Post-processed sensor control signal

Calibration signal

Control signal

Self-Repairing actuator (s)

Post-processed actuator signal

Mixed-signal electronics

Self-mon. & Reconfig

Figure 0.0.1.: Prinzipieller Demonstrator der betrachteten Selbst-x-Eigenschaften auf System-und Komponentenebene für ein Magnetsensorsystem.

Acknowledgment

I would like to express my special appreciation and thanks to my supervisor Professor Dr.-Ing Andreas Koenig, who has been a good mentor for me. I would like to thank you for suggesting this research topic. Your advice, guidance and encouragement for my research as well as on my career have been priceless.

Secondly, I would like to thank my colleagues Robert Freier, Abhaya Chandra Kammara and Lingaselvan Palanichamy for the fruitful discussions throughout this research journey. All of you have been there to support me especially during experimental works and data taking.

Special thanks to my wife Aziyah Ashak and my three kids; Nurin Akma Alya, Muhammad Ammar Haziq and Nayla Aisha Iman who were always there for me at all time sharing your smile, laugh and tears. Thanks you to my parents who are continously praying for my success.

1. Introduction

The sensor market has been growing steadily over the years with a significant increase in the last ten years. The German sensor market alone reached 180% in 2012, with turnover as shown in Figure 1.0.1 [1]. This trend is partly a result of the advances in micro and nano technology which have made sensors smaller in size, cheaper in price and better in performance. Sensor technology has also benefited from the diversification of sensing physics, which has added various modalities in acquiring data and also opened new sensing domains, such as those in the biological field, which was not possible earlier.

Sensor application trends are moving from specific market segments, such as the military and avionics, to mass market segments such as the automation industry, the automotive industry, and mobile devices. Accelerometers and gyroscopes are perfect examples: having been initially developed for military applications in aircraft, submarines, and missiles [3] for inertial measurement system, they are now available in tiny packages, making them more feasible for mass market applications. This emergence of various sensing modalities, such as the gyroscope from DTGs (dynamically tuned gyroscope), FOGs (fibre optic gyroscope), RLGs (ring laser gyroscope) and the more recent technology in MEMS and AO (atom optic sensors) have consistently improved sensor performance in sensitivity, selectivity and stability [4, 5]. A similar trend has taken place in camera sensors, from the bulky size of CRTs (cathode ray tubes) cameras to CCD (charge-coupled device) cameras, and then to CMOS (complementary metal-oxide semiconductor) sensors. The sensor's miniaturization has continued, until the development of the capsule endoscopic camera with wireless communication [6] for medical applications.

The integration between multi-sensor elements, sensor electronics and sophisticated signal processing algorithms has resulted in intelligent sensor systems with a significant level of complexity. Unfortunately this complexity, diversity and the associated failure mechanisms and probabilities of each of the constituents parts leads to greater vulnerability when performing their respective functions, including component degradation, offset measurement error, soft error, dynamic error, transient error, etc. At the same time, society demands maintenance of high standards of reliability and dependability. Approaches such as the use of simple feed-forward architecture with restricted configuration capabilities via fault tolerant and redundant systems are not adequate. These pre-determined and static calibration techniques are often not adequate to combat these dynamic changes. A holistic approach is

---

[1] http://www.ama-service.com/
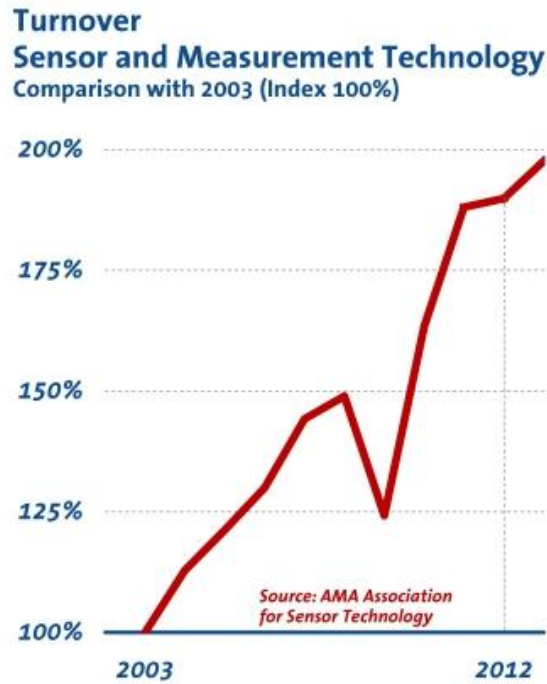
Figure 1.0.1.: Turnover of sensor and measurement technology between 2003 to 2012

needed in order to fulfil the need for improvement at various levels, and from system to component level. Nature inspired self-x features can be implemented to achieve this goal [1, 2]. Abilities in self-monitoring, self-calibrating, self-trimming, self-repairing and other self-x possibilities will produce smarter systems that are responsive towards the dynamic changes which occur during operations. The open challenge is how to implement self-x in simple and systematic ways without affecting reliability.

1.1. Smart Sensory System Applications and Design Challenge

Organic computer systems are one vision for the future of computer system architecture [7, 2]. They are equipped with capabilities in various forms to respond with dynamic changes during operations. Highly robust systems are able to perform dynamic evolution in their configurations so as to adapt with either planned or unplanned changes. Self-x is a concept to provide dynamic evolution in response to various changes in environment. The big challenge is to embed system with such capabilities without compromising system complexity and performance.

Maximising organic computing potential requires various levels of implementation. Much research has been reported especially about software level implementation
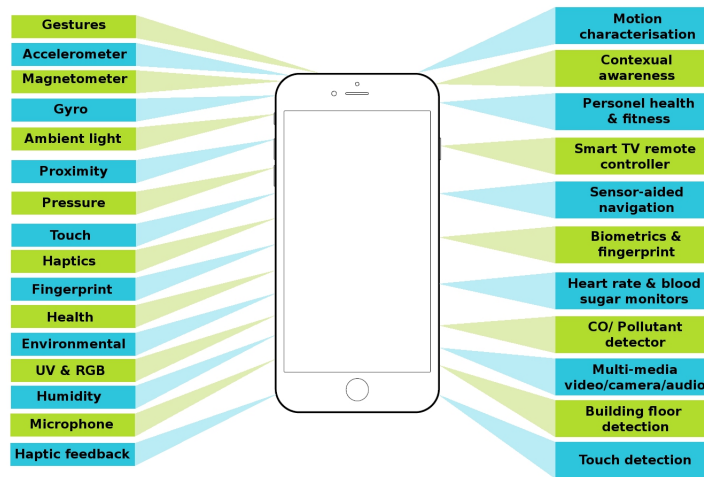
Figure 1.1.1.: Emerging sensors in mobile devices

[8, 9, 10, 11, 12]. Further advances in the implementation of embedded systems and electronic hardware are another work in progress [13, 14]. A smart sensory system is the first step to achieving this future organic computing system and this research tries to fill the gap in implementation at the sensor front-end and in the analogue electronics area.

Mobile computing devices are an example of smart sensory system application. Smart phones are embedded with various sensors, as depicted in Figure 1.1.1, and more sensors will be introduced in the near future [15]. The automotive industry has also benefited significantly from advances in sensor technology. Cars nowadays are equipped with various sensory elements that improve their safety, comfort and performance. MEMS accelerometers assist in airbag systems that are widely used in cars. The tyre pressure monitoring system (TPMS) is standard in the USA automotive industries [16]. A research project in tyre pressure monitoring system by the European countries via Apollo Project [17] was also reported. Future autonomous assisted-driving systems such as self-parking and mapping surrounds for the Google car project [18] already use many sensory systems.

The integration of smart sensory systems with network capability has led to the introduction of the Cyber-Physical System (CPS). In CPS, multiple smart sensory devices collect, process and share data with each other. This harmonious integration of various pieces of hardware in one system offers many benefits in terms of economy and society, to enrich human life. In order to realise the true potential of CPS, however, issues of system reliability and robustness issues are a the design challenge [19]. Similar issues have also been highlighted as a requirement in NAMUR road maps for industrial sensor application, and Foresight Vehicle technology road maps [20] for automotive applications.

1.2. Self-x as a Way to Achieve Robust and Reliable Sensors

In recent years, the Institute of Integrated Sensory Systems (ISE) has been investigating ways to increase the performance of smart sensory systems. A new enhanced design methodology for intelligent multi-sensor systems that emphasises on the ability to implement local and global parameter optimisation has been reported [21]. This research framework outlines several parameter optimisation possibilities for future implementation in smart sensory systems, as shown in Figure 1.2.1. Part of the research has concentrated on designing and developing reconfigurable analogue circuitry for the sensor front-end and the related algorithm for synthesising it [22, 23]. This research explores possible implementation at the next level in sensory applications.

Sensor performance can be affected by various factors. The aging effect, temperature dependency, static and dynamic deviations are some of the issues that lead to sensor errors. A great deal of effort is required to extend conventional self-monitoring features via the introduction of more self-x concepts, as mentioned above. Enabling these reconfiguration features may require active structuring in the form of actuator and/or switching devices. The plethora of switching applications has different requirements.

Traditional static configurations in the form of zapping diodes [24] and fuse-based techniques [25, 26] offer one time configuration. Switching elements in the form of CMOS transmission gates and electromagnetic relays are normally used for dynamic configurations. The former causes current leakage problem during off-state and potentially huge parasitic capacitance which becomes a source of error, especially in the analogue signal domain. Electromagnetic relays are always considered devices with high power consumption, that are huge in size and difficult to integrate in smaller devices, but which also offer high signal isolation. Switching devices based on MEMS technology are emerging as a potential complement to the CMOS switch in integrated circuits. This offers the promise of superior properties in providing high signal isolation, high power handling, low on-resistance and low parasitic capacitance.

There are many remaining issues in MEMS switches, however, especially the DC MEMS switch, before they can enter the mass market. MEMS switches can be divided into two categories: RF MEMS switch and DC MEMS switch. The former has reached a relatively advanced stage in product development, for example as an application for reconfigurable high frequency antenna in circuit filters. The latter has adapted more slowly to the mass market largely due to the concern of switch reliability. The lower reliability of DC MEMS switches is mainly due to the physical contact during the switching action, which can lead to fatigue in mechanical structures and micro-welding phenomenon in contact areas. The RF MEMS switch involves no physical contact, and thus higher reliability can be easily achieved. Fur-
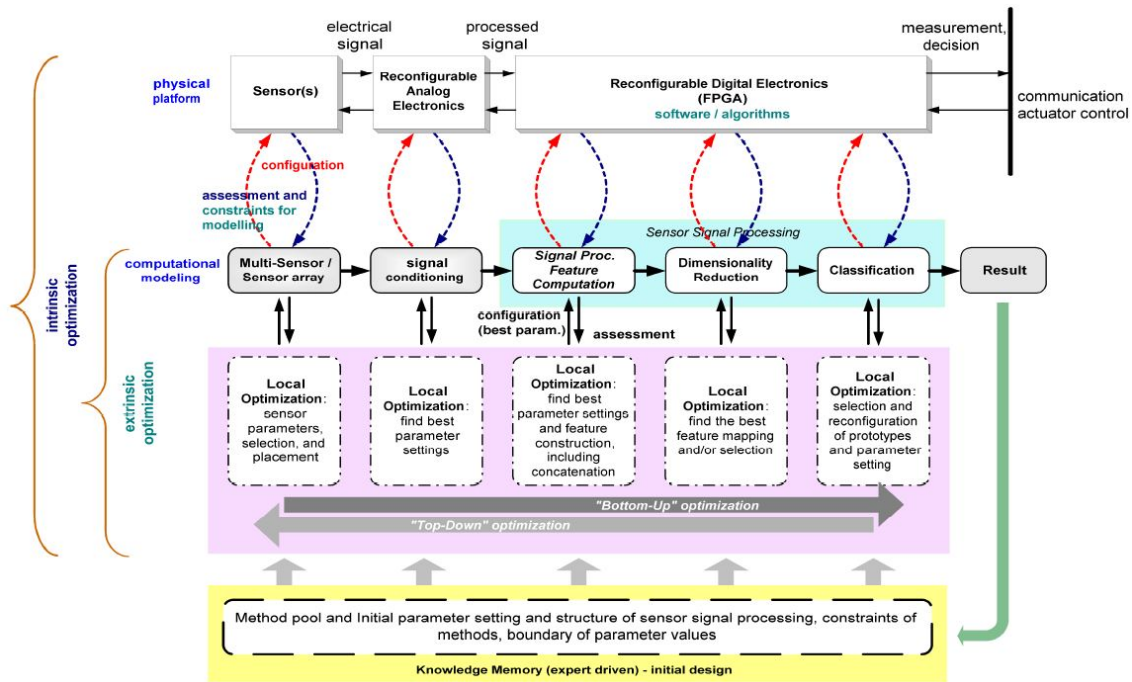
Figure 1.2.1.: The reconfigurable potentials in a sensor signal system

ther investigation of DC MEMS switch technology is needed to optimise the design with regard to size, micro-actuation techniques, scaling driving voltages, power consumption, contact reliability, chip level integration and reliability. A bottom-up design approach is needed to evaluate the potential for improvement in every aspect of DC MEMS switch components.

The challenge is to design and embed these new functions in a clever way that produces better performance with minimal cost. This is in line with the ITRS road map [27] and More than Moore direction [28], which predicts that more functions and active materials will be embedded in System-in-Package(SiP).

1.3. Goals of the Thesis

The potential in extending implementation of self-x features at sensory levels is enormous. The first step in the research was a holistic investigation of implementing the self-x feature in integrated sensory systems. The trends in current research into self-x feature implementation will be reviewed. The expected outcome of this first goal is a comprehensive assessment of the feasibility studies for implementing self-x features in target applications. Chapter Two will describe this in detail.

The next goal is to evaluate the DC MEMS switch potential for enabling dynamic reconfiguration capabilities. This investigation will include a feasibility study of MEMS technology, including manufacturing availability and process compatibility

for the intended device. The groundwork is further extended to investigate design methodologies for the integration of sensor systems with MEMS devices. There will be emphasis on the design flow integration of CAD software between MEMS technology and analogue CMOS technology.

The third goal is to propose several DC MEMS switch concept designs with special attention to finding an efficient means of self-x features integration. The proposed design will partly fulfill the goal of implementing self-x features at the component level. The importance of identifying the scaling properties of MEMS devices is duly noted. The behavioural model generated using CAD software will be investigated and evaluated. A description of this goal will be given in Chapter 4.

The next goal is to propose and evaluate the improvement of a behavioural model for DC MEMS switches. Performance comparisons will be made between ISE-DC-MEMS switches and transmission gates. This goal, together with post layout validation, will be discussed in Chapter 5.

Characterisation of the DC MEMS prototype is the next research goal. Electrical and mechanical characteristics will be investigated and measured, and the results discussed. The outcome of the investigation in relation to this goal will be detailed in Chapter 6.

The final goal is to demonstrate the implementation of the self-x concept via a research vehicle in the form of a 3-axes AMR sensor node. A sensor node was initially developed to provide localisation capability in fluidic ambiance for monitoring a fermentation tank in the brewing industry [29, 30]. The proposed demonstrator will be described in the Chapter 7, and offers a solution for improving AMR sensor node performances via implementation of self-x features. The DC MEMS switch prototype will be used in this demonstrator to further enhance the self-x implementation capabilities of the system.

Finally, Chapter 8 will discuss the conclusion of the research and its contribution, and suggest directions for future research.

2. Self-x Capabilities

2.1. Current State of MEMS Devices in the Market

2.1.1. Industrial Requirements for New Products

The rapid development of micro-scale manufacturing technology since the early 1990s has resulted in many new micro-sensors and MEMS products entering the market. The sensor market has been growing since then, and continues to do so due to increasing demand in the industry.

The automotive industry is one of the industries that has significant impact on the sensor market due to the mass production of vehicles. Electronics in vehicles have played a key role, especially in the areas of improving driver safety, comfort, engine efficiency and performance. These important areas have strict requirements in terms of reliability, accuracy and low cost sensors. In general, the reasons for these strict requirements for sensors for automotive application can be listed as follows [31]:

- Accuracy and reliability

- Multiple functionality

- Highly robust against harsh and changing environmental conditions

- Working temperature from -40 ˚C ~ 150 ˚C

- Ability to withstand mechanical vibrations and acceleration values of up to 200 times the acceleration due to gravity

The stringent requirements of the automotive industry may not be necessary in general consumer electronics. Working conditions may not be as harsh as for cars, so consumer electronic products are less demanding. The cost is one key factor in new sensors being adapted in consumer electronics. Sensors used for mobile electronic products generally do not require high accuracy but do require multiple functionalities at low cost.

Cost, device functionality, reliability, manufacturability and integration feasibility are factors that need to be evaluated, and these factors need to be evaluated carefully for a new MEMS device that is intended to be used in the current market.

2.2. Overview of Self-x Features

2.2.1. The Importance of Self-x Features

Self-x or self-* features are the mechanisms embedded into a system in order to make it more dependable when performing tasks in a dynamic environment. The basic concept is that of biological creatures. The human body, for example, is a very complex system with such mechanism. For example, our skin has a specific mechanism to repair and heal itself in case of small injuries, without needing external intervention. Researchers try to mimic these abilities by learning from nature, and implement this learning in our technology.

The implementation of self-x features can significantly improve system dependability. High reliability and robustness are common requirements of present consumer products. As the DC MEMS switch has been inferior with regard to its reliability, this research will look into the potential to implement self-x features in a DC MEMS switch. The currently implemented self-x features will first be discussed, followed by discussion of the previous work in self-x implementation MEMS devices.

2.2.2. Self-x Feature Implementation in the Literature

2.2.2.1. Self-Monitoring

The concept of self-monitoring can be defined as the ability to monitor the condition of a device without external intervention. A complete self-monitoring system comes with self-test, self-calibration and self-repair. A self-test function will allow the system to test sensor functionality. If the sensor makes an error in measurement, the self-calibration algorithm can be applied to correct the output. If the sensor is found to be damaged a signal to inform the main controller will be sent. The signal can also be extended to introduce the self-repair function, where a redundant sensor replaces the one diagnosed to be malfunctioning.

A recent sensor trend report [32] has listed five self-monitoring procedures that have been implemented for autonomous sensors. Table 2.1 shows the percentage implementation for each self-monitoring procedure [33] of 25 autonomous systems. Generating a reference signal has been the most commonly implemented procedure due to the feasibility to implement with least effort. While analysing the influence of disturbance requires a more complex system, and thus has least number of implementation.

2.2.2.2. Self-Test

Self-monitoring or self-testing is one of the earliest self-x concepts to have been successfully applied in a real MEMS product. The term 'self-test' has been widely

Procedures	Percentage of implementation
Redundancy method	25%
Generating a reference value	30%
Analysing measured signal	20%
Analysing the influence of disturbance	5%
Analysis of additional signals in the measurement	20%

Table 2.1.: Percentage of self-monitoring procedures implemented in an autonomous system

used in the industry since the MEMS manufacurer used it in the MEMS data sheet more often than the term 'self-monitoring'. The term 'self-test' means the device has the ability to check all its functions without external intervention. By testing sensor functionality via a self-test, sensor performance can be ensured and the reliability of the system will improve significantly. The most common implementation technique involves providing additional hardware within the device for testing purposes.

A MEMS product with a self-test function has many advantages over a MEMS product without it. The first advantage is the elimination of dependency on external testing equipment. Testing can be done within the device, and so minimum effort is required to determine functionality. This reduces the cost of the test. The second advantage is that a highly efficient testing system can be designed, tailored only to the needs of the devices. A shorter test time with higher test frequency can also be achieved without much affecting the overall system. The most significant advantage is the ability to perform testing on field applications. This allows consumers to test chips prior to their mounting on a final product, and also during field applications.

In order to realise the self-test function, the ability to produce a physical input signal is required. For example, the physical input of a temperature sensor can be realised via an embedded heater element in the sensor. In general it is necessary to add actuators in a self-test sensor system to allow self-test functionality by producing physical input signal. This reference for the physical reference signal will test the functionality of the sensor element by knowing the expected result from the given input.

Since this feature has been applied for quite some time in micro technology products, several MEMS products have also embedded this ability, such as the MEMSIC accelerometer MXA2050A [34], which provides continuous self-testing, and the gyroscope from STMicroelectronics LYPR540AH [35] which has the same feature.

2.2.2.3. Self-Calibration

The function of actuators for self-test functionality can be extended into realising self-calibration capabilities. Where the self-test function is to determine whether

a sensor is damaged or not, self-calibration is a corrective process for the sensor output when a sensor has made an error in measurement.

Errors in measurement can happen for several reasons. The most common is that they are due to process variations during the manufacturing of sensors. It is a well known fact that, in micro technological sensor batch production, the manufactured sensor instances will substantially differ from each other in their properties due to process variations. An additional source of dynamic deviation is due to drift and the aging of sensor materials, which compromises sensor measurement.

One way to tackle this problem is to carry out a calibration process so as to correct the sensor output. Calibration of the static source of error can easily be done in the factory before releasing a product onto the market, as a controlled environment can be set up for batch calibration processes. Compensation for the dynamic source of error is somewhat complicated and requires a self-calibration function in the sensor system. Suitably integrated actuators are required to produce physical signals, so that a periodic self-test can be performed and self-calibration can subsequently be performed, where small errors in measurement are detected.

2.2.2.4. Self-Repair

As self-testing has been successfully applied in industrial products, researchers are now venturing into another feature, self-repair capability. This is an active mechanism to eradicate faulty components or errors. A common technique involves adding redundant subsystems within a system. Several researchers have experimented with this idea, and a technique providing redundancy modules, for example, has been applied by Xingguo Xiong [36] in his MEMS accelerometer design. He proposed multiple redundant structure modules embedded in a single MEMS chip. In a fault event where malfunctions occur in the subsystems, a redundant system can be activated to replace it and resume the operation. This approach will increase system dependability and reliability.

In some scenarios, including smart sensor application, the redundant system approach is still susceptible to common cause failure [37]. Common cause failure involves the failure of multiple redundant subsystems from a common source. To improve the redundant system approach, diversity in subsystems need to be introduced. For sensing applications, diversification in sensing physics of redundant systems will improve the conventional redundant system approach.In the redundant system approach, self-repair is executed by switching elements to deactivate the malfunctioning subsystem and replace it with the other.

Another approach involves using an additional active mechanism which is not redundant but can be implemented. In certain areas of applications, a more elegant approach can be implemented via adding one or more micro actuator/s to the system as active mechanisms. These actuators must be designed and placed in a strategic area in order to perform repairs. The redundant system approach generally increases

cost and takes up more space, and thus it may not be feasible for implementation in consumer products, especially mobile devices.

2.2.2.5. Self-Organisation

Self-organising has been discussed since in the early 1970s. Inspired by several theories about the brain (pattern formation, biological, cooperative phenomena), self-organising is a phenomenon whereby a simple mechanism of growth and interaction leads to the establishment of a complex structure of global order [38]. A prominent researcher in neurocomputing, von der Malsburg, suggested the existence of self-organisation in the human brain. Up to this point the term had mostly been applied in research areas of soft computing, such as neural networks [39, 40], and algorithms of wireless sensor networks. There have been no reports of MEMS sensor hardware applying the self-organising concept.

2.3. Self-x Features in MEMS Devices

As the interest in MEMS devices has increased in recent years, there has been much research into using the functionality and reliability of MEMS devices. This section will report on a focused survey about MEMS devices equipped with self-x features.

2.3.1. Electrically Induced Stimulation for Self-Test in MEMS

One of the challenges of introducing self-x features is to provide the right stimulation in order to initiate the functions. The stimuli must be integrated into the system in order to minimise system complexity. Charlot et. al in [41] listed methods to induce the self-test feature in MEMS. Three techniques to electrically induced test stimuli are presented below.

The first stimulation technique is via parallel plate capacitor. This is a popular method in MEMS accelerometers, using electrostatic force generated by a parallel plate capacitor to initiate movement of seismic mass. The induced displacement is then measured against similar structures that act as capacitive sensors. Figure 2.3.1a shows one example of parallel plate capacitor design in a MEMS accelerometer. This technique requires minimal power consumption in every testing cycle, however, without careful design, it may take up a large area in order to produce enough electrostatic force.

The second stimulation technique involves using a piezoresistive cantilever beam that is sandwiched with materials that have different thermal expansion. The beam construction is shown in Figure 2.3.1b. In a sensing operation, the deflection is detected via resistive change in the piezo material. To initiate the self-test function, a

(a) Parallel plate capacitor stimuli   **(b)** Piezoresistive beam   **(c)** Thermopile based sensor
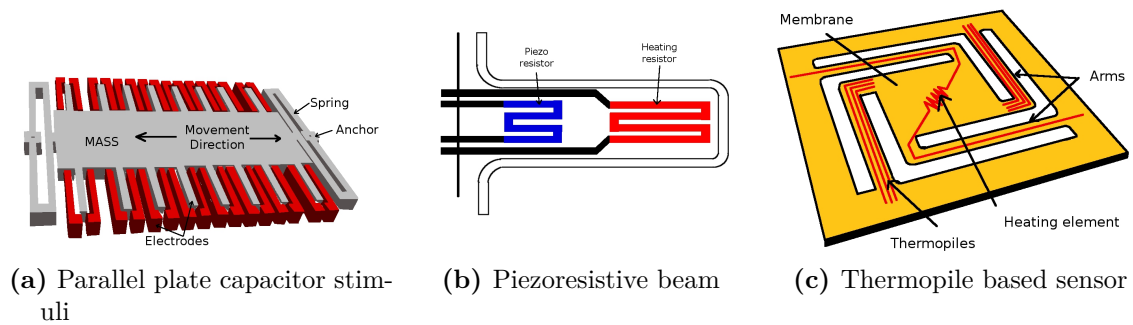
Figure 2.3.1.: Various techniques of electrical stimulation for self-test

small current is applied in the material that produces deflection due to the difference in thermal expansion in the material.

The third stimulation technique uses thermopile based sensors that apply the Seebeck effect. Thermopile is built using a series of thermocouples that convert thermal energy into electrical energy. It has been used for self-testing a MEMS membrane. The membrane is equipped with a heating resistor at the centre and a thermopile sensor as holding arms as shown in Figure 2.3.1c. In self-test mode, the resistors heat up the membrane and the temperature gradient at the arms is measured by the thermopile sensors.

These three methods are the most common techniques used to implement the self-test function in MEMS. The selection criteria for the stimuli technique particularly involves compatibility with the MEMS fabrication process. The first stimulation technique generally requires a greater area, and thermal based techniques require more power. These are also factors that influence the suitability of the new MEMS design.

2.3.2. Accelerometer System with Self-Test Feature

Allen et al. reported on the earliest effort to introduce a self-test feature in a MEMS accelerometer in 1989 [42, 43]. The accelerometer structure is shown in Figure 2.3.2. The self-test feature was used to test whether the mass was free to move for the acceleration measurement. It also provided feedback or calibration purposes about temperature changes over the time. The known quantitative value of the test signal gave information on how much calibration of the sensor output was needed. The self-test actuation was done using electrostatic force from a parallel plate capacitor. An electrode is embedded in the silicon cap on top of the seismic mass. Piezoelectric material was used to quantify the acceleration.
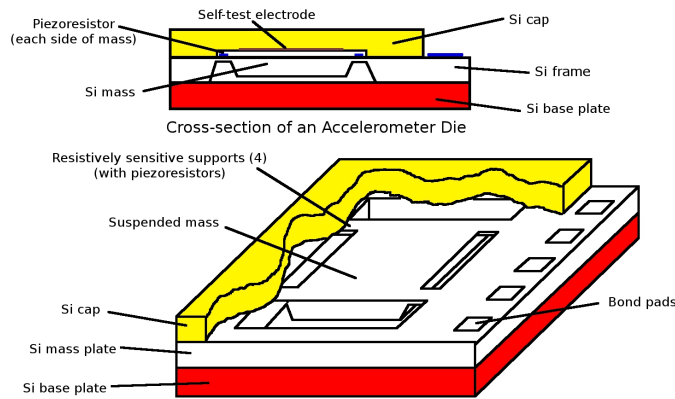
Figure 2.3.2.: Accelerometer with self-test

2.3.3. MEMS Accelerometer with Self-Test

Deb and Blanton reported on the implementation of self-testing in MEMS accelerometers [44, 45]. The self-test mechanism is based on a capacitive sensor build, and is in the form of a comb structure. The comb structure is divided into two parts. One part acts as the actuator for testing the mechanism and the other acts as sensor. This mechanism relies on electrostatic actuators to initiate the movement during testing cycle. The sensing element is used for both functionalities, acceleration sensing and self-testing.

The accelerometer has two modes of operation controlled by a two by two crossbar switch. In normal operation, the sensor will measure the acceleration, and during the test operation, electrostatic actuator will provide a reference stimulus for the sensor to measure. Using the same hardware for sensing and testing will definitely save some chip area, however continuous measurement and testing could not be implemented due to the need to interchange these functionalities.

2.3.4. Micro-Machined Accelerometer with Self-Test

Another study reported on an implementation of the self-test feature in MEMS accelerometer [46] that used electrostatic force for actuation and sensing. Figure 2.3.4 shows the MEMS accelerometer structure with a self-test electrode. The electrodes are in the form of comb fingers with lateral movement. The design is simple and utilises the existing process without any additional cost, however, the introduction of self-test electrodes slightly increased the overall size of the MEMS device.

2.3.5. MEMS Accelerometer with Thermal Self-Test Mechanism

Another effort to introduce the self-test mechanism to MEMS accelerometer was reported in 1992, and in this attempt [47], a thermal actuator was used to initiate
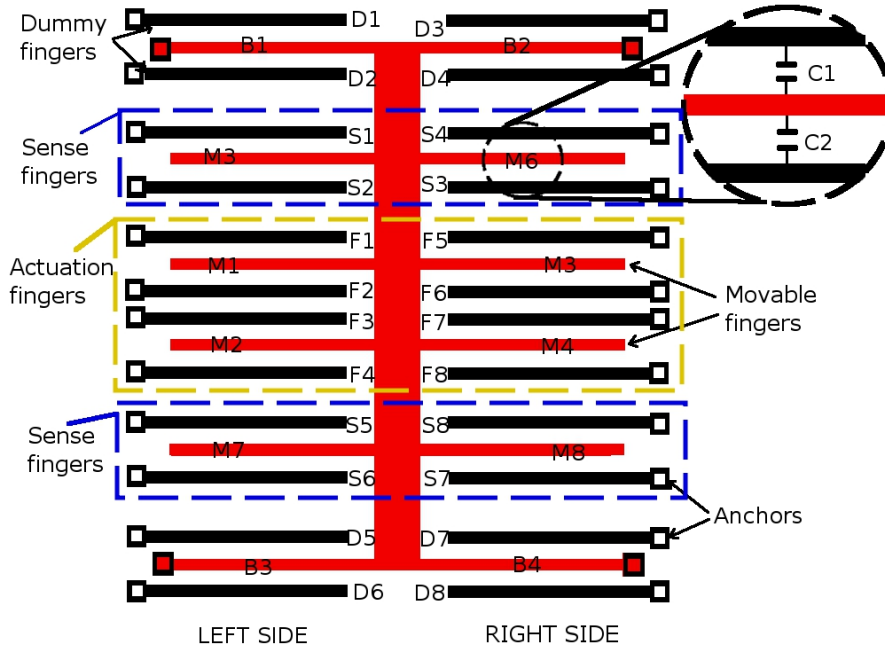
(a) Simplified top view of MEMS accelerometer

Applied Voltage	Normal operation	Self-test operation
V_{Act}	-	F_1, F_3, F_5, F_7
V_{Nom}	$F_1 - F_8$	F_2, F_4, F_6, F_8
	$M_1 - M_8$	$M_1 - M_4$
	$D_1 - D_8$	$D_5 - D_8$
	$B_1 - B_8$	

(b) Voltage biasing for different mode of operation

Figure 2.3.3.: Built-in self-test accelerometer

movement for the self-test mechanism. The construction of the accelerometer is shown in Figure 2.3.5. During this test routine, small voltage pulses were applied to the heat resistor and caused the beam to expand. This beam bent towards the seismic mass and pushed the mass down. This test routine will determine the state of the mass of this accelerometer. The writers suggest the accelerometer for airbag applications and that a routine test is implemented during engine starts. This ensures that airbag functionality is known before a journey starts.

2.3.6. CMOS-Based Monitoring of Contact Events

A research group from Purdue University has focused on improving the long term reliability of RF MEMS. They proposed a new technique to implement self-monitoring
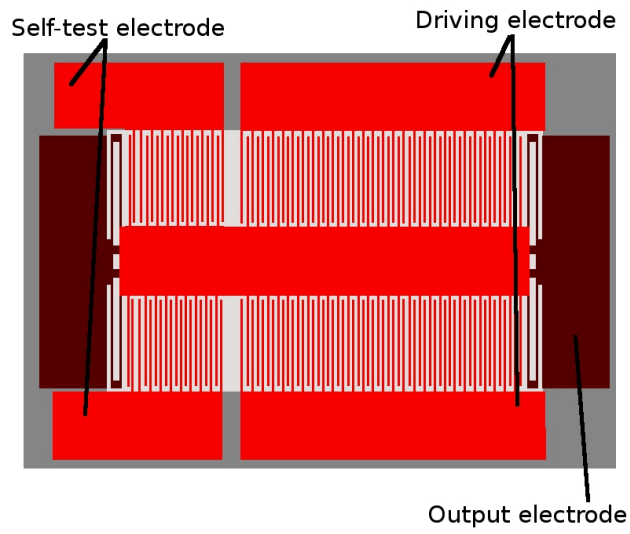
Figure 2.3.4.: MEMS accelerometer with lateral electrostatic actuation
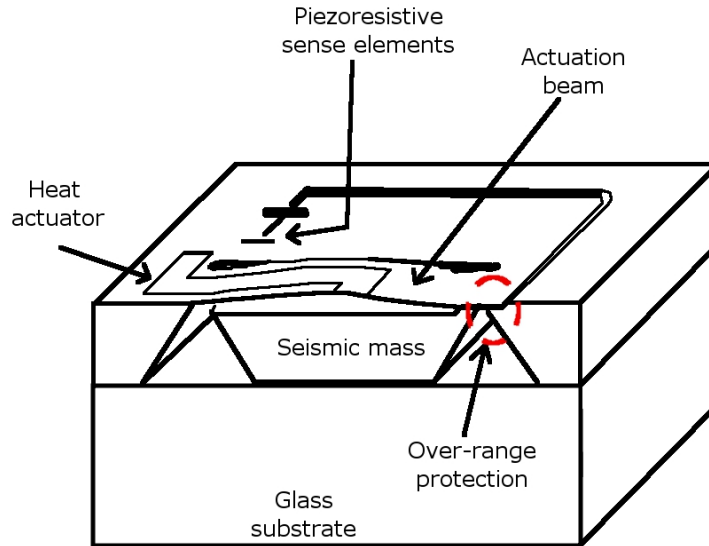
Figure 2.3.5.: Accelerometer with thermal self-test mechanism

of contact events in RF MEMS switches. Previous contact event investigation methods are not feasible for embedding in the final system. Some of the methods used previously are: a) direct measurement of contact resistance during contact events, b) optical measurement of mechanical structure behaviour during contact events, and c) surface analysis methods via physical and chemical composition studies. The new self-monitoring method proposed by Fruehling et al. in [48] uses CMOS technology to build a read-out electronics circuit [49]to measure the contact event in RF MEMS. The resistance measurement circuits require an area of $(105 \times 105)\,\mu m^2$, and are used to measure the R_{On} between the signal-in and signal-out line during contact events. The measurement setup is shown in Figure 2.3.6.
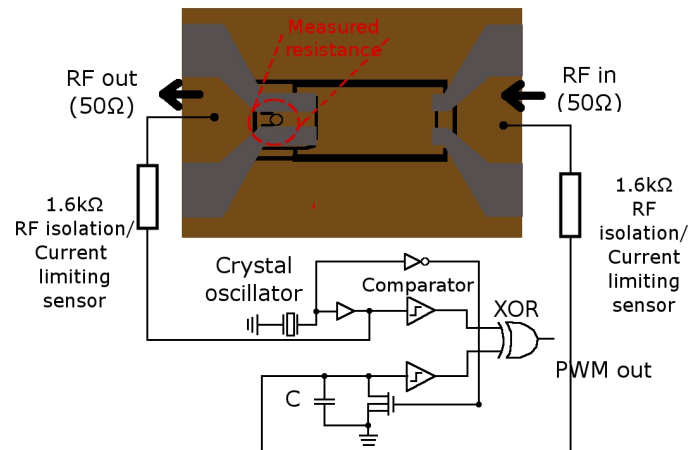
Figure 2.3.6.: Measurement of contact event for self-monitoring

2.3.7. Self-Test and Self-Repair of a MEMS Accelerometer

A research group from the University of Cincinnati has ventured to implement two self-x features in a MEMS accelerometer. Xiong et al. has reported an accelerometer design with these features [36, 50, 51, 52, 53]. The accelerometer design is based on capacitive sensing and actuating. The accelerometer structure for self-test features is shown in Figure 2.3.7a. It uses lateral movement of capacitive actuators, labelled as driving fingers. The actuator can be driven into both sides of the mass.

Xiong et al. proposed a redundant system method for self-repair implementation. The proposed accelerometer system [50] has six identical modules of accelerometer in one accelerometer system. Four modules are connected as the main sensing device and two modules serve as a redundant system. The implementation of a redundant system in the accelerometer has increased the overall area of the accelerometer. The device with the self-repair unit used an area of $(1500 \times 900)\,\mu m^2$ compared to a device without this feature which is only $(980 \times 900)\,\mu m^2$. An increment of 53% in area is due to redundant accelerometer modules in the system.

(a) Accelerometer with self-test structure   **(b)** Redundant system for self-repair in accelerometer
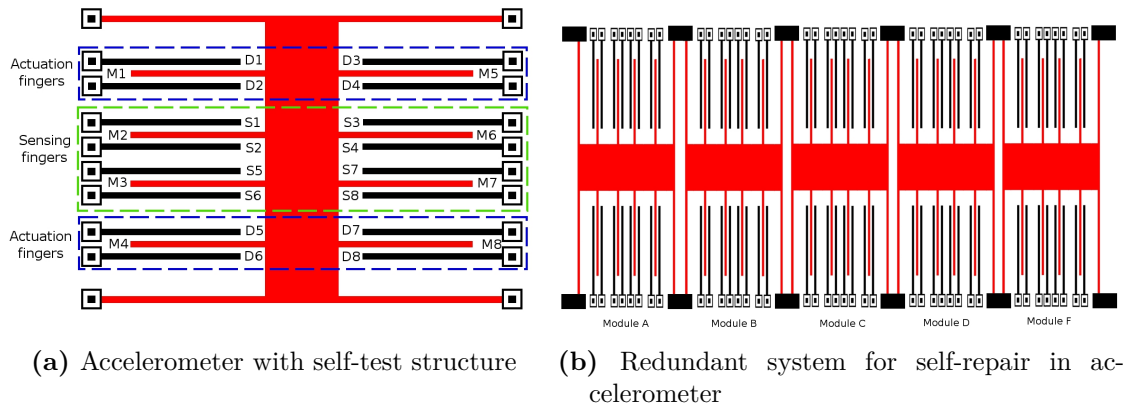
Figure 2.3.7.: Accelerometer with self-test and self-repair

2.4. Discussion of Existing Self-x Features in MEMS

After reviewing the current literature, it can be seen that most self-x features implementations are intended for MEMS accelerometer sensor. This is due to the fact that the accelerometer is one of the most successful MEMS products accepted in the market right now. A great deal of effort has thus gone into improving the design, performance, reliability and robustness.

Self-test implementation is the current research focus. A variety of methods used to initiate testing in the MEMS structure have been reported and discussed. Method selection is based on material and manufacturing feasibility. Other design factors that require consideration are design simplicity, power consumption, durability, low production cost, and repeatability, and the simplicity of controlling the mechanism.

Self-repair in MEMS is starting to garner attention from researchers in this field. The introduction of this ability is considered a step up in self-x implementation. It provides an active role through which the device can correct errors that may occur. So far implementation via redundant system has been reported and discussed. Even though this approach has increased the reliability of the system, it is still not immune to symptoms of 'common cause failure'. A different approach to self-repair implementation is required to really increase the robustness of the device.

In conclusion, there must be a trade-off in order to implement self-x features, involving the necessary cost and effort vs. the potential benefits in measurement quality and robustness and dependability of operation.

Table 2.2.: Summary of self-x feature implementation in the general literature and MEMS systems

Author	Summary	Applications	Year
Malsburg et al. [1, 38]	Self-organisation of orientation sensitive cells in striate cortex	Biology, brain system	1973
Eigen et al. [54]	A principle of self-organisation	Biology	1977
Kawahara et al. [55]	US patent of self-monitoring of computer system	Computer Hardware	1990
Pourahmadi et al. [47]	New thermal self-test mechanism	MEMS Accelerometer	1992
Charlot et al. [41]	Electrically induced stimuli for MEMS self-test	MEMS Accelerometer	2001
Deb et al. [44, 45]	Self-test MEMS accelerometers discussing the simulation result	MEMS Accelerometer	2002, 2006
Zhang et al. [56]	Self-configuration and self-healing in wireless sensor network	Wireless network	2003
Xingguo et al. [36, 50, 51]	Self-repairable MEMS accelerometer via redundancy	MEMS Accelerometer	2005, 2006
Isamoto et al. [57]	Self-assembly for MEMS vertical electrostatic actuator	MEMS Scanning Mirror	2005
Carlson et al. [58]	A flexible, self-healing sensor skin	Smart Sensor Material	2006
Ghosh et al. [59]	Self-healing for network system	Network	2007
Mohamed et al. [60]	Self-configured multiple-network interface socket	Computer Network	2007
Marikinis et al. [61]	Self-calibration of a vision based sensor network	Sensor Network	2009
Fruehling et al. [48]	CMOS based contact events monitoring up to 4 MHz using piezoresistive bridge for monitoring purposes	MEMS RF Switch	2010

3. Survey of Switching Devices and MEMS

3.1. State of Reconfigurable Circuits

In some applications, electronic circuits require reconfiguration capability. There are two potential categories. The first category offers a static reconfiguration in which only one-time reconfiguration is possible. It has been used as a corrective measure in manufacturing variations of the CMOS process by trimming passive component values for better precision. One of the examples [25] used a fuse-based method to trim the offset in the operational amplifier circuits. The reconfiguration is performed after evaluation of the circuit in the complete package. An array of fuse structures in the form of a snap-back NMOS transistor is embedded in the circuitry. This one-time trimming process will increase the output yield of the manufacturing process but it is vulnerable to dynamic effects such as drift due to temperature or moisture change, and aging effects.

In other static configuration applications, a zapping diode has been used for one-time programming capability [24].

A switch device is one method to enable a reconfigurable analogue circuit. Passive components such as resistors, capacitors and inductors can dynamically change values through series and parallel connections. A reconfigurable analogue circuit can be realised by having arrays of passive components with connections controlled
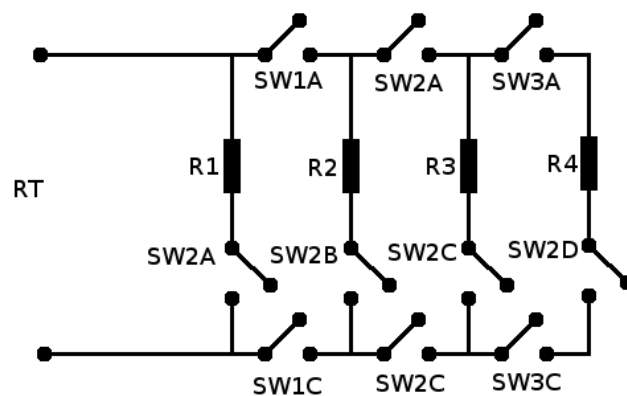

Figure 3.1.1.: Passive component array with switches for connection control

by switches. A switching element is an important component in electronic circuits. There are many switching devices that serve different kinds of applications and purposes. In general, switching devices can be categorised into several categories:

3.1.1. Electromechanical Relay (EMR)

Electromechanical relay is one type of switching device that uses electrical energy to produce mechanical energy for switching actions. Most of the relays use solenoids for switching actuation. Electrical current flows across the solenoid and produces a magnetic field that attracts movable armature to close the contacts. Electromagnetic relays have superior performance when compared to other types of switches in terms of power handling, high signal isolation and low insertion loss, however, they also have drawbacks in terms of size, power consumption during operation, and switching speed. Relays remain popular, especially in the automotive and manufacturing industries, due to their high power handling capability. A recent development in electromechanical relays has added self-monitoring capability to the relay to further enhance it capability [62, 63].

3.1.2. CMOS Transistor-Based Switches

Switching action is commonly realised using a semiconductor component in the form of transistor. There are many types of transistors, such as the bipolar junction transistor (BJT) and the field effect transistor (FET), which are catered for by various switching applications from low to high power circuits. For low power application, transistors act as a logic gate in the digital signal domain, and high power applications include switched-mode power supply. Transistors remain popular in many switching applications because of their small size and low cost, however for certain applications, reverse leakage current during the off-state might become a problem.

3.1.3. Solid State Relay (SSR)

Solid state relay [64, 65] is a by-product of semiconductor switching transistor devices that is able to handle high load current or voltage. The output signal is controlled by a light source from LED that activates a photo sensitive diode that turns the MOSFET transistor to the on-state. It gives total isolation of the control circuit from the load and that makes it similar to an electromechanical relay but without any movable structure. It has several advantages over electromechanical relays in terms of higher switching speed, increased operation lifetime because there is no movable structure, no audible noise during switching, and lower power consumption. There are also several disadvantages, however, especially in electrical performance. In closed state, higher resistance generates heat in the device, thus adding to the

electrical noise. In open state, a reverse leakage current is possible as in other semiconductor based switches.

3.2. Overview of MEMS Products

MEMS devices have played a prominent role among electronic devices. They are miniaturised multifunctional devices with a lower cost, are easy to integrate with other electronic circuits and have high reliability. In general, MEMS devices are categorised into two types based on their use and applications, sensory elements and actuator elements.

Miniaturised sensory elements from MEMS technology allow more possibilities to acquire more information in our electronic devices. The intelligence level of the product will be increased with better decisions and responses. Mechanical information such as acceleration, rotation and pressure can now be obtained via MEMS devices. Prior to MEMS, a fully mechanical accelerometer was so huge and heavy that it was only feasible for avionic applications. The introduction of MEMS accelerometers has made it feasible for use in the automotive industry for airbag applications. New markets in consumer electronic devices such as cameras, game controllers and mobile phones have increased the demands for the MEMS accelerometer. The MEMS gyroscope also has had a similar impact to the accelerometer. It has been used in cars to detect yaw, which has increased safety levels. The MEMS gyroscope has been used in smartphones to detect device rotation and positions.

The availability of micro actuators in electrostatic, electromagnetic, piezoelectric, and thermo-mechanical devices has opened the possibility of miniaturising many devices to microscale [66]. MEMS actuator devices have a huge impact in various fields of applications. Micro-pumps and nozzles in ink-jet printers have improved the print quality of computer printers [67, 68]. In medical instruments, the MEMS device for drug delivery and lab-on-chip for analysis has been introduced [69]. In display technology, a digital micro-mirror device (DMD) is used in projectors [70]. MEMS microphones have been implemented in consumer products. Switching devices also can be realised using MEMS technology [71, 72]. Optical switching for data communication is done using micro-mirrors as the actuator. RF-MEMS switches are another type of switch that can handle high frequency signals. The MEMS relays or DC-MEMS switches are designated to handle DC to moderate frequency signals.

MEMS technology has opened new doors of opportunity for new markets and new products. The market will continue to grow, as shown in Figures 3.2.1 [73] and 3.2.2 [74]. A total worth of almost 3 billion US dollars for the MEMS pressure sensor alone is projected by the year 2018, with the main application still dominated by automotives [4]. A recent market survey reported by Yole Development also projects that the market will reach over 6000 million US dollars in value for Bio-MEMS applications by 2018. These market reports show that MEMS devices are expected to become more prominent in the future.

MEMS Pressure Sensor Market Forcast by Applications 2012-2018
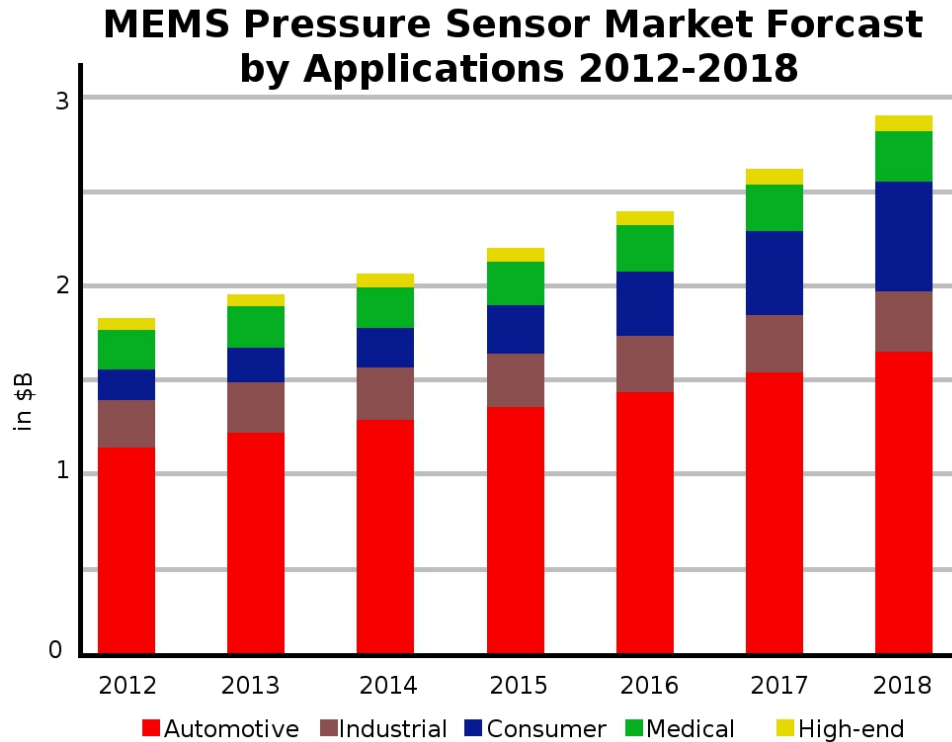
Figure 3.2.1.: Market research for MEMS pressure sensor published by Yole Development

There are many challenges before a new MEMS device can become a successful commercial product, however industry standard product reliability is one of the factors that MEMS devices need to fulfill before manufacturers start to use it in new products. MEMS can be categorised into four different classes based on reliability factors, as suggested by Tanner et al. [75].

A Class I MEMS device is one that has no moving parts; such as pressure sensors with a membrane layer that changes when stress is applied. The reliability of the Class I device is at lower risk since there is a low risk of damage during operation, and thus it is much easier for the device to be accepted the market.

Class II is defined as a MEMS device that has moving parts with no rubbing or impacting surfaces such as an accelerometer. In an accelerometer, a movable mass is used to detect the movement direction of the device, but there is no physical contact during operation. An extended fatigue test is required for the movable structure to ensure it can withstand operational cycles.

The risk to reliability is higher in a Class III MEMS device. This device consists of moving parts with impacting surfaces. A DC MEMS switch or MEMS relay is an example of a Class III MEMS device. Problems with wear and tear in the contact area are the main reliability concern. Repetitive impact will degrade the performance of the device. It is much more difficult to achieve a good standard of

BioMEMS and microsystems for life science market (in $M)
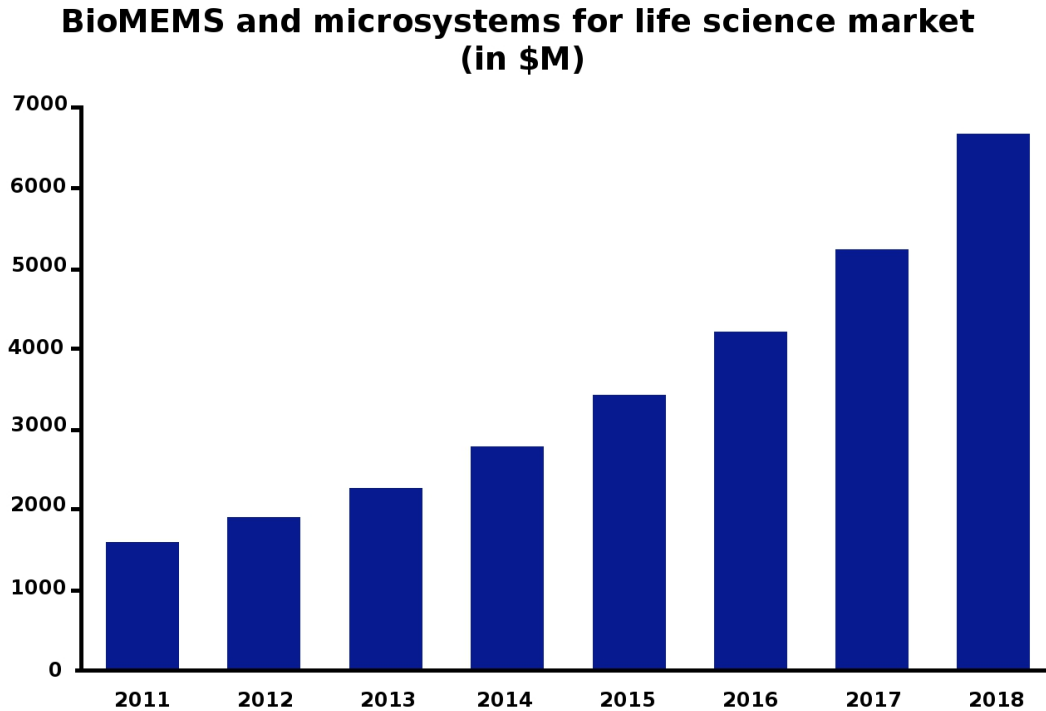
Figure 3.2.2.: Market research for Bio-MEMS published by Yole Development

reliability for this type of device.

Class IV devices have the highest reliability concerns. MEMS have moving parts with impacting and rubbing surfaces, and so the surfaces involved in these actions are prone to failure faster than those of other MEMS classes. Micro motors and microgears are two examples of MEMS that possess these features. Even though the concept design of these devices has been proved at a laboratory scale level, the product reliability issues have become the main obstacle to reaching the mass market.

3.3. Overview of MEMS Fabrication and Foundry Technology

The early stage of MEMS fabrication technology was derived from CMOS integrated circuit technology. Setting up MEMS manufacturing facilities requires a huge amount of money and fundamental knowledge. ISE and the Technical University of Kaiserslautern (TUKL) did not have their own MEMS fabrication facilities and thus it was necessary to outsource the manufacturing process. In Europe the initiative to expand MEMS technology is led by Europractice-IC services. Through Europractice, participant universities can use the MEMS facility offered of their

industrial partner to develop MEMS prototypes.

There are many advantages to using this method. The cost of a MEMS prototype can be lowered significantly, as a single wafer contains various designs from many participants. The manufacturing technology is also well proven and complete with the precise design rules. This gives a MEMS designer information about the design limits. When using this stable technology, the outcomes of the MEMS prototypes are closer to the simulation results.

There are also drawbacks from the perspective of research development. A controlled manufacturing environment will limit a researcher's creativity. Fixed material lists and manufacturing processes will limit the possibilities for the researcher to try new things, as they are bound by the technology's design rules. This research will thus concentrate only on producing new MEMS designs with additional functions, rather than improving device performance via introduction of better material or a new manufacturing process.

Europractice-IC services offer several MEMS prototyping technologies from their industrial partners. In 2011 and 2012, three different foundries offered MEMS prototyping services, namely IMEC-CMORE, Tronics Microsystems and MEMSCAP, although the latest offering of 2013 showed only the MEMSCAP foundry providing this prototyping service. For unknown reasons, the other technologies are no longer open for prototyping submission.

The IMEC's CMORE offers SiGeMEMS technology where monolithic integration with CMOS IC can be realised. The MEMS structure based on SiGe material is built on top once the CMOS process has been completed. Monolithic integration with CMOS will reduce parasitic capacitances, create fewer interconnections and a compact design, however at this point it is relatively high in cost compared to the price of MEMSCAP technology.

The MEMSCAP foundry offers a special programme called Multi-User MEMS Processes, or 'MUMPs'. This special programme provides prototyping services for realising new MEMS designs at lower cost. There are three different MEMS technologies: PolyMUMPs, SOIMUMPs and MetalMUMPs. These three technologies are suitable for different types of MEMS devices. The first task is to evaluate and determine which technologies are suitable for building DC MEMS switches.

PolyMUMPs technology is built using three poly-silicon layers and one metal layer. This technology has a minimum structure size of $2\mu m$ which is important when making a small MEMS device. Examples of MEMS devices that have been developed using PolyMUMPs are MEMS microphones, accelerometers, microfluidic devices and display technology. A single metal layer in this technology allows only for electrical signal routing and metal pad construction. There are three different polysilicon layers which enable lateral and vertical movement structure, however the desirable feature of metal-to-metal contact is not possible to realise in this technology. As a result PolyMUMPs technology is not a suitable technology for DC MEMS switches.

SOIMUMPs technology offers silicon on the insulator features. The main structure can be built using a silicon layer with a thickness of $10\mu m$ or $25\mu m$. It has two metal layers of $0.52\mu m$ and $0.65\mu m$, which are too thin to be a stable contact structure. SOIMUMPs has been used to build gyroscope and optical devices. Lateral and vertical movement using electrostatic actuation is possible using this technology, however building a DC MEMS switch using this technology will produce an inefficient design. This is because the technology relies on the silicon layer as the main MEMS structure and a switch with low contact resistance is difficult to achieve. For vertical actuation movement, metal-to-metal contact cannot be realised in the design. A metal-to-polysilicon contact is possible but it will produce high on-resistance in a DC MEMS switch. Metal-to-metal contact is possible for the lateral actuation movement, but this metal layer is on top of polysilicon. Since the metal layer is about $1\mu m$ in thickness, in the long term, the contact quality of the switching operation will deteriorate which will eventually result in polysilicon-to-polysilicon contacts. This is the main reason SOIMUMPs is not suitable for DC MEMS switches.

MetalMUMPs technology uses a high aspect ratio nickel layer with $20\mu m$ thickness as the primary structure. A $0.5\mu m$ gold layer on top of the nickel helps to increase the conductivity of the metal layer. It is also possible to grow a sidewall metal from gold of up to $3\mu m$ thickness, which is useful in the case of switches with lateral movement. A doped polysilicon layer at lower levels can be used to build passive elements such as resistors or electrical routing. A silicon nitride layer will act as an electrical isolation layer, and a trench structure in the silicon substrate can give additional thermal and electrical isolation. Metal-to-metal contact can be realised in this technology using lateral movement. The combination of nickel and gold in the layer will provide low resistance in the contact area and along the signal path. A combination of thermal actuation and electrostatic actuation is also possible in this technology. Based on these characteristics, MetalMUMPs technology is the most suitable technology for designing a DC MEMS switch.

3.4. Overview of MEMS Assembly and Packaging Technology

Assembly and packaging a MEMS device involves a new set of technological challenges. In general, there are six factors that influence these future technologies [76]. These factors are cost, integration level, form factor, speed, power consumption and functionality. Some MEMS devices require direct interaction with the environment, unlike an integrated electronic circuit that requires hermetic seal packaging. MEMS packaging techniques differ from one type of device to another, depending on the level of interaction with the environment. Moore's law is the most applicable to a digital domain circuit in which miniaturisation is the main target, and MEMS and the analogue domain are more acquainted with More than Moore direction [28]. In

this direction, the main motivation is circuit diversification in terms of functionality that produces systems with higher value. ITRS road map [27] have set the target for the future of packaging technology to enable System-in-Package (SiP) products.

Putting many functions in a single package sometimes requires more than one manufacturing technology. The monolithic design concept refers to a whole circuit being built on a single die and then packaged. This is easy to realise for integrated circuits since they are built on the same technology, such as CMOS technology, however the scenario changed slightly when MEMS technology started to evolve. The huge difference in the structure, scale, and different manufacturing processes meant that a new approach to device packaging was required. In the early days, the manufacturer produced and packaged the integrated circuit and MEMS device separately. There are not many company that possess both technologies at the same time. For a higher production yield, integration only takes place at the PCB level.

As MEMS devices were introduced into the market, a System-in-Package (SiP) started to evolve. In this second degree of circuit integration, the dice are manufactured separately and integrated into the same packaging via wire bond. This gives a significant advantage in terms of size and the cost. Until now this integration technique has remained popular due to its cost effectiveness and the production yield.

The next level of integration is called the 2.5D-system in the package [77]. This technology miniaturises the I/O pitch up to $50\mu m$ and the wiring pitch to $2\mu m$. In this technology, a silicon interposer is used as a medium to combine two separate dice from different technology. Microchip bump and Through Silicon Vias (TSV) is used for interconnection wiring. This allows smaller sizes, and more function can be embedded in a single package.

A 3D-system in the package is another level of integration where dice from different process technologies are stacked on top of each other. The connections between dice use $\mu bump$ and TSV technology. This integration will reduced the chip area but increase the chip's height.

A 3D-system in chip is a system that is built on the single die. Each layer represents a specific function from digital to analogue electronics, and finally a MEMS structure at the top of the die. IMEC Belgium has a research group dedicated to enabling this technology in Si-Ge-CMOS-MEMS on top technology [78]. The main challenge of this technology is to have compatible processes for all types of structure and achieve a high yield output. Since each layer is an active layer with specific functions, the next manufacturing process must not affect the complete layer from the previous processes.

In this research, with regard to physical/equipment restrictions, the first level of integration will be used, as it focuses on designing and developing new functions for DC MEMS switches. The MEMS dice are evaluated and tested using a wafer probe machine that is available in the laboratory of ISE.

3.5. Overview of MEMS Design Tools from Coventor

Coventor is one of the leading software companies in 3D modelling and simulation for micro-electromechanical system (MEMS). It offers several solutions in MEMS design and simulation including *Coventorware* and *MEMS+*. These two pieces of software complement each other in providing a better platform for MEMS product development. This section discusses the capabilities, advantages and disadvantages of both pieces of software.

3.5.1. *Coventorware*

Coventorware software offers an integrated suite from the design to simulation of MEMS. It offers good simulation speed combined with high accuracy and design flexibility. The hybrid techniques in combining 'Boundary Element Method' (BEM) and 'Finite Element Method' (FEM) for electromechanical physics produce a faster and more accurate simulation process. Unlike the other FEA tools, which compromise the number of meshing elements in the model to get a faster simulation speed, this hybrid technique uses the advantages of the BEM method without compromising the meshing elements. The design approach in *Coventorware* is based on the process-driven approach in which the manufacturing process has been set and considered at the initial stage of the design process. This approach provides a better design work flow with high efficiency. Every structure added to the design was done so with consideration for the manufacturing process. This eliminates potential manufacturing problems based on incompatible design.

Basic *Coventorware* software is comprised of two different modules called DESIGNER and ANALYZER. DESIGNER is a platform to create and generate both 2D layout and the 3D-solid models. Users are not limited to specific constructed libraries and they have the freedom to create any desired geometry for the design. In the DESIGNER interface, the material and manufacturing process information needs to be added. The information about material properties is used by the physics solver to obtain the accurate simulation results. The manufacturing process information, especially that for layer thickness, will be used in generating the 3D-solid models with high precision.

After design completion, the 3D-solid model will be imported to the ANALYZER interface. Here users will choose among the appropriate physics solvers that need to be studied for detailed physical analysis. ANALYZER has several multi-physical domains which are widely used in MEMS devices. In the electromechanical solver the effects of electrostatics, mechanics, piezoelectricity, piezoresistivity, thermomechanics and damping effects can be studied. The MemPZR solver will compute the resistance field, equilibrium potential and current density fields of resistors under mechanical stress. The MemHenry solver solves for the frequency-dependent resistance and inductance of a MEMS model.

The 3D-solid model needs to be meshed before running the simulation. The meshing process of the solid model is customizable according to user needs. When optimising the mesh output, ANALYZER provides the assessment in mesh quality. This will help inexperienced users to obtain a better mesh result for their MEMS model. After obtaining the appropriate mesh model, the boundary conditions need to be set accordingly before starting the simulation process.

The simulation results of ANALYZER can provide several analyses. These include modal analysis, harmonic analysis, contact boundary analysis, damping analysis and transient analysis. Parametric studies are also possible in this simulator, to find optimum parameter values by studying the trends or sensitivity of effects. The results can be visualised either in 2D format via graph or 3D visualisation via movie output (.avi files are generated).

3.5.2. $MEMS+$

$MEMS+$ software is another MEMS design and tool from $Coventor$. It is intended to provide software solutions for experienced Cadence software users in analogue and mixed signal design for introducing the MEMS device in their design. $MEMS+$ becomes the software bridge that connects analogue-mixed signal chip design with the MEMS design. It offers easier conversion between two platforms by importing the MEMS model into the Cadence software system for system level simulation. Electrical and MEMS behaviour can both be studied simultaneously using this approach. This is in line with the More than Moore principles [28] where more technologies and functionalities are embedded in a single chip.

The design approach of $MEMS+$ is the same as the $Coventorware$ design approach. The process-driven approach is used for better design work flow and high efficiency. For modelling and simulating a MEMS device, $MEMS+$ uses a different approach than $Coventorware$ or other FEA software. It has specific libraries that contain standard MEMS elements. A specific mathematical model with respect to the element geometry is embedded in each element library. This approach provides good accuracy and produces faster simulation computation when compared to conventional finite element analysis (FEA).

The $MEMS+$ software interface has three different tab interfaces. The first interface tab is the $Material\ Database$ tab. This tab is for adding the material database that will be used in the design. The material database is normally provided by the foundry that controls the manufacturing process. Users also have the ability to introduce new materials to the database for research purposes.

After introducing the material database, the next required information is the manufacturing process database. This needs to be added in the $Process\ Editor$ tab. Here the process information, layer name, type of material, thickness and other process properties will be given. It will use the material database file introduced in the previous tab as material reference. A warning error sign will be provided if

there any referencing problems. The process database is provided by the foundry that controls the process parameters. This is important in order to ensure that the model is reflecting the correct manufacturing process.

The third interface tab is called the *Innovator* tab. This tab can be activated only after the previous two tabs have been initialised properly. This is the area in which to build the 3D-solid model of the intended MEMS device. The *Innovator* tab provides three different viewing modes. The first mode is 'Component Viewing Mode' where a 3D-solid structure can be previewed. The second mode is the 'Mechanical Connector Viewing Mode' and shows the available mechanical connections between the elements inside the model. Users need to join these connections properly in order to obtain the correct mechanical behaviour. The mechanical joints can be set as either static or dynamic points. A function called *Expose* is used to select the important mechanical joints that require behaviour observation. The exposed joints will appear as output pins with the Cadence symbol. The third viewing mode is called the 'Electrical Connector Viewing Mode'. This mode will show the electrical components that exist in the model. For each electrical point, users need to define whether it is a ground point or a voltage potential point. The *Expose* function is implemented on the points that need to be investigated.

A 3D-MEMS model can be constructed by choosing the elements from the given library. For each element parameters can be introduced in the model for enabling parametric analysis during simulation process. All elements in the library are embedded within the mechanical domain. For multi-physical simulation, MEMS+ software is able to simulate electrostatic and piezoelectric effects. These effects are available for certain elements of the library. When designing a MEMS model in MEMS+, users need to have prior information about which parts of the design will include multi-domain effects. A working model can be produced with this cautious approach.

After completion of the 3D-MEMS model, it is exported to the Cadence software system where the 2D-layout, symbol and parametric model files are created. A system level simulation can then be performed as usual in cadence design workspace. The simulation results can be seen in 2D via graph plotting and 3D visualisation. The 3D visualisation can be viewed using the Scene3D interface in the MEMS+ model.

3.5.3. Discussion

Both pieces of software offered by Coventor have advantages and disadvantages. Coventorware offers a greater multi-physical simulation domain with high precision results. This advantage comes at the expense of requiring too high computational power and being time consuming. MEMS+ on the other hand offers the most common multi-physical simulations used in MEMS, which are electrostatic and piezoelectric. It produces good simulation results with a shorter simulation

time when compared to Conventorware. Fast simulation process with less accuracy is acceptable especially when it involves parametric analysis, as it is used to study trend and sensitivity effects. MEMS+ also has seamless integration with Cadence software workspace for system level simulation. This is suited perfectly to the available infrastructure in the ISE laboratory where Cadence has been used for years in designing analogue and mixed signal chip applications. Based on these factors, MEMS+ has been chosen as the design tool for MEMS in this research.

3.6. Overview of MEMS Switch Devices

The evolution of MEMS fabrication technology allows the integration of electrical and mechanical structures at micro-scale. This inspired researchers to design and develop new switch elements to replace conventional switch elements. In general, these can be divided into two categories, DC MEMS switches and RF MEMS switches. A DC MEMS switch is a switch that works in the DC to medium range of switching frequency (in the early GHz range). It provides a physical contact in the switching action, thus allowing DC signal flow with low resistance. It can be used as a direct replacement for electromagnetic relays, with superior features in term of size, switching speed, and power consumption. RF MEMS switches operate at a much higher frequency range mainly for microwave and telecommunications applications in GHz range. Physical contact does not take place in the switching actions since capacitive contact is used.

This section will review various MEMS switch designs. The reviews can be grouped into two, those of university-research products and of commercial products. The comparisons are made based on manufacturing technology, size, functions and switch configurations.

3.6.1. Electro-thermal Switch with Latching Mechanism

Electro-thermal DC MEMS switches with latching mechanisms have been reported by Khazaai et.al [79]. The MEMS switch is driven by two types of electro-thermal actuator; the V-shape actuator (VSA) and the modified-U-shape actuator (mUSA).The switch design is equipped with a latching mechanism so the switch only consumes power when changing states. Figure 3.6.1a shows the contact and the latch structures of the design.

The switch is built using MetalMUMPs technology provided by MEMSCAP Inc. It uses a nickel layer to provide metal contact which will obviously produce low contact resistance. The switch movement is lateral movement and has a series connection for DC signal application. The design is intended to achieve highly energy-efficient thermal micro actuators with low actuation voltage and high contact force.

3.6.1.1. Switch Designs

Two switch design configurations have been reported, their difference based on the heat actuator configurations. The first configuration is denoted as 'Config A' in Figure 3.6.1b using four VSAs to drive the contact and switch mechanism. The movable contact is attached to two VSAs at both ends in order to provide large displacement and force. Each latch is driven by a single VSA. These actuators need to activate in a specific sequence for single switch movement. Both of the latch mechanisms need to be activated first in order to make way for the contact mechanism to move. When the required gap is ready, the driving contact mechanism is activated. Once the contact is closed, the VSA latches are turned off, followed by the contact VSAs. The latches prevent the contact from returning to the original position and thus the power is only consumed during the changing state of the switch.

The second design, denoted as 'Config B' in Figure 3.6.1c, has a different actuator configuration. Only a single VSA is used to drive the contact and two mUSAs are used to drive both latches. In this configuration, the movable contact is equipped with capacitive sensors at both ends to detect mass displacement. This design is smaller overall compared to the previous design. Each VSA generates $\sim 13.5\mu m$ displacement with $\sim 8mN$ force at $1V$ with electrical power of $\sim 0.68W$.

3.6.1.2. Discussion

The switch design presented in this research solved the main problem of the heat actuator consuming power during switch operation. Limiting the power consumption the changing state only, via the latching mechanism is a good concept, however this solution may lead to another issue, which particularly concerns product reliability. Wear and tear in rubbing and touching components in MEMS is one of the serious concerns. The introduction of latching mechanisms increases the risk since the number of touching components has been increased. In the long run, the switch may fail when the wear between contact and latches causes a gap between two contacts.

The second problem that may arise is the stiction in the contact latch area. Since there is no reported self-repairing mechanism, the stiction may happen at any switching cycle that prevents the switch from turning from the on-state to the off-state. This kind of failure is critical, especially when the switch is used in safety-related applications.

Switching speed is another issue that requires attention. The heat actuator is already one of the slowest micro-actuators in response. The fact that these designs require several heat actuators to activate in specific sequence greatly hampers the switching speed performance. Total reliance on the heat actuator needs to be avoided, perhaps by combining other actuation methods.
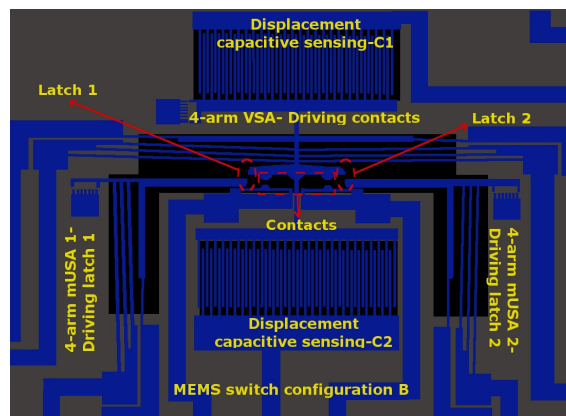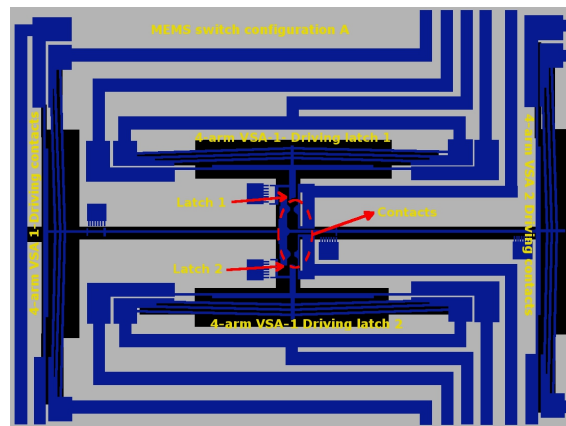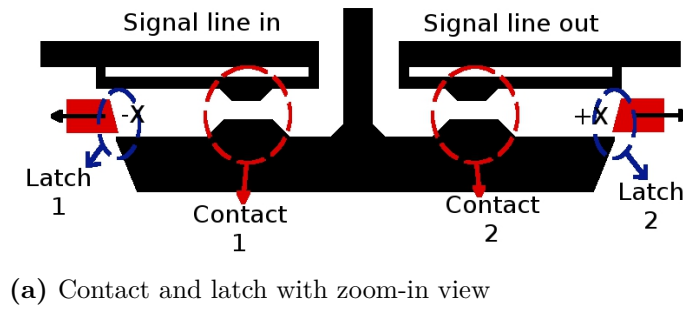
(a) Contact and latch with zoom-in view

(b) 'Config A'

(c) 'Config B'

Figure 3.6.1.: Electro-thermal switch configurations

3.6.2. Latching MEMS Switch from MEMSCAP Inc.

MEMSCAP Inc. has reported a DC MEMS switch with latching capability [80]. This allows the design to exist in bistable state without consuming power. It can handle signals from DC-6 GHz. The switch is built using MetalMUMPs technology and driven by a modified design of a Bi-morph heat actuator to provide a latching mechanism. The switch has lateral movement with a metal-to-metal contact config-

uration. The heat actuator uses $250mA$ of current for $40ms$ during each changing state operation.

3.6.2.1. Switch Design

A single SPST switch design requires two sets of heat actuators which are arranged in perpendicular arrangement as shown in Figure 3.6.2. The modified heat actuator is built by two hot arms and a single cold arm with flexures. Unlike a conventional heat actuator, the modified version has no electrical connection between hot arm and cold arms. The electrical current will flow between these two hot arms from one end to the other. A dielectric layer is used to connect these three arms and transfer the heat from hot arms to cold arms and produces deflection. The cold arm also acts as a signal line.

The switching mechanism needs a special actuation sequence in order to perform correctly. As shown in Figure 3.6.2 (b), the horizontal actuator is activated first in order to make clearance to allow the contact from the vertical actuator to move. The vertical actuator is then activated (Figure 3.6.2 (c)) to move the contact. The horizontal actuator will deactivate first followed by the vertical actuator. During switch-closed state, the horizontal actuator returns to the rest position but the vertical actuator remains under slight stress to produce the contact force needed. The reversal sequence is needed in order to turn the switch to open-state again.

In terms of size, 32 arrays of SPST switch are possible to produce in the area of $2.5mm \times 10mm$. The actuator resistance is measured at around 0.5Ω. A switching cyclic lifetime is measured at up to 500 000 cycles with current flow at $100mA$.

3.6.2.2. Discussion

This is another design that provides a latching mechanism to avoid continuous current consumption during thermal actuator during operation. This design has a simpler actuation sequence, is smaller in size compared to previous designs and minimises the rubbing area to only the signal contact areas. Gold remains the best contact material, and provides low contact resistance compared to rhodium and Pd/Co materials.

3.6.3. Electrothermal-Magnetostatic Actuated Micro Switch by TU Darmstadt

A research group from the Technical University of Darmstadt has reported a novel design to produce a bistable MEMS switch [81]. The switch is driven by two types of actuator. The electrothermal actuator is used as a primary actuator and in order to achieve bistable switch operation, a magneto-static force is used to hold the switch
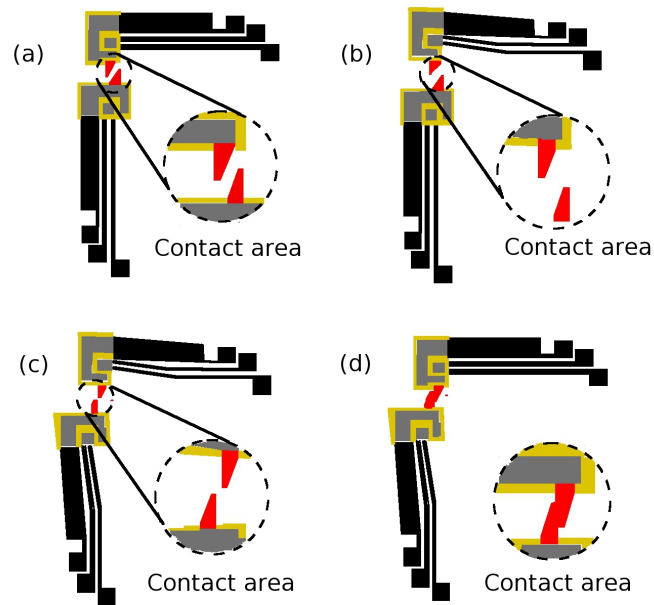
Figure 3.6.2.: Latching mechanism of MEMS relay by MEMSCAP

state. The design intent is to minimise the electrothermal actuator usage time but still obtain the benefits of this type of actuator in producing great force and large displacement of the micro-mechanical structures.

3.6.3.1. Fabrication Technology

The switch is built on ceramic substrate with nickel as the main layer for contact, signal line structures, and magnetic flux guide. Sacrificial layers of AZ9260, AZ nXt 125 photoresist and copper are used in the process. An Su-8 epoxy based material is used as electrothermal structure with a nickel layer as heat element.

3.6.3.2. Switch Design

The switch design as shown in Figure 3.6.3a consists of two U-shaped thermal actuators, one pendulum-like nickel contact, which is also a signal-in line, two signal-out lines and a magnet on the backside of the substrate. A connection to signal out A can be made by activating the U-shaped thermal actuator B. The thermal actuator will bend and push the nickel contact to signal out A. A complete magneto-static circuit shows in Cross Section A-A in Figure 3.6.3b, driven by rare earth magnetic material under the substrate, and provides magneto-static forces needed to hold the on-state of the switch. These mechanisms allow the switch state to remain stable without consuming power.

For every changing state cycle, the switch consumes $\sim 200mW$ power with actuation time of $< 400ms$. The switching time is recorded at $< 8ms$. The dimensions of a

single switch are $3.6 \times 5.8 \times 0.25 mm^3$. The contact resistance is recorded at $87.2 m\Omega$ with $12.4 mN$ force.

3.6.3.3. Discussion

This is a unique design that combines thermal actuator with magneto-static forces to create a bistable switch. The switch is relatively large in size and thus can achieve low contact resistance with huge actuation force. In most cases, the level of magnetic output force is difficult to control, however in this design, the magneto-static forces are applied in a smart way, where there is no control level needed.

3.6.4. NEMS/MEMS Switch by the University of California, Berkeley

A research group led by Hei Kam from the University of California has undertaken extensive research in the area of NEMS/MEMS relays. They focus on design, and on developing a MEMS switch for a digital logic circuit to replace the role of the CMOS transistor in digital circuits. Various digital logic functions such as buffer, NOT (inverter), AND and OR can be implemented using MEMS relay. Another design requirement is to use a compatible CMOS fabrication technology to allow easy integration and monolithic design with other CMOS circuitry.

A MEMS switch for digital logic application has slightly different requirements if compared to DC switch applications. For digital logic application, a high resistance value of R_{On} in the region $10 - 100 k\Omega$ is acceptable since the throughput of a relay circuit is limited by mechanical pull-in time rather than electrical charging delay. In contrast, an analogue DC switch application requires low R_{On} resistance.

3.6.4.1. Fabrication Technology

The MEMS relay is fabricated using 4-mask process flow as shown in Figure 3.6.4. Si-wafer is used as a substrate with a layer of SiO_2 on top. An amorphous-silicon layer of $50 nm$ thickness is then deposited to help better adhesion between the SiO_2 and W (Wolfram: tungsten) layers. The tungsten layer is also $50 nm$ in thickness. The first sacrificial layer of LTO, of $100 nm$ thickness, is deposited on top of the tungsten layer to create a mould of the contact dimple. The second sacrificial layer of LTO, of the same thickness, is deposited. The next step is to deposit a tungsten layer only in the area of the contact dimple to create a hardened contact. A $1 \mu m$ -thick layer of boron-doped polycrystalline $Si_{0.4}Ge_{0.6}$ was then deposited at $410°C$. This layer serves as the mechanical structure of the relay. The structure is then released by time etch in the vapour of hydrofluoric acid at $27°C$. The entire relay structure is then coated with ~ 0.25Å- thick TiO_2. All these processes are suitable
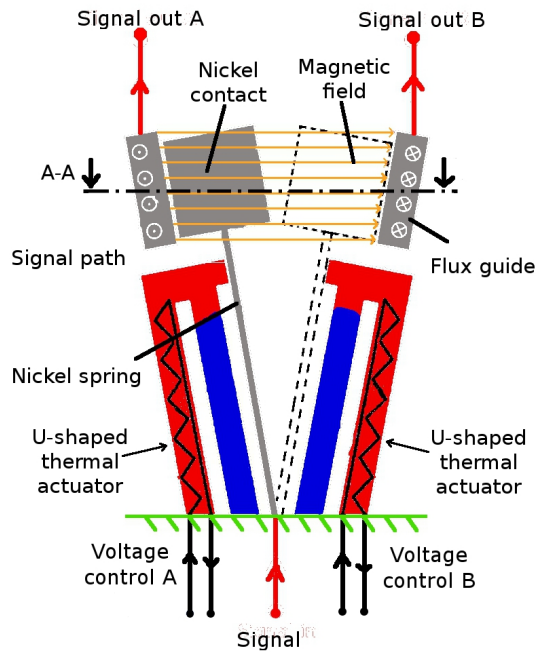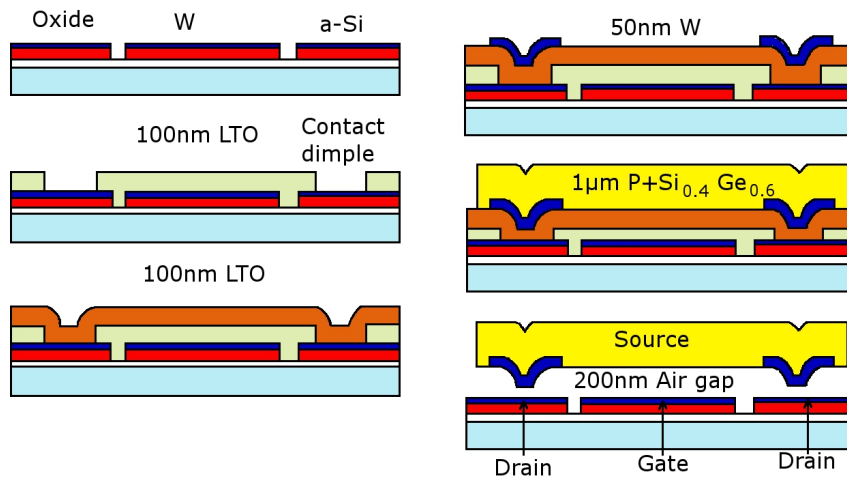
(a) Functional principle of MEMS Switch
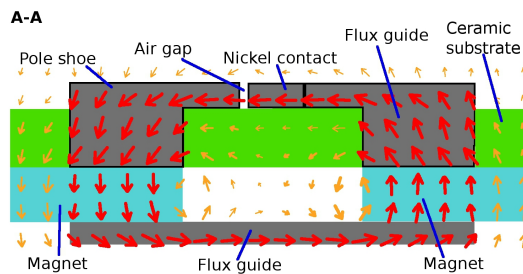
(b) Cross-section A-A show magnetic circuit to generate bi-stability of the switch

Figure 3.6.3.: Bistable electrothermal-magnetostatic MEMS switch

Figure 3.6.4.: The 4-mask process flow used at the University of California

for fabrication over CMOS circuitry since the maximum working temperature is only $410°C$.

3.6.4.2. Switch Designs

This group has reported two switch designs, seesaw relay logic [82] and 4-terminal relay design [83, 84, 85]. Seesaw relay logic, as shown in Figure 3.6.5a, is driven by electrostatic actuator. It has metal-to-metal contact using a tungsten layer with a vertical switch movement. A single see-saw design has two SPST switches that can produce three switching states. The movable structure is held by two torsion beams. Each side of the beam has a gate for electrostatic actuation and contact. The contact size is measured at $2 \times 7\mu m$ and will make a connection between the source and drain when the actuator is activated. The gap at the contact area is only $0.1\mu m$ and the gap in the electrostatic actuator is only $0.2\mu m$. Only a small deflection is required to activate the switch and thus the voltage to actuate the relay (V_{On}), which is about $7V$. The size of a single relay logic is $\sim (90 \times 46)\,\mu m$. The endurance is recorded as 10^9 switching cycles with V_{DS} set to less than $2V$ to avoid micro-welding in the contact area.

The second switch design is built using four serpentine springs as seen in Figure 3.6.5b. It uses a similar fabrication technology, however it has only a single SPST switch in a single switch structure. The switch movement is vertical and driven by electrostatic actuator. It has metal-to-metal contact in the form of a dimple and is built using hardened tungsten material to improve reliability. The MEMS relay recorded a contact resistance R_{On} of around $8.1k\Omega$ from a total apparent contact area of $8\mu m^2$. The overall size of a single MEMS relay unit is $(74 \times 63)\,\mu m$.

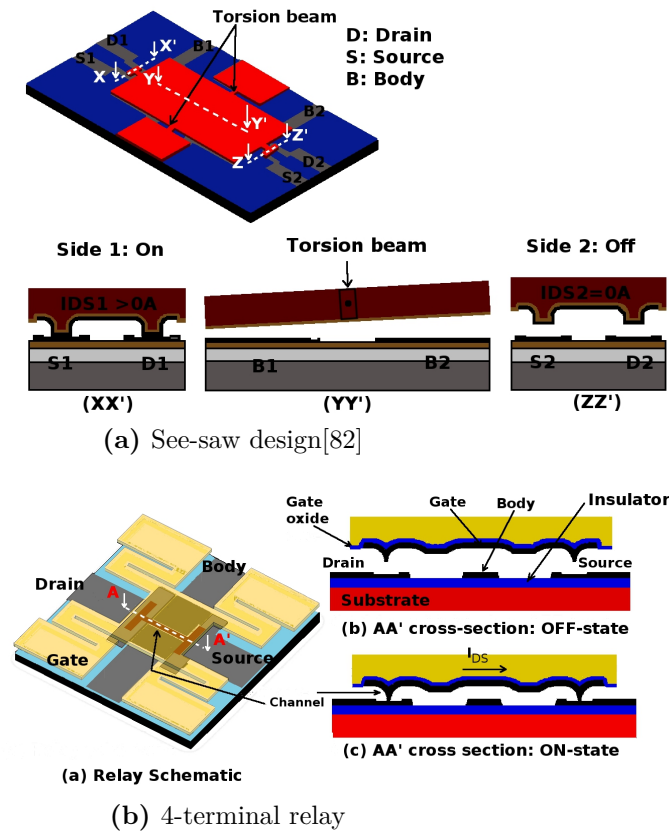**(a)** See-saw design[82]

(b) 4-terminal relay

Figure 3.6.5.: NEMS/MEMS switch design by University of California
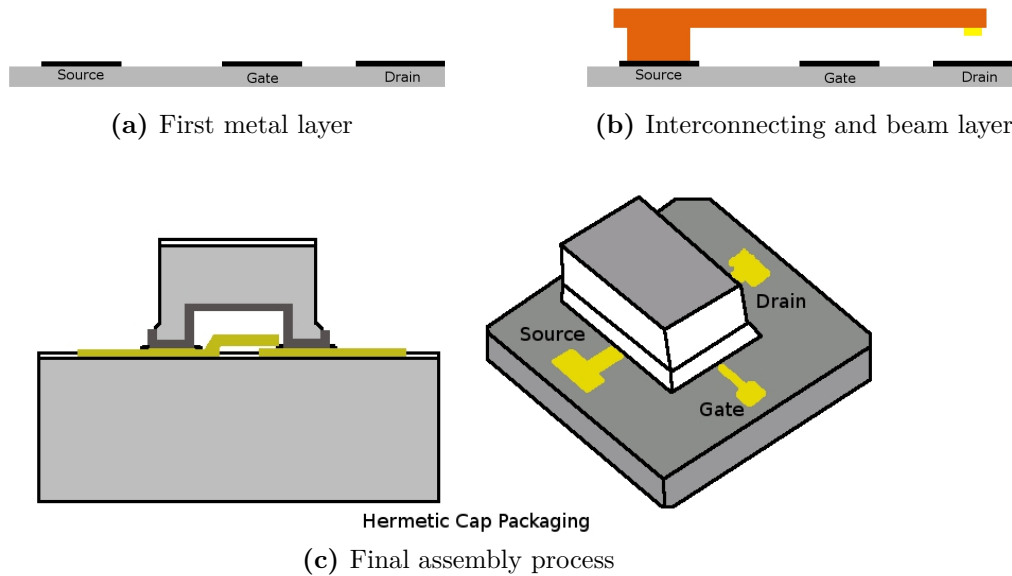
3.6.4.3. Discussion

Both switch designs have shown great potential to replace CMOS transistors in digital circuitry with the advantages of being small in size, and compatible with CMOS technology with real switch performance. However due to high contact resistance, they are not suitable for applications in the analogue circuit where low contact resistance is desired. The designs also have no additional self-x feature, however precautions have been taken to increase reliability by using tungsten as a contact material at the expense of increased contact resistance.

3.6.5. Radant MEMS Switch

Radant MEMS Inc. is one of the companies that produces wide ranging MEMS switches from DC to RF MEMS switches [1]. They claimed that their RF MEMS switches deliver the highest reliability, which is up to 1.5 trillion cycles of operations (cold switch). Various types of switches are offered such as SPST, SPDT, SP4T and SP6T. The signals that can be handled range from DC up to 40GHz with low

---

[1]http://www.radantmems.com/radantmems/products.html

(a) First metal layer

(b) Interconnecting and beam layer

(c) Final assembly process

Figure 3.6.6.: Fabrication process of Radant MEMS Switch

insertion loss. A typical handling power is 2W and some of 'high power' switches can handle up to 10W of signal.

3.6.5.1. Fabrication Technology

Radant MEMS established the fabrication technology to make MEMS switches in 1999. It uses three metal layers in the process. The first metal layer is used to define the source, gate, drain and bond pad metal areas. The second metal layer is for interconnecting and the third layer is for beam structures, which use an electroplating process over the source area. Finally the cap wafer is developed separately using a micro machined process. The final assembly process involves the switch and cap wafers being aligned and bonded together. The bond pad metal area will be left exposed for possible connections via wire bonding.

3.6.5.2. Switch Design

Radant MEMS switches use electrostatic actuation with a vertical switch movement. Metal-to-metal contact is used for DC signal handling with contact resistance $\sim 3\Omega$. A voltage actuation of $90V$ is required for most of the design. The switch sizes are relatively small, ranging from $1850 \times 1900\mu m$ to $1960 \times 1960\mu m$. The switch is delivered either in die packaging or a QFN package, depending on the customer's requirement. There is no additional structure for additional self-x feature available in the switch design.

3.6.5.3. Discussion

Radant MEMS is one of the leading commercial products in MEMS switches. It is a good balance between performance and reliability, which is needed in a commercial product. Since the switch requires $90V$ of actuation, DC-DC converter circuitry is required to produce the actuation voltage. This will limit the integration level of the overall system design to only discrete component integration. A single MEMS chip with an actuator driver could not be integrated in a single package since HV-CMOS technology can handle voltage up to $50V$ maximum. To increase the integration level, the MEMS switch needs to rescale so the actuation voltage can be lowered to less than $50V$.

3.7. ISE-DC-MEMS Switch Design Configuration

Four main elements are required for MEMS switch configuration in order to design a MEMS switch: the contact switch, the actuation mechanism, the switch movement and the circuit configurations. Every MEMS switch must have these four elements. In total there are 32 possible configurations required to build a MEMS switch. Figure 3.7.1 shows the possible configurations of MEMS switch.

The first factor is the contact type of the switch. Switch contact is an area where the two signal lines combine or separate. It will determine several switch parameters in signal isolation, power handling and signal frequency handling. There are only two possible contact types for a MEMS switch, as mentioned before. The type is metal-to-metal contact. In this type, a physical contact is present during the switch-
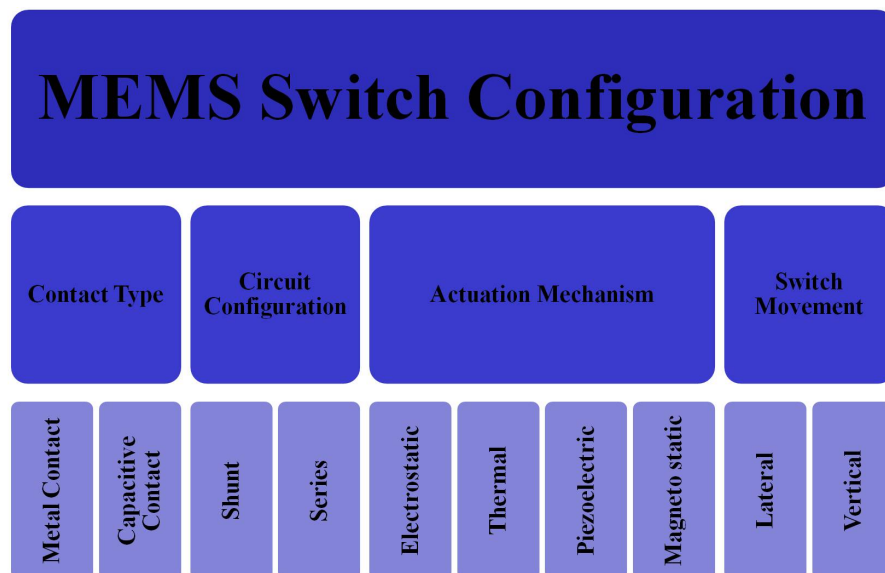
Figure 3.7.1.: Possible MEMS switch configurations

Actuator type	Voltage	Quiescent Current	Power	Size	Switching Time	Contact Force
	(V)	(mA)	(mW)		(μs)	(μN)
Electrostatic	20-80	0	0	Small	1-200	50-1000
Thermal	3-5	5-100	0-200	Large	300-10000	500-4000
Magneto-static	3-5	20-150	0-100	Medium	300-1000	50-200
Piezoelectric	3-20	0	0	Medium	50-500	50-200

Table 3.1.: Comparison of actuation mechanism performance

ing action for DC signals, and thus this type of device falls into Class III products which have a moderate risk of reliability concerns. The second type is capacitive contact. This contact does not involve any physical contact during switching operations and thus it falls into Class II MEMS devices that have lower reliability risk. Capacitive contact means it only allows AC signals with designated frequency to flow through. The working frequency can be altered via changing the gap of capacitive contact. Since the goal of this research is to enable self-reconfigurability in analogue electronics, only metal-to-metal contact seems to be suitable for the designated switch.

Actuation mechanism is another important element that drives the switch structure. There are four different types of actuators available; electrostatic, thermal, magneto-static and piezoelectric. Each type of actuator has their own advantages and weaknesses. Table 3.1 summarises a comparison of actuation mechanism features for MEMS switch [86]. The selection of actuator type depends on the MEMS fabrication technology that will be used, which is MetalMUMPs. In general, switches that consume virtually no power during operation are desirable. Electrostatic and piezoelectric actuators are suitable for this. The piezoelectric material is not available in MetalMUMPs technology. Thermal and magnetostatic actuators consume power during switching operations, thus, make it less appealing in the selection. The implementation of magneto-static actuators is not possible due to unavailability of the material in the selected technology. In conclusion, only electrostatic and thermal actuators can be implemented in MetalMUMPs technology.

The third element in MEMS switches is the switch movement. A vertical switch movement involves movement in the z-direction between two different layers. Normally this type of movement results in small switch size. For electrostatic actuators, a large actuation area can be easily achieved in vertical switch movement. Lateral switch movement involves structure movement in direction x and/or y. In general, it will produce a bigger switch size, especially when using electrostatic actuators. This is because the area for the electrostatic actuator is determined by the thickness of the layer. Since the thickness is a fixed value and normally small (e.g. $20\mu m$ for a metal layer in MetalMUMPs), increasing the length is the only way to obtain a bigger area. Because MetalMUMPs has one metal layer and one polysilicon layer, low contact resistance could not be achieved when using vertical switch move-

Element	Selection	Reason
Contact types	Metal-to-metal	• DC signal only works with metal-to-metal contact • Low contact resistance can be achieved
Actuation mechanism	Electrostatic and thermal	• Electrostatic as main actuator due to zero power consumption • Thermal as sub-actuator to provide high contact force
Switch movement	Lateral	• To achieve lower contact resistance in metal-to-metal contact
Circuit configuration	Series	• Suitable for DC and low frequency application • Theoretically it has infinite isolation in off-state

Table 3.2.: Summary of ISE-DC-MEMS switch configuration

ment. This is because the conductivity of the polysilicon layer is significantly lower $(6.5 \times 10^{10} \mathrm{pS}/\mu\mathrm{m})$ than a nickel layer $(1.25 \times 10^{13} \mathrm{pS}/\mu\mathrm{m})$ thus producing greater contact resistance. Lateral switching will be implemented for MetalMUMPs, but at the expense of size and resonance frequency.

In RF MEMS switches, there are two basic switch connections: the series switch and the shunt switch. The series switch can be described as a switch that is an open circuit in the off-state, and a short circuit in the on-state. In the ideal case, it provides infinite isolation in off-state, and zero insertion loss in on-state. For RF application, a series switch is used for relatively low frequency (DC to $40GHz$) applications. The shunt switch is placed in shunt between the signal line and the ground line. Ideally in off-state, it will have zero insertion loss, and in on-state it has infinite isolation. This type of connection is normally implemented in high frequency $(5 - 100GHz)$ applications. Figure 3.7.2 shows the difference between both MEMS switch electrical models. The series connection will be used in this research, since the application is in the DC signal range.
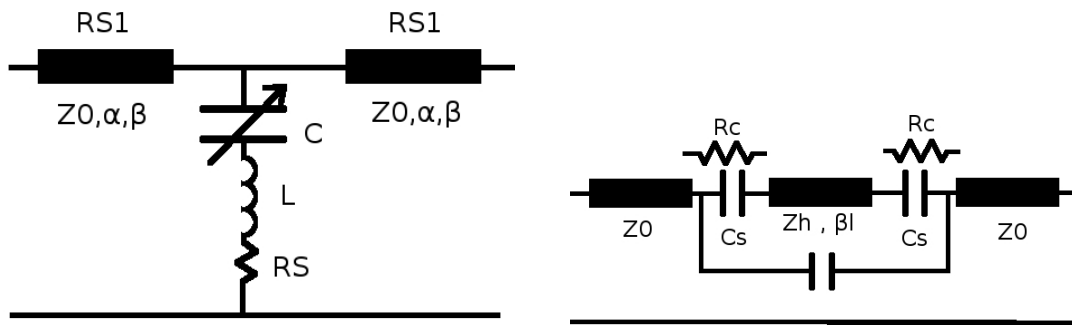
Figure 3.7.2.: Comparison of electrical model between two types of configuration

3.7.1. Challenges in DC MEMS Switch Design

In order to efficiently replace electromagnetic relays, there are several challenges that DC MEMS switches need to overcome [87]. The first challenge is the currently all-too-small gap between the contacts in the DC MEMS switch design. A typical switch gap is in the range of $10\mu m$ to $20\mu m$. Although it is possible to have a bigger gap, the limiting factor will be the micro actuator design. Most micro actuators can travel less than $20\mu m$ depending on the design. The achievable small gap can cope with low to medium signal voltages and provide mediocre isolation for higher frequencies, however it might be difficult to implement a sufficiently large gap from the technological point of view to replace a relay that is able to withstand thousands of volts and/or provide high isolation for very high frequencies.

The second design challenge is to generate a huge contact force in MEMS. The micro actuators have smaller contact force which can affect switch performance in producing a constant contact force and low contact resistance R_{On}. The electromagnetic relay produces several hundreds of micronewtons compared to micro-actuators. So a proper design in terms of contact material, and optimum actuator design, is required.

Reliability and endurance in contact area is another design challenge. Low contact resistance is desired in DC MEMS switches. In order to achieve this, a gold layer has been chosen since it has the best electrical conductivity properties, however gold is considered a soft metal that deteriorates over a the number of switching cycles. In the long run, gold may be not a good choice. Nickel is another metal that has good conductivity and is considered a hard metal. As discussed in Section 3.6.4, tungsten has been used by one research group in UCL Berkeley, but the hardness advantage from this material has a counterproductive effect in low conductivity behaviour. The search to find the best material for contact design needs to be continuously pursued in order to optimise DC-MEMS switch ability.

4. ISE-DC-MEMS Switch Design

4.1. Designing MEMS with MEMS+ Software

The MEMS+ software, as explained in Section 3.5, has been used to design a 3D-model of the ISE-DC-MEMS switch for this research. Figure 4.1.1 shows a snapshot of the three interface tabs when using MEMS+ for designing the MEMS switch. The material database and the process file has been provided by Coventor and verified by the MEMS foundry (MEMSCAP Inc.) who control the manufacturing process.

There are limitations, however, especially with regard to the electrical models of electrical components. Firstly, electrical component models neglect resistance along the electrical path[1] by considering it an ideal conductor. The second limitation is the restriction on introducing electrical components into structures. An electrical component can be introduced by selecting a mechanical structure and then adding an electrode feature to it. There are two types of electrode that can be introduced, bottom plate electrodes and side electrodes. In the case of an ISE-DC-MEMS switch, the side electrode is used due to the lateral movement of the switch.

The electrode can be introduced only in certain mechanical libraries. The side electrode can be created on a structure using only a rectangular and arc beam library [2]. Any structure which does not fulfill this requirement cannot be introduced as an electrical component. The implication of this restriction is that some of the areas intended for electrical components cannot be initialised properly. An example of this problem will be further explained in Section 4.9.4. This restriction means that the final electrical model does not adequately represent the actual device.

The third limitation is that the comb structures for electrostatic actuators can be built only under a rigid body [3]. The model makes an assumption that all comb fingers are rigid throughout the simulation and this behavioural model does not produce accurate results. Evidence of this problem can be seen via the stiction problem in the ISE-DC-MEMS switch. This is why stiction occuring in the actual device, as reported in Chapter 6 cannot be detected during simulations. The solver considers the fingers of the electrostatic actuator as a rigid body and thus no bending behaviour is modelled in it.
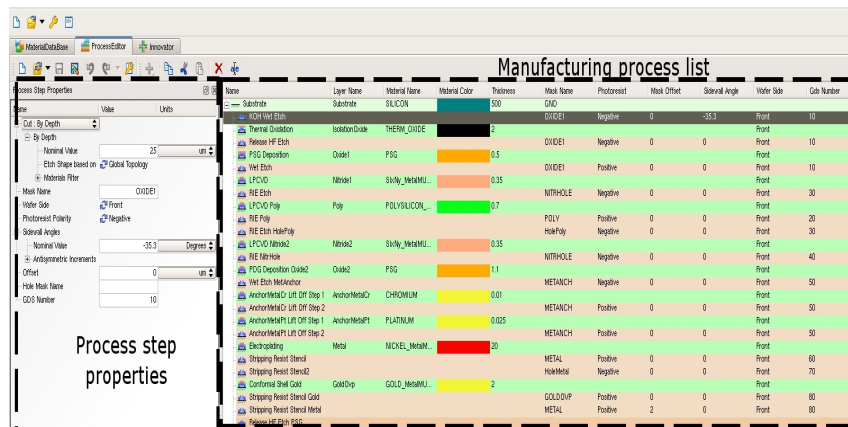
---

[1]MEMS+ USER Guide and Reference pages 4-18, 6-27, 6-78
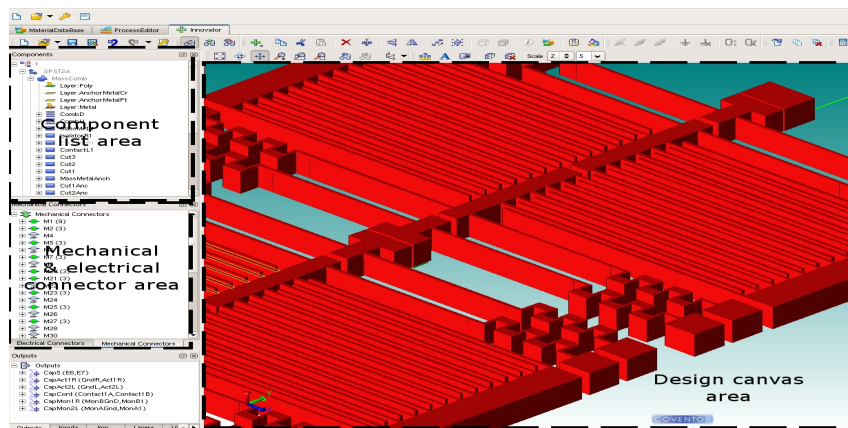[2]MEMS+ USER Guide and Reference pages 6-38
[3]MEMS+ USER Guide and Reference pages 6-44
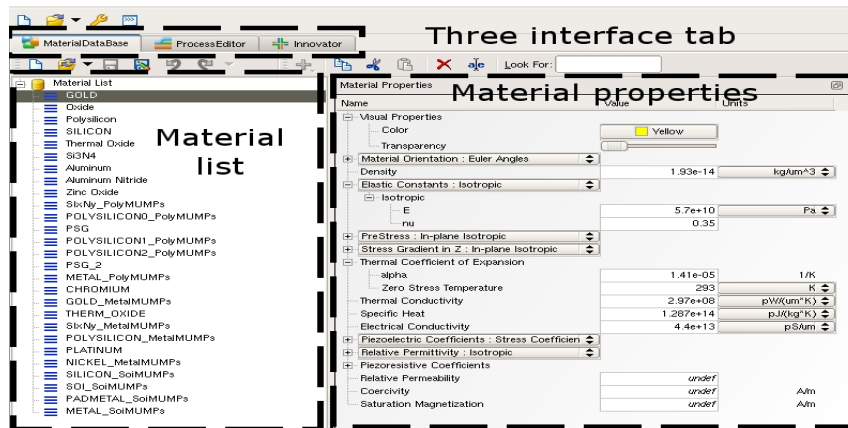
(a) Material Database tab

(b) Process Editor tab

(c) Innovator tab

Figure 4.1.1.: Three interface tabs for designing 3D Model in MEMS+ software

4.2. ISE-DC-MEMS Switch Requirement Analysis

The main purpose of this research is to study the feasibility of using a MEMS switch to complement the transmission gate typically used in integrated analogue circuits for switch applications. There is a need for a viable DC-switch that is small in size, and low in power and voltage during operations. The ability to handle high power signals, provide good signal isolation during the off-state and low resistance during the on-state are the desired properties of a DC switch. In this research, efforts have been made to reach the stated goals. The design requirements of a MEMS switch have to be divided into two different domains, electrical and mechanical. Table 4.1 shows the initial design requirements of desired switch.

This research involves two design cycles for prototyping development. In the first design cycle, several targets were set and implemented. The main objective is to design a DC MEMS switch based on the MEMS switch configuration that has been set. One of the main features involves evaluating the feasibility of using electrostatic actuation in MetalMUMPs technology, as this technology formerly relied on a thermal actuator in the nickel layer [88, 89, 79]. The actuators feature unidirectional design and bi-directional design in lateral movement. Two types of switches in SPST and SPDT are also designed and developed, and additional features for self-repairing and self-monitoring are implemented in the first design.

In the second design cycle, different design targets were set. The main focus was to improve the electrostatic actuator design for lower voltage actuation, in order to be compatible with HV-CMOS technology. This will allow a higher integration level in System-in-Package (SiP) between the MEMS switch, HV-CMOS die and the sensor element. Experiment results from the first prototype showed loopholes in the MEMS design process and simulation. A further study to eradicate these problems has been proposed and implemented in the second design process. The second prototype will be used to validate the proposed design process.

After determining the general MEMS requirements, the focus is now to identify the sub-element of the MEMS switch. The design configuration of the MEMS switch has been summarised in Table 3.2. There are two types of switch designs: SPSTV1 and SPDT switches. The design of these two concepts will be presented and discussed.

4.3. SPST ISE-DC-MEMS Switches

SPST refers to the Single Pole-Single Throw switch which has two signal terminals to handle one signal-in and one signal-out line. It has two movable body mass structures. Each of the body masses controls one signal line. The SPST switch is equipped with two types of actuators. Electrostatic actuators are considered the primary actuators while heat actuators are secondary. During switching actions, each actuator needs to produce a minimum $5\mu m$ of lateral movement.

Electrical Domain	Mechanical Domain
Contact Resistance: $<3\Omega$	Size: As small as possible
Power Consumption: As low as possible	Max. Switching Freq.: As high as possible
Self-monitoring: To monitor the movability of body mass structure	Self-repairing: To release any possible stiction in the MEMS structure
Actuation voltage: $< 90V$ (lower than Radant MEMS switches)	Resonance frequency: As high as possible

Table 4.1.: MEMS requirement analysis of first design cycle

Electrical Domain	Mechanical Domain
Electrostatic Actuator: Scaled the design to be lower than 50V for HV-CMOS compatibility	Study of the optimum value of safety design factor, S in the electrostatic actuator
Switch Type: Concentrate on SPST switches with many design variables	Higher integration level under single package between MEMS dice and CMOS dice
Self-monitoring: Improvement of the capacitive sensor with guarded rings design	

Table 4.2.: Analysis of MEMS requirements for second design cycle

Each of the movable bodies has a set of four anchor springs. Two of these springs act as heat actuators which provide bi-directional movement. One of the spring lines acts as a signal line while the other acts as a capacitive sensor. The capacitive sensor is used to enable the self-monitoring function. It is built using two parallel plates, with one movable plate attached to the body mass and the other embedded on the substrate. The change of capacitance in this sensor will provide information on the position of the body mass.

The bi-directional heat actuators enable the self-repairing function in case of stiction. The two areas that are susceptible to this failure are in the metal contact area and the electrostatic actuator fingers. The actuator that provides an opposite movement against the switching action, labelled as 'self-repair' in Figure 4.3.1, will help to release the stiction in these areas.

The sub-elements in ISE-DC-MEMS switches are summarised in Table 4.3, and Figure 4.3.1 shows the isometric view of a SPST MEMS switch model.

Element	Descriptions

Actuator	• Electrostatic actuator:
	  ○ Primary source as there is no power consumption during operation. In the form of comb structure with offset
	  ○ Uni-directional only for SPST switches
	  ○ Uni- and Bi-directional for SPDT switches

	• Heat actuator: Secondary source in case of high contact force required. Consumes power during switch operation
Switch Contact	• Nickel layer and gold layer on top are used to provide low contact resistance with lateral movement
Signal Line	• Identical structure to heat actuator built from nickel layer for low resistance loss
Body Mass	• A beam structure to hold comb structure, contact area, capacitive sensor and signal line
	• Built by nickel layer and oxide layer with special cut in nickel layer to provide isolation between signal line and electrostatic line
Spring structure	• A special form of beam that is built from nickel and that holds the contact, body mass and capacitive sensor
	• Serves different functions as signal line, heat actuator and self-repair element
Self-monitor	• A similar structure to contact structure but provides different function to monitor the movement of body mass
Self-repair	• A structure incorporated with heat actuator that provides an opposite direction of movement from the switch closed action

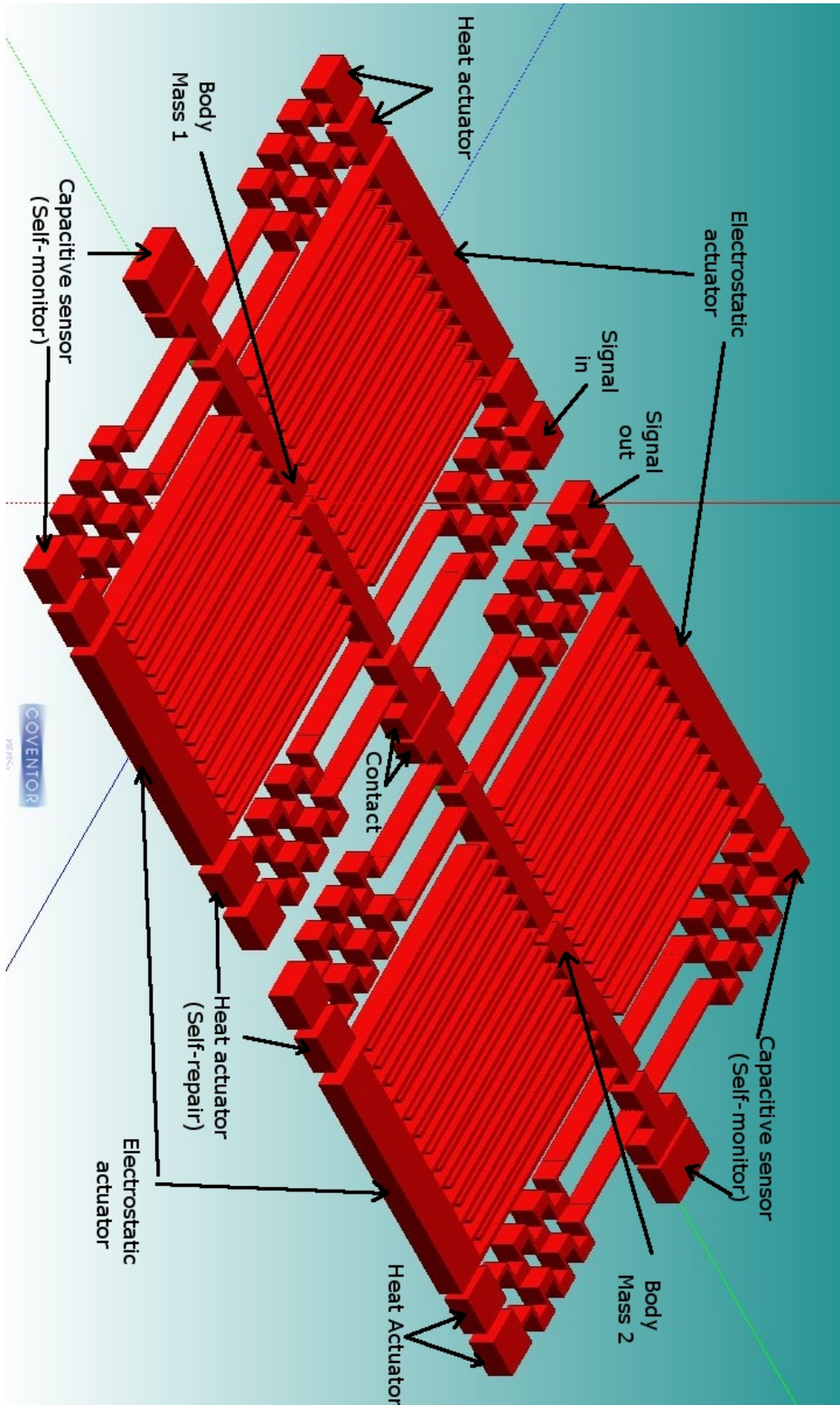**Table 4.3.:** Summary of sub-elements of ISE-DC-MEMS switches

Figure 4.3.1.: The SPST MEMS switch

4.4. SPDT ISE-DC-MEMS Switch

In the first prototype, a single pole double throw (SPDT) type switch is included. The SPDT MEMS switch design is only available in the first prototype sample due to limited space in the dice. The SPDT switch is built with three movable masses equipped with electrostatic actuator and heat actuators as shown in Figure 4.4.1.

The left and right masses have unidirectional electrostatic actuators, and the actuator design is identical to the SPST V1 design. On the other hand, the electrostatic actuator for centre mass has a bi-directional movement capability. The difference is due to the need for centre mass to make contact with either contact one or contact two. The centre mass is anchored by a four axis beam that can act as heat actuator. The overall length of the centre mass is slightly bigger at $1500\mu m$ compared to the side masses which are $1000\mu m$ in length.

This design is also equipped with self-x features in self-monitoring and self-repairing. In self-monitoring, only the side body masses have the dedicated structure of capacitive sensors. Although the centre mass has no capacitive sensor, the self-monitoring feature is still applicable in this switch with the information provided by the two capacitive sensors from the side masses.

The self-repair feature is enabled by a pair of heat actuators in each mass that provide bi-directional movement. The actuator construction and design principles are similar to those of the SPST switch design.

4.5. Mode of Operation

One of the unique features of the ISE-DC MEMS switch is that it can operate in various modes of operations depending on the target application. This section discusses the possibilities for operating and using SPST and SPDT switches in an optimum way.

4.5.1. Mode of Operation for SPST Switches

There are three different possibilities for operating the switch in SPST switches. These possibilities are due to the switch design which has two micro actuators embedded in it. The electrostatic actuator consumes minimum power but with less output force. The second actuator is the heat actuator which produces high output force and deflection but consumes relatively high power.

4.5.1.1. Electrostatic Actuation Only Operation

In this operation, the switching action uses only electrostatic actuation. This operation is suitable for battery powered devices since it consumes minimal power during
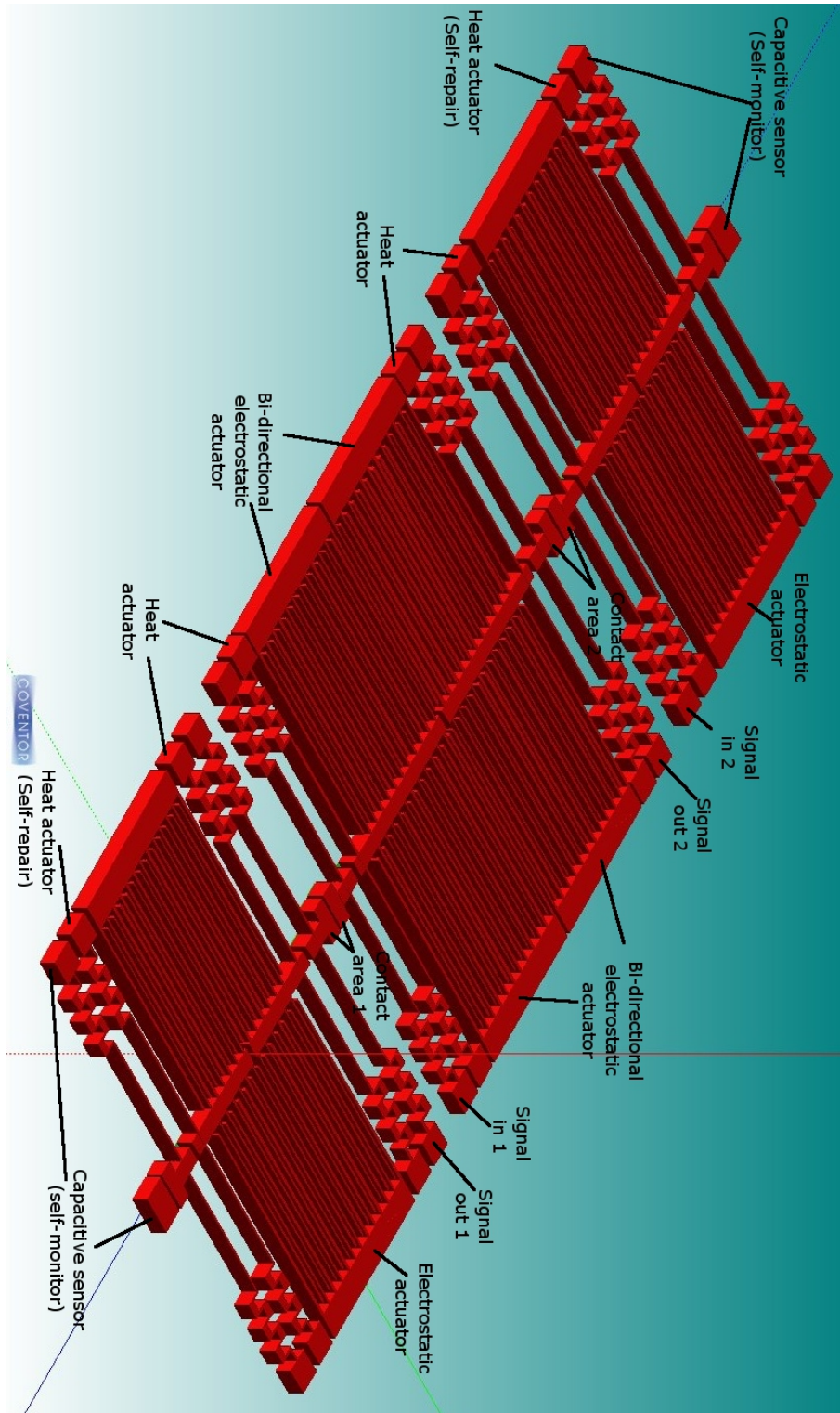
Figure 4.4.1.: A SPDT MEMS Switch

the switching operation, although a higher voltage DC-DC converter driving circuit maybe required. Only a single SPST switch is available for each MEMS device. Self-repair is realised by the heat actuators. The self-monitoring function is realised by the capacitive sensor on each mass, however, this sensor offers low sensitivity due to the small size of capacitance detection.

Due to the linearity of the electrostatic actuator, the MEMS switch can be also turned into a varactor (variable capacitor). This can be applied in the dynamic region phase before it enters the pull-in region phase as shown in Figure 4.6.1. Here the gap between contacts can be controlled, which in turn varies the capacitance value. This is also possible for tunable filters with a limited range of capacitance value.

4.5.1.2. Heat Actuator Only Operation

For applications in which power supply is not an issue, such as automated test equipment in the manufacturing industry, the ISE-DC MEMS switch can be operated using only heat actuation. The power consumption will be in the range of hundred milliwatts during switching operations.

The main advantage of using this scheme is that there are more switch elements available from a single MEMS device. The switch can be configured as three separate SPST switches with a maximum of two switches operating at the same time (SPST 1 and SPST3). It can also turn into a single DPST (Double Pole Single Throw) plus a single SPST via external connection. Both configurations are shown in Figure 4.5.1.

In this mode of operation, the self-monitoring function is realised by the electrostatic comb structure. This provides a higher sensitivity in capacitive sensing since a bigger capacitance value can be created from the comb structure. The self-repairing function is also provided by bi-directional heat actuators.
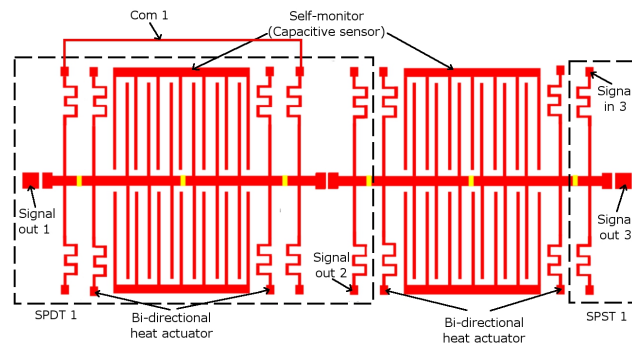
4.5.1.3. Hybrid Actuation Operation

Hybrid actuation mode is a condition where both electrostatic and heat actuators are used during switch operation. For a complete switch action, each of the body masses needs to travel $5\mu m$ for metal contact to make physical contact. In this mode a smaller current is used to provide half an initial switch movement and the other half is contributed from the electrostatic actuator. The electrostatic actuators are used to maintain the contact throughout the switching process.

The advantage of this mode is that it will provide better power consumption when compared with heat actuator mode and provide a better contact force when compared with electrostatic actuator mode. Each of the comb structures in this mode are divided into two parts. One part is used for electrostatic actuation and the other part is used for the self-monitoring function.
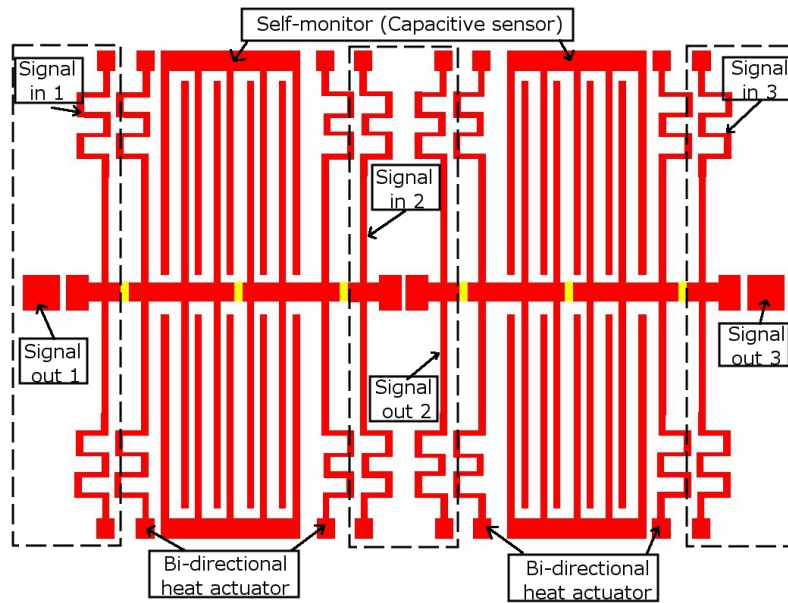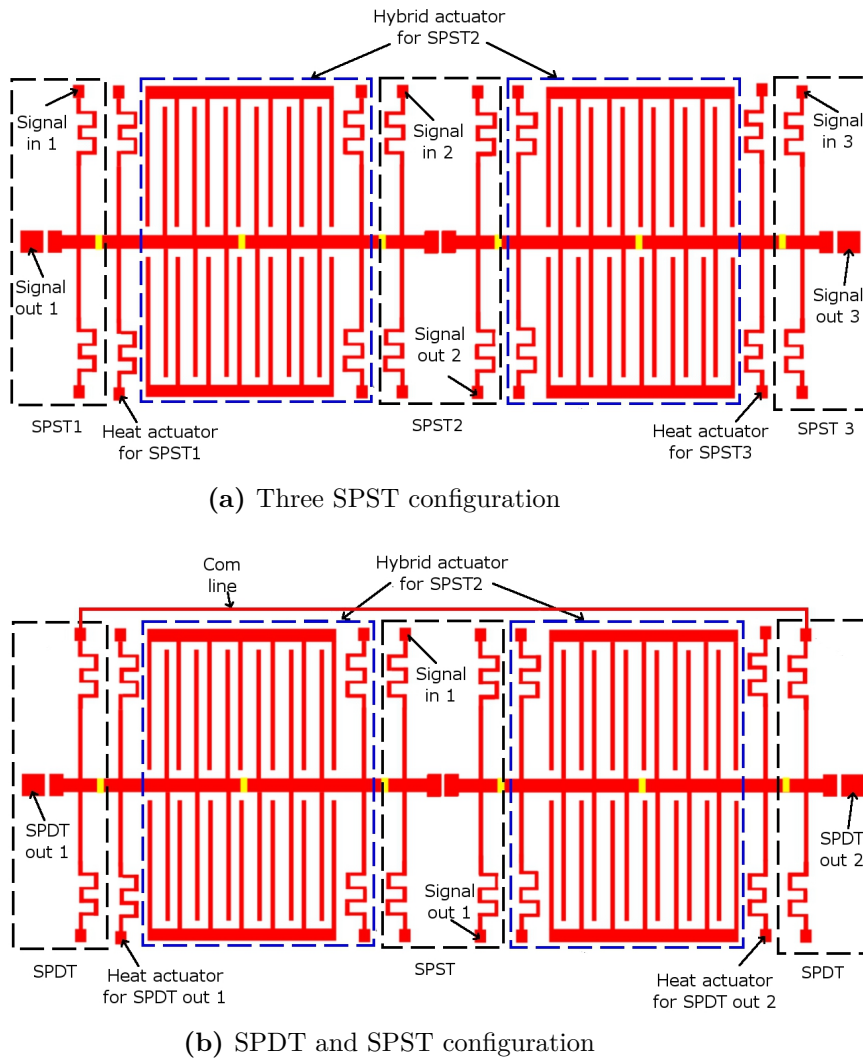
(a) Three SPST switch configuration

(b) Switch configuration SPDT and SPST

Figure 4.5.1.: Heat actuator only operation switch configuration

(a) Three SPST configuration


(b) SPDT and SPST configuration

Figure 4.5.2.: Hybrid actuation operation

The switch configurations are a similar configuration to the heat actuator, but operation means more switching operations in a single MEMS device. Three SPST switches can be set, but only SPST 2 can be driven with hybrid actuation function. The other two SPST switches will rely solely on heat actuation. Figure 4.5.2 shows the switch configuration and the MEMS sub-element functions.

4.5.2. Mode of Operation for SPDT Switch

Similar to SPST design, this switch can be reconfigured into two types of switch configuration. Figure 4.5.3 shows the standard configuration setup for SPDT MEMS switches. The standard configuration will be a SPDT switch design with one common line and two separate signal lines labelled Com Line, Signal Out 1 and 2. In
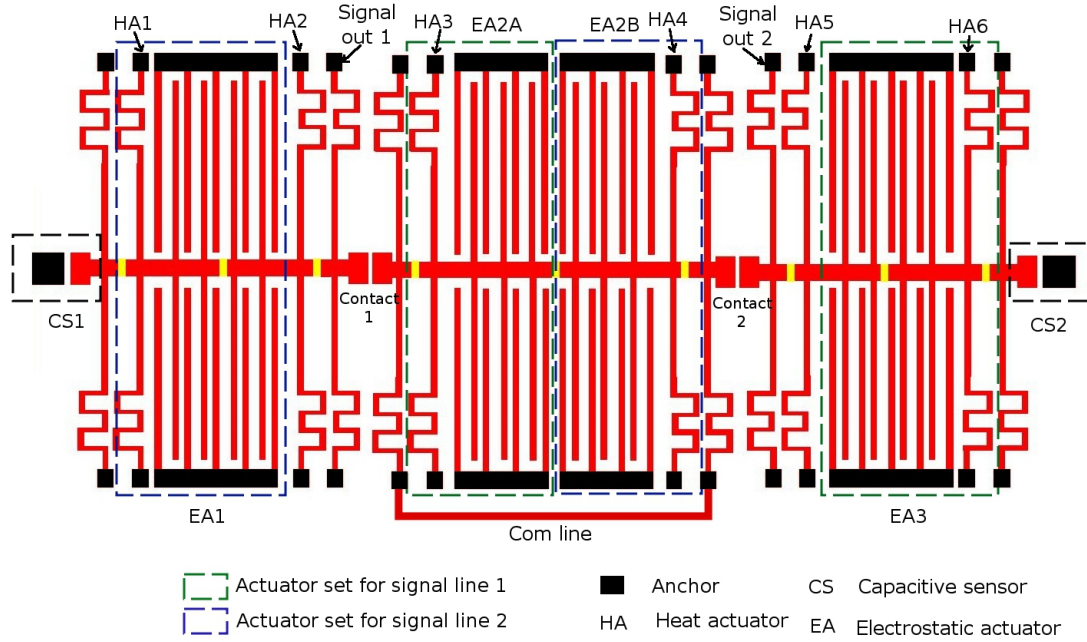
Figure 4.5.3.: SPDT standard configuration

this configuration, the switch can be driven by either electrostatic actuator or hybrid actuation. The full functionalities of self-monitoring and self-repairing are made available for this configuration.

For Contact 1, the self-monitoring feature is enabled by capacitive sensor CS1, and the self-repairing feature is driven by heat actuators HA2 and HA3. As for Contact 2, the self-monitoring feature is enabled by capacitive sensor CS2, and the self-repairing feature is driven by heat actuators HA4 and HA5.

The second possible configuration consists of two SPST switches and one SPDT switch in a single MEMS device. Figure 4.5.4 shows the setup configuration. In this configuration, the SPST switches are driven by heat actuators only. HA2 will control the SPST1 switch, with CS1 becoming the contact area. On the other side, the HA5 controls the SPST 2 switch with CS2 becoming the contact area. The self-monitoring feature for both switches will be handled by EA1 and EA2. The previous electrostatic actuation structures are now turned into capacitive sensors for the SPST1 and SPST2 switches with higher sensitivity. The self-repairing features are empowered by heat actuator HA1 for SPST1 and HA6 for SPST2.

The SPDT signal line remains as in the previous configuration. The difference is in actuation control, as the connection in Contact 1 is made possible by the heat actuators HA1 and HA4. As for Contact 2, the actuators HA3 and HA6 are responsible for switching actions. The self-monitoring features in SPDT are enabled by EA1, EA2 and EA3. These capacitive sensors with higher sensitivity will allow self-monitoring function in all three masses.
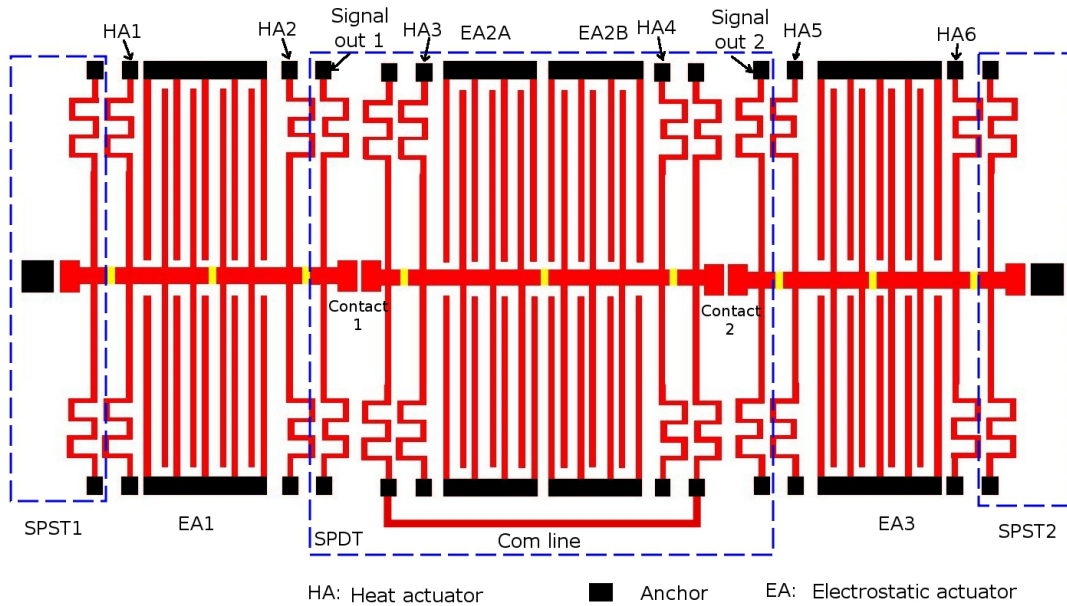
Figure 4.5.4.: Second possible configuration with one SPDT and two SPST switches

4.6. Mechanical Model of the MEMS Device

In this research, the design and simulation process requires a tool that is capable of handling the electrical and mechanical domain. One of the emerging pieces of software in this field is the MEMS+ software from Coventor. This software offers direct integration with Cadence CAD/CAE software for electronics design and simulation. As this research group is mainly involved in mixed signal analogue chip design using Cadence software, the addition of MEMS+ software is the perfect software companion for design and simulation activities for MEMS devices.

In designing a MEMS switch device, several types of simulations are required to ensure the functionality of a new MEMS model. The most critical part in MEMS is the actuation element. In order to implement self-x features in the switch, two actuation types in the electrostatic actuator and heat actuator have been implemented. These core elements influence the overall MEMS structures and behaviour. Various types of simulation for validating the MEMS device behaviour will be discussed in the next sections.

4.6.1. Electrostatic Actuator Design

The simulation of electrostatic actuation for determining the pull-in voltage needed by the MEMS switch can be done via mechanical DC analysis. A DC simulation analysis shows the behaviour of an electrostatic actuator between two plates when
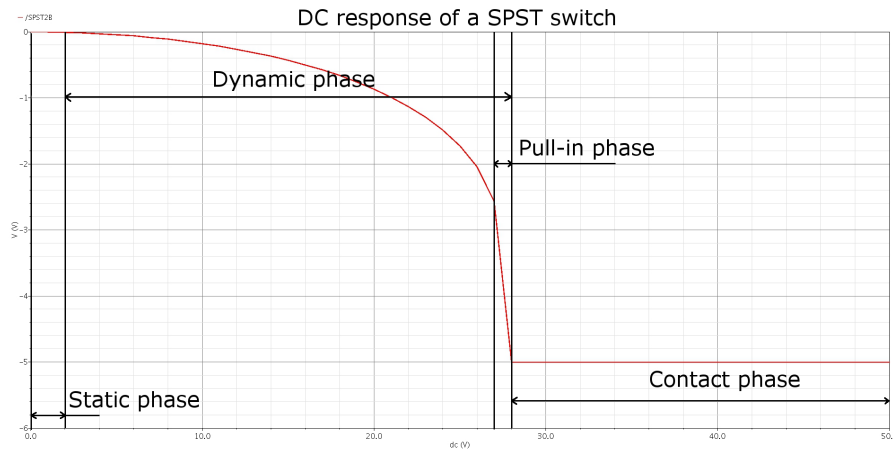
Figure 4.6.1.: Mechanical DC-analysis of an ISE-DC-MEMS switch

DC voltage is applied to it. It shows the mechanical movement of the MEMS structure when the electrostatic force overcomes the spring force. Every DC simulation has three different phases: a static phase, dynamic phase and contact phase. Based on the results of this simulation, the behaviour of the structure with an increase in actuation voltage can be observed.

A static phase is a phase where the electrostatic force is very much less than the spring force which results in no movement in the MEMS structure. As the voltage applied is increased, the MEMS structure will enter the dynamic phase. The MEMS structure starts moving when the electrostatic force is greater than the spring force. In the dynamic phase, there are two different states, linear and non-linear movement. A linear movement state shows the linear increment of deflection with respect to voltage. A non-linear state, also known as 'pull-in state', shows huge deflection with a small increment of voltage.

The final phase is known as the contact phase, where the physical contact is established between two plates. There is no additional movement in this phase since the plates are blocking each other. Any voltage increment will increase the force between two contacts, which helps to reduce the contact resistance between them.

The second structural analysis in the MEMS switch is the mechanical AC analysis. This analysis will simulate the structural behaviour of MEMS when operating in the high frequency range. The outcome will show the resonance frequency of the MEMS structure. This information will determine the maximum bandwidth of the switching commutation rate. The switch will not work properly if it switches at the same or close to the resonance frequency. The resonance effect will not allow the switch to make a settled and proper contact. Figure 4.6.2 shows an example of a mechanical analysis result. In this example, the MEMS device recorded a resonance behaviour at $6.31kHz$ with amplitude at $32.96nm$.

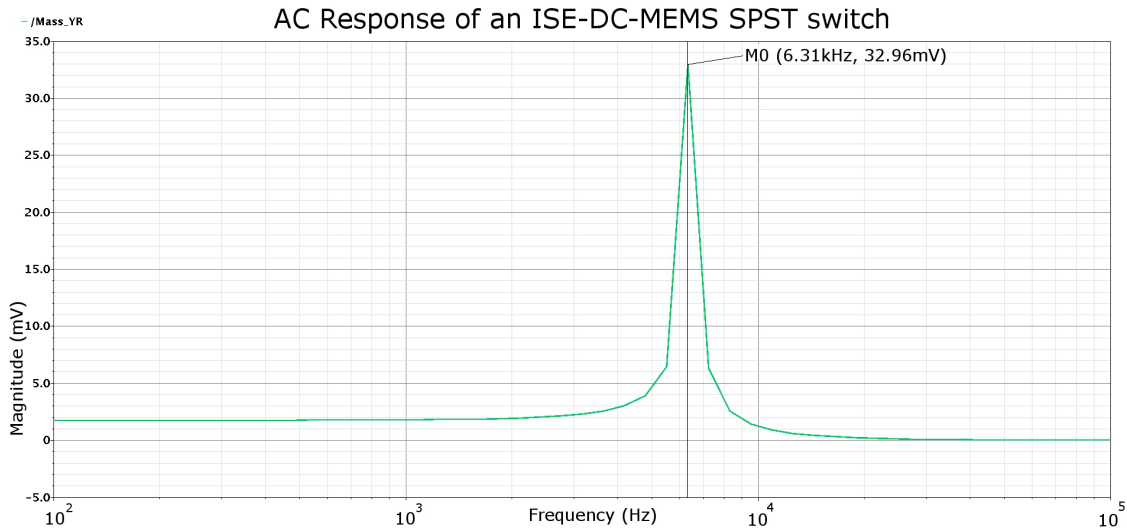The third structural analysis is mechanical transient analysis. In cases of electro-

Figure 4.6.2.: Mechanical AC-analysis of an ISE-DC-MEMS switch

static actuation, the analysis allows us to study the MEMS structural response over time. It will show bouncing effect behaviour and determine the settling time of the design. Figure 4.6.3 shows an example of a typical transient analysis. The red line in the graph shows the application of voltage actuation in the electrostatic actuator. The green and purple lines indicate the movement of both body masses in response to the voltage actuation. In this example the settling time has been reached at around $600\mu s$ after the actuation voltage is applied.
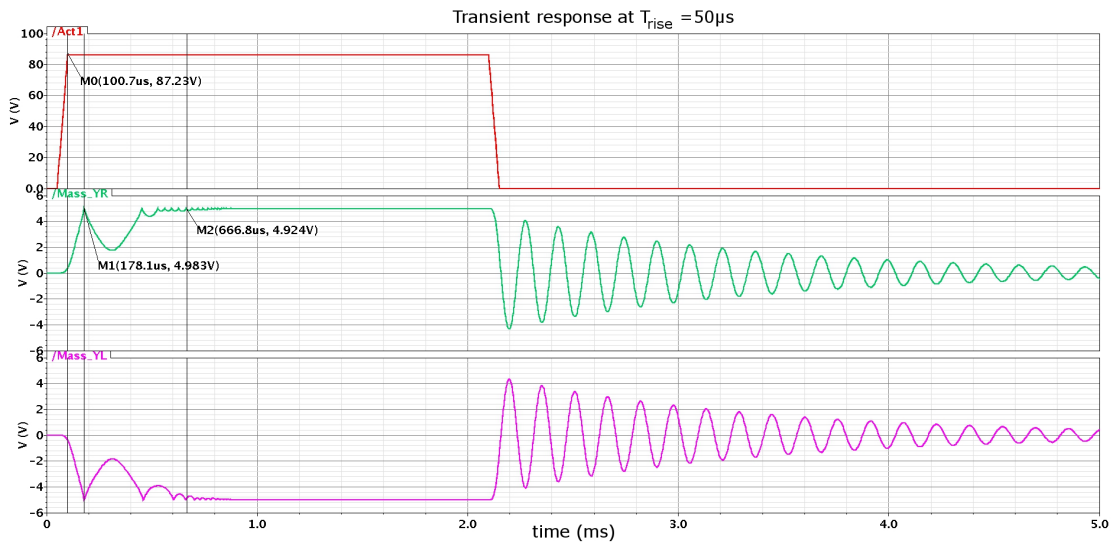
Figure 4.6.3.: Example of transient response analysis of a SPST ISE-DC-MEMS switch

4.6.1.1. SPST Electrostatic Actuator Design

The SPST switch has a unidirectional electrostatic actuator for each mass. The electrostatic actuator is built in the form of comb structures. There are two sets of comb, one of which is movable and the other is fixed. In order to make these comb structures function as electrostatic actuators, a positioning offset is required between the two set of fingers. This offset is needed to produce the actuation force when the actuation voltage is applied. Figure 4.6.4 shows the two different designs of electrostatic comb structures.

In Figure 4.6.4(a), the comb structures have no positioning offset. It has an equivalent gap for $G1$ and $G2$. When the voltage is applied the forces produced in the left and the right sides are equivalent but in the opposite direction. This makes the sum of the produced force zero and no actuation effects are produced. This setup is suitable only for capacitive sensing.

The comb structure with positioning offset is shown in Figure 4.6.4(b). In this setup $G1$ is smaller than $G2$ and force $F1$ is larger than force $F2$. The actuation force is thus produced in the direction of force $F1$.

For a unidirectional electrostatic actuator, each mass has one set of electrostatic actuators. Two body masses are available in every SPST switch and the electrostatic actuators are arranged to produce the movement of both masses towards each other.

4.6.1.2. SPDT Electrostatic Actuator Design

The electrostatic actuator design in the SPDT switch has some differences when compared to the SPST switch. In the SPDT switch, there are three body masses the left, centre and right masses. The left and right masses are similar to the SPST V1 design which has unidirectional electrostatic actuators. On the other hand, the centre mass has a bi-directional electrostatic actuator. The realisation of the centre mass is performed using a similar offset configuration method, however, a slight design adjustment is required in order to enable this feature. Figure 4.6.5 shows the bidirectional actuation configurations. It consists of a single movable body mass and two separate offset configurations for each movement direction. For Direction 1, offset configuration EA1 was used and for Direction 2, offset configuration EA2 was used.

The centre mass has a longer body length of $1135\mu m$ but with only 22 actuation fingers for each direction of movement. The reduced number of fingers means that a higher pull-in voltage required by the centre mass at $89.5V$ as the side masses retain an $86.5V$ of pull-in voltage. The simulation recorded a capacitance value of $0.7785pF$ during off-state and a capacitance value of $1.0915pF$ during switch on-state, as shown in the Figure 4.6.6.
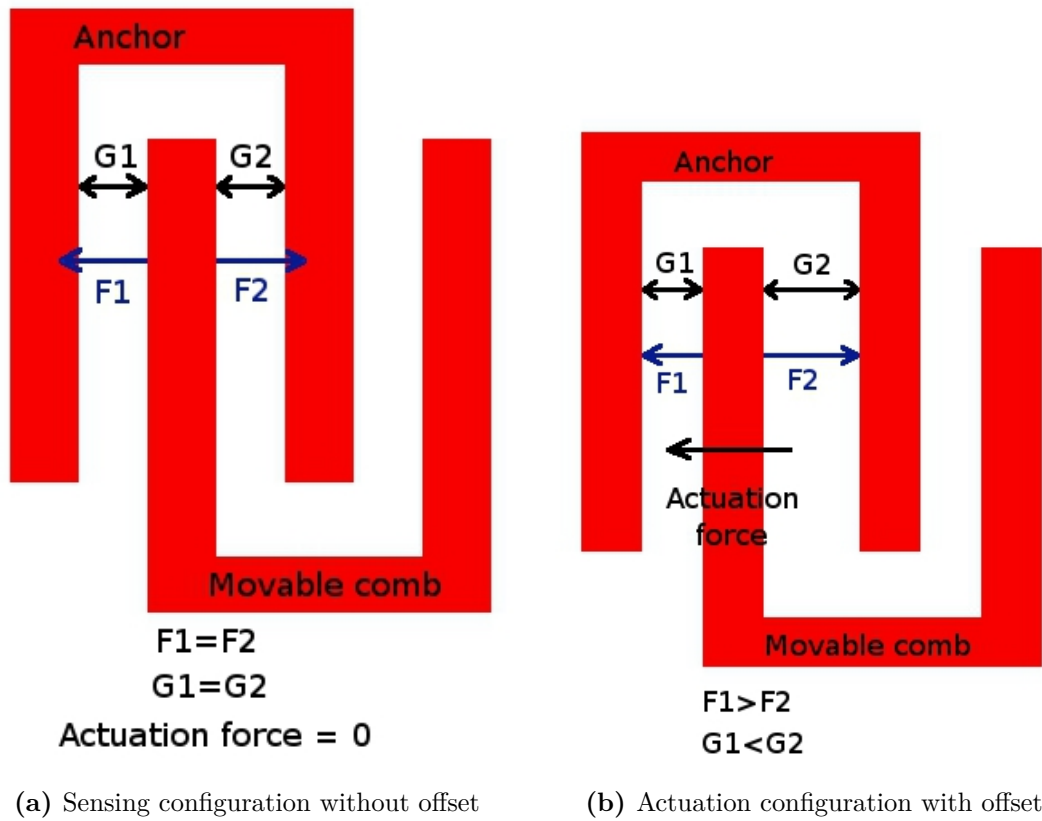
(a) Sensing configuration without offset

(b) Actuation configuration with offset

Figure 4.6.4.: Comb structures for electrostatic sensing and actuation
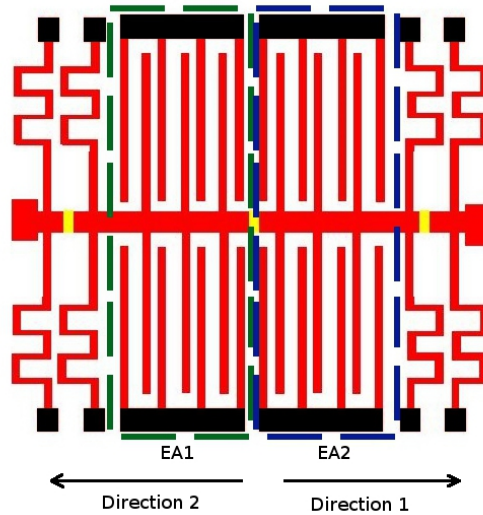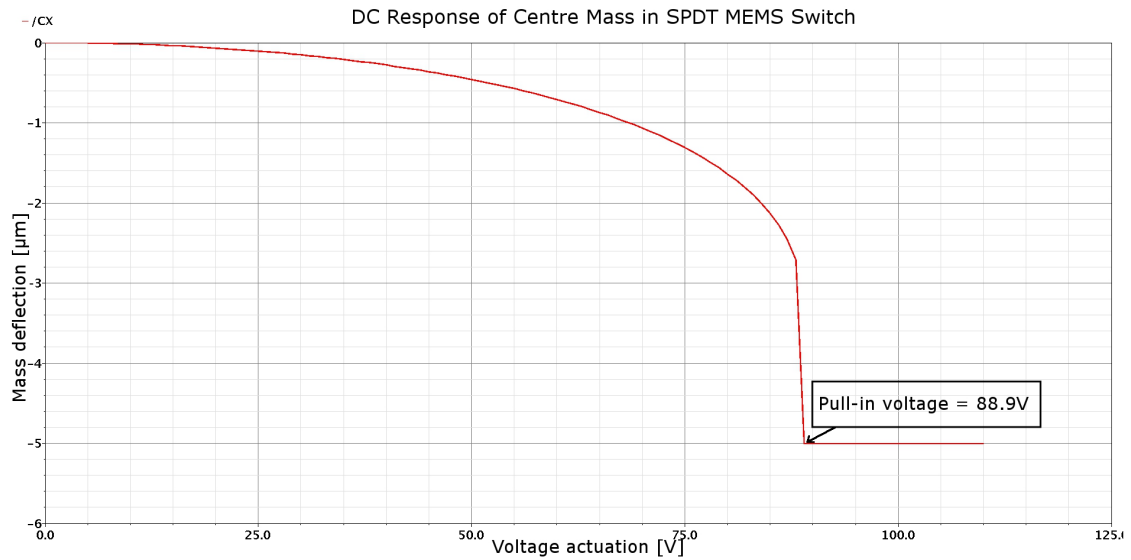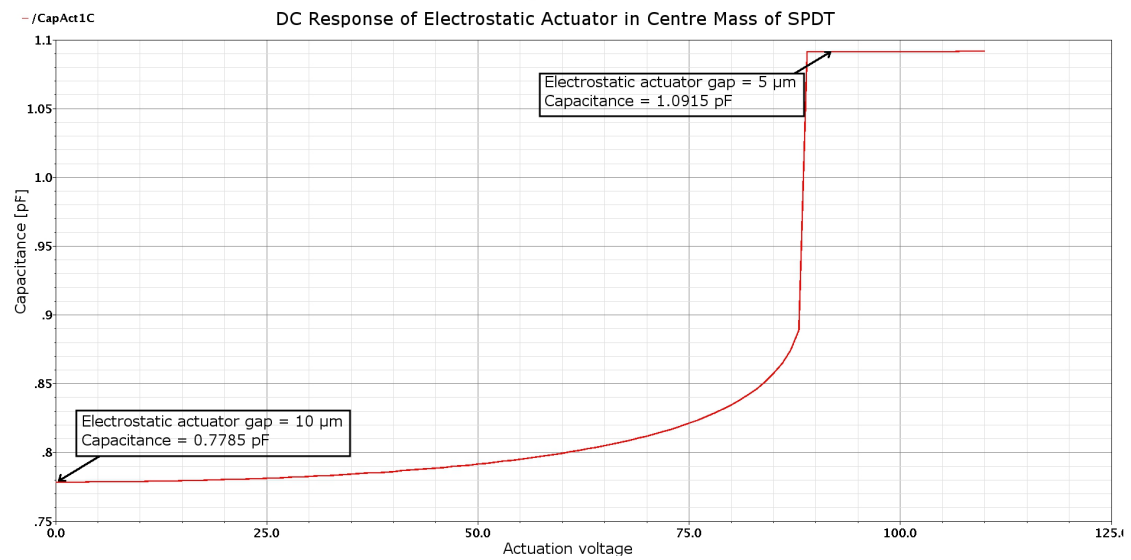

Figure 4.6.5.: Bi-directional electrostatic actuator in centre mass of SPDT switch

(a) Pull-in voltage of centre mass simulation

(b) Centre mass capacitive values
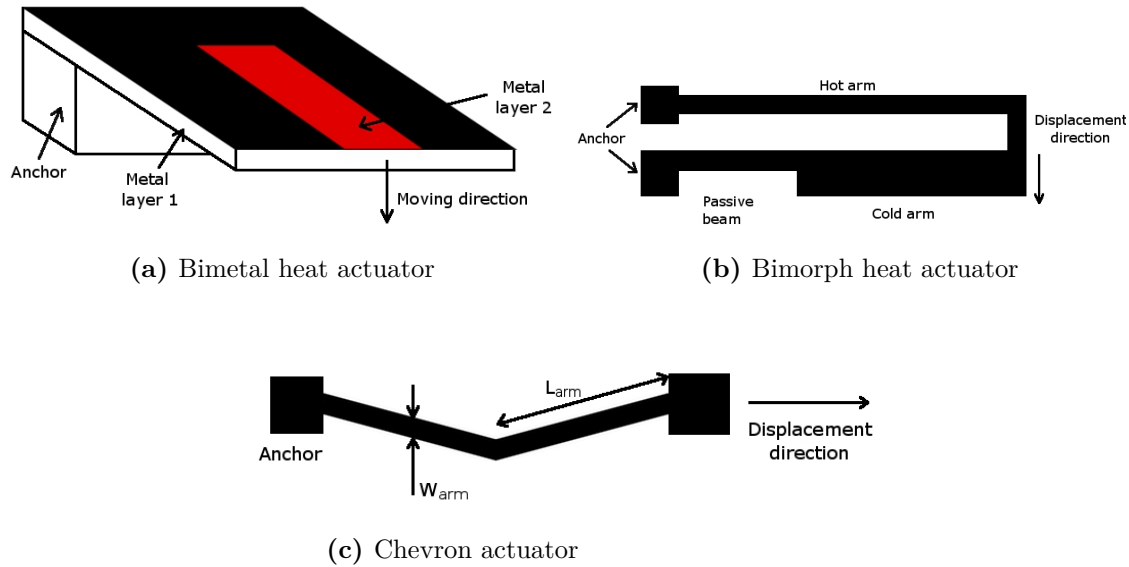
Figure 4.6.6.: DC response of centre mass in SPDT switch

(a) Bimetal heat actuator

(b) Bimorph heat actuator

(c) Chevron actuator

Figure 4.6.7.: Heat actuator variants

4.6.2. Heat Actuator Design

The heat actuator is the one of the earliest actuators in the MEMS device. It can produce huge deflection with strong output force and is favourable for applications which require these two properties. This actuator has always been linked with high power consumption, however, and is not suitable for mobile device applications. In general, there are three well-known types of heat actuators. A bimetal thermal actuator design is usually used to produce vertical movement. Two different materials with different thermal expansion are used to build the actuator [90] as depicted in Figure 4.6.7a. The current flows will generate heat due to material resistance and produce deflections. The material with higher thermal expansion, labelled Metal Layer 2, will expand more compared to the Metal Layer 1 material and the expansion force will bend the beam down.

The second heat actuator types are called thermal bimorph actuators [79, 80]. They consist of a single material with special structures called hot arm and cold arm. The current flows through this structure and due to the difference in width between these two arms, a lateral movement is produced as shown in Figure 4.6.7b.

The chevron actuator is another type of heat actuator [91, 89, 79]. In this design, a single material layer with special geometry as shown in Figure 4.6.7c, amplifies the displacement of the beam. The lateral displacement is produced in the tip of the chevron structure.

One of the design challenges in this research is the need to use a heat actuator for the huge force and displacement but at the same time requiring less power consumption. One of the targets that has been set during the conception process is to maximise

each MEMS structure to be multi-functional and with minimum passive components. The choice of heat actuation is based on its advantages in enabling the self-repair feature in the MEMS switch. The currently available options in heat actuator design offer displacement capability only on the tip of the beam structure. The process has been rethought to redesign the heat actuator structure to make it more flexible and to produce different maximum movement points.

In these switch designs, simplicity has always been one of the design principles. Despite the need to add functionality for self-repair in the switch design, it has to be realised without adding additional structures or increasing the design complexity. A redesign of typical beam form structure is undertaken to incorporate with the heat actuator element. Since the mass is attached to the centre beam, the deflection points of these heat actuators must also be at the mid-point of the beam structures.

A new design of beam structure with heat actuation has been introduced and implemented in this research. Figure 4.6.8 shows the difference between a typical beam and a beam with a heat actuator element. In this new design, a new shape of heat actuator category is created. The structure is built from nickel and gold layers. It has special serpentine structures at both anchor ends. By using a similar actuation concept in bimorph heat actuator design, these serpentine structures have a difference in width due to what are called hot arms and cold arms with ratio 3:1.

During heat actuation, the current flows through the beam and the difference in width, causing different thermal expansion in the structure. As the serpentine is available at both ends, the forces and deflections are accumulated at the midpoint of the beam. The simulation result in Figure 4.6.9 shows that the movement direction is determined by the positions of the final beam that connects two serpentine structures. The maximum deflection direction is perpendicular to the beam axis and always at the midpoint of the beam structure.

4.7. Analysis of Stiction Problem in ISE-DC-MEMS Prototype

The characterisation results of the first ISE-DC-MEMS prototype as reported in Section 6.4.1, detected one functioning problem. The electrostatic actuators in both designs showed a stiction problem during operation. A stiction phenomenon is a phenomenon that happens in any MEMS device that causes unintentional adhesion on the microstructure. Stiction can be categorised based on the stages in which it occurred. There are two types of stiction:

1. During manufacturing: In this stage, stiction happens during the removal process of the sacrificial layer to release the microstructure. It can be prevented by improving the manufacturing process and following design rules provided by the MEMS foundry. The stiction problem at this stage will affect the output yield of MEMS production.

(a) Typical beam structure


(b) Beam structure with heat actuator element
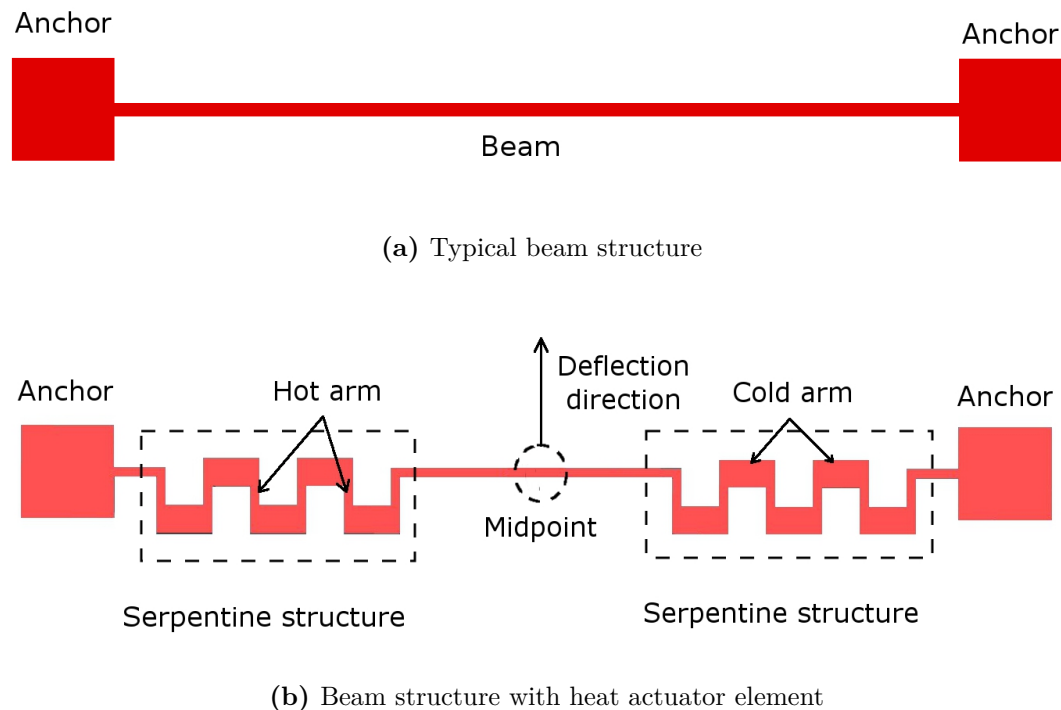
Figure 4.6.8.: Different structures of typical beams

2. During MEMS deployment: This happens during the operation of a MEMS device after embedding in the system. It will affect the reliability of the overall system that is equipped with this MEMS device due to MEMS failure during operational use. A MEMS designer needs to identify the reason behind this and how to prevent it in future design.

With regard to the ISE-DC-MEMS stiction problem, based on the prototype samples, there is no reported stiction event after releasing process in die manufacturing. These results show that the stiction is not due to a manufacturing process error or any violation of design rules. The initial conclusion is that the stiction problem falls into the second category. When referring to simulation results from the design stage, there is no error reported on the possibility of stiction. There are two problems that need to be addressed here:

1. The root cause of the stiction problem in electrostatic actuator design.

2. The need to introduce a preventive action during design and simulation stages to avoid stiction problems in the electrostatic actuator.

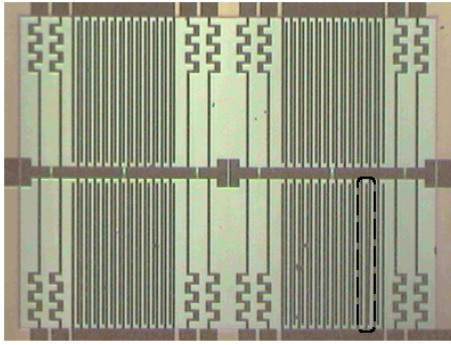Both issues will be discussed and addressed in the next section.
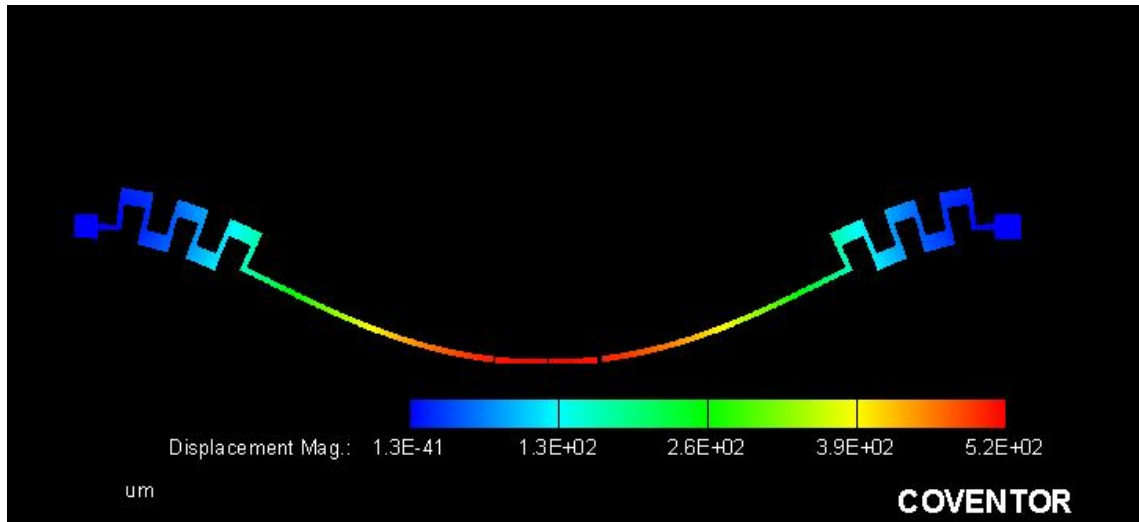
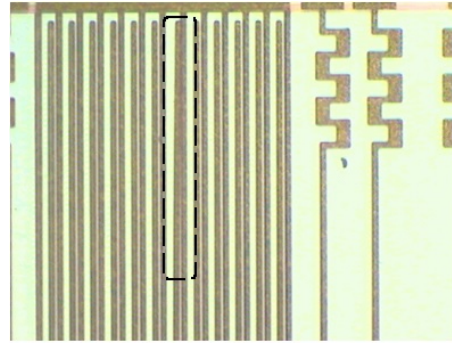**(a)** 2D simulation result
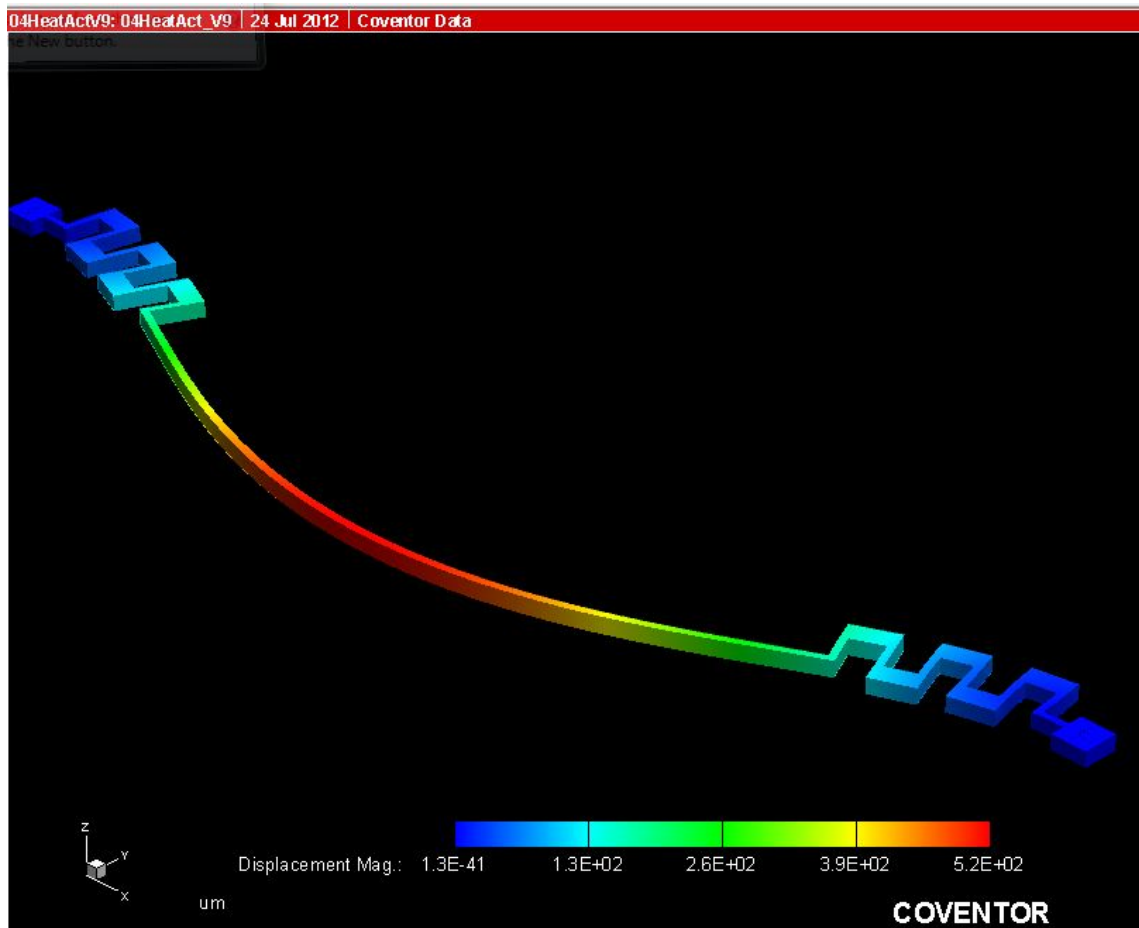
(b) 3D simulation result

Figure 4.6.9.: Simulation result of serpentine beam with heat actuation

(a) A SPST switch with stiction problem in the electrostatic actuator

(b) Zoom view of stiction occurrence in electrostatic actuator

Figure 4.7.1.: Stiction problem in electrostatic actuator

4.7.1. Stiction Problem in Electrostatic Actuator

The stiction problem in the electrostatic actuators can be identified by analysing the mechanical forces involved. This problem has been analysed and a stiction conformity test procedure has been proposed and reported [92]. An electrostatic actuator produces mechanical force from electrical energy. The mechanical force generated will cause a reaction in the mechanical beams in the form of bending. In order to simplify the calculation several assumptions need to be made. Based on observation when testing the prototype, assumptions are made based on the time and location of the stiction event.

Two possible assumptions were made for stiction occurrence with regard to time frame:

1. Off-state condition: Stiction takes place as soon as the voltage actuation is applied to the actuators without any movement of the mass. The gap is still in the original condition with $g1 = 10\mu m$ and the electrostatic force generated is at the lowest value.

2. On-state condition: Stiction takes place after the actuation force moves the mass and brings the switch into a closed state. At this point the gap of $g1$ is reduced to $5\mu m$ and the electrostatic force generated is at the highest value.

At the location which initiates the movement where stiction occurs, the end of the beam is assumed to be a likely point. The reasoning behind this assumption is that the smallest force required to bend a beam is recorded at the furthest point from the fixed beam point.

4.7.1.1. Force Generated by Electrostatic Actuator

The first step is to quantify the mechanical force produced by the electrostatic actuator. Figure 4.7.2 shows a part of an electrostatic actuator with a single set
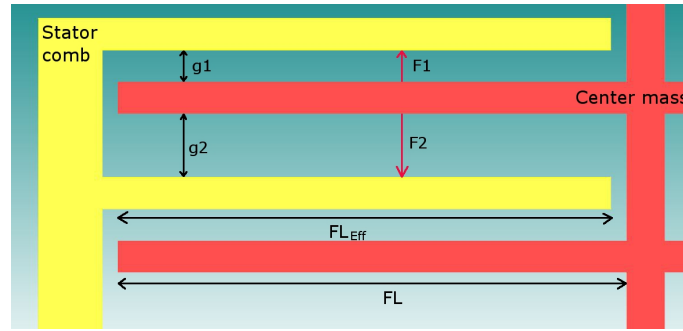
Figure 4.7.2.: The structure of a single electrostatic actuator

of actuator structures. It has fixed beams and movable beams. The moving mass beams are located in the offset position, which creates a different gap of $g1$ and $g2$ respectively. Each of the gaps creates pulling force between beams in opposite directions, denoted as $F1$ and $F2$. The force can be calculated using Equation 4.7.1. The effective force (F_{Eff}) is the sum of both forces acting on the beams.

$$F = \frac{\varepsilon \cdot FL_{Eff} \cdot b_c \cdot V^2}{2 \cdot g^2} \tag{4.7.1}$$

The design parameters of the electrostatic actuator are mentioned in Table 4.3a. The effective forces are quantified at various possible gaps of the actuator as the body mass moves. The gap $g1$ will move from $10\mu m$ to $5\mu m$, and gap $g2$ will move from $20\mu m$ to $25\mu m$. The effective forces generated can be found in Table 4.3b. The force generated by $g1$ increases as the gap is reduced and the force generated by $g2$ decreases as the gap increases. The effective force is thus significantly increased from $3.77\mu N$ to $19.30\mu N$.

4.7.1.2. Reactance Force by Mechanical Beams

The reactance force in the mechanical beam of the electrostatic comb structure is determined by the mechanics of material theory. A similar theory to that of macro level is used at micro level. Figure 4.7.3 shows the design parameters of a single beam comb structure. The force required to bend the beam is denoted by F_{BMin} and calculated using Equation 4.7.2.

$$F_{BMin} = \frac{w_c \cdot FL^3}{3 \cdot E \cdot I} \tag{4.7.2}$$

w_c is the deflection of the beam, E is the Young's modulus of the nickel, I is the inertia and FL is the length of the beam. The Young's modulus of nickel in the

(a) Design parameters of electrostatic actuator

Parameter	Value
Permittivity of vacuum, ε_0 $[Fm^{-1}]$	8.854×10^{-12}
Finger Length, FL_{Eff} $[\mu m]$	750
Finger Thickness, b_c $[\mu m]$	20
Actuation Voltage, $[V]$	87

(b) Forces created by electrostatic actuator at various gaps.

Gap $(g1)$ $[\mu m]$	Force $(F1)$ $[\mu N]$	Gap $(g2)$ $[\mu m]$	Force $(F2)$ $[\mu N]$	Effective Force (F_{Eff}) $[\mu N]$
10	5.03	20	1.26	3.77
9	6.21	21	1.14	5.07
8	7.85	22	1.04	6.82
7	10.26	23	0.95	9.31
6	13.96	24	0.87	13.09
5	20.11	25	0.80	19.30

Table 4.4.: Electrostatic design parameters and resulting output forces generated
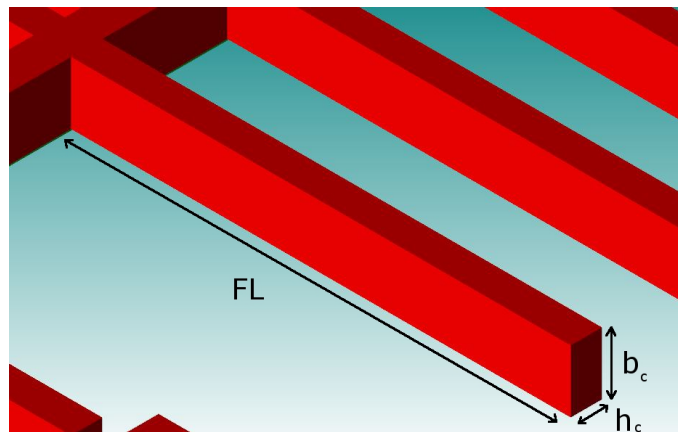
Figure 4.7.3.: Parameter definition of a comb beam

(a) Design Parameters electrostatic actuator design

(b) F_{BMin} values in various switch states

Parameter	Value
Finger Length, FL $[\mu m]$	800
Finger Width, h_c $[\mu m]$	10
Finger Thickness, b_c $[\mu m]$	20
Moment of Inertia, I $[m^4]$	1.67×10^{-21}
Young's Modulus at $<80°C [GPa]$	205
Young's Modulus at $>80°C [GPa]$	100

Temp $[°C]$	Deflection(w_c) $[\mu m]$	F_{BMin} $[\mu N]$
	10	19.53
<80	5	9.77
	1	2.00
	10	9.77
>80	5	4.88
	1	0.98

Table 4.5.: SPST comb design parameter

micro domain demonstrates a slight difference in terms of value when compared to bulk nickel as reported in [93]. In general the Young's modulus value of nickel is $205GPa$ however, in micro scale, the nickel layer shows different behaviour with regards to temperature. A same value of Young's modulus is recorded from room temperature till $60°C$. As the temperature rises to above $80°C$ the Young's modulus is drops by half to $100GPa$. This change in behaviour needs to be considered in the analysis in order to ensure minimal calculation results.

For a lateral movement in the electrostatic actuator, the moment of inertia, I can be determined by Equation 4.7.3.

$$I = \frac{b_c \cdot h_c^3}{12} \tag{4.7.3}$$

Parameter values of the comb design are shown in Table 4.5. Several deflection points are considered, at $1\mu m$, $5\mu m$ and $10\mu m$. The first value is needed to show how big a force is needed in order to initiate a beam bending to $1\mu m$. The second value is considered in order to determine the total force required for stiction to take place during the on-states of the switch. The third value is needed to show the bending force required for stiction to happen in the off-state condition.

4.7.1.3. Comparison between Forces

After obtaining values for both types of forces, a comparison can now be made between F_{BMin} and F_{Eff}. The first comparison is of the switch off-state where $g1 = 10\mu m$. F_{Eff} is $3.77\mu N$, as the bending force required for $1\mu m$ is $2.00\mu N$ while operating at normal temperature. Since the force produced is slightly bigger than the bending force, the beam will start to bend at this point. The situation is worse when the operating temperature rises to over $80°C$. At this point, only $0.98\mu N$ is needed to initiate bending.

In the switch on-state where $g1 = 5\mu m$, a higher effective force is generated, $19.30\mu N$. Obviously stiction will occur in this case since the total force required to bend the beam for $5\mu m$ at normal temperature is only $9.77\mu N$ and $4.88\mu N$ at high operating temperature.

In conclusion, the stiction occurs in electrostatic actuators due to the inability of the comb fingers to withstand the electrostatic force applied to them. Since a huge force is required for the switching action and to achieve low resistance contact, design optimisation of the comb finger structure is needed.

4.7.1.4. Stiffness Factor, EI

The factor $E \cdot I$ is also known as the stiffness factor of the structure. In order to increase the ability to withstand the force, scaling parameters need to be identified. These depend on the Young's modulus of the material and the inertia of the structure. For a square cross section beam like the comb finger in Figure 4.7.3, the factor I, is dependent on the beam width, b_c and thickness, h_c of the beam structure. In this case, b_c is the thickness of the nickel layer determined by the foundry process. The scaling factor of the moment of inertia, I, will depend on the h_c value.

In the design optimisation process the worst case scenario value for Young's modulus will be considered, which is $100GPa$. In conclusion, the stiffness of the comb structure can be increased by increasing the h_c value.

4.7.1.5. Safety Design Factor, S

The simplified calculations shown in the previous sections give a good estimation of the size of the forces involved in the system however, there are several uncertainties that have been neglected due to complexity of the calculation. In order to eliminate these uncertainties, the safety design factor, S is introduced to the calculation to determine the optimised parameters.

In general in order to achieve a sustainable design, the design rules below need to be introduced.

$$F_{BMin} > F_{Eff} \tag{4.7.4}$$

The safety design factor, S is then introduced to eliminate all uncertainty factors and thus the Equation 4.7.4 becomes:

$$F_{BNew} = S \cdot F_{Eff} \tag{4.7.5}$$

with F_{BNew} as the optimised value of F_{BMin} and $S = 1.5, 2, 3...$

4.7.1.6. Stiction Conformity Design Procedure

In order to optimise the design parameters, the worst case scenario with the highest generated forces (at $g1 = 10\mu m$) and the lowest point of material strength (at $E = 100GPa$) are considered. Using Equation 4.7.5, with $S = 1.5$:

$$F_{BNew} = 1.5 \cdot 19.30 \, [\mu N]$$

$$F_{BNew} = 29\mu N \tag{4.7.6}$$

A new moment of inertia, I_{New} that can withstand the force of F_{BNew} can be calculated as:

$$I_{New} = \frac{F_{BNew} \cdot l^3}{3 \cdot w_c \cdot E} \tag{4.7.7}$$

Now the thickness value of h_{cNew} can be determined using:

$$h_{cNew} = \left(\frac{I_{New} \cdot 12}{b_c}\right)^{1/3} \tag{4.7.8}$$

4.7.1.7. Optimised Value of the Comb Design Parameters

After implementing the stiction conformity test, the optimised parameters are shown in Table 4.5b. According to the table, the reason the current electrostatic actuator failed is clearly because the h_c that was used is only $10\mu m$, and the suggested value, with safety factor, $S = 1$, is $16\mu m$.

(a) Original design parameters of comb structure

Parameter	Value
Finger Length, $FL\,[\mu m]$	800
Finger Width, $h_c\,[\mu m]$	10
Finger Thickness, $b_c\,[\mu m]$	20

(b) h_{cNew} values with varied safety design factor

Safety Factor, S	$h_{cNew}\,[\mu m]$
1.0	16
1.5	18
2.0	20
3.0	23

Table 4.6.: Optimised h_{cNew} values with varied safety design factor, S

4.7.2. Improvement in Design and Simulation Methodology

After identifying the root cause of the problem, the second need is to improve the design cycle. Since the cost of prototyping MEMS devices is high, it is important to eliminate known potential problems at the design and simulation stage. In the original design process, as shown in Figure 4.7.4a, three main simulations have been performed to evaluate the mechanical behaviour of a MEMS model.

A DC sweep simulation was performed to test the functionality of the electrostatic actuator by determining the pull-in voltage of the MEMS switch. An AC simulation is performed to identify the resonance frequency and the respective maximum amplitude. The previous simulation results show that there is no failure reported and the simulation outputs show that the electrostatic actuators are working well with the original design parameter. This shows that the behavioural model does not especially consider the stiffness integrity of the MEMS structure during the activation of electrostatic force.

In order to improve this situation, an additional test routine is required to implement the finding explained in the previous section. A stiction conformity test is proposed to check the structural integrity of the MEMS structure in terms of stiffness. In this test, the MEMS sub-elements are confirmed as able to withstand the applied forces without failing under stress. The new design and simulation chart, with proposed stiction conformity test, is shown in Figure 4.7.4b.

In this research, the application of the test routines is still not embedded into CAD software. The calculation is made in Microsoft Excel software and the result is applied to the MEMS design in MEMS+. The stiction conformity test routine is shown in Figure 4.7.5. The test routine begins by extracting the design parameters involved. The sub-component of the electrostatic actuator will be evaluated and the new finger width, h_{cNew} is determined.

After obtaining h_{cNew} value, the implementation of this new value will lead to two different paths that affect the design. The first path represents the fixed value of switch width, SW and length, SL. The increment value in h_{cNew}, will lead to a reduction of the total number of fingers in the electrostatic actuator. A higher voltage of $V_{Pull-In}$ is required to produce similar forces.

The second path represents the fixation value of $V_{Pull-In}$ when maintaining the same number of fingers of electrostatic actuators. This will cause an increment in the overall switch length. The switch will generally get bigger and the resonance frequency will be reduced.

A rerun of AC and DC analysis is required in order to see the impact of h_{cNew} in overall MEMS behaviour. The maximum allowable actuation voltage is determined as one parameter input in the transient analysis. The transient analysis is performed to determine the response time and reaction time of the switch.
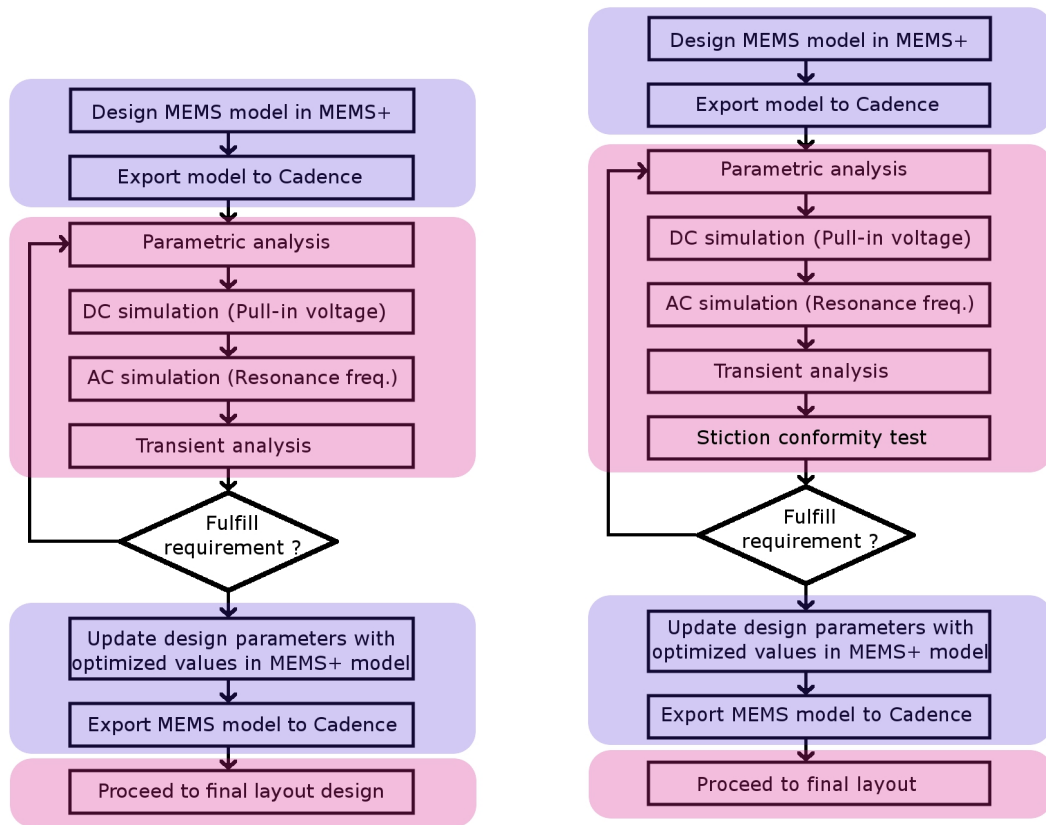
(a) Original design and simulation flowchart

(b) Proposal on a new design and simulation flowchart

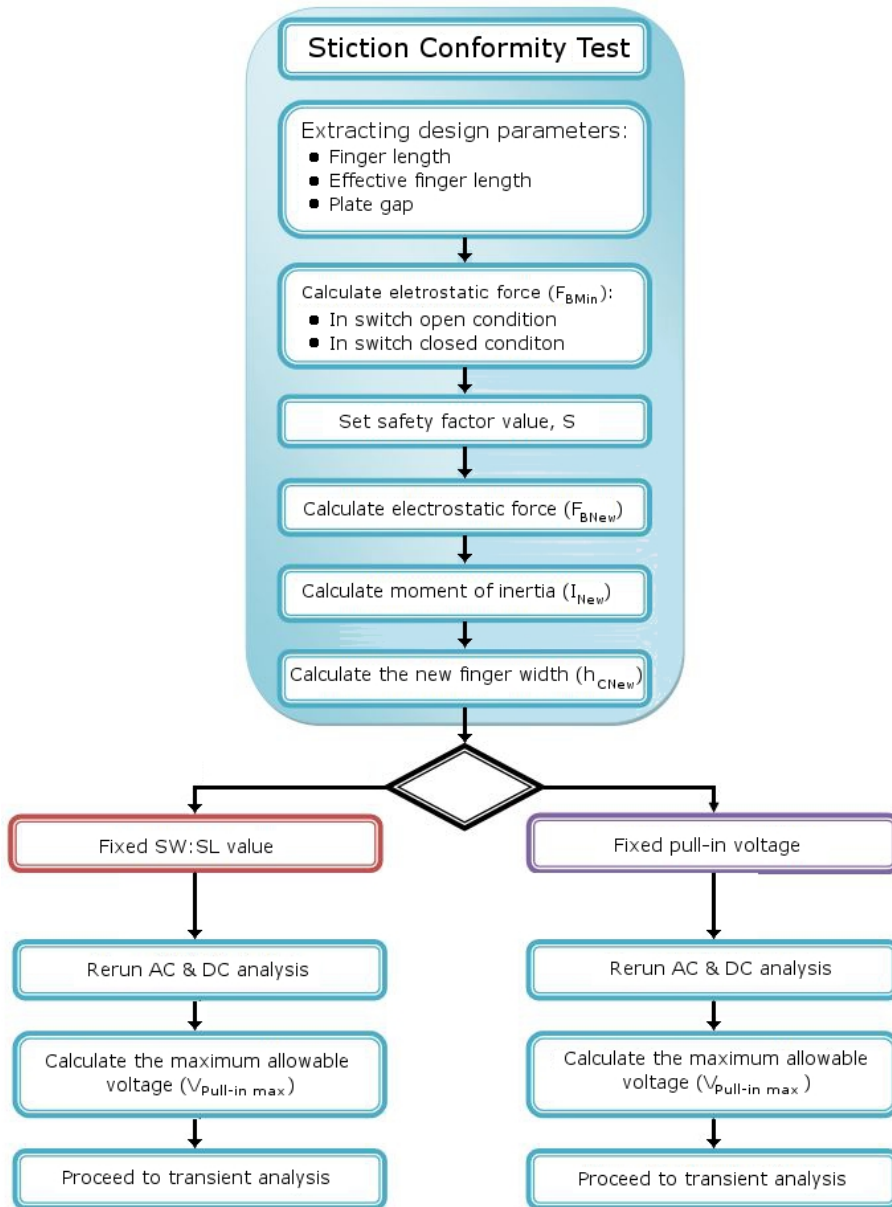**Figure 4.7.4.:** Design and simulation flowcharts of a MEMS device using Cadence and MEMS+ software

Figure 4.7.5.: Stiction conformity test routine

4.8. ISE-DC-MEMS Switch Scalability

The scalability properties of the ISE-DC-MEMS switches are one of the important aspects that will be investigated. In this research, the scalability investigation concentrates on the sub-components that build the switch. In this design, there are three main sub-components that are connected and influence each other. These sub-components are:

1. Electrostatic actuators

2. Heat actuators

3. Switch contact

The design process is started by reconstructing the design parameters involved in the SPST MEMS switch design. In order to ease the parametric analysis process of electrostatic actuators, two main parameters are introduced to represent the overall length, SL_M and width, SW of a single mass body.

The switch length (SL_M) comprises several parameters: contact length (CL), anchor distance (AD), anchor beam width (ABW), cut width (CW) and comb width (CbW) as shown in Figure 4.8.1b. The first four parameters have a fixed ratio from the both ends, and the comb width represents the rest of the SL_M value. The comb width is an important factor that determines the number of electrostatic actuator fingers. The comb width can be calculated using Equation 4.8.1 below:

$$CbW = SL_M - 2 * ((AD + CL) + 2 * (ABW + CW)) \qquad (4.8.1)$$

The switch width (SW), comprises several parameters: stator anchor width (SAW), finger length (FL), stator gap (SG) and centre mass width (MW). The stator anchor width, stator gap and centre mass width have a fixed ratio value from the switch width. The remaining values are twice the length of a finger. A finger length is one of the parameters that determines the area of electrostatic actuators and can be calculated using Equation 4.8.2.
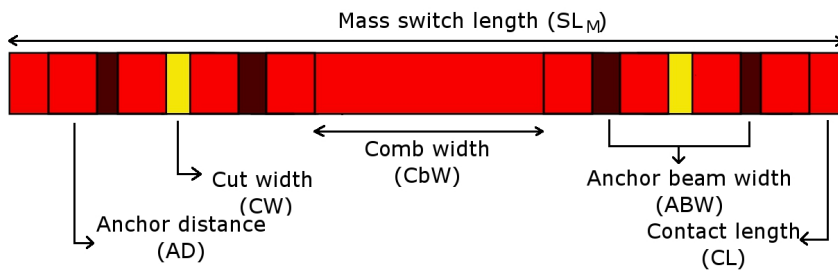
$$FL = \frac{1}{2}(SW - 2 * (SAW + SG) - MW) \qquad (4.8.2)$$

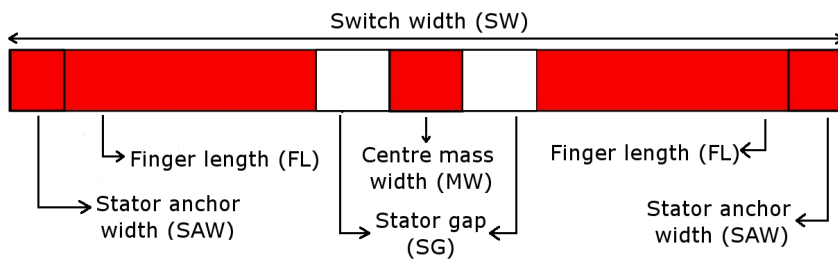## 4.8.1. Electrostatic Actuators

The ISE-DC-MEMS switches make use of the MetalMUMPs technology. Initially, the technology was intended for MEMS switches which are driven by heat actuation using a thick metal layer from nickel. This research explores the feasibility of using
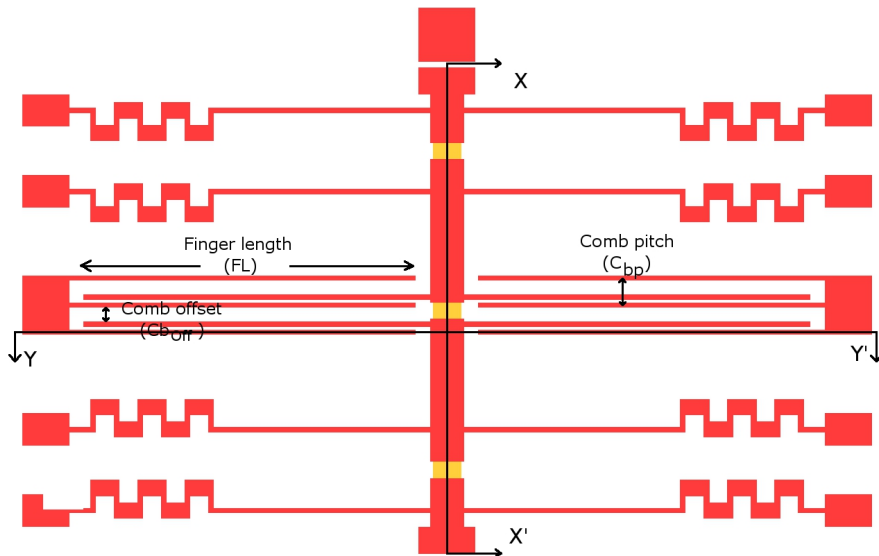
(a) The design parameter of a single mass switch body

(b) XX' cross section

(c) YY' cross section

Figure 4.8.1.: The design parameter ratio

an electrostatic actuator using the same nickel layer. The lateral switch movement is suitable for a MEMS manufacturing technology that has a single metal layer, such as MetalMUMPs.

The design of electrostatic actuators in the MEMS switch is driven by two goals of domain. The electrical domain requires a low actuation voltage to drive the electrostatic actuator, while the mechanical domain requires high mechanical resonance frequency and a smaller area. These two goals are contradictory to each other. The positives in one dominant factor will have a negative impact on the others. The main task is to decide the best value that fits with the needs of all domains.

An electrostatic actuator is predominantly determined by the factor of the capacitance value that needs to be produced. A low pull-in voltage for an electrostatic actuator can be realised with a huge area of parallel plate and low spring constant in the anchor mass however, a huge electrostatic area with low spring constant increases the body mass, with low structural stiffness. Optimisations of these two parameters are required to produce a robust design that produces high output yield and reliability. In order to move the body mass, a force larger than the spring force that has been introduced by the mass anchor structure needs to be generated. The main design challenge is to build a small electrostatic actuator with a big capacitance area.

In this SPST design, the capacitive area is determined by the factors below:

1. Thickness of nickel layer, T_{Nic}

2. The length of comb finger,(FL)

3. The total width of comb structure,(CbW)

4. The comb pitch (Cb_P) and the comb offset(Cb_{Off})

The parametric analysis for the above factors was performed using the MEMS+ model and simulated using Cadence software. The results were then populated and presented to show the trends for each parameter.

4.8.1.1. Nickel Layer Thickness Factor, T_{Nic}

For a lateral MEMS switch movement, the area of the electrostatic actuator is determined by the thickness layer of the parallel plate. In MetalMUMPs plus technology, the nickel layer can be increased from $20\mu m$ to $30\mu m$. In theory, by increasing T_{Nic}, the total capacitance area will also increase however this increment will result in a higher value of overall mass and also a higher spring constant value. Figure 4.8.2 shows the simulation results of various T_{Nic} values for $20\mu m$, $25\mu m$ and $30\mu m$. These simulations are performed by fixing the other parameters of the MEMS structure. The width and length ratio are set to 1:1.

The result shows that a thicker nickel layer will cause increments in the pull-in voltage of the MEMS switch of $1V$ for every $5\mu m$. This is due to the increment
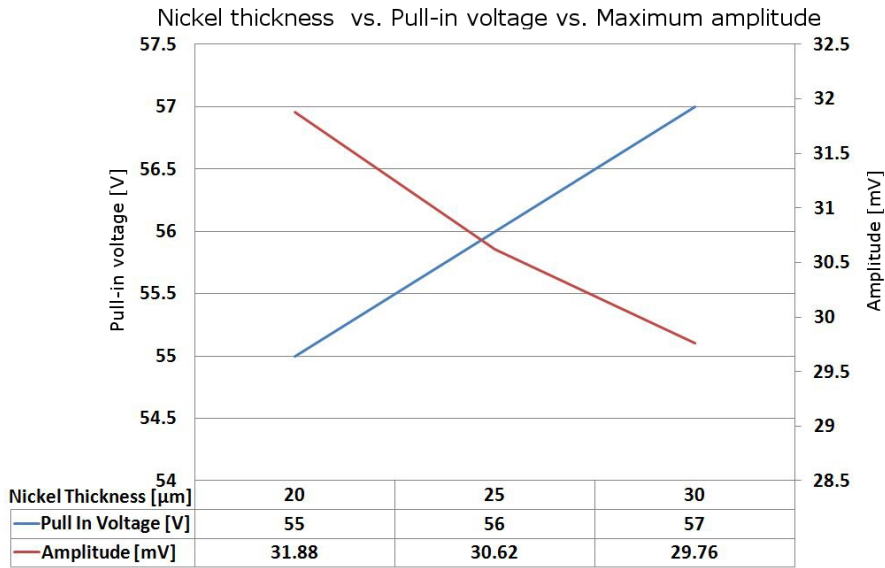
Figure 4.8.2.: Pull-in voltage result of various T_{Nic} values

Nickel Thickness [μm]	20	25	30
Pull In Voltage [V]	55	56	57
Amplitude [mV]	31.88	30.62	29.76

in spring constant demanding more force in order to move the structure. This force is larger than the additional electrostatic force produced from the increment of the parallel plate area. Since body width and length ratio remain the same, the resonance frequency remains the same at $4.285kHz$. The maximum amplitude at this frequency is slightly reduced from $31.88mV$ at $20\mu m$ to $29.76mV$ at $30\mu m$. To conclude, the T_{Nic} factor should remain at minimum $20\mu m$ since it does not reduce the pull-in voltage as desired.

4.8.1.2. Finger Length Factor, FL

The finger length factor is the second factor influencing the capacitance area in the electrostatic actuator. Increasing the value of FL will reduce the pull-in voltage of the switch, however, improving this factor will cause a reduction in mechanical resonance frequency and increase switch width. Figure 4.8.3 shows the influence of FL values towards resonance frequency and pull-in voltage. The trend shows that an increase in finger length also causes an increase in the anchor length. Since the total anchor length is equivalent to the overall switch width, the spring constant is reduced at the same time, which results in lower pull-in voltage and the structure's resonance frequency. The optimum value of FL is dependent on other geometrical values of the electrostatic actuator, especially in the width of the comb structure (CbW).
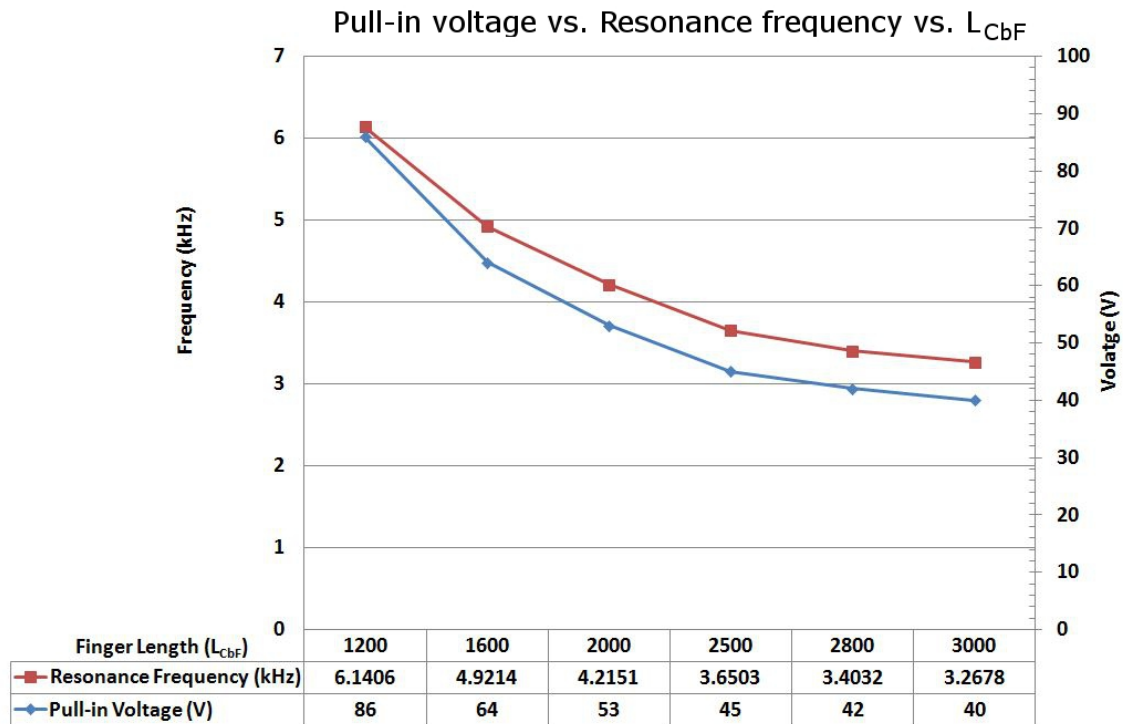
Figure 4.8.3.: FL vs. $V_{Pull-In}$ vs. Resonance Frequency

4.8.1.3. Width of Comb Structure, CbW

The CbW factor determines the number of fingers in the electrostatic actuators. A higher value for this factor will increase the capacitance force but at the expense of lowering mechanical resonance frequency and increasing the switch size. The best way to find the optimum value of CbW is by using the ratio of switch length and switch width ($SL : SW$). This ratio shows better correlation between switch sizes, mechanical resonance frequency and voltage pull-in factors.

4.8.1.4. Switch Width and Length Ratio, $SW : SL_M$

An evaluation of switch width and length ratio towards resonance frequency, switch area and pull-in voltage is another way to find the optimum size of a MEMS switch. Several runs of DC analysis and AC analysis with various values of SW and SL_M were performed. The SW and SL_M values were kept in the range of $900\mu m$ to $3000\mu m$ with a step of $200\mu m$. Results were then observed based on their ratio. A case study based on the fixed value of SW at $1400\mu m$ is used to show the relationship between these factors.

Figure 4.8.4 shows the behaviour of pull-in voltage and resonance frequency in different $SW : SL_M$ ratios. The SL_M values range from $1200\mu m$ to $3000\mu m$. The results show a reduction trend in both factors as the SL_M value increases. Reduction of the

pull-in voltage is desirable but not with lower resonance frequency. The selection of the optimum value cannot be made based on these two factors alone since it shows the same trend with a different desired value, so a third parameter of area size needs to be considered the deciding factor.

The relationship between switch area and pull-in voltage is shown in Figure 4.8.5. These two factors display opposite behaviour towards the increment of the SL_M values, where increasing the switch size decreases the pull-in voltage. The cross over point between these two lines can be considered the optimum point for these two factors. Based on this graph, the ratio 1400: 2000 is the optimum value.

As in the previous discussion, Figure 4.8.6 shows the same trend between switch area and resonance frequency. The optimum value of these two factors will be the smallest ratio at 1400:1200. This ratio provides the smallest area with the highest resonance frequency however, a compromise needs to be made as this point produces the highest pull-in voltage, which is undesirable. In conclusion the ratio 1400:1200 in this case study, is the optimum value since it gives a good balance between these three factors.

Table 4.7 summarises the design parameters for all switches developed in this research. The SPST-V1 and SPDT design were developed in the first generation prototype and the other SPST designs were developed in the second generation prototype. The design parameters presented in this table are tailored to fulfill the requirements set out in Tables 4.1 and 4.2 on page 56.

In the second prototype, three different switch categories were designed. The first switch category, denoted as '**I**' has an actuation voltage set to less than $30V$; the second category is marked by '**II**' and has an actuation voltage of less than $60V$; and the third category is marked by '**III**' and has an actuation voltage of less than $80V$.

For each category, two design variants with different safety factors were implemented. Two safety factor values, set at 1.5 and 2.0, produced a slight difference in terms of switch sizing. The switch designs noted as '**-A**' have a safety factor of 1.5 and the notation '**-B**' represents the safety factor 2.0.
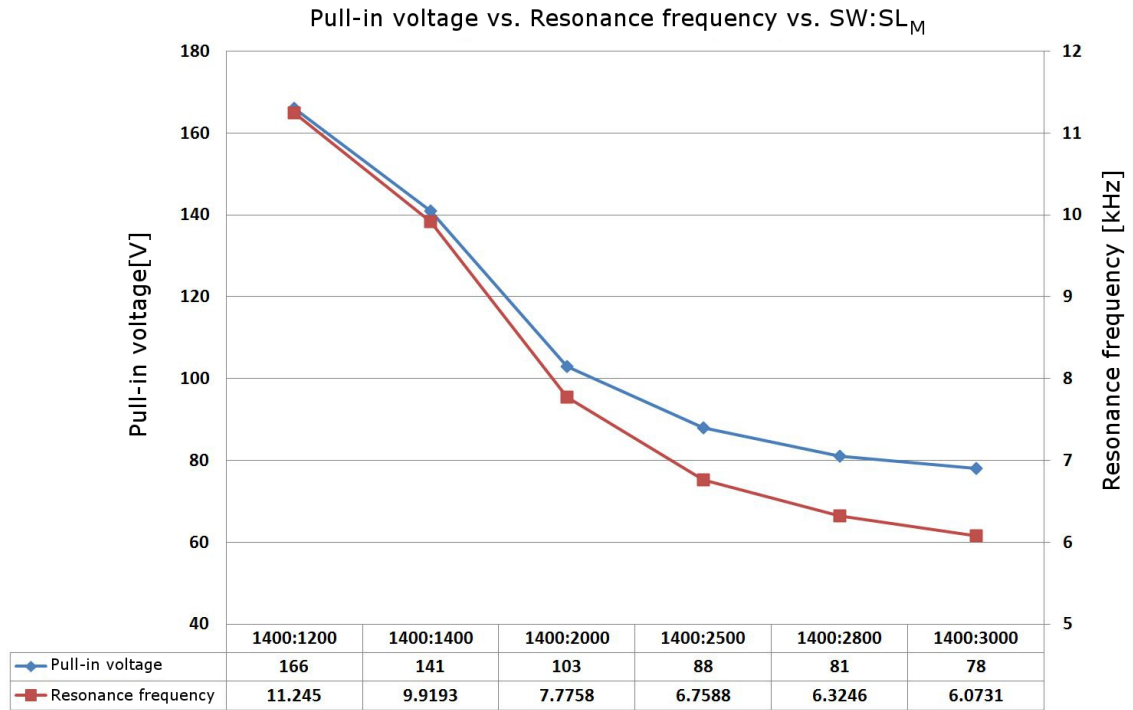
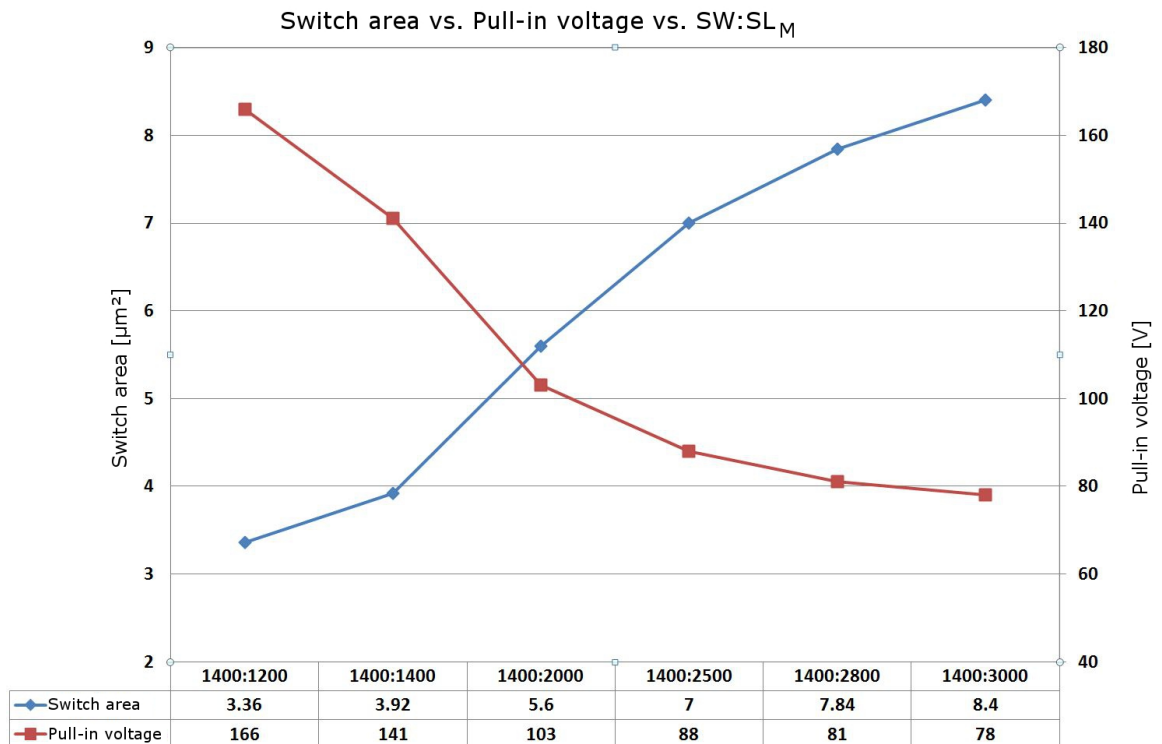**Figure 4.8.4.:** Pull-In Voltage vs. Resonance Frequency vs. $SW : SL_M$

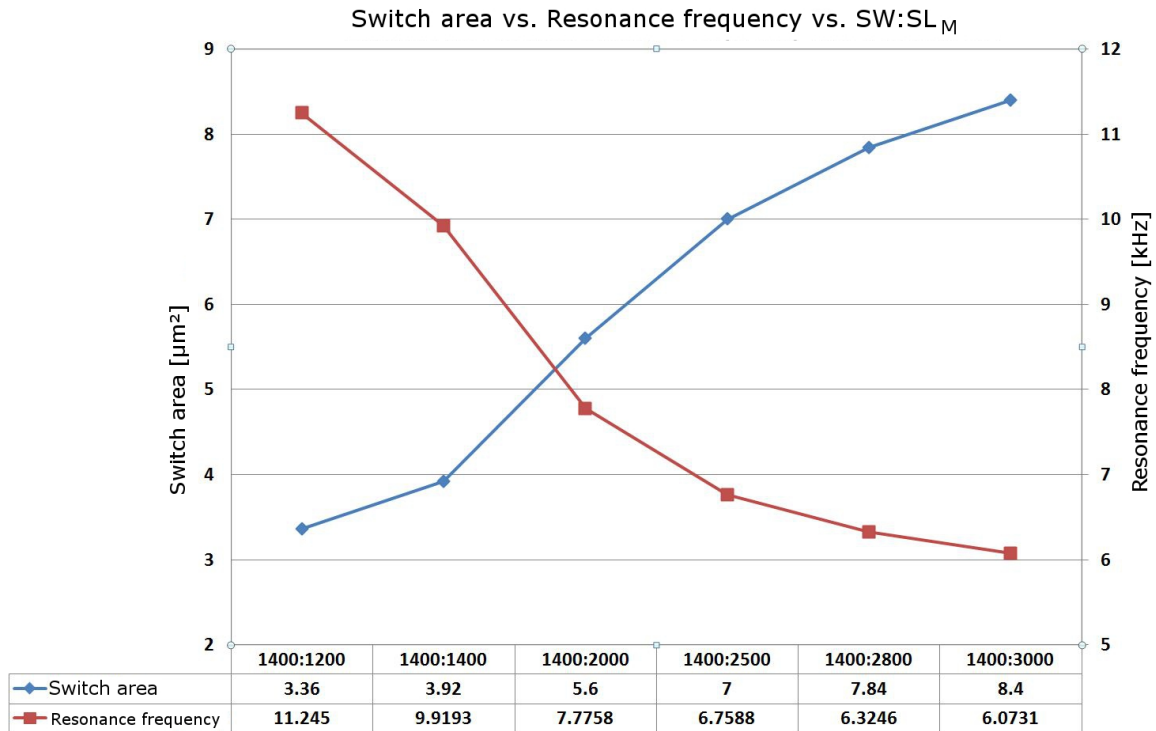**Figure 4.8.5.:** Switch Area vs. Pull-In Voltage vs. $SW : SL_M$

**Figure 4.8.6.:** Switch Area vs.Resonance Frequency vs. $SW : SL_M$

4.9. Electrical Models of SPST Switch

The electrical characteristics of MEMS switches designed using MEMS+ software can be simulated using the Cadence circuit simulation software package. The behavioural model of MEMS switches from the MEMS+ model is exported to the Cadence software. During the export process, four different files were created under Cadence file system. First the layout view provides the structural view of the intended design. There are spectre, ultrasim and symbol views that give the behavioural information of the MEMS model. A library that provides the netlist information was created by MEMS+ and saved under a file with *.scs* file extension. An example of this netlist code can be found in Appendix E.

Figure 4.9.1 shows the symbol of the MEMS generated model of the ISE-DC-MEMS switch. The pin connections of the MEMS model can be divided into two types. First, four pins were allocated for monitoring the mechanical behaviour of the MEMS device. In the SPST switch, the mechanical movements of both masses were observed for Y and Z directions since the SPST switch has a lateral movement in Y-direction. Observation in the Z direction is required to determine any out of plane movement in the body masses.

Switch Type	SPST							SPDT	
Parameter	**V1**	**I-A**	**II-A**	**III-A**	**I-B**	**II-B**	**III-B**	**Uni**	**Bi**
Overall Size									
Width, $SW[\mu m]$	1910	3025	2520	1800	3024	3430	1800	1920	
Length, $SL[\mu m]$	2675	4230	3930	4230	4230	2520	4730	4400	
Thickness,$[\mu m]$	20	20	20	20	20	20	20	20	
Electrostatic actuator-direction	Uni	Uni	Uni	Uni	Uni	Uni	Uni	Uni	Bi
Comb Width, $CbW[\mu m]$	610	1335	1132	1290	1256	876	1575	610	1135
Finger Length, $FL[\mu m]$	800	1290	1065	745	1290	1065	745	800	800
Finger Width, $FW[\mu m]$	10	15	16	14	16	18	15	10	10
Finger Pitch, $FP[\mu m]$		60	62	58	62	66	60	60	
Total Finger/Actuator	24	44	36	44	40	26	26	24	44
Heat Actuator									
Overall Length, $HtL[\mu m]$	1700	2688	2240	1600	2688	2240	1600	1700	
Cold Arm Width, $CdW[\mu m]$	30	30	30	30	30	30	30	30	
Cold Arm Length, $CdL[\mu m]$	60	94	80	60	94	80	60	60	
Hot Arm Width, $HaW[\mu m]$	10	10	10	10	10	10	10	10	
Hot Arm Length, $HaL[\mu m]$	20	30	30	30	30	30	30	20	
Centre Beam Length, $HCL[\mu m]$	1090	1670	1390	990	1670	1390	990	1090	
Contact Size/Capacitive Sensor									
Width, $CntW[\mu m]$	150	150	150	150	150	150	150	150	
Gap, $Gf[\mu m]$	10	10	10	10	10	10	10	10	
Safety Design Factor, S	1.0	1.5	1.5	1.5	2.0	2.0	2.0	1.0	

Table 4.7.: Design parameters for all ISE-DC-MEMS switch designs
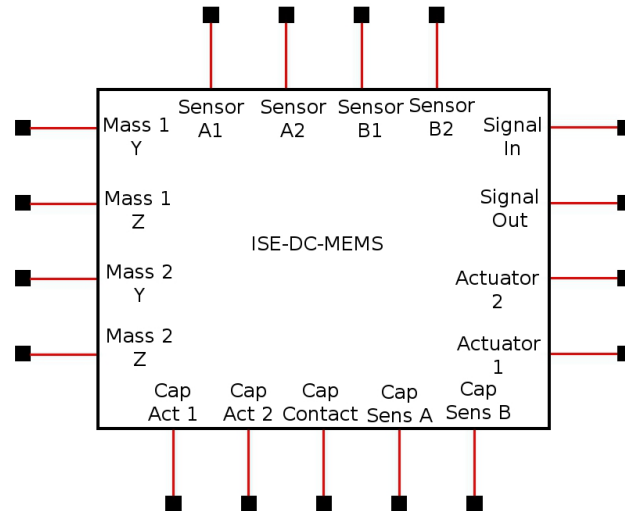
Figure 4.9.1.: The symbol of a MEMS generated model of ISE-DC-MEMS switch

The second type of pins were allocated for electrical components. Two electrical input pins were allocated for the electrostatic actuators in SPST switches. Six input-output pins were created in the Cadence model. Two of the pins were for signal-in and signal-out lines. Another two pairs were for capacitive sensors A and B. Finally, the output only pins consist of five pins in total. These output pins are used to monitor the values of the capacitive components. The five different components were made up of two from electrostatic actuators, two from capacitive sensors and one from contact capacitance.

The dynamic electrical characteristics of the sub-elements in the MEMS device are evaluated. This section discusses the electrical models of the MEMS switch provided by the MEMS+ model. Three elements exist in the model, namely the electrostatic actuator, capacitive sensor and capacitive contacts.

4.9.1. Electrostatic Actuator

The SPST switch has one pair of electrostatic actuators for each body mass. These body masses are identical, and using the design parameters listed in Table 4.7, the capacitance value can be simulated. Figure 4.9.2 shows the capacitance value of an electrostatic actuator in an SPST switch. The initial capacitance during actuator gap at $10\mu m$ is recorded at $0.8492pF$. As the voltage is increased, the capacitance value increases due to a reduction of the gap between the parallel plates. The capacitance value reaches its maximum point at $1.1907pF$ where the switch is closed and the actuator gap is reduced to $5\mu m$.
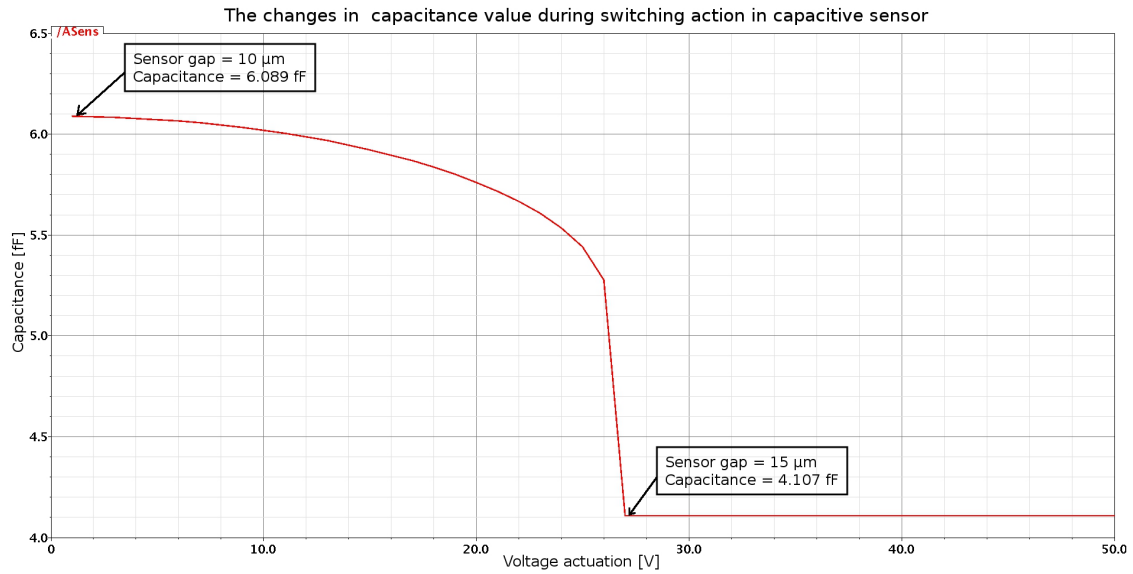
Figure 4.9.2.: DC response of electrostatic actuator in SPST MEMS switch

4.9.2. Capacitive Sensor, C_{Sens}

The self-monitoring feature is enabled by a capacitive sensor, C_{Sens} in each body mass. During switching actions, the capacitance value dynamically changes, following the movement of the body mass. Figure 4.9.3 shows capacitance behaviour during switching actions. In the off-state the capacitance is recorded at $6.089fF$ where the capacitor gap is $10\mu m$. As the switch closes, the gap is increased to a maximum value of $15\mu m$ and the capacitance is reduced to $4.107fF$. These two extreme values will provide information for the body mass positions.

4.9.3. Contact capacitance, C_{Cont}

The appropriate electrical model for contact areas should be the combination of a capacitor and a resistor. This is because these contacts move from the off-state, which is represented by a capacitor, to the on-state which is represented by a resistor however, Cadence simulation showed no dynamic transition between these two models during switching actions.

Figure 4.9.4 shows the DC response analysis between capacitive sensor, movement of mechanical mass and contact capacitance. Voltage was applied to the electrostatic actuators, causing the moving body mass to close the contacts. The contact capacitance,C_{Cont} increased from $9.4786fF$ to $17.11fF$ as the gap between the two contacts was reduced. The opposite effect took place in the capacitive sensor as the capacitance was reduced from $9.587fF$ to $7.118fF$, due to the increasing gap in the capacitive sensor.
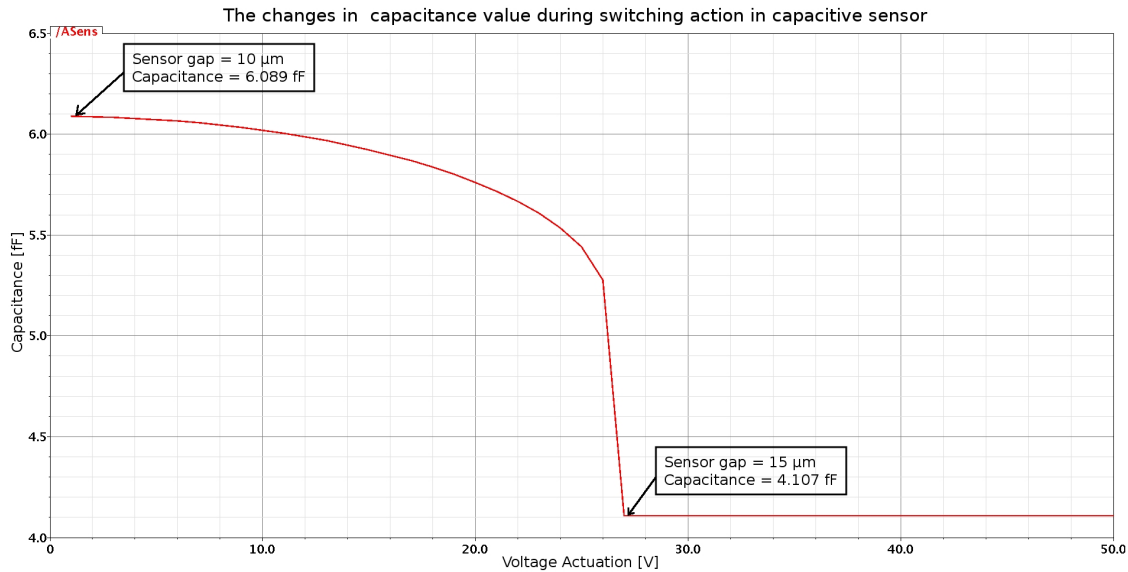
Figure 4.9.3.: DC response of capacitive sensor,C_{Sens} in SPST MEMS switch

After the switch turns to the off-state, the contact capacitance plot in Figure 4.9.4 shows a sudden drop from the peak point to the lowest point. This is because the electrical model of the contact is changing from a capacitance model to a resistance model. The resistance model of the contacts can be shown in transient response, as in Figure 4.9.9.

4.9.4. Missing Elements in the MEMS+ Model

After evaluating the electrical model of MEMS+, there were several elements that were not included in the MEMS+ model. The missing components in the model are due to limitations in defining the electrical component in certain mechanical structures only. Figure 4.9.5 shows an example of the defined and undefined areas of electrical components in SPST-V1 design. The areas with yellow colouring represent the defined areas of electrical components and the red areas are the undefined electrical components. The reason these components cannot be defined is because they are built using a serpentine library structure, which is required to form the heat actuators. A side electrode cannot be introduced to this and so is omitted from the electrical model.

Two important elements were line resistance and parasitic capacitance. It is important to know the line resistance along the signal path so as to know the signal loss across the MEMS switch. As explained in Section 4.1 on page 53, the line resistance in the MEMS+ model is neglected in the model however, the contact resistance (R_{Cont}) of the switch exists only during the on-state in series with line resistance. This value is influenced by several factors, such as size of the contact area, the
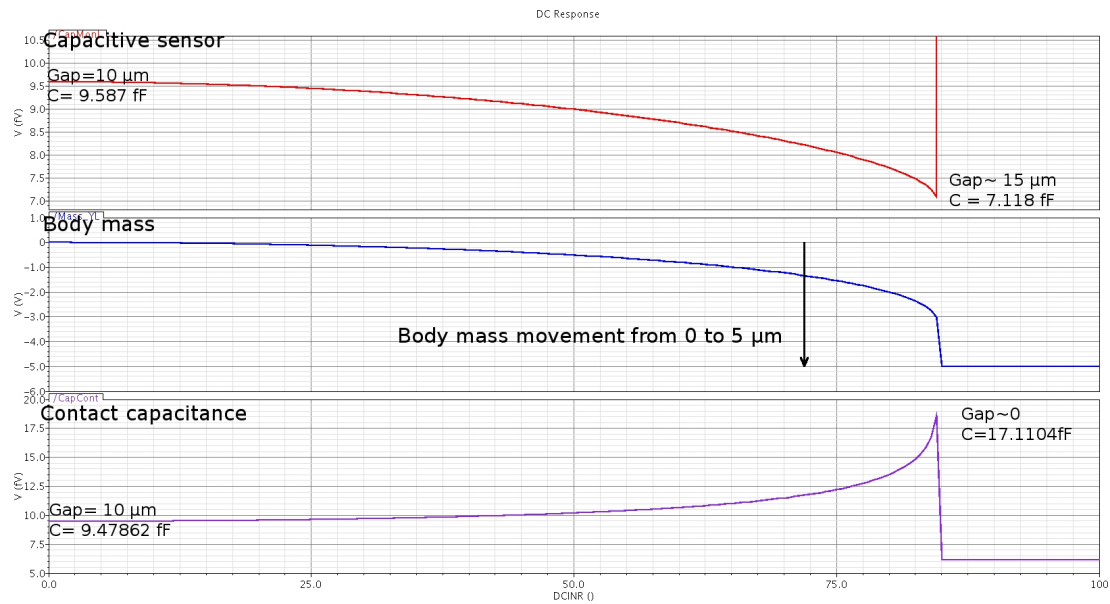
Figure 4.9.4.: DC response of capacitive sensor, contact capacitance and body mass movement in SPST MEMS switch

mechanical force applied, and the surface roughness of the contact area [94]. The contact resistance is modelled in MEMS+ using the default value[4].

Another important missing element is the parasitic capacitance. In the MEMS+ model, there is no parasitic capacitance extraction in the model produced due to a limitation in introducing the electrical components. Parasitic capacitance value is important in order to investigate its influence on signals, especially in the high frequency range. The crucial areas are the parasitic capacitance along the signal-in and signal-out paths.

4.9.5. Behavioural Model of ISE-DC MEMS Switch

In order to evaluate the switch performance, an appropriate model is required to evaluate electrical performances. A DC MEMS switch behavioural model can be modelled based on the switch states. This section discusses switch behaviour during the off-state and the on-state.

In an off-state condition, the equivalent circuits of the switch can be modelled as a capacitor, as shown in Figure 4.9.6a. The off-state characteristics are important for determining the signal bandwidth that the switch can handle. AC response simulations were executed to determine the cut-off frequency of the switch. Based on the AC simulation result shown in Figure 4.9.7, high signal isolation can be achieved with a MEMS switch. Figure 4.9.7(a) shows the input and output of the

---

[4]MEMS+ USER Guide and Reference page 6-81
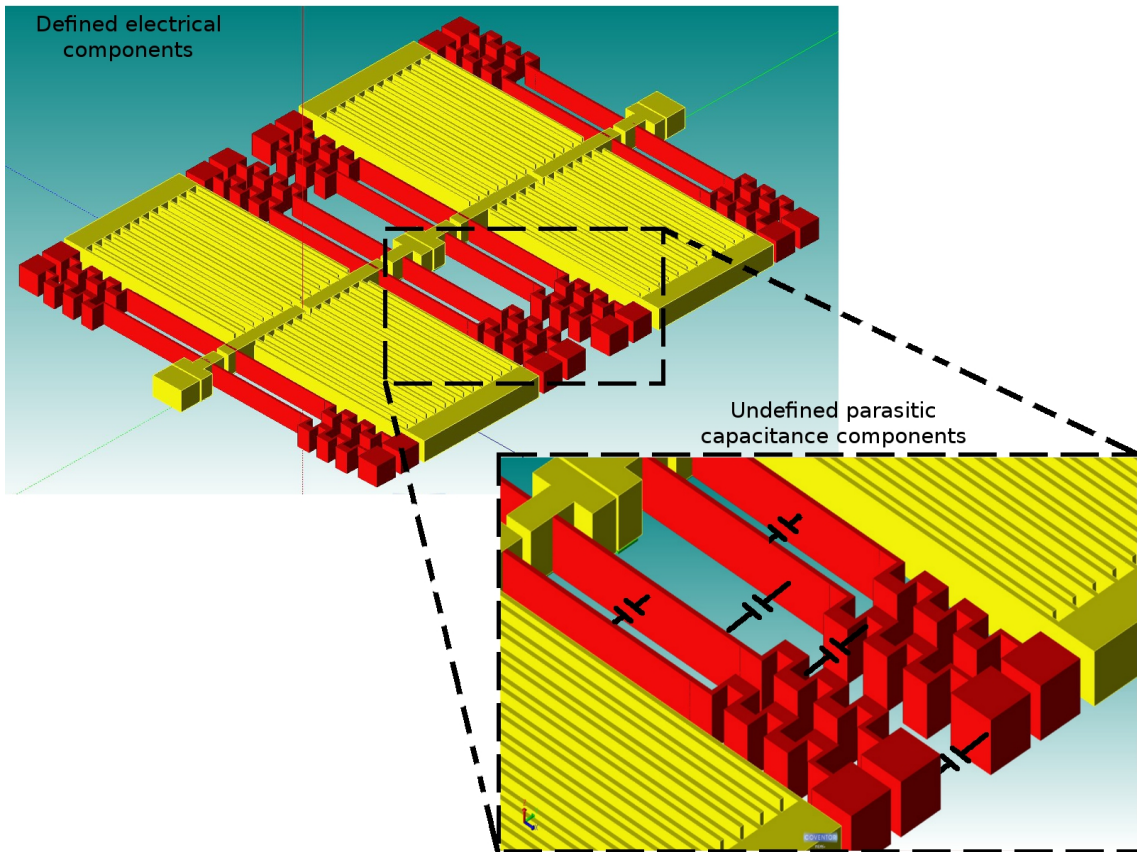
Figure 4.9.5.: The defined and undefined areas of electrical component in ISE-DC-MEMS switches

(a) Equivalent circuit of switch contact in off-state for ISE-DC-MEMS switches

(b) Equivalent circuit of switch contact in on-state for ISE-DC-MEMS switches
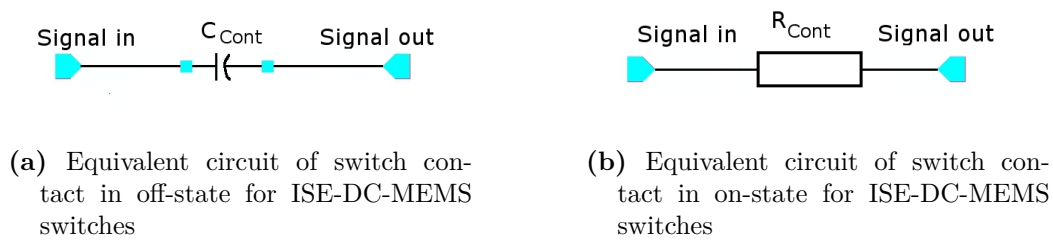
Figure 4.9.6.: Equivalent circuit of switch contact for on and off-state for ISE-DC-MEMS switches

97

Switch Type				SPST				SPDT	
Simulation	V1	I-A	II-A	III-A	I-B	II-B	III-B	Uni	Bi
Pull-In Voltage [V]	85.5	27-30	42-51	69-79	29-35	49-59	63-80	85	89
Resonance Frequency $[kHz]$	6.4269	1.8584	2.7174	4.6393	1.8861	2.9800	4.1995	6.4269	6.293
Area$[mm^2]$	5.11	12.00	9.25	7.20	12.00	8.00	8.10	8.448	
Electrostatic Actuator,C_{Act}									
* C_{Act} at gap=10μm,$[pF]$	0.8492	2.697	1.533	1.8408	2.479	1.357	1.8337	0.8492	0.7785
* C_{Act} at gap=5μm,$[pF]$	1.1907	101.356	57.75	68.265	92.17	49.33	68.27	1.1907	1.0915
** C_{Act} at gap=10μm,$[pF]$	0.4246	1.3485	0.7666	0.9204	1.239	0.6785	0.9169	0.4246	0.3893
** C_{Act} at gap=5μm,$[pF]$	0.59535	50.678	28.873	34.133	46.09	24.666	34.135	0.59535	0.5458
Capacitive Sensor,C_{Sens}									
C_{Sens} at gap=10μm,$[fF]$	6.089	6.089	6.089	6.089	6.089	6.089	6.089	6.089	
C_{Sens} at gap=15μm,$[fF]$	4.107	4.107	4.107	4.107	4.107	4.107	4.107	4.107	
Contact Area									
C_{Cont} at gap=10μm,$[fF]$	5.9524	5.9524	5.9524	5.9524	5.9524	5.9524	5.9524	0.8492	
R_{On},$[m\Omega]$	0.5227	0.5227	0.5227	0.5227	0.5227	0.5227	0.5227		

* For each pair of actuators

** For each half pair of actuators

Table 4.8.: Simulation results of electrical components for all ISE-DC-MEMS switches based on model simulations using Cadence

V_{Act} $[V]$	86	88	90
V_{Switch} $[\mu V]$	8.40	7.56	6.92
I_{Switch} $[mA]$	1.49999618	1.49999656	1.49999685
R_{On} $[m\Omega]$	5.6000	5.0667	4.6133

Table 4.9.: Simulation results of R_{On} resistance with various voltage actuation

switch in AC response analysis. The figure shows that as the input signal frequency increases, the output voltage also increases accordingly when the input frequency is in the MHz range. This trend continued until the input signal frequency reached more than $100GHz$. A further increase of input frequency signal will lead the switch to turn to the on-state. It is known that the simulation results at very high frequency in the GHz range might be not as accurate as depicted but the intention here is to show the general response of the ISE-DC-MEMS switch.

Figure 4.9.7(b) shows the same simulation results in output gain representation. It shows that the switch has high signal isolation of more than $-100dB$ up to $16.79kHz$. A $-50dB$ signal isolation was achieved by the MEMS switch for a signal frequency of $5.31MHz$ and $-3dB$ isolation between signal in and signal out was recorded at $1.683GHz$.

When the switch state changes from the off-state to the on-state, the model behaviour is also changed. The contact capacitance, C_{Cont} in the off-state turns into a contact resistance R_{On}. The equivalent circuit of the switch model during the on-state is depicted in Figure 4.9.6b. In order to determine the resistance value across the switch, a transient simulation was implemented in the model. Figure 4.9.8 shows the simulation circuits for transient analysis. The symbol depicted in this figure is the above hierarchy of the standard symbol shown in Figure 4.9.1 on page 93. This was done for simplification purposes in representing a simulation circuit for transient analysis. In this setup the electrostatic actuators were activated with a voltage pulse of $88V$ for $2.0ms$. After electrostatic actuation was activated, the MEMS switch required about $700\mu s$ before it reached the closed state. When the switch reached the final state, the voltage drop across the switch was recorded at $7.6\mu V$ with a current of $1.4999966mA$. The resistance across the switch can be calculated, which results in R_{On} at $5.0667m\Omega$.

The initial R_{On} results given by the simulation results are comprised of R_{Cont}. Several transient analyses have been implemented with actuation voltage set at $86V$ and $90V$ to show the R_{Cont} variance with regard to actuation force. Table 4.9 shows the results of voltage drop across the switch and the resulting R_{On} of the switch with various actuation voltages. The results show that as the actuation voltage is increased, the R_{On} resistance is reduced as a result. This pattern of results demonstrates that the MEMS+ model includes contact resistance in its behavioural model.
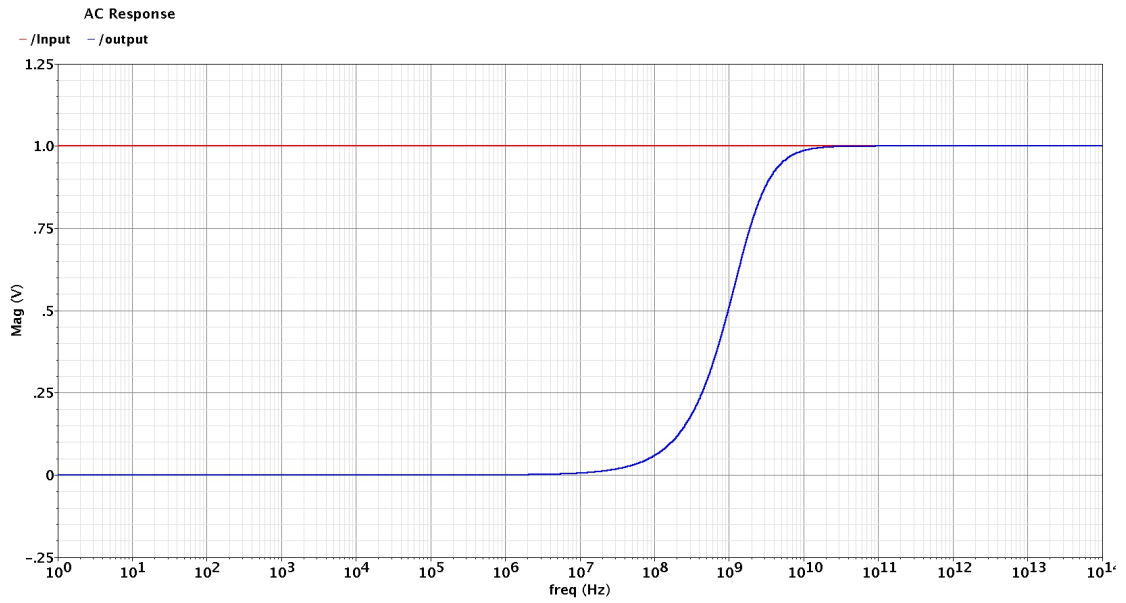
(a) Signal-in and signal-out response of AC analysis in the MEMS switch during off-state
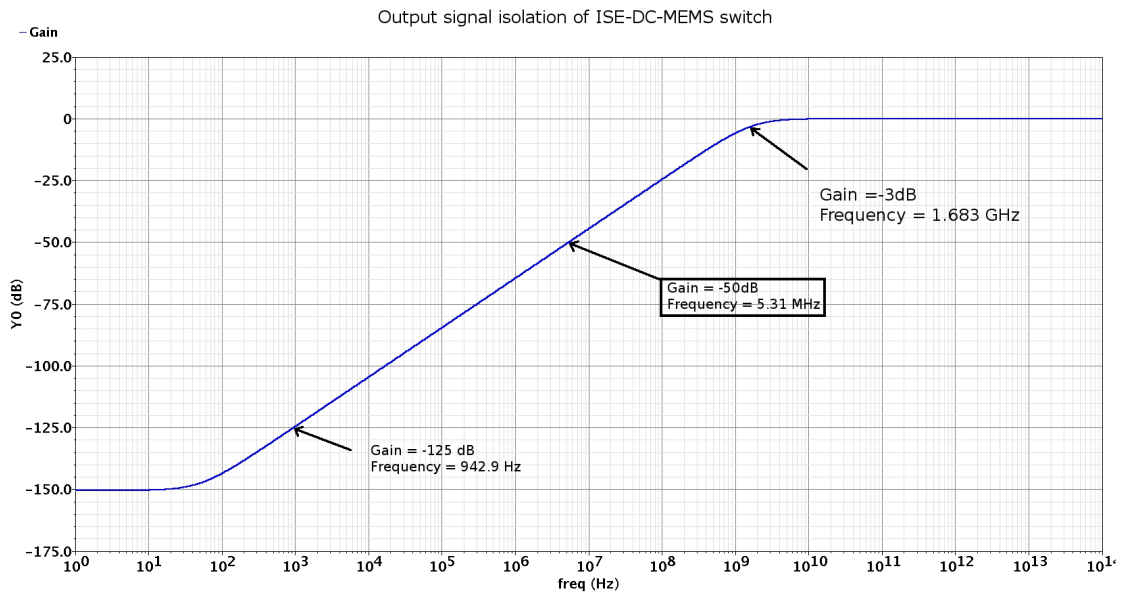
(b) Output gain of AC response analysis in the MEMS switch during off-state

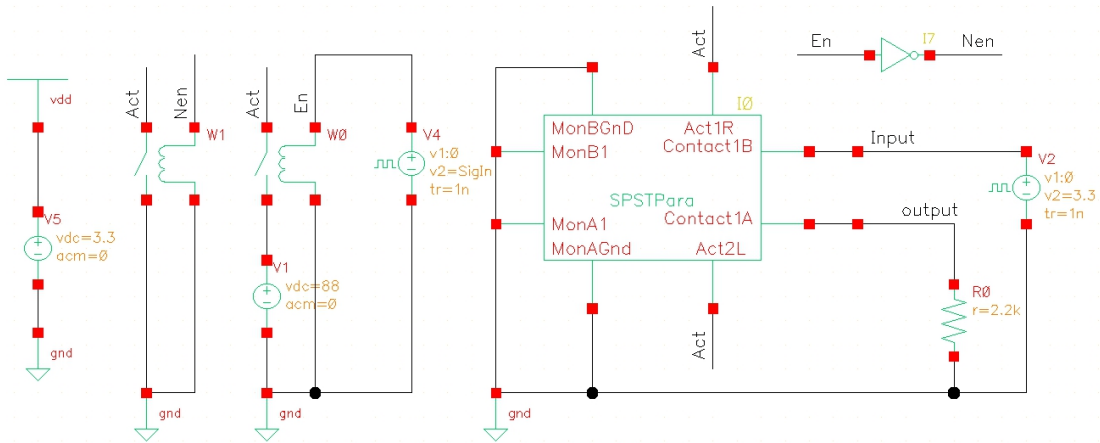**Figure 4.9.7.:** AC analysis of DC MEMS switch to check signal bandwidth

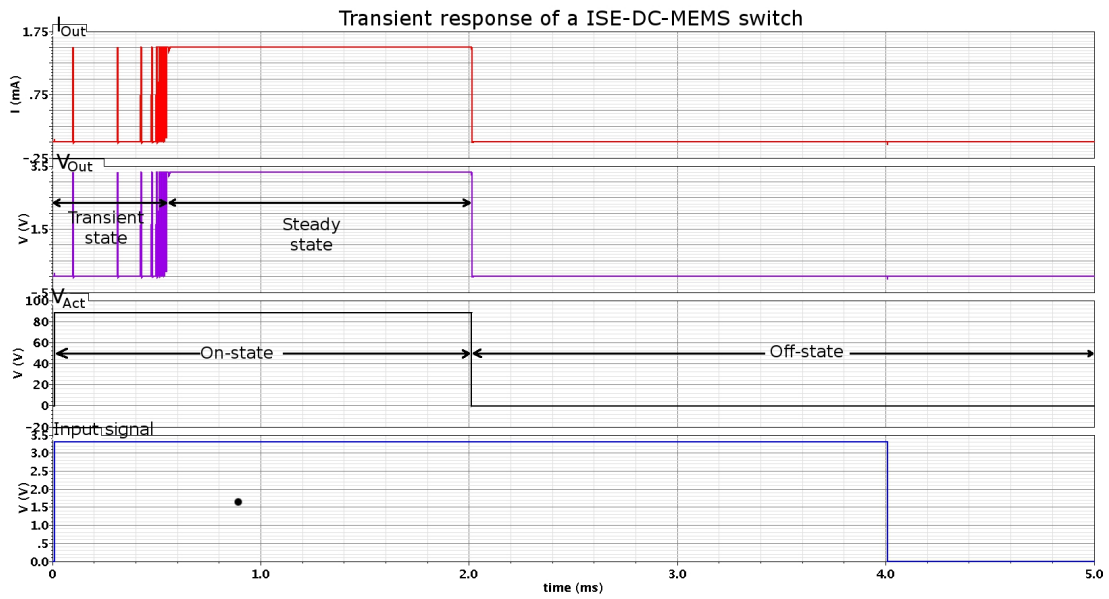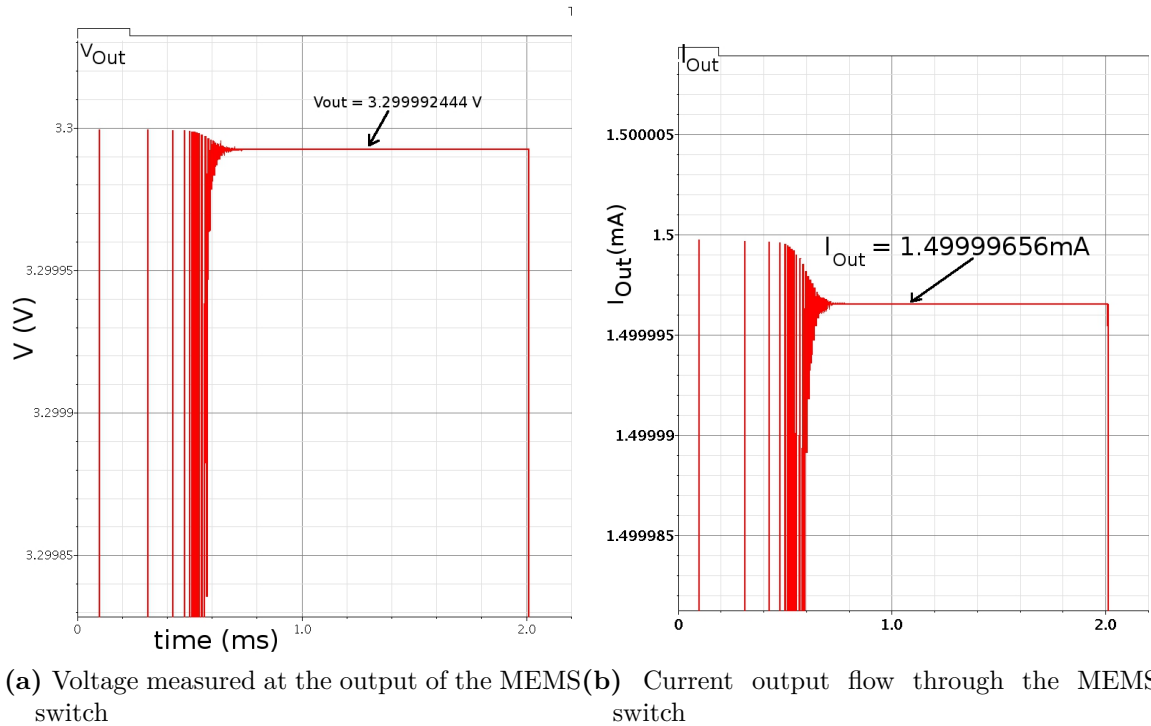**Figure 4.9.8.:** Simulation circuits for transient analysis of a MEMS switch

Figure 4.9.9.: Plot of transient response of an ISE-DC-MEMS switch using 88V of actuation voltage

(a) Voltage measured at the output of the MEMS switch

(b) Current output flow through the MEMS switch

Figure 4.9.10.: Voltage and current transient response in MEMS switch simulation

4.10. Discussion

This chapter discussed the ISE-DC-MEMS switch designs of SPST and SPDT. The design process for MEMS switches using MEMS+ and Cadence software has simplified the design and simulation process for new MEMS products. The 3D computer aided design (CAD) approaches in the MEMS+ software make it easy for designers to visualise and realise new ideas in MEMS design. The goal of introducing self-x features to the ISE-DC-MEMS switch has been achieved. Self-monitoring and self-repairing features have been embedded in the design. The self-monitor is used to monitor the mobility of the body mass via the capacitive sensor. The self-repairing feature uses the heat actuation principle to produce force to release the MEMS structure in a stiction event.

In the mechanical domain, it is easy to create mechanical structure using MEMS+ software. The mechanical behavioural models are well defined but, after completion of the first prototype evaluation, there was a need to add the design conformity test in the electrostatic actuator areas. This is because the MEMS+ model considered the behaviour of the electrostatic actuator as a rigid structure during simulation, and thus it did not model the dynamic behaviour of the electrostatic fingers. The outcome of the first prototype demonstrated stiction failure during operations. The investigation showed that the mechanical behavioural simulation did not consider the stiffness of the comb fingers when electrostatic force was applied. The original

simulation results show no bending effect on the individual fingers during electrostatic actuation but in the actual device the opposite happened, which lead to the stiction problem.

An improvement in design and simulation flow has been proposed with the introduction of stiction conformity test. A stiffness failure in the electrostatic actuator fingers has been detected, which causes the finger to bend in the presence of electrostatic force. As a result, a new parameter for safety design factors, S, has been proposed for inclusion in the design and simulation stage of the electrostatic actuator. Until a better algorithm to determine the dynamic numerical values of the electrostatic form is found, the S factor is used to compensate for these undetermined capacitance quantities. This proposal for improvement has been implemented during design and simulation activities for the second prototype of ISE-DC-MEMS switches. The results, after implementing the new design and simulation flow, will be presented in Chapter 6.

In the electrical domain, the MEMS+ software has a limitation in terms of introducing electrical elements in the MEMS model. The electrical elements can be created only by selecting certain mechanical structures and then creating the electrode contact in either lateral or horizontal positions. This approach limits flexibility to introduce electrical elements in the MEMS model. This leads to electrical behavioural models produced by MEMS+ software lacking parasitic capacitance and resistance along the signal paths. The capacitance and resistance models are limited only by the contact areas and not along the signal lines. This inadequate model will be improved and discussed in Chapter 5.

A better approach to introducing electrical components is needed. As an alternative approach, the electrical component could be introduced after the mechanical structures of the design are completed. The electrical component can be introduced by selecting the intended mechanical components that have electrical functions, either as resistance, capacitance or inductance. In this approach, a better electrical model can be produced from the MEMS+ behavioural model.

This research concentrated on the scalability of the MEMS switch in the area of electrostatic actuators with lateral movement as implemented in the ISE-DC-MEMS switch. Several parameters determining the electrostatic actuator behaviours have been discussed and presented. The other sub-components, especially in the new design of the heat actuators, required further investigation. Since the MEMS+ software could not be modelled and simulated with the physics of heat actuation, further investigation could not be pursued in this research. The current heat actuator was designed and simulated with Coventorware software in which can be accessed during a software trial version for a very limited time.

5. Test Chip Design and Post Layout Validation

5.1. Electrical Model Improvement for ISE-DC-MEMS Switches

In Chapter 4, the lack of resistance and parasitic capacitance elements in the electrical model generated by MEMS+ software was discussed. An inadequate electrical model caused inaccurate simulation results. This chapter proposes additional components on top of the original MEMS+ behavioural model in order to better represent the ISE-DC-MEMS switches. Two different models are proposed to represent the off-state and the on-state of the switch. Figure 5.1.1(a) shows the proposed electrical model of the MEMS switches for the off-state and Figure 5.1.1(b) shows the on-state MEMS switch model.

In this proposed model, several resistors and capacitors were added to the original model. Resistors in the signal-in and signal-out line were added in series to the signal line. The two R_{Line} resistor values were determined using two different methods. The first method is via geometrical calculation of the signal path. Appendix A demonstrates how the calculation is done. The second method is done by measuring the actual prototype. The measurement technique and respective results were discussed in Section 6.2.

Another resistor was added specifically in the on-state of MEMS model. The R'_{Cont} was added to represent the contact resistance during on-state. Although the original MEMS+ model considered contact resistance, based on the characterisation results, the value proposed by the original model is not adequate to represent the resistance value. As a result, R'_{Cont} resistors are added in series to the on-state MEMS switch model.

The capacitance introduced in this proposed model represents the parasitic capacitance between the MEMS lateral structures. There are two particular areas of interest between signal-in and signal-out for investigation as well as the parasitic capacitance surrounding the capacitive sensor area.

Chapter B discusses in detail the calculation in determining the parasitic capacitance values. The parasitic capacitance between the signal-in and signal-out paths is called C_{PLL}. The characterisation process to obtain the C_{PLL} value is explained in detail

Extraction Method	C_{PLE} $[fF]$	C_{PLL} $[fF]$	C_{SLA} $[fF]$	Extraction Method	R_{Line} $[\Omega]$	R'_{Cont} $[\Omega]$
EIS	3.900	14.00	0.900	DC Measurement	2.77	2.93
Calculation	3.445	1.608	0.2299	Calculation	0.4048	NA

Table 5.1.: Parameter values of parasitic capacitance and resistance component using different extraction methods

in Section 6.3.2.2 on page 140. The parasitic capacitance between the signal line and the electrostatic actuator is denoted as C_{PLE}. The explanation of characterisation process through which to obtain the C_{PLE} value can be found in Section 6.3.2.5 on page 153.

5.1.1. Electrical Simulation of MEMS Switch Model Behaviour

Electrical simulations were performed to evaluate the effects of the parasitic capacitance elements toward ISE-DC-MEMS switch behaviour. The proposed MEMS switch models were simulated and the results were then compared with the original MEMS model. Comparisons are made for off-state and on-state switch characteristics. All simulations presented in this chapter are based on the ISE-DC-MEMS SPST V1 model. The parasitic capacitance values were obtained via calculation methods and characterisation of the actual device. The EIS Spectrum Analyser software has been used to process the raw data and produce the best fitting value of the equivalent circuit model.

The most important part of resistance characteristics is the signal in/out line. The signal paths will determine the R_{Line} value of the proposed model. Another method, via geometrical calculations, is presented in Appendix A. Since the static and dynamic offset could not be determined using the available equipment, the calculation results are more reliable in this case.

5.1.1.1. Off-State Switch Characteristics

The additional parasitic capacitance in C_{PLL} turns the ISE-DC-MEMS switch model from a high-pass filter model into a band-pass filter model. Figure 5.1.2(a) shows a comparison of the AC response for three different parasitic capacitance values during the off-state. The green line represents the AC response of the model with no parasitic capacitance, which showed a high-pass filter response. The blue line represents the ISE-DC-MEMS switch AC response of the model with parasitic capacitance obtained via EIS fitting results. The AC response to the parasitic capacitance value obtained via the calculation method is represented by a red line. Both AC responses with parasitic capacitance showed a band-pass filter response. An AC simulation was performed to validate this model with sweep frequency set from $1Hz$ to $10^{18}Hz$.
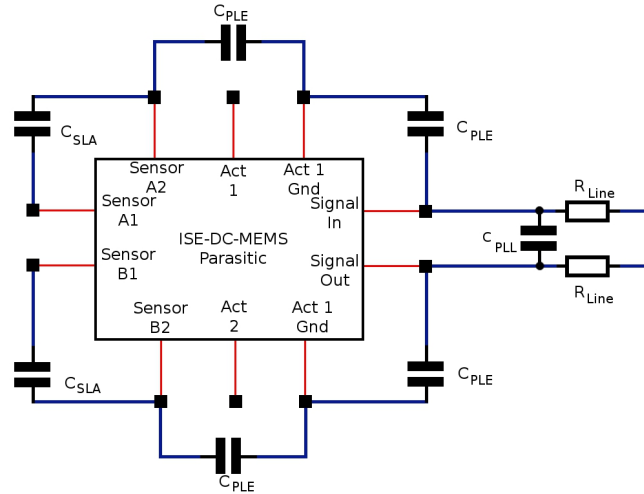
(a) Off-state MEMS switch model
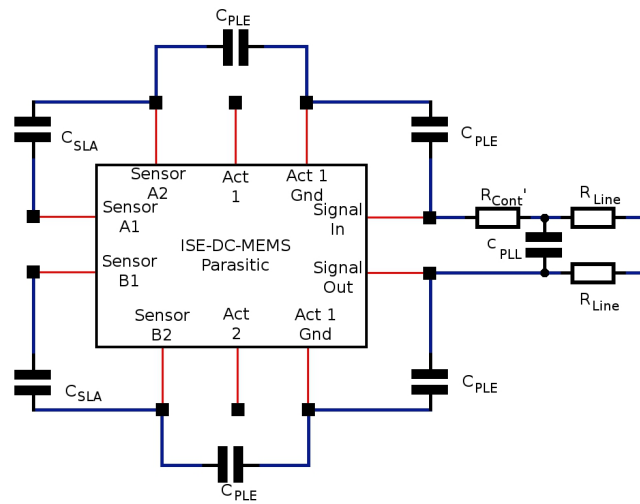
(b) On-state MEMS switch model

Figure 5.1.1.: ISE-DC-MEMS switch electrical model with additional parasitic components

V_{Act} [V]	86	88	90
V_{Switch} [mV]	4.2174	4.2166	4.2159
I_{Switch} [mA]	1.498083	1.4980834	1.49808367
R_{On} [Ω]	2.8152	2.8146	2.8142

Table 5.2.: Simulation results of R_{On} resistance with various voltage actuation

A very wide band frequency was implemented in order to show the overall response of the circuits with the given parasitic capacitance value. It is recognised that the simulation results at very high frequency presented here are inaccurate but they are included to show the overall electrical model behaviour of the ISE-DC-MEMS switch.

5.1.1.2. On-State Switch Characteristics

Transient analysis is used to study on-state switch characteristics. Figure 5.1.1(b) shows the proposed on-state MEMS switch model with additional R'_{Cont} resistance with a value set to 2Ω for all simulations. Three different actuation voltages were applied in the test, ranging from $86V$ to $90V$. A similar output response was recorded in the transient simulation and Table 5.2 shows the results. When the state changed from off- to the on-state, the switch response showed a bouncing effect in the contact area, represented by the transient region in which there were around $600\mu s$ before it reached a steady state of the switch. A higher voltage drop was recorded in these simulations when compared to simulation results using the original MEMS+ model. This is because of the introduction of R_{Cont} and R_{Line} in the MEMS switch model.

5.2. ISE-DC-MEMS Switch and Transmission Gate Comparison

5.2.1. R_{On} Resistance Comparison

As discussed in previous sections, the ISE-DC-MEMS switches produce a rather low R_{On} resistance. This section will compare the R_{On} resistance between ISE-DC-MEMS switch and the transmission gate. The simulation was performed using a simple circuit with one DC voltage source set at $3.3V$, one transmission gate as switch and one resistive load with $2.2k\Omega$ of resistance as shown in Figure 5.2.1. The transmission gate is taken from the A_cell library provided by the Austria Microsystem hit-kit c3.80 for $0.35\mu m$ CMOS process, which has a standard size of $5\mu m$ in width and $0.35\mu m$ in length for both P-channel and N-channel MOS transistors. The switch is turned on for $1ms$ and the voltage drop across the transmission gate is measured. Figure 5.2.2 shows the R_{On} behaviour of the standard size and large
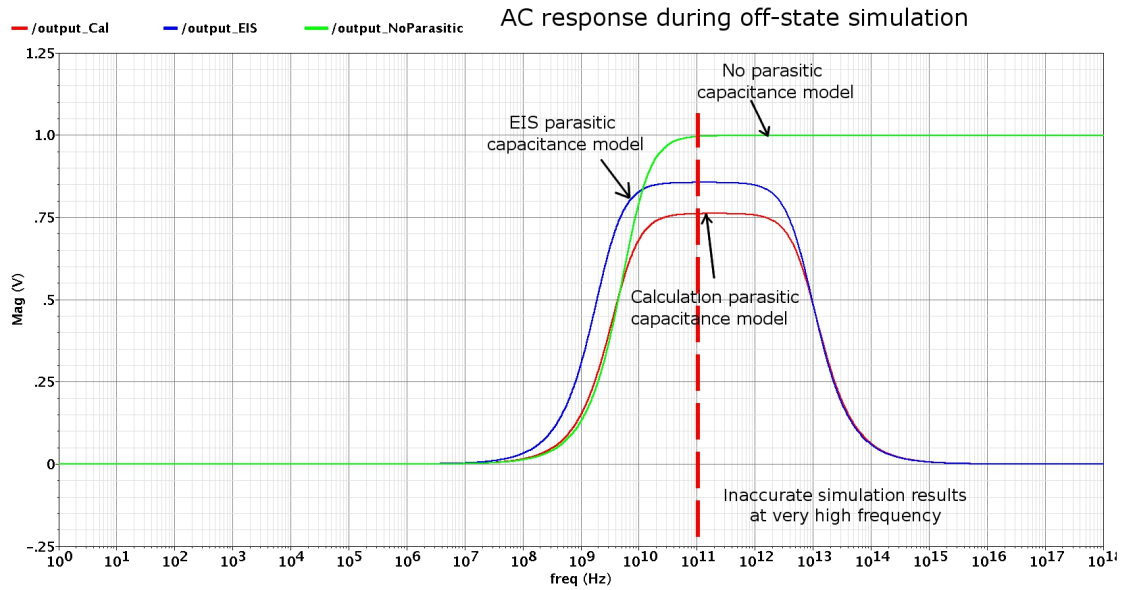
(a) Signal-in and signal-out response of ISE-DC-MEMS switch during AC simulation
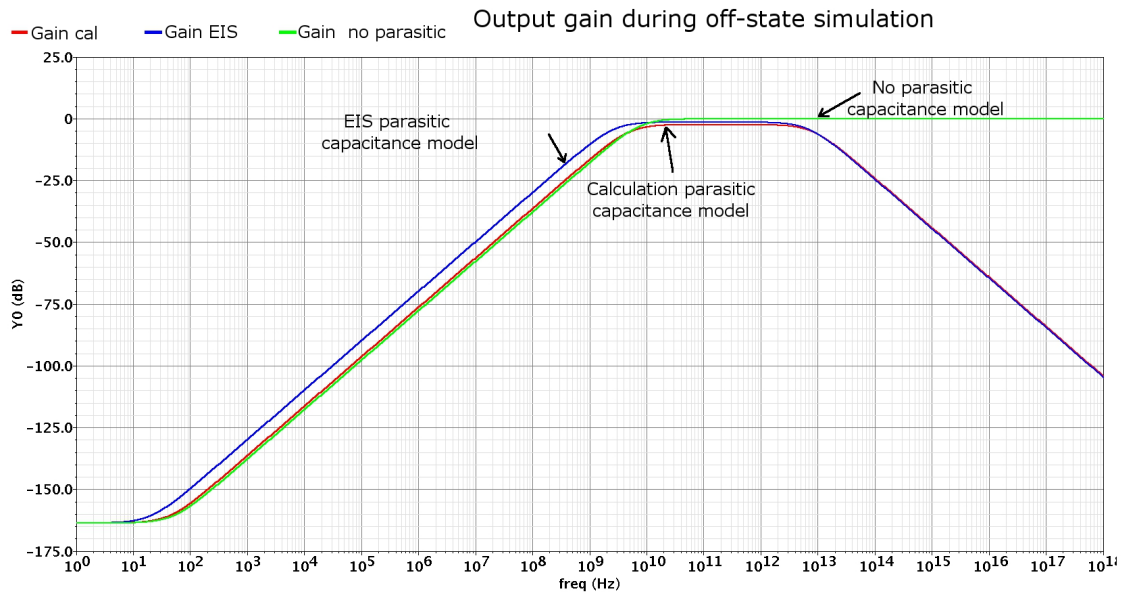
(b) Band-pass filter characteristics shown by the output gain of the MEMS switch

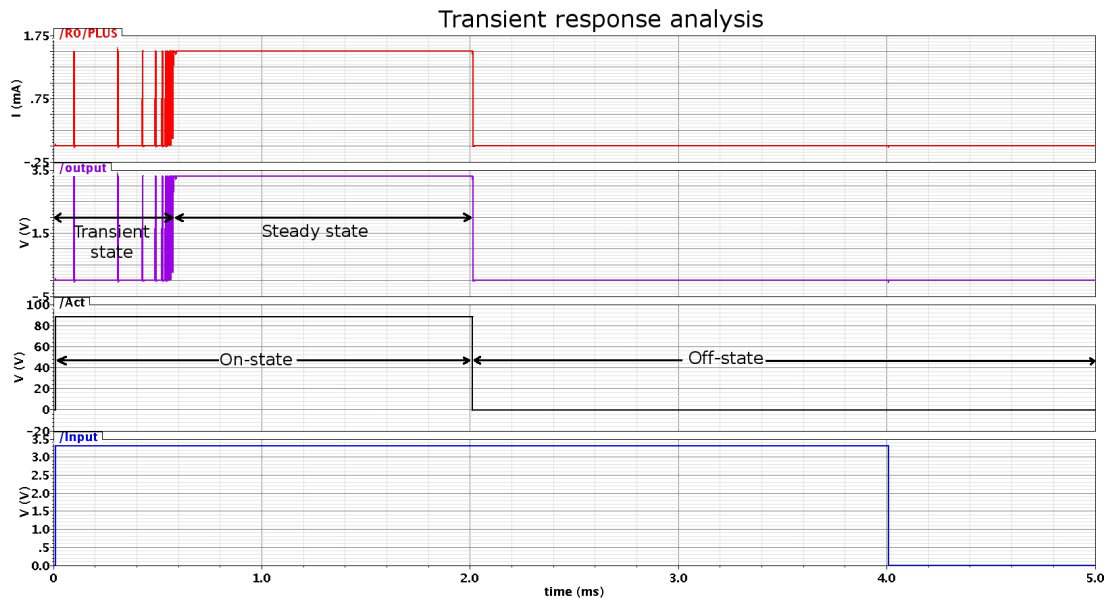**Figure 5.1.2.:** AC simulation of ISE-DC-MEMS switch with parasitic elements

Figure 5.1.3.: Transient response of MEMS switch during on-state

transmission gate with a DC sweep of input voltage. The voltage drops across both the transmission gate are varied with input voltage sweep.

A small transmission gate has a high R_{On} resistance but it also has a high switching rate since there is no structural movement as on a MEMS switch. Table 5.3 compares the R_{On} resistance and switching speed between the transmission gate and MEMS switch.
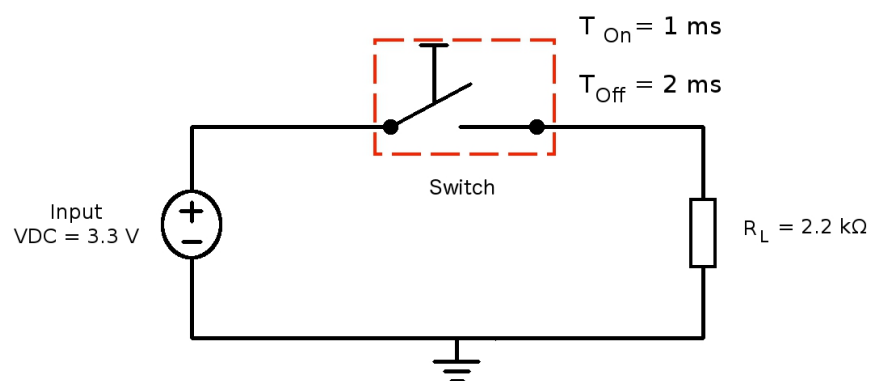
Figure 5.2.1.: Circuit for R_{On} simulation
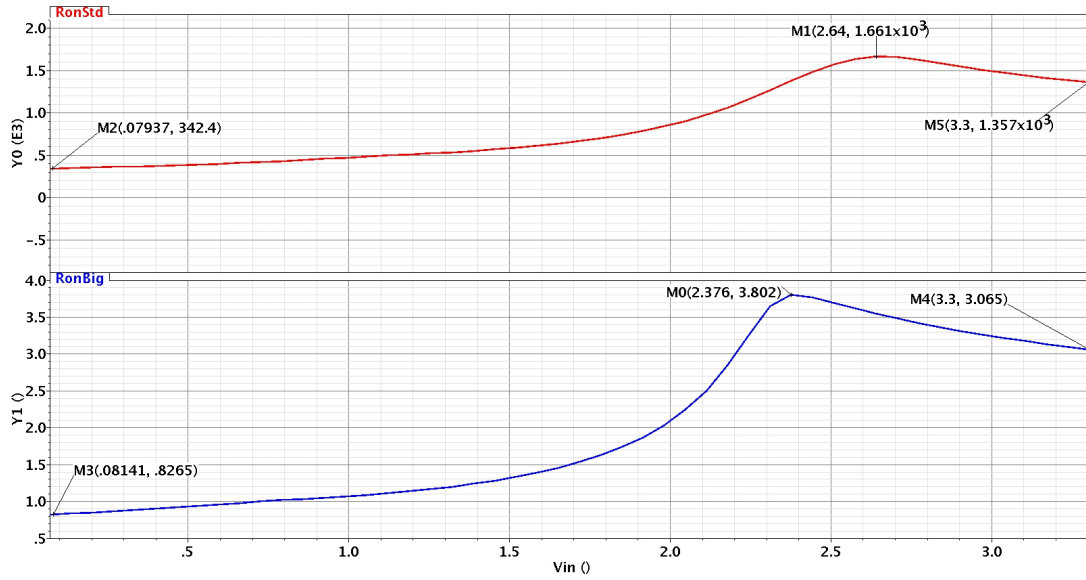
Figure 5.2.2.: R_{On} behaviour of standard and large transmission gate during on-state with DC sweep of input voltage

Switch	R_{On}	Switching Time
Transmission Gate	$1.452k\Omega$	$0.5\mu s$
MEMS switch	2.814Ω	$600\mu s$

Table 5.3.: Comparison between transmission gate and MEMS switch

Parameter	N MOS	P MOS
Width [μm]	0.35	0.35
Length[μm]	10	2000

Table 5.4.: Parameter values of a transmission gate that produced $R_{On} = 3\Omega$

5.2.2. Sample-and-Hold Circuit Comparison

A sample-and-hold circuit can be used as a vehicle for comparison between an ISE-DC-MEMS switch and a transmission gate. Two effects can be studied using this circuit are charge injection effects which can be seen during the on-state to off-state, and the leakage current problem which is during the off-state.

The first set of simulations is performed to show the charge injection effect in the transmission gate and ISE-DC-MEMS switch. There is a problem in a CMOS transmission gate of charge injection or clock feed-through effect. This effect is due to the coupling capacitance from the gate to both the source and drain channel. A simple circuit with capacitive load and DC voltage input controlled by a switch is used to demonstrate this effect as shown in Figure 5.2.4. The capacitance load is set to $10pF$ and the input DC signal is set to $3.3V$. The switch is triggered to on-state for $1ms$ for the sample cycle and then turned to the off-state for the hold cycle. $1ms$ of on-state time was used for easy visualisation of the effect in the simulation results. The V_{Error} is measured at the peak point of beginning the hold-cycle. In this simulation, comparison was made between three different switches. The first switch is a transmission gate called TG2B, taken from the standard cell from the A_cell library[1] in Cadence software. This is the same switch model that was used in the R_{On} resistance comparison.

The second switch is a transmission gate that has specific size and produced small R_{On} resistance in the region of 3Ω. Table 5.4 shows the parameters this transmission gate and Figure 5.2.3 shows the layout of the transmission gate which is measured at $90\mu m \times 60\mu m$ an produced an area of $5400\mu m$. This second switch is used to compare the performance of the transmission gate and MEMS switch that has the same R_{On} value. The third simulation will use an ISE-DC-MEMS switch.

Figure 5.2.5 shows the timing diagram of sample-and-hold circuits with the standard transmission gate of TG2B. In this simulation, the V_{CL} value jumped from $3.3V$ to $3.300887V$ after the sample cycle was finished. This produced the V_{Error} of $887\mu V$ or an additional 0.0267% of voltage contributed by the charge injection from channel coupling capacitance.

In the second simulation using a transmission gate with the same R_{On} resistance as the MEMS switch, a bigger V_{Error} was produced when compared to previous simulation results, as shown in Figure 5.2.6. The V_{Error} is recorded with a value

---

[1]Library from Austria Micro Systeme (AMS) hit-kit c3.80 for $0.35\mu m$ CMOS process
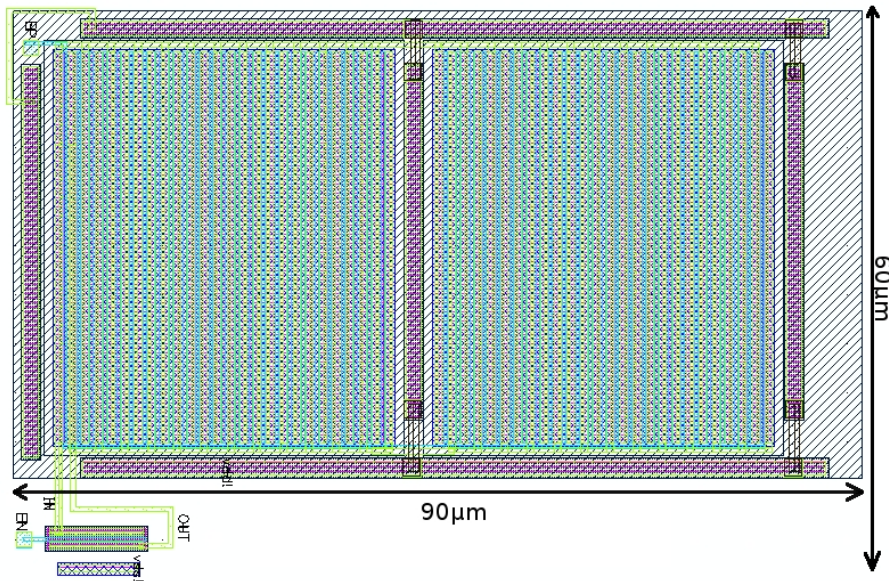
Figure 5.2.3.: Layout of transmission gate with 3Ω on-resistance

of $0.12756V$ or an additional 3.8% of voltage contributed by charge injection effect. This shows the effort required to reduce the R_{On} of the transmission gate leads to increase the charge injection effect.

In MEMS switches, a small ripple is shown at the beginning of the holding state before reaching to the steady state after a few milliseconds. This is because of the bouncing effect in the contact area, which turned from a resistance equivalent model into a capacitance equivalent model. This bouncing effect changes the gap between two parallel contacts. The maximum peak to peak ripple is measured at $24.27\mu V$. The MEMS does not face any charge injection effect like the CMOS transmission gate, which has ripple effect in the output voltage at the beginning the holding state.
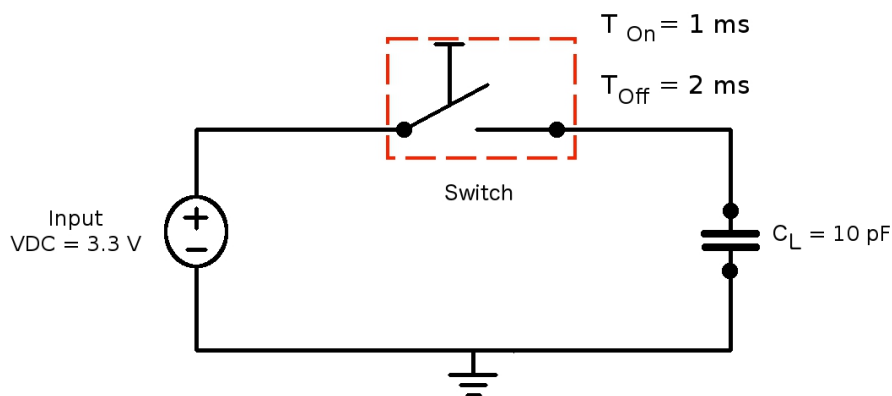
Figure 5.2.4.: Circuit for sample and hold simulation
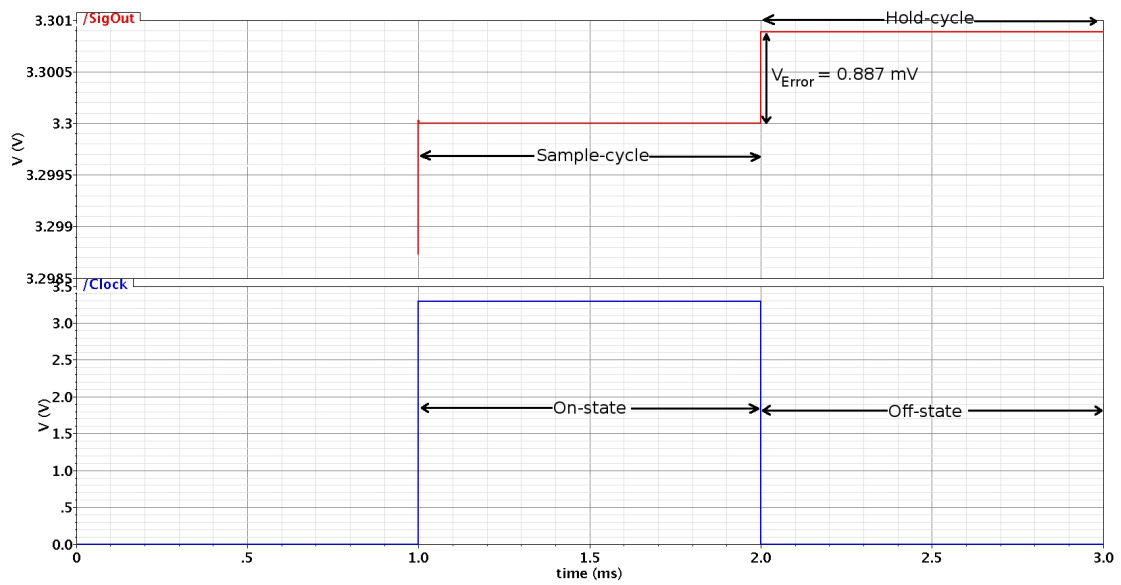
Figure 5.2.5.: Timing diagram of a sample-and-hold simulation using the standard cell of a transmission gate
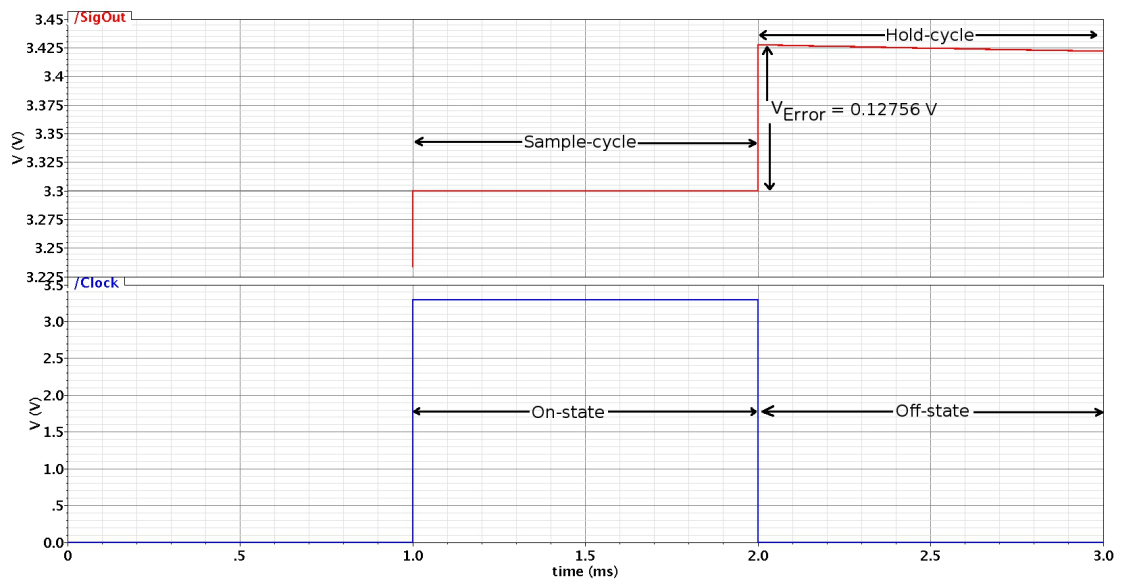
Figure 5.2.6.: Timing diagram of a sample-and-hold simulation using a big transmission gate with low R_{On} value
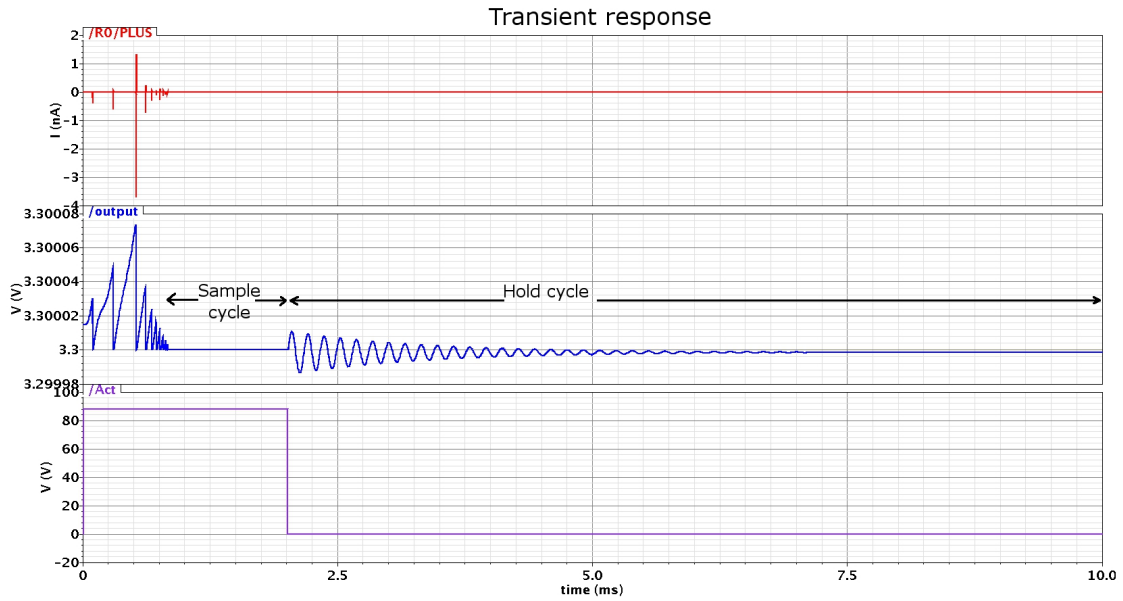
(a) Timing diagram of ISE-DC-MEMS switch response
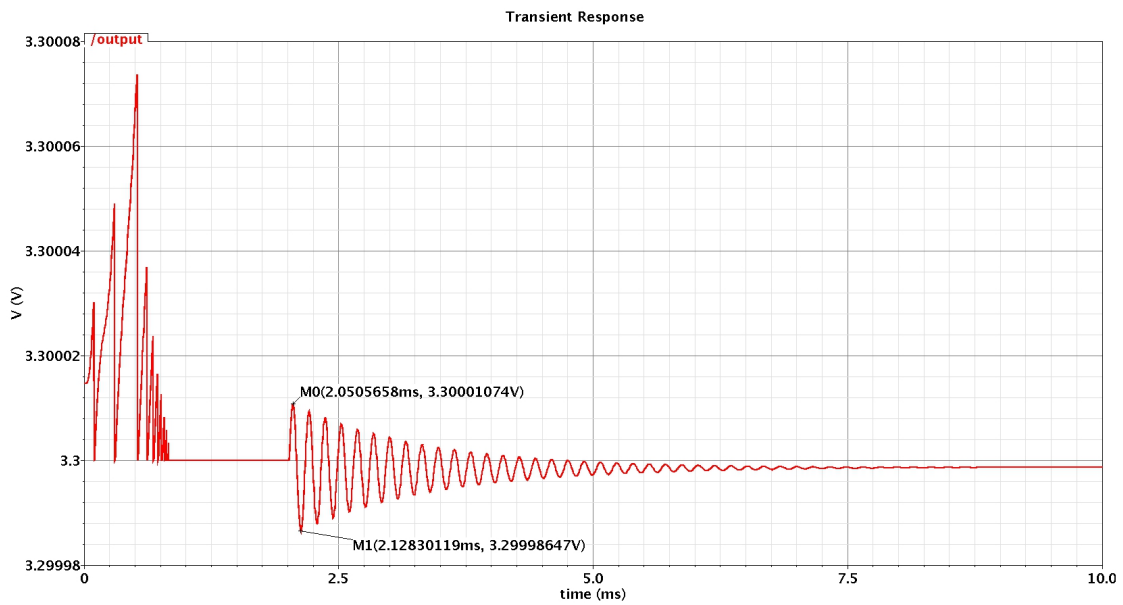
(b) Zoom result of the ISE-DC-MEMS switch response

Figure 5.2.7.: Timing diagram of a sample-and-hold simulations using the ISE-DC-MEMS switch.

The second set of simulations is performed to show the leakage current effect in these switches. A similar simulation circuit is used with a smaller capacitance load at $1pF$ and longer simulation time set to $500ms$. The simulation parameters were altered in order to provide a better visualisation of the effect. The leakage current effect can be observed in the hold-state, where the switch is in off-state.

In the first simulation (Figure 5.2.8), a standard transmission gate was used. At the beginning of the holding state, the output voltage was recorded as $3.307962626V$. At $500ms$, a voltage drop of $5.678mV$ was recorded, with the voltage continuing to decrease over time. This simulation validates the leakage current effect that took place in the transmission gate.

The second simulation used the large of transmission gate with a low R_{On}. Figure 5.2.9 shows the transient response of the given transmission gate. There was a huge output of voltage at the start of the hold-state, of approximately $3.673V$. This is the charge injection effect due to the large size of the transmission gate and the small capacitive load. This voltage is reduced rapidly from $2ms$ to $150ms$ and then it is slowly decreased over the time. The voltage drop between $2ms$ to $500ms$ is recorded at $0.3781V$ and there is a smaller voltage drop at $2.454mV$ from $150ms$ to $500ms$.

In the third simulation, the ISE-DC-MEMS switch is used with the same simulation set up. When the transient effect at the beginning of the holding state is finished, a different outcome can be observed from the simulation result. As the simulation time increases, the output voltage level did not fall as with the transmission gate. It slowly increased over the time until it reached steady-state at around $2s$. After reaching steady state, the voltage was maintained over time showing no leakage current effect in the ISE-DC-MEMS switch. The simulation result in Figure 5.2.10 shows an additional voltage at around $0.2mV$ which was contributed by the parasitic capacitance in the ISE-DC-MEMS switch.

5.2.3. Crosstalk Performance Comparison

The analogue multiplexer, or 'mux', is a device that is built from several switches with several input signals and a single output. Transmission gates are often used to build multiplexers in the integrated circuits. This section discusses ISE-DC-MEMS switch performance in functioning as a multiplexer, and explicitly the crosstalk performance.

In order to evaluate the MEMS switch performance as an analogue mux, a two channel mux was built using two ISE-DC-MEMS switches, and called the MEMS-Mux. Figure 5.2.11 shows the simulation circuits of a 2 channel MEMS-Mux using the ISE-DC-MEMS switch model as given in Figure 5.1.1. In this simulation, the MEMS-Mux is switched to input signal 1, which is connected to a $3.3V$ DC voltage source at the beginning of the simulation. After $600\mu s$, the output voltage reached the steady state output. Input signal 2 is connected to a sine wave source with $1V$ peak to peak value and $1kHz$ frequency. Figure 5.2.12 shows the timing diagram
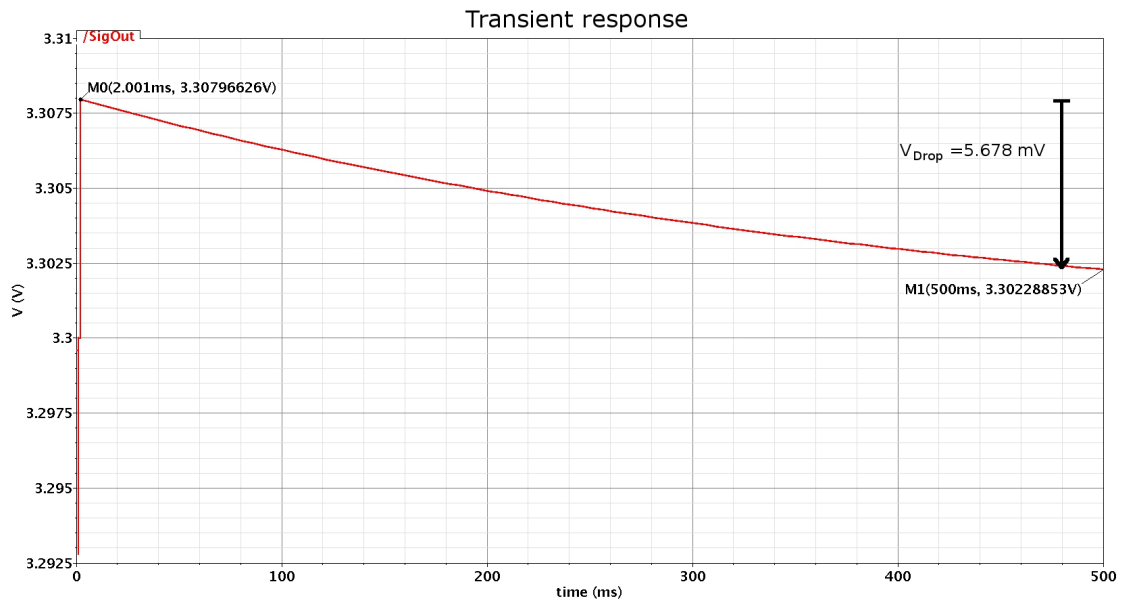
Figure 5.2.8.: Transient response of standard cell of a transmission gate with leakage current effect
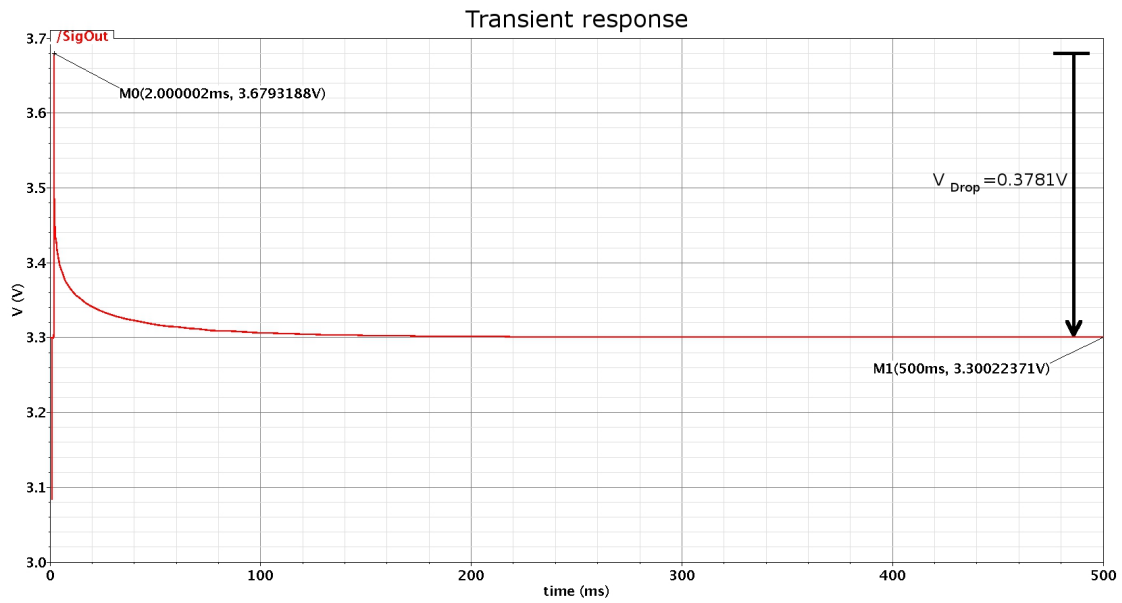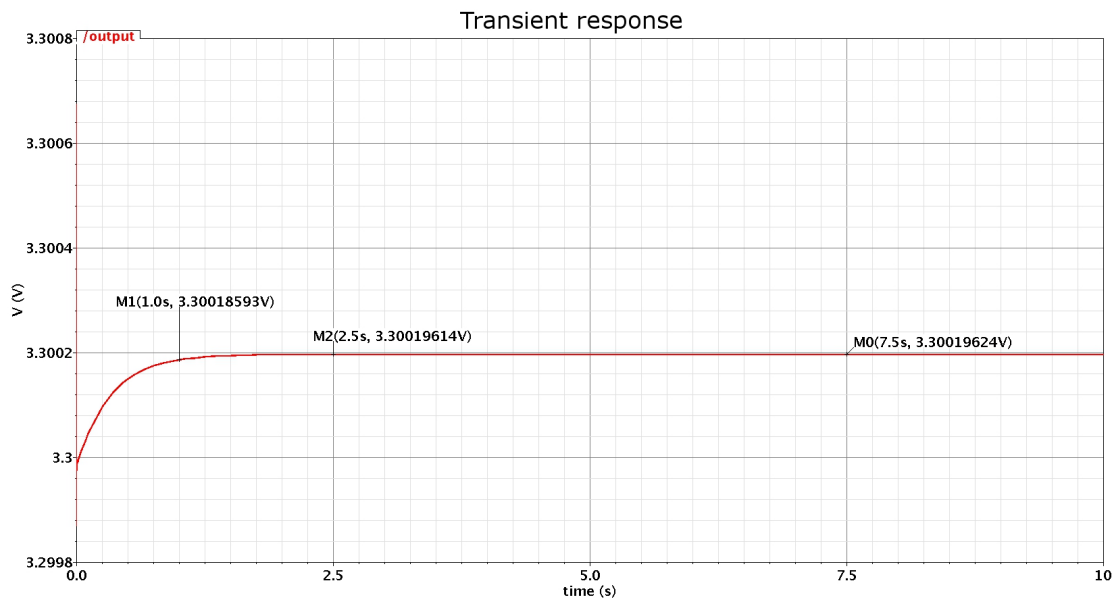

Figure 5.2.9.: Transient response of huge size with low R_{On} of a transmission gate with leakage current effect

Figure 5.2.10.: Transient response of ISE-DC-MEMS switch

response of the 2 channel MEMS-Mux. The sine voltage source was activated only after $2ms$, as shown by the $Input2$ label in the timing diagram. The MEMS-Mux output appears similar when the sine voltage source was activated. Close observation revealed that in the time slot before and after the sine wave activation, the signal crosstalk appeared in the output channel with a sine wave with a very small voltage peak to peak (V_{P-P}) value. The crosstalk investigations were measured in five different frequency points, $1kHz$, $20kHz$, $40kHz$, $1MHz$ and $4MHz$.

The first comparison was implemented between the signal isolation performances in a single MEMS switch and the crosstalk of 2 channel MEMS-Mux. Figure 5.2.13 shows the V_{P-P} between these two conditions. The V_{P-P} for signal isolation in a single MEMS switch was followed according to the AC simulation as shown in Figure 5.1.2. In contrast, the V_{P-P} results for a 2 channel MEMS-Mux demonstrate better performance when compared to a single MEMS signal isolation. At every point, some 3-decades lower V_{P-P} was achieved by the 2-channel MEMS-Mux. This is because the equivalent circuits in the 2-channel MEMS-Mux changed due to the combination from the two MEMS switches that suppressed the output crosstalk signals to lower levels when compared to the equivalent circuits of single MEMS switches.

The second comparison was made between a two channel mux built from MEMS switches and a transmission gate. A similar transmission gate, which was used in R_{On} investigation, was implemented to build this 2-channel mux. Figure 5.2.14 shows the comparison between five frequency points. The V_{P-P} response of mux using the transmission gate produced better results compared to MEMS-mux as the frequency increased. This shows that crosstalk is very minimal in a mux built from
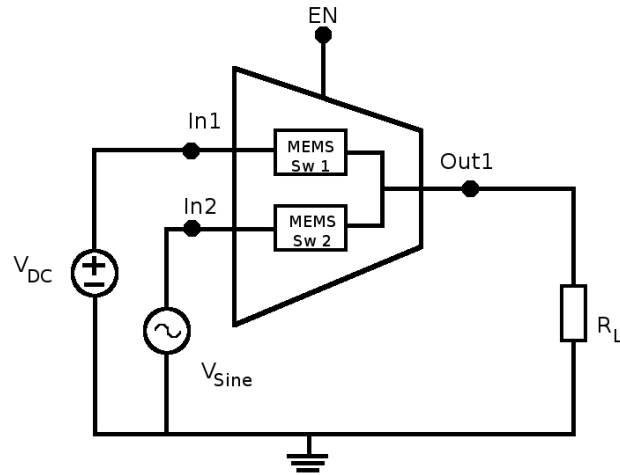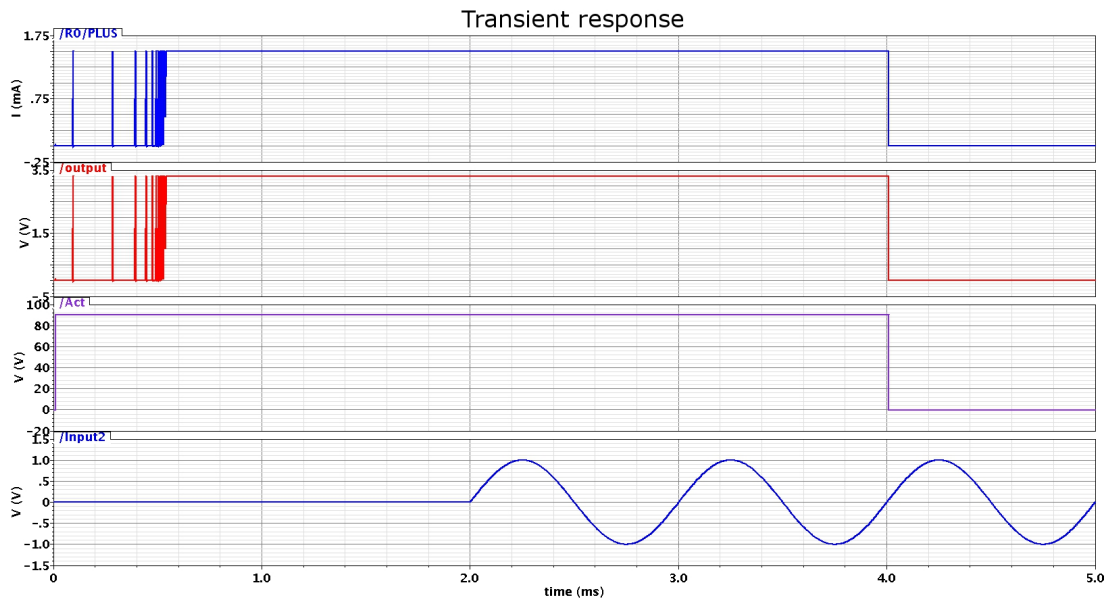
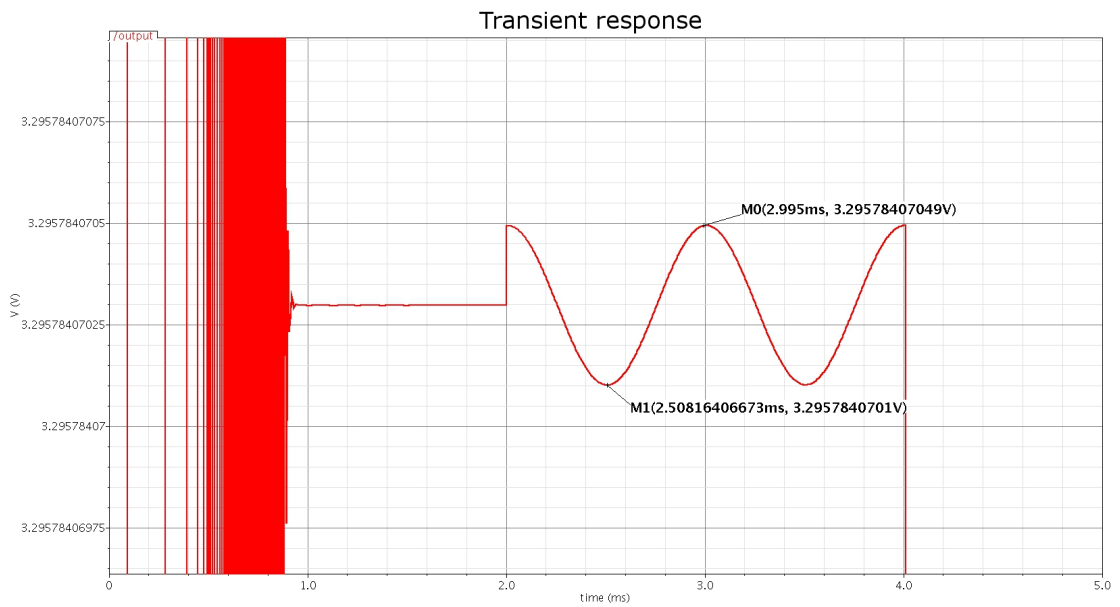**Figure 5.2.11.:** Circuit for crosstalk analysis using an Analogue-Mux by ISE-DC-MEMS switch

a transmission gate.
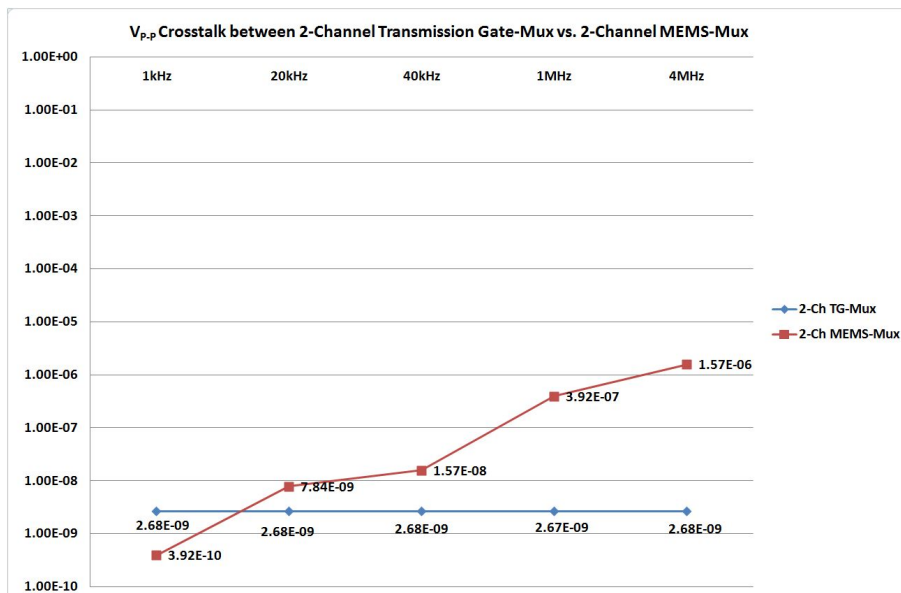
Figure 5.2.14.: Comparison between V_{P-P} of crosstalk in 2-channel transmission gate-Mux and 2-channel MEMS-Mux
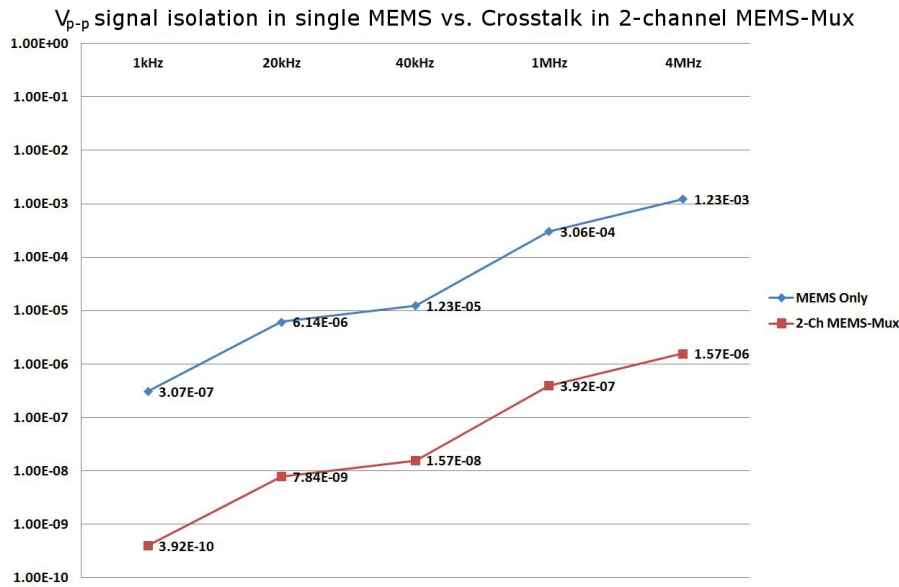
(a) Timing diagram of input and output responses for 2-channel MEMS-Mux

(b) Crosstalk in mux using MEMS occurred when a sine wave was introduced

Figure 5.2.12.: Simulation of 2-channel MEMS-Mux with AC and DC input source

Figure 5.2.13.: Comparison between V_{P-P} of signal isolation in single MEMS and crosstalk in 2-channel MEMS-Mux

5.3. The Layout of 1st Prototype ISE-DC-MEMS Chip

The first prototype consists of two types of MEMS switch. In a single die of $1cm \times 1cm$, there are six identical SPST MEMS switches and two identical SPDT MEMS switches. In this first batch, the switches are not cut into sub-dice. Figure 5.3.1 shows the overall layout of the MEMS die prototype.

In the final layout, both designs have pads larger than the minimum requirement. This extension is performed for two purposes. Firstly, it is intended to accommodate our wafer probing facility unit which uses needles from Micromanipulator model 7B-10 which have a point radius of 10 microns. The bigger size is needed to make the pads easily accessible during the later characterisation process.

The second reason is to embed on-chip resistance for heat actuator components. Due to the space limitation, the on-chip resistors are applied only in SPST switch design. The resistors are made from polysilicon material and can be identified by the red strip in the Figure 5.3.1. The main purpose of this is to study the effect of an on-chip resistor in heat actuator behaviour. The heat actuation performance will be characterised with and without on-chip resistance. A close observation will be done to compare the performance between these two heat actuator designs.

In each die, the switches are labelled according to their types and positions. Each label contains of two letters and one number, for example AS1. The first letter is the die identification of the samples. There are 16 dice which have the identifications from A to P. The second letter in the label determines the type of switch. The
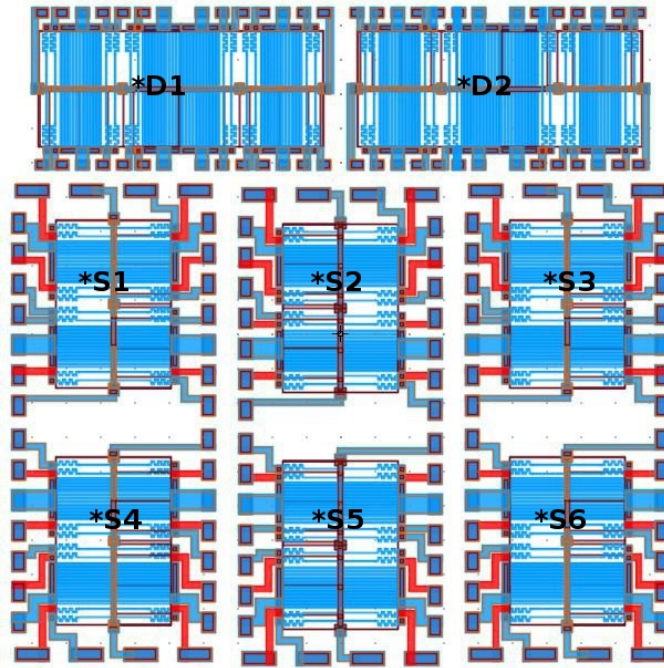
Figure 5.3.1.: MEMS die layout

SPST switch will be labelled 'S' and the SPDT switch labelled 'D'. The number in the label determines the position of the switch in the dice. Figure 5.3.1 shows the label of the MEMS switches in a die.

In SPST switch designs, there are two different resistor set ups. The A type has three actuators with a resistor and one heat actuator with no on-chip resistor. In the B type all four actuators come with on-chip resistors. With the resistor embedded, both ends of the resistor are covered with the gold layer pads. This is important in order to bypass the resistor if necessary during characterisation phase.

The SPDT switch, on the other hand, has no resistor embedded in it and thus only extends the bigger pad. In general, the extension pads are $300\mu m \times 200\mu m$.

5.4. The Layout of the 2nd Prototype ISE-DC-MEMS Switch

In the second prototype, all findings and suggestions for improvement were implemented. Due to limited space and cost, the design process concentrated on the relevant size of SPST switch designs. As explained in Chapter 4, the design requirements for the second prototype are slightly different. The designs of the second prototype are targeted for a wider range of MEMS switch applications. For application in the area of reconfigurable electronics circuitry, in which low switching
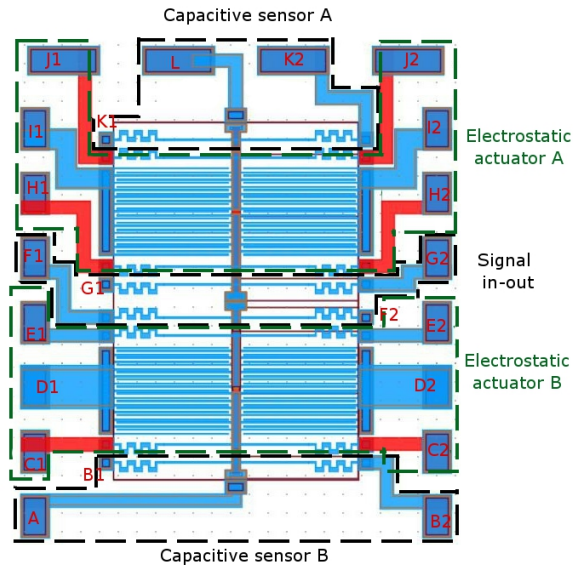
(a) SPST switch A
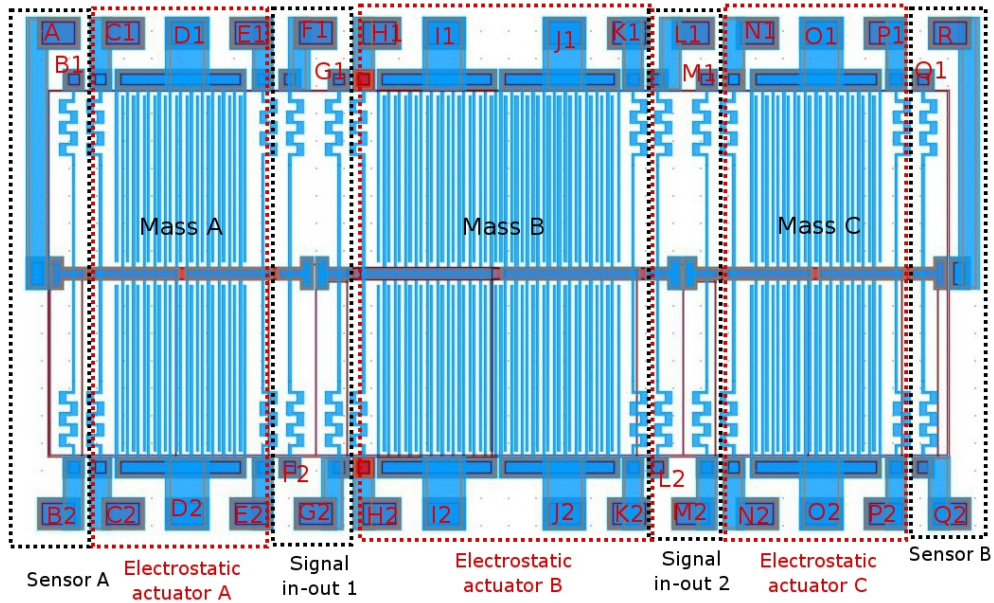
(b) SPDT switch

Figure 5.3.2.: ISE-DC MEMS switch sub component and ports label

frequency change were applied, low actuation voltage is required. In this application, the most important thing is to obtain an easier integration at chip level, where MEMS die and analogue CMOS die can be integrated under one package. In order to achieve that integration, the voltage actuation must be lower than the maximum voltage that HV-CMOS technology can handle, which is $60V$.

In the second prototype, three different switch categories were designed. The first switch category, denoted as 'I', has an actuation voltage set at less than $30V$, the second category is marked as 'II' and has an actuation voltage less than $60V$ and the third category is marked as 'III' and has an actuation voltage less than $80V$.

For each category, two design variants with different safety factors were implemented. Two safety factor values were set at 1.5 and 2.0, and produced a slight difference in terms of switch sizing. The same category of switches with different safety factors was arranged in the same sub-die for easy evaluation later on.

In the second prototype, as shown in Figure 5.4.1, the main die is cut into three separate sub-dice according to their design categories. Each sub-die will consist of two switches which have different safety factors. Special marks, in the form of Roman numerals I, II and III, were added to each sub-die for easy identification. The switches which are closer to these marks are those that achieved Safety Factor 1.5. The foundry also required special marking in the form of polylines, to show the sub-dicing cutting areas. These marks were located between the switch design.

Another design improvement was the implementation of a guard ring in the capacitive sensor in the SPST switch. In the former design, the type-D sensor with a simple parallel plate structure was used. This design was unstable in total sensing capacitance due to fringe capacitance in the side area (Figure 5.4.2a). A better structural design with a guard ring, which provided better accuracy in the capacitive sensor as in Figure 5.4.2c was implemented. This will improve the accuracy of the capacitive value with greater homogeneity of the electric field.

In the final layout, there will be no more on-board resistance embedded in the heat actuator structure. This decision was made based on the results obtained from the previous prototypes in which on-board resistance offered only a small improvement in performance. As a result a smaller pad design could be achieved in the second prototype.

5.5. Discussion

In this chapter, additional electrical models were proposed to improve the accuracy of the model simulations. Two proposed models representing the on-state and the off-state were analysed. A comparison was made between the original MEMS+ model and the proposed model. The element value of the proposed model was obtained via calculation and characterisation of the prototype. The additional parasitic elements
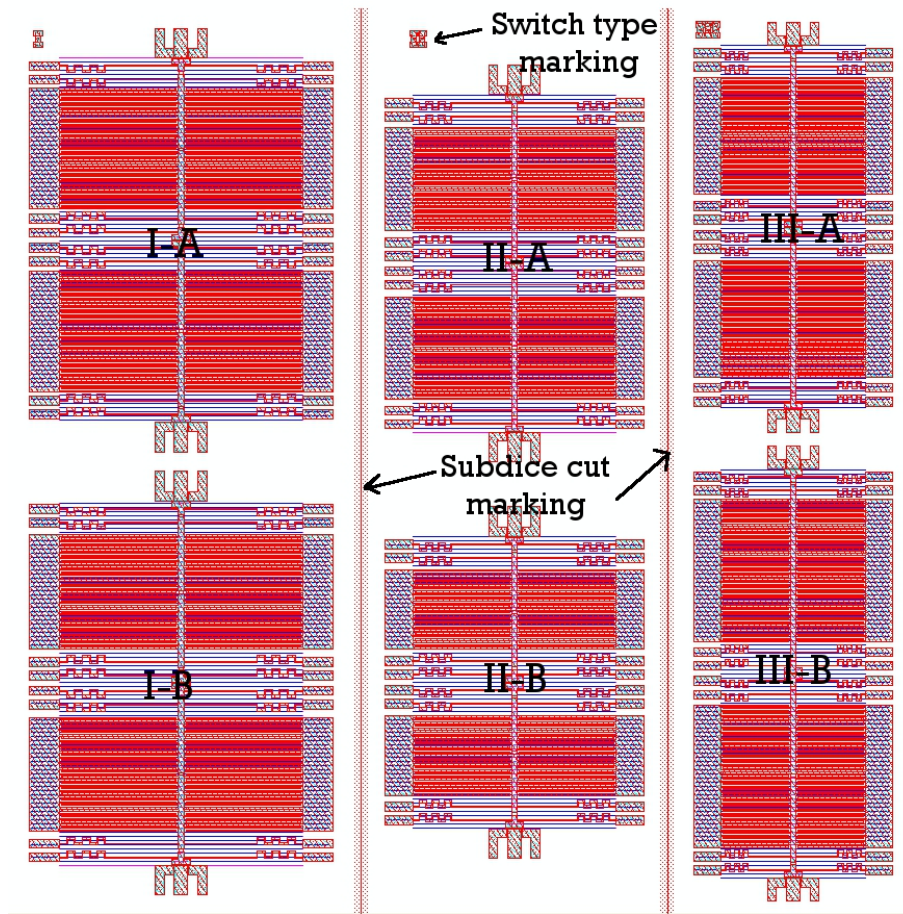
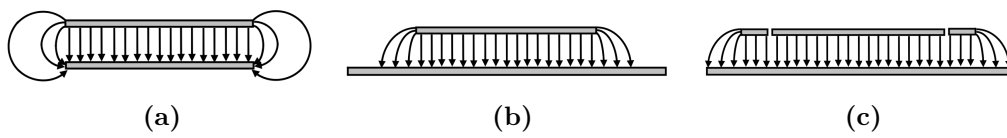**Figure 5.4.1.:** Second ISE-DC-MEMS switch prototype layout

Figure 5.4.2.: Three variants of the D-Type capacitive sensor

	ISE-DC-MEMS SPST-V1	Radant MEMS	TUD	UCL	MEMSCAP	Transmission Gate Std	Big
Switch Type	SPST-V1	Radant MEMS	TUD	UCL	MEMSCAP		
Actuation — Actuation Method	E and/or H	E	H and M	E	H	Voltage	Voltage
Pull-In Voltage [V]	85.5	90	NA	6	NA	3.3V	3.3V
Heat Act Current[mA]	< 300	NA	< 200	< 300	< 300	NA	NA
Res. Freq.[kHz]	6.4269	NA	NA	NA	NA	NA	NA
Area[mm²]	5.11	1.974	20.88	0.05	25*		
Length [μm]	2675	1450	3600	74	2500		
Width [μm]	1910	1400	5800	63	10000		
	uni-stable	uni-stable	bi-stable	uni-stable	bi-stable	uni-stable	uni-stable
Self-x Feature	Self-monitor & repair	NA	NA	NA	NA	NA	NA
Signal Isolation, — Output gain=−19 dB	348.7 MHz	< 10 GHz	NA	NA	NA	NA	3.423 GHz
Output gain=−17 dB	441.3 MHz	< 20 GHz	NA	NA	NA	NA	NA
Output gain=−12 dB	809.6 MHz	< 35 GHz	NA	NA	NA	NA	NA
On-Resistance $R_{on}[\Omega]$	< 3**	< 4	87.2 m	8.1 k	0.3		
Switching speed, — On[μs]	< 600	< 10	< 400	NA	∼80	< 1	< 1
Off[μs]	< 10	< 2	NA	NA	NA	< 1	< 1

Legend: E=Electrostatic; H=Heat; M=Magnetostatic; V=Voltage; NA=Not available
* with 1x32 switch array; ** Pessimistic value
*** varies with design

Table 5.5.: Comparison table of DC-MEMS specifications from ISE-DC-MEMS, commercial and other research groups

in the ISE-DC-MEMS switch models improved the behavioural model of the MEMS switch. The implementation of this new model resulted in a different output response behaviour from a standard high pass filter in the standard MEMS+ model into a band pass filter performance.

The performance comparisons between ISE-DC-MEMS switches and the transmission gate show the results expected. MEMS switches demonstrated superior R_{On} resistance when compared to a standard transmission gate size. The low R_{On} resistance will be of benefit the front-end sensor area in particular, where minimal signal loss is required during measurement process to ensure high accuracy.

Lower R_{On} resistance in the transmission gate can be achieved but only with a very large transistor size which lead to bigger problems in leakage current and charge injections as shown in the sample and hold simulations. MEMS switches on the other hand show no charge injection effect in the sample and hold simulation but had a transient effect on the output load after changing the state of the switch. This produced a slower response in the voltage read out of the hold state of the circuits.

There is no significant difference in crosstalk performance in mux circuits between transmission gate and MEMS switch mux when handling less than $20kHz$ frequency, but for the higher range frequency, the transmission gate is able to maintain its performance at $2.6nV$ peak to peak, while the MEMS switch reached $1.57\mu V$ peak to peak at $4MHz$. In a specific application for handling audio signal lines which normally operates at less than $20kHz$, the MEMS-Mux can be a good alternative since it offers a low level of crosstalk and low R_{On} resistance.

6. ISE-DC-MEMS Switch Functional Test and Characterisation

6.1. Classification of Analysis

This chapter presents the measurement and characterisation of first and second generation ISE-DC-MEMS switch analysis. Analysis of the first generation ISE-DC-MEMS switch emphasises the modelling of the given switch. Analysis of the second generation involves the design improvements that have been implemented. The testing and characterisation of the switches were performed in the ISE-Laboratory. A Karl Suss PM 5 wafer probe station was used to test these prototypes. The characterisation test can be divided into three categories:

1. Electrical signal characteristics - DC signal

2. Electrical signal characteristics - High frequency signal

3. Mechanical characteristics - Microactuator functionality

6.2. Electrical Characteristics of MEMS Switches - DC Signal

6.2.1. Measurement Setup

The characterisation of ISE-DC-MEMS switches at DC signal is important. This is because the switch design is intended for DC signal application in the analogue signal domain with a moderate switching frequency. The measurement is performed using a Keithley 238-source measuring unit. The source-delay-measure technique is used with this equipment as shown in Figure 6.2.1. In this method, the test equipment will supply the current source to the DUT and then the voltage drop will be measured. A supply current in the range of $10mA$ to $30mA$ was applied across the ports. Four samples each of SPST and SPDT were used for this measurement, with five repetitions.

The precision of the measurement results were influenced with the measurement offset. There are two types of measurement offset, static offset and dynamic offset.
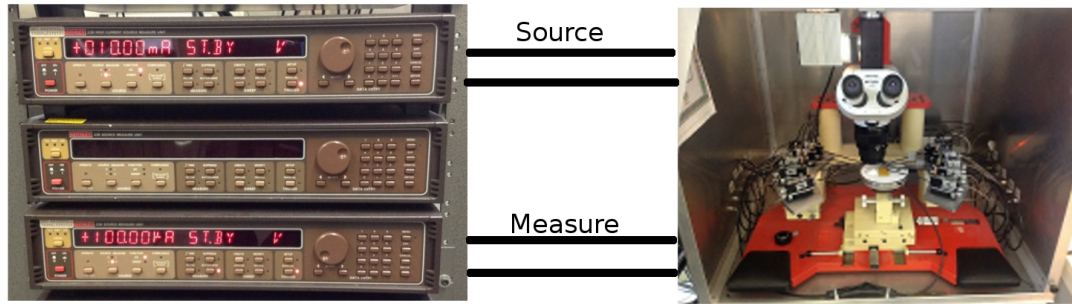
Figure 6.2.1.: Source-measure concept

The static offset is the offset due to an internal resistance and wiring setup during measurement. It depends on the wire connections from the Keithley 238 measurement unit to the tip of the needle. The dynamic offset on the other hand, involves the contact resistance between the needles of the micro-manipulator and the test pads. It is dependent on the force applied by the micro-manipulator, and therefore it is difficult to determine the force that has been applied in each measurement setup. Measuring with a four-wire setup minimises the static offset but introduces another pair of dynamic offset sources. It is also difficult to use another set of wire connections directly to the needle as it can cause unintentional force on the micro-manipulator. This will lead to sample damaging that will limit exploration space. The data presented in this section are the mean values of the measurement results that were taken without offset compensation.

6.2.2. SPST Resistance Characteristics

The characterisation of the DC signal is important in order to identify the behaviour of the MEMS switch in this region. The measurement from two points of the same structure has been taken to determine the resistance value. The data was taken from the four SPST switches labelled : AS1, AS2, AS3 and AS4. Table 6.1 shows the average measurement value with five repetitions for each sample.

Port labelled with C, D, H and J are structures for heat actuators. These structures were constructed by combining a gold layer and a polysilicon layer. The polysilicon layer is used to increase the resistance which will in turn produce heat. The measurements vary from around 200Ω to 400Ω depending on the length of the polysilicon layer.

6.2.3. SPDT Resistance Characteristics

The SPDT switch is slightly different in design to the SPST switch. It is bigger due to the fact that it is equipped with three moving masses to accommodate two signal-

Test Point		Resistance	Remarks
1	**2**	(Ω)	
B1	B2	2.5	Self-monitoring for left mass
C1	C2	227.4	Heat actuator
D1	D2	Open Circuit	Electrostatic actuator
E1	E2	227.5	Heat actuator
F1	F2	3.07	Signal-in line
G1	G2	2.88	Signal-out line
H1	H2	415.8	Heat actuator
I1	I2	Open Circuit	Electrostatic actuator
J1	J2	389.0	Heat actuator
K1	K2	2.3	Self-monitoring for right mass

Table 6.1.: Resistance values of SPST from port to port

in/out lines. The centre mass, labelled Mass B has a bi-directional electrostatic actuator which is almost double the size of uni-directional electrostatic actuators in Masses A and C. Four SPDT switches were used for resistance characteristic measurements, labelled AD1, AD2, BD1 and BD2. Five measurement repetitions were performed for each sample.

In the resistance measurement results, the median value of the data for heat actuators in the SPDT switches was 5.2167Ω at test points C, E, H, K, N and P. This is due to the absence of a polysilicon layer in the construction of the heat actuators. The intention is to validate the heat actuator functionality without the heat resistive element in it. Table 6.2 shows the port to port measurement results.

6.3. Electrical Characteristics - High Frequency Signal

6.3.1. Measurement Setup

The high frequency impedance measurement is used to determine the impedance value of the MEMS structure. Several parts need to undergo this test in order to characterise the MEMS prototype. A Network/Spectrum analyser HP4195A was used to perform the tests. This network analyser is able to measure and compute the impedance value of a device. The HP4195A is capable of performing frequency sweep tests from $0.01Hz$ to $500MHz$.

The measurement setup combines HP4195A with HP41915A (Impedance Test Adapter) and HP16092A (Spring Clip Fixture). A two-wire measurement method is used in this high frequency measurement. The setup may require two or four needles depending on the measurement area. In order to eliminate any error in measurement, this

Test Point		Resistance	Remarks
1	**2**	(Ω)	
B1	B2	2.10	Self-monitoring for left mass
C1	C2	5.25	Heat actuator
D1	D2	Open Circuit	Electrostatic actuator
E1	E2	4.10	Heat actuator
F1	F2	2.67	Signal-in 1
G1	G2	2.77	Signal-out 1
H1	H2	5.20	Heat actuator
I1	I2	Open Circuit	Electrostatic actuator
J1	J2	Open Circuit	Electrostatic actuator
K1	K2	6.80	Heat actuator
L1	L2	2.67	Signal-in 2
M1	M2	2.77	Signal-out 2
N1	N2	4.25	Heat actuator
O1	O2	Open Circuit	Electrostatic actuator
P1	P2	9.02	Heat actuator
Q1	Q2	2.60	Self-monitoring for right mass

Table 6.2.: Resistance values of SPDT from port to port

measurement setup contains calibration and compensation functions. The calibration function is used to eliminate the noise introduced by HP4195A and HP41915A. The compensation function is used to eliminate the noise produced by HP16092A and the BNC cable wires to the DUT. By implementing the calibration and compensation function, a better measurement result can be achieved from this measurement setup.

The measurement procedure which has been implemented follows the standard measurement techniques as described in the HP4195A operating manual. The frequency sweep is set from $100kHz$ to $500MHz$ due to the a limitation of the impedance test kit HP41951A. It produces good impedance measurement accuracy when applied in this frequency range, however, since the targeted capacitance values are in the pico to femto Farad range, the low frequency behaviour does not really matter in this case.

The source amplitude power of the test signal is set to $12dBm$ and the input attenuators (Ref and Test input) are set to $20dB$ to avoid overload in the input level. BNC cables are used to connect the spring clip fixture to the Karl Suss PM5 wafer probe bench. The probe head holds a needle with a point radius of 10 microns. There are two different types of wiring settings for measurement. A four needle wiring setup is used specifically for electrostatic actuator measurement. Since each side of the electrostatic actuator is divided into two, four needles are required for proper
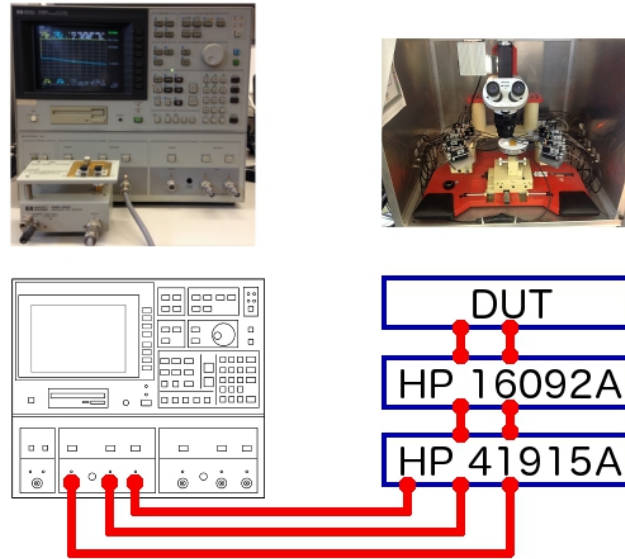
Figure 6.3.1.: Measurement setup for high frequency signal

measurement. The other type requires two needles set for these five measurement points:

1. Signal-in and signal-out lines
2. Capacitive sensor A
3. Capacitive sensor B
4. Signal-in and electrostatic actuator
5. Signal-out and electrostatic actuator

For every measurement point, 10 measurement cycles were taken continuously in each sample for statistical data evaluation. In general, 12 different samples of SPST switches and 8 samples for SPDT switches were used for high frequency measurement. The SPST switch samples are numbered with number CS1 to CS6 and ES1 to ES6, taken from chip dice C and E respectively. Finally the data will be plotted in the form of box-plot to show the data variation and the median value of the data.

The raw data was measured by HP4195A is then processed with the selected equivalent circuit. This network analyser has the ability to compute the equivalent impedance value from the frequency response result. There are five different equivalent circuits available in the network analyser. Of these five, two equivalent circuits are suitable for impedance evaluation of sub-components in the ISE-DC-MEMS switch. The capacitor equivalent circuit (Figure 6.3.2a) has been chosen for measuring the electrostatic actuator because in the electrostatic actuator structure, the important information is the total amount of capacitance value that can be created by the actuator. This capacitance equivalent circuit is thus the best option for evaluating the data measurement.

(a) Capacitor equivalent circuit   **(b)** Band-pass equivalent circuit
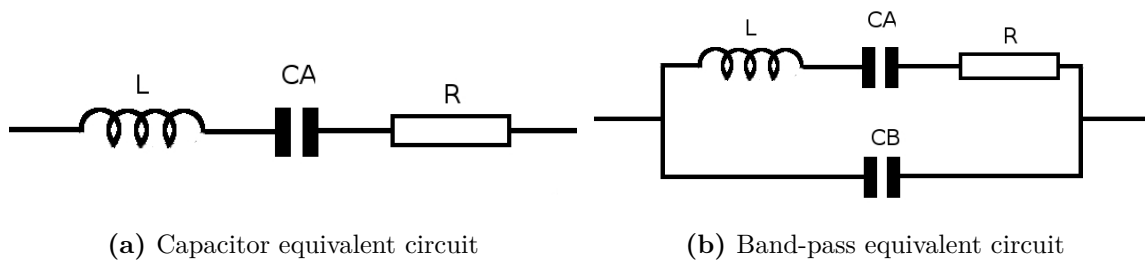
Figure 6.3.2.: Equivalent circuit available in the HP4195A Spectrum analyser

The other five sub-components used the band-pass filter equivalent circuit as shown in Figure 6.3.2b. In this equivalent circuit, two capacitor values, one inductor and one resistor are identified, namely CA,CB, L and R. Further explanation of these impedance representations will be provided in each sub-component measurement.

The fitting algorithm for equivalent circuit evaluation is not described clearly in the operating manual or any online references. The simulation process needs to be treated as a black box simulation, however, it is important to investigate the statistical behaviour of the algorithm to determine whether there is any variance in results due to repetitive evaluations. The initial experiment was conducted to investigate this. The experiments were performed by feeding the frequency response data of a single measurement and then repeatedly executing the equivalent simulation function with this same data. The process was performed ten times for both equivalent circuits 4 and 5. A one-time measurement for each type of equivalent circuit in the contact area was performed. The raw data of impedance, Z, with their respective phases was plotted in Figures 6.3.3 and 6.3.4.

The outcome of these experiments shows that the algorithm embedded in HP4195A for equivalent circuits 4 and 5 will produce exactly the same result for each repetition. There is no variation in the calculated result when the simulation is performed from a single data set. Table 6.3 shows repetition results using the equivalent circuits 4 and 5. The fitting error of these algorithms is the only information lacking in this procedure. The only information about the error behaviour is based on the error chart provided when using the HP4195B impedance measurement unit.

Although HP4195A gives a consistent output over repetitive measurements with similar raw data, as demonstrated earlier, there is no information about the error between the calculated impedance value and raw data. Furthermore, the machine only offers limited equivalent circuit models and there is no possibility to feed-in with our desired model. Additional effort was made to further analyse this data with an alternative algorithm using the same raw data collected during measurements.

The EIS spectrum analyser software [95] provides the flexibility which is needed in extending this analysis. The software allows users to create their own desired electrical model, and then a fitting analysis will determine the appropriate values based
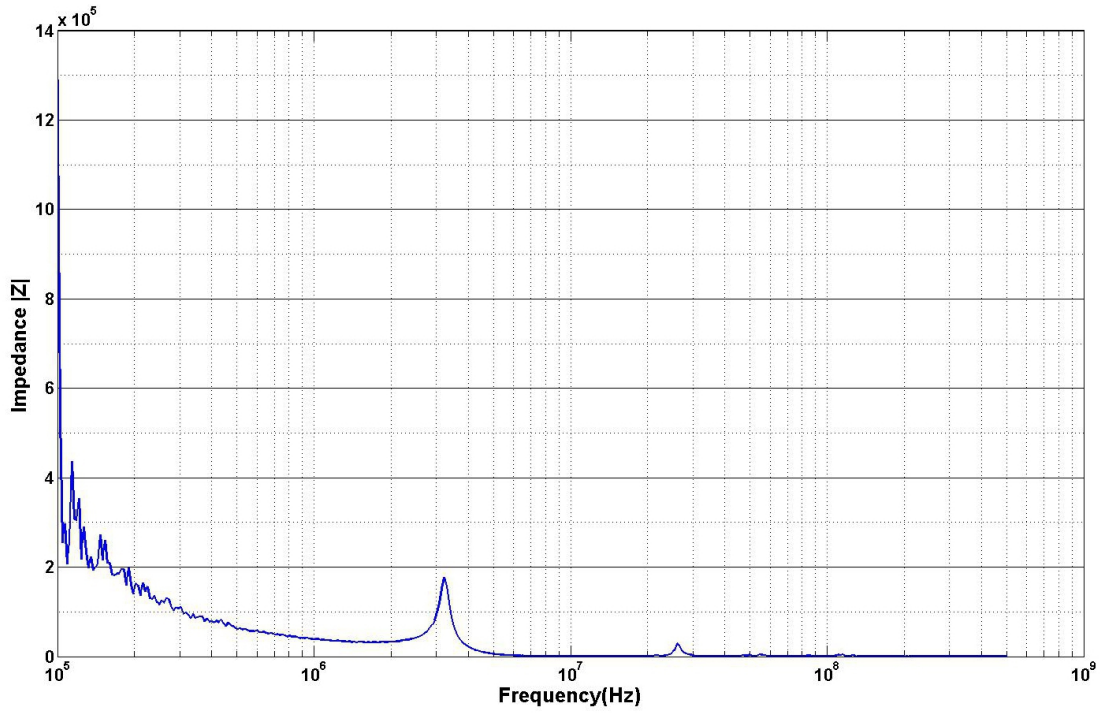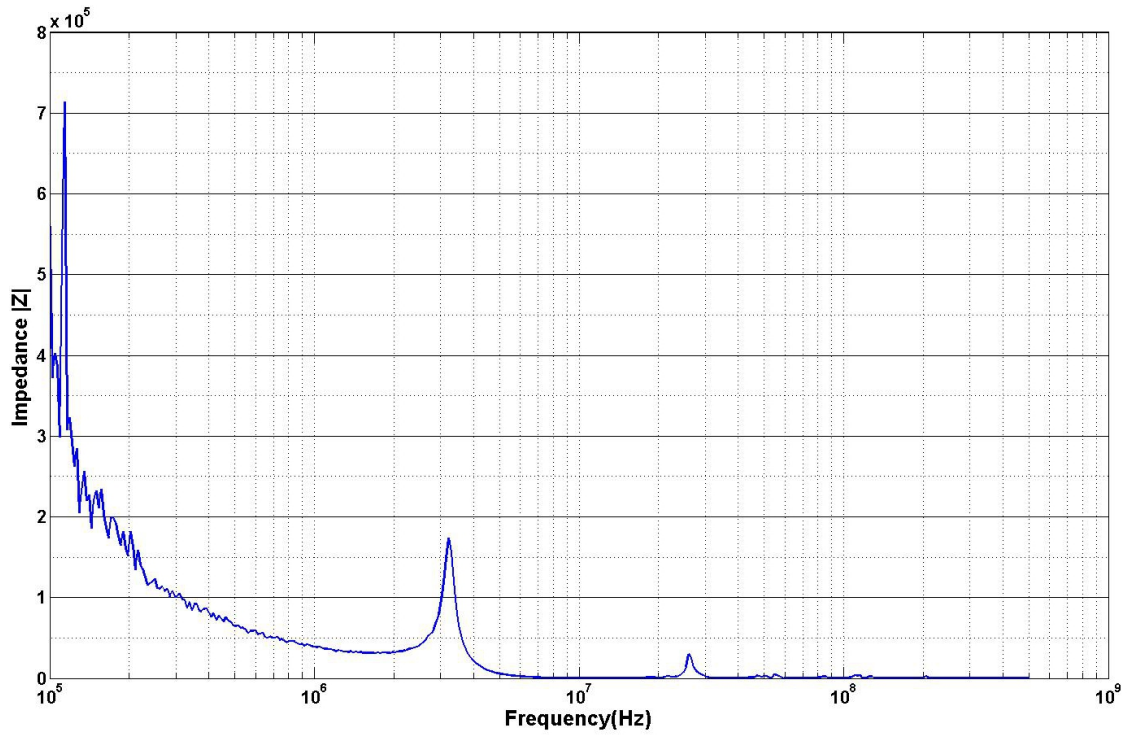
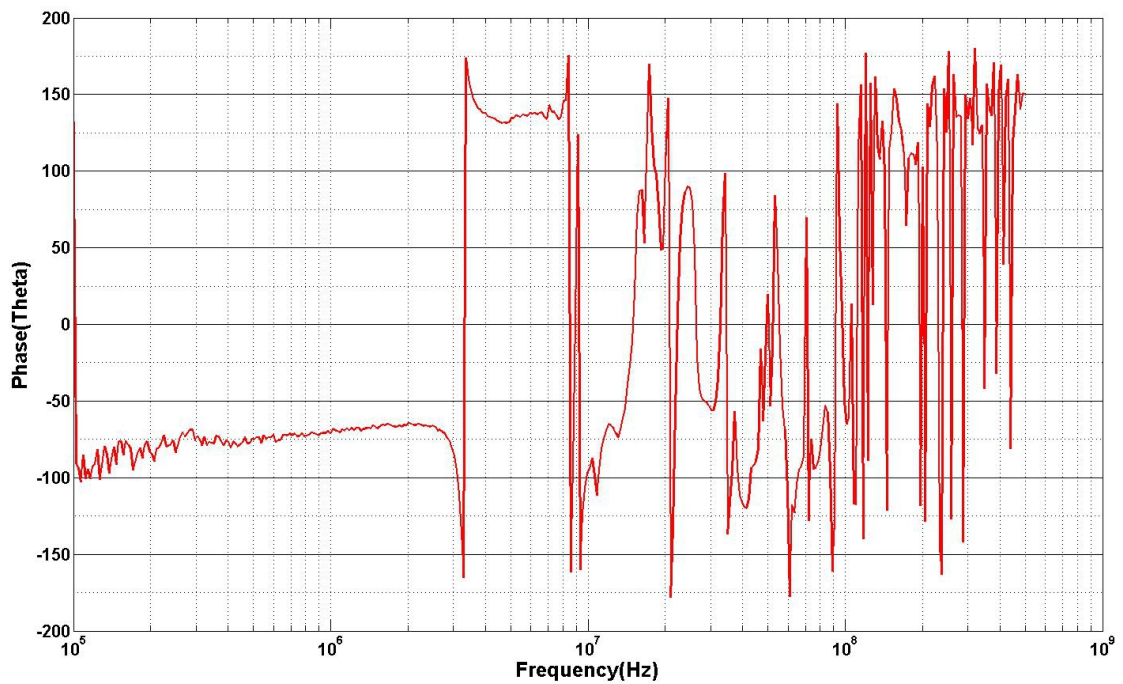**(a)** Raw data of impedance |Z| measured at contact area
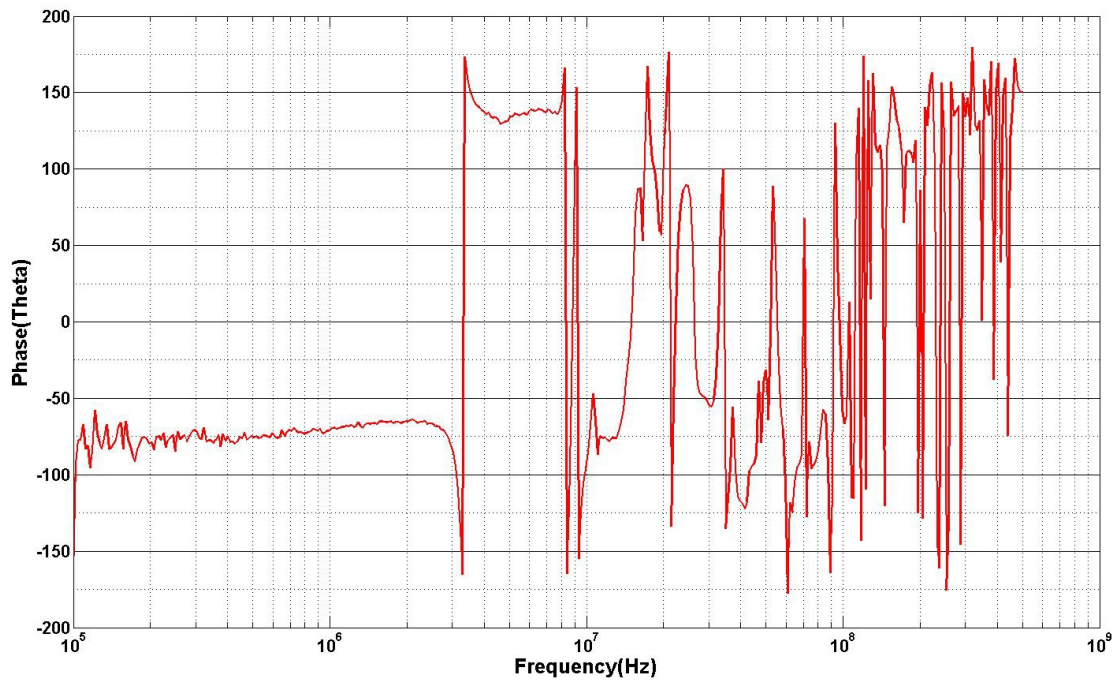
(b) Raw data of phase [θ] measured at contact area

Figure 6.3.3.: Plot of raw data measured in the contact area for equivalent circuit 4 evaluation

(a) Raw data of impedance |Z| measured at contact area

(b) Raw data of phase [θ] measured at contact area

Figure 6.3.4.: Plot of raw data measured in the contact area for equivalent circuit 5 evaluation

(a) The equivalent circuit 4 results with repetitive evaluation from raw data shown in Figure 6.3.3

(b) The equivalent circuit 5 results with repetitive evaluation from Figure 6.3.3

	CA$[pF]$	**L**$[\mu H]$	**R**$[\Omega]$
1	1.0705	2.8765	200.22
2	1.0705	2.8765	200.22
3	1.0705	2.8765	200.22
4	1.0705	2.8765	200.22
5	1.0705	2.8765	200.22
6	1.0705	2.8765	200.22
7	1.0705	2.8765	200.22
8	1.0705	2.8765	200.22
9	1.0705	2.8765	200.22
10	1.0705	2.8765	200.22

	CA$[pF]$	**CB**$[pF]$	**L**$[\mu H]$	**R**$[\Omega]$
1	1.0576	8.1640	2.9379	6.9261
2	1.0576	8.1640	2.9379	6.9261
3	1.0576	8.1640	2.9379	6.9261
4	1.0576	8.1640	2.9379	6.9261
5	1.0576	8.1640	2.9379	6.9261
6	1.0576	8.1640	2.9379	6.9261
7	1.0576	8.1640	2.9379	6.9261
8	1.0576	8.1640	2.9379	6.9261
9	1.0576	8.1640	2.9379	6.9261
10	1.0576	8.1640	2.9379	6.9261

Table 6.3.: The equivalent circuit with repetitive evaluation

on raw data. Four minimisation methods for analysing this nonlinear continuous data, 'Powell's algorithm', the 'Nelder-Meed algorithm', the 'Levenberg-Marquardt algorithm' and the 'Newton algorithm', are available. In this investigation, Powell's algorithm was chosen for its robustness and fast computational ability for high numbers of iterations. It also provides information on the error percentage for each individual element in the fitting simulation. These two advantages of EIS software give the possibility of better DC MEMS switch characterisation.

In the next section, the measurement data of four different sub-elements of the MEMS switch will be presented. In each sub-component, three different analyses will be presented. The first analysis will consist of statistical median data taken from various measurement samples. A box plot and a table will be used to present the results in detail.

A comparison analysis based on the results obtained from the MEMS+ model using Cadence simulation, HP4195A network analyser and EIS Spectrum Analyser software was performed. The simulation results are based on the data presented in Chapter 4. Each of the results from HP4195A and the EIS Spectrum Analyser software is based on the same raw data and same equivalent circuit model. These comparisons will provide better insight for selecting the best equivalent circuit model.

Finally, a further analysis was made using an EIS Spectrum Analyser with a more complex electrical model for better characterisation of the MEMS switch. In particular, the parasitic capacitance value of the two signal lines is important for determining switch behaviour during the off-state. Since the MEMS design and simulation tools provide no appropriate model for evaluating the parasitic capacitance, the evaluation needs to be performed by characterising the actual device. The EIS Spectrum
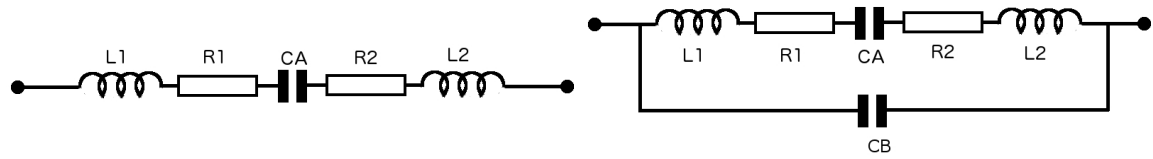
(a) The proposed second equivalent circuit model
for electrostatic actuator

(b) The proposed second model switch during off-state

Figure 6.3.5.: Extended equivalent circuit models implemented in EIS Spectrum
Analyser software

Analyser offers the ability to add various types of circuit models. Two extended versions of the equivalent circuits were introduced and tested. Figure 6.3.5a shows the second equivalent circuit that was used to evaluate the electrostatic actuator in this analysis. It has an additional inductor and resistor which are located at the other end of capacitance CA. This model is believed to represent the electrostatic actuator in a better manner than the available model implemented in HP4195A.

The second model implemented in the EIS is shown in Figure 6.3.5b. This model will be compared to a similar model of equivalent circuit 5 in HP4195A. In this new model, another pair of resistors and inductors was added. This model will be implemented in the analysis of sub-elements as follows:

- Signal-in and signal-out

- Capacitive sensor

- Signal line and electrostatic actuator

In the third analysis, a comparison will be made between the result obtained using the standard equivalent circuit model in the HP4195A and the extended model introduced in the EIS Spectrum Analyser. Both results were from the same raw data and the same algorithm in EIS Spectrum Analyser software.

6.3.2. SPST MEMS Switch Measurement Results

6.3.2.1. Measurement Points: Electrostatic Actuator A and B

The electrostatic actuators are those areas that have high capacitance value. Four needles were required to measure each of the actuators, as shown in Figure 6.3.6, because both anchors for movable mass, labelled as -VE pads in Figure 6.3.6, are electrically isolated. The same situation applies to the +VE pads and they thus require four needles to make the measurement.

For every single SPST switch, there are two sets of electrostatic actuators, actuator A and actuator B. They are identical in size and the only difference is the routing to the pads area. For characterisation purposes, eight samples were used in high frequency

response measurement for actuators A and B. The measurements were performed in the off-state condition which means the gap at the electrostatic actuators is in the original position. For each sample, the frequency response was measured 10 times and this means a total of 160 raw data sets were obtained. The raw data was then processed using the fitting algorithm of the HP4195A network analyser. The equivalent circuit shown in Figure 6.3.2a was used to obtain the component values.

The equivalent circuit evaluation results from both actuators were then populated using box plots for simple representation. Figure 6.3.7 shows the box plot for electrostatic actuators A and B. Table 6.4 provides the statistical distribution of the data from the box plot. The lower quartile, upper quartile and the interquartile range give the distribution information for the data. Based on the results from a series of several measurements, both actuators recorded almost the same median value of the CA capacitance. Electrostatic actuator A recorded a median capacitance value of $1.1437pF$ while actuator B recorded $1.1389pF$. The same patterns of median data are shown in the other components, RA and LA. The measurement results show good consistency and small variance along the measurement process.

The analysis of high frequency measurement is extended using EIS Spectrum Analyser software. Initially, the same model implemented in HP4195A, as shown in Figure 6.3.2a, was used. Unlike HP4195A, the EIS Spectrum Analyser software provides fitting error information for each element. Table 6.5 shows comparison results for each element produced by HP4195A, EIS software and Cadence simulation. The fitting simulation results were obtained using the same set of raw data.

The simulation results produced a capacitance value of $0.8492pF$ for one electrostatic actuator. HP4195A reported a value of $0.798pF$ with an unknown error percentage and the EIS software produced a fitting result of $1pF$ with an error of 0.3787%. A bigger value is expected from the Cadence Simulation and thus the fitting result from the EIS software is believed to be closer to the actual value.

The analysis of searching for a more accurate equivalent circuit is continued by implementing new equivalent circuit models. Two additional equivalent circuit models for electrostatic actuators were implemented in order to evaluate the fitting trends using the same raw data. Table 6.6 compares the fitting result of Model 2, which is represented by Figure 6.3.5a, and Model 3, which is represented by Figure 6.3.5b. Model 2 produced a CA value of $0.9pF$ with a higher error percentage of 0.6386% while Model 3 produced a value of $0.96pF$ with 0.9187% error. Based on these results, Model 1 remains the best fitting model producing the smallest error percentage.

The observation of the LA values showed a similar trend as capacitance value. The lowest error percentage was recorded by Model 1 as $0.3282\mu H$ with 36.436% of error. Model 2 produced a lower LA value of $0.2663\mu H$ with 64.582% error while Model 3 recorded an LA value of $0.1923\mu H$ with a bigger error percentage of 66.582%.

Based on the trends shown by these two elements, Model 1 has produced the lowest error percentage and remained the best fitting model for the electrostatic actuator

(a) Electrostatic actuator A

(b) Electrostatic Actuator B
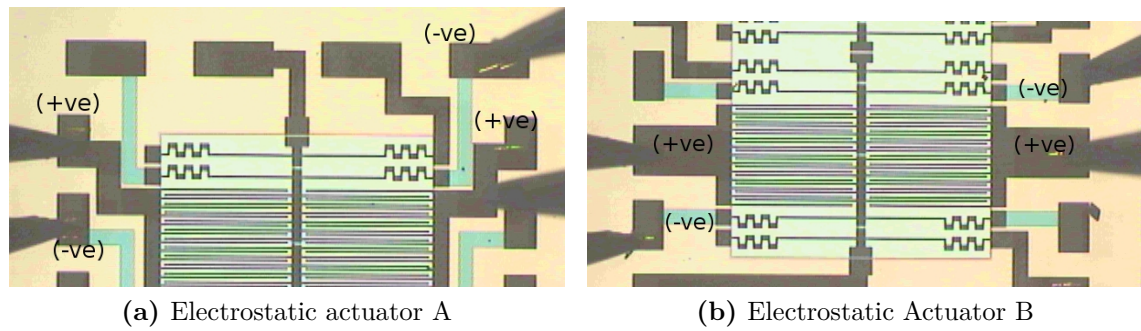
Figure 6.3.6.: Four needles arrangement for electrostatic actuator measurement

than Model 2 or Model 3.

6.3.2.2. Measurement Points: Signal-In and Signal-Out

The second important area that needs to be analysed in MEMS switches is the signal-in and signal-out lines. These lines determines the isolation between these two signals during the switch off-state. The impedance value between these two lines gives information about the frequency bandwidth of signal that the switch can handle. The equivalent circuit of both signal lines in the off-state is similar to a band-pass filter as shown in Figure 6.3.2b. A two needle measurement setup

(a) Box plot parameters for equivalent circuit components in electrostatic actuator A measurement

Parameter	$\mathbf{CA}[pF]$	$\mathbf{L}[\mu H]$	$\mathbf{R}[\Omega]$
Lower quartile, Q_1	0.9156	0.0112	15.913
Median, Q_2	1.0674	0.2882	22.232
Upper quartile, Q_3	4.2713	0.4195	105.721
Interquartile range, IQR	3.3557	0.4083	89.809

(b) Box plot parameters for equivalent circuit components in electrostatic actuator B measurement

Parameter	$\mathbf{CA}[pF]$	$\mathbf{L}[\mu H]$	$\mathbf{R}[\Omega]$
Lower quartile, Q_1	0.9128	0.0315	10.405
Median, Q_2	1.1224	0.1982	16.884
Upper quartile, Q_3	90.957	0.4178	30.036
Interquartile range, IQR	90.044	0.3863	19.631

Table 6.4.: Statistical evaluation of equivalent circuit data obtained from the HP4195A network analyser for the electrostatic actuator in the SPST-V1 of the ISE-DC-MEMS switch
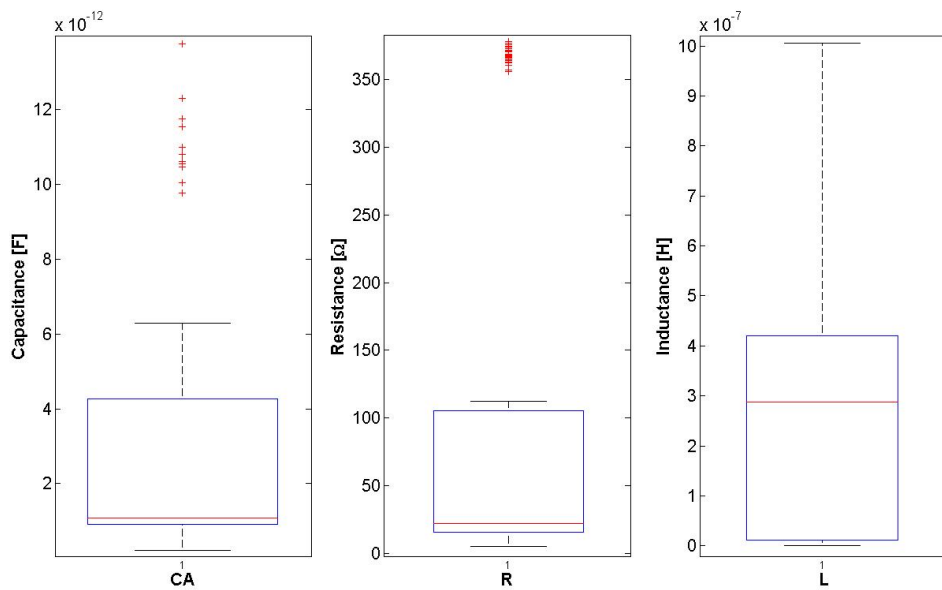
(a) Electrostatic actuator A
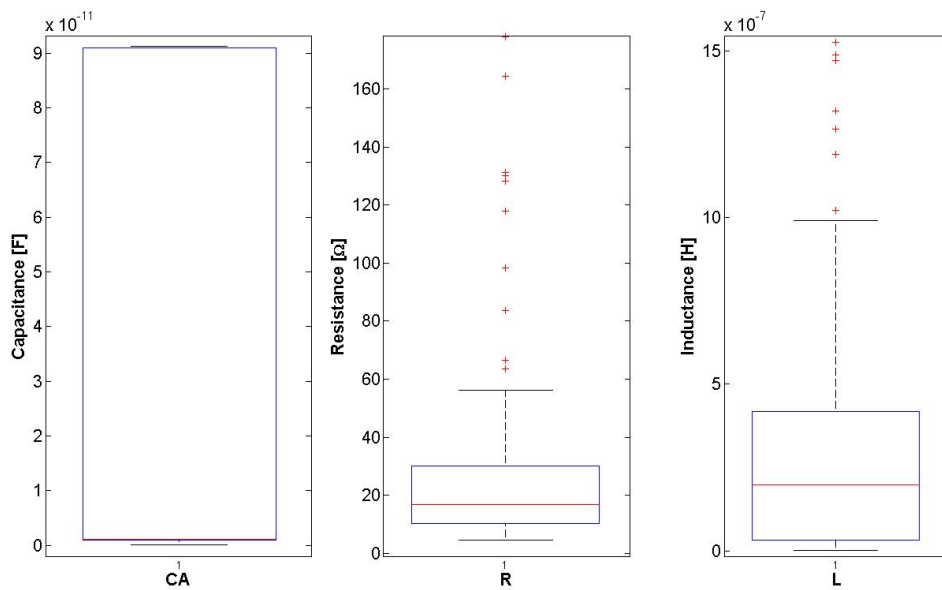
(b) Electrostatic actuator B

Figure 6.3.7.: Box plot for electrostatic actuators A and B impedance measurement

Software/ Analyser	CA [pF]	Error [%]	LA [μH]	Error [%]	RA [Ω]	Error [%]
HP4195A	0.798	NA	0.1868	NA	35.3664	NA
EIS	1.00	0.3787	0.3282	36.436	1.3741	##
MEMS+ Model	0.8492	NA	NA	NA	NA	NA

##: Fitting error more than 1000%

NA: Not available or not applicable

Table 6.5.: Result for electrostatic actuator equivalent model parameters using HP4195A, EIS Spectrum Analyser and Cadence simulation

Element	Model 1	Error	Model 2	Error	Model 3	Error
CA$[pF]$	1.00	0.3787%	0.90	0.6368%	0.960	0.9187%
CB$[fF]$	NA	NA	0.0984	0.5280%	190	4.6748%
LA$[\mu H]$	0.3282	36.436%	0.2663	64.582%	0.1923	66.465%
LB$[\mu H]$	NA	NA	NA	NA	0.1328	96.267%
RA$[\Omega]$	1.3741	##	1.7416	##	3.247×10^{-5}	##
RB$[\Omega]$	NA	NA	1.925×10^{-9}	##	3.760×10^{-4}	##

Table 6.6.: Results of comparison between electrostatic actuator equivalent models using EIS Spectrum Analyser

was used and it is adequate for measuring the response between the signal-in and signal-out ports. Figure 6.3.8 shows needle positions on the signal-in and signal-out pads in the actual die during measurement. The measurements were performed in the off-state condition to obtain the original gap between the contact structures. A total of 6 samples were used and for each sample 10 repetitions of high frequency measurements were performed. A total of 120 raw data sets were collected and processed using the equivalent circuit in the HP4195A shown in Figure 6.3.2b.

The statistical behaviour of the measurement is studied in the first part of the analysis. The results were then populated into the box plot as shown in Figure 6.3.9 to show the statistical distribution of the processed data. There are four elements in the model, CA, CB, L and R. The capacitor denoted as CA represents the parallel plate of the contact area. The capacitor CB represents the parasitic capacitance that exists between signal-in and signal-out. This parasitic capacitance is also denoted as C_{PLL} in the proposed electrical model mentioned in Section 5.1. Table 6.7 shows the median values and the IQR data of the sub-element of the equivalent circuit between the signal-in and signal-out lines. A very small median value of CA was expected, and around $113.74 fF$ was recorded. This is because there is a very small area of capacitance between the contact areas. The median value for parasitic capacitance along the signal line was recorded at $2.4722 pF$.

Based on the results, there was a greater variance of data, especially when the

capacitance values in the femto Farad range were recorded. The maximum data points for CA can reached up to $1.5763pF$, however, 50% of the data was populated between $71.395fF$ to $274.12fF$. One of the reasons for this is that the measurement was not taken inside a shielded room, where a controlled environment could be created from an outside modulated frequency. FM radio station signals operate in the MHz frequency range, for example, and can be a source of noise during measurement. A more precise CA value can be obtained if the measurement is performed inside a shielded room.

The second analysis compared the results from one set raw data obtained by the HP4195A network analyser, EIS Spectrum Analyser software and Cadence simulation results. The raw data is plotted as shown in Figure 6.3.10. Table 6.8 shows a comparison of the results of these three methods. The Cadence simulation result was obtained from the simulation model discussed in Chapter 4 and presented in Table 4.8.

The HP4195A algorithm produced $9.3340fF$ for the CA value and $7.2684pF$ for the CB value. Meanwhile, Powell's algorithm in the EIS Spectrum Analyser suggested a slightly bigger CA value of around $20fF$ but a smaller parasitic capacitance CB value of around $14fF$. The results produced by the Powell algorithm show similar trend as the Cadence simulation results. Although the HP4195A gives a closer CA value to the Cadence simulation results, the EIS Spectrum Analyser produces an overall better result with a known error percentage.

In the third analysis, the extended version model which closely resembles the real physical switch is implemented. Figure 6.3.5a shows the proposed switch model which consists of six elements with two identical resistors, two identical inductors and two non-identical capacitors. The resistors and inductors in the series represent each of the signal lines. Since they have identical structures, the resistor and inductor values are almost identical. The CA value represents the capacitance between the switch contact plates and the CB value represents the parasitic capacitance between the signal-in and signal-out structures.

The findings got more interesting when the raw data was tested with the second proposed switch model. The fitting algorithm behaviour can be evaluated by comparing results that were calculated using both switch models with the same data. Equivalent circuits as shown in Figure 6.3.2b represent Switch Model 1, and Switch Model 2 represents the equivalent circuits shown in Figure 6.3.5b. Table 6.9 shows the comparison between Model 1 and Model 2. The introduction of R and L to the model resulted in a better fit during the fitting simulation. The CB error of was reduced from 1.2341% to 0.2598%.

Model 1 produced an LA result of $6.3\mu H$ with a 43.308% fitting error for the inductor components. For Model 2, inductors LA and LB produced similar results of $200\mu H$ with 0.3928% fitting error. The inductance errors were reduced from 43.308% to 0.3928% when using Model 2. This matches the initial prediction which suggested that the two inductors should be identical due to the similarity in their structures.

Resistor values of around 18Ω to 20Ω in Model 2 with an error larger than 1000% were recorded. Increasing the iterations in Powell's algorithm did not help in converging to a better result, however, the resistance across the signal path is always better measured in the direct current signal rather than high frequency signal, as reported in Section 6.2. Since the measurements were taken in medium to high frequency from $100kHz$ to $500MHz$ range, the outcome of this analysis in evaluating the resistance value can be ignored.
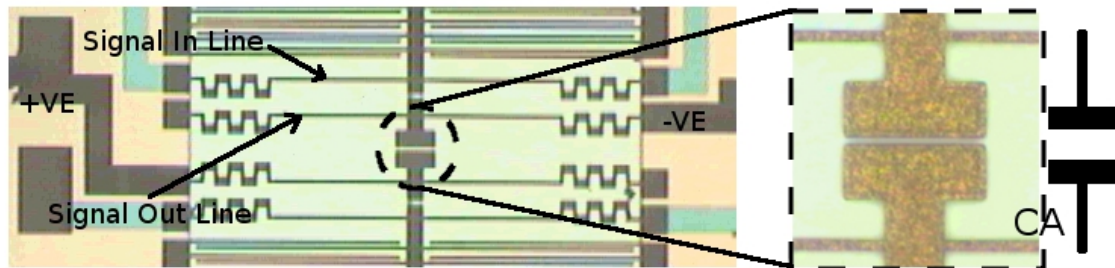
Figure 6.3.8.: A two-needle arrangement for measurement between signal-in and signal-out in SPST switches
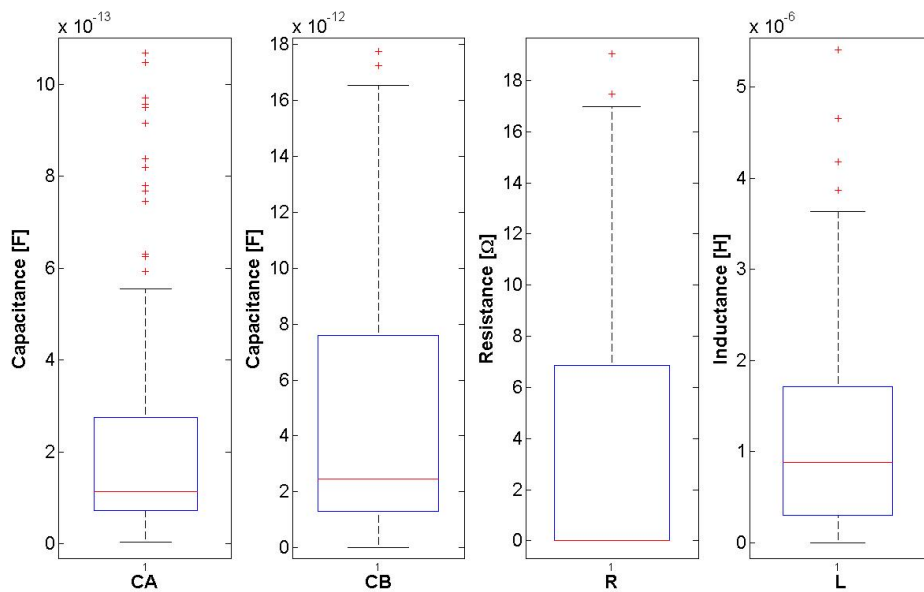
Figure 6.3.9.: Box-plot of SPST switch impedance measurement data for signal-in and signal-out lines
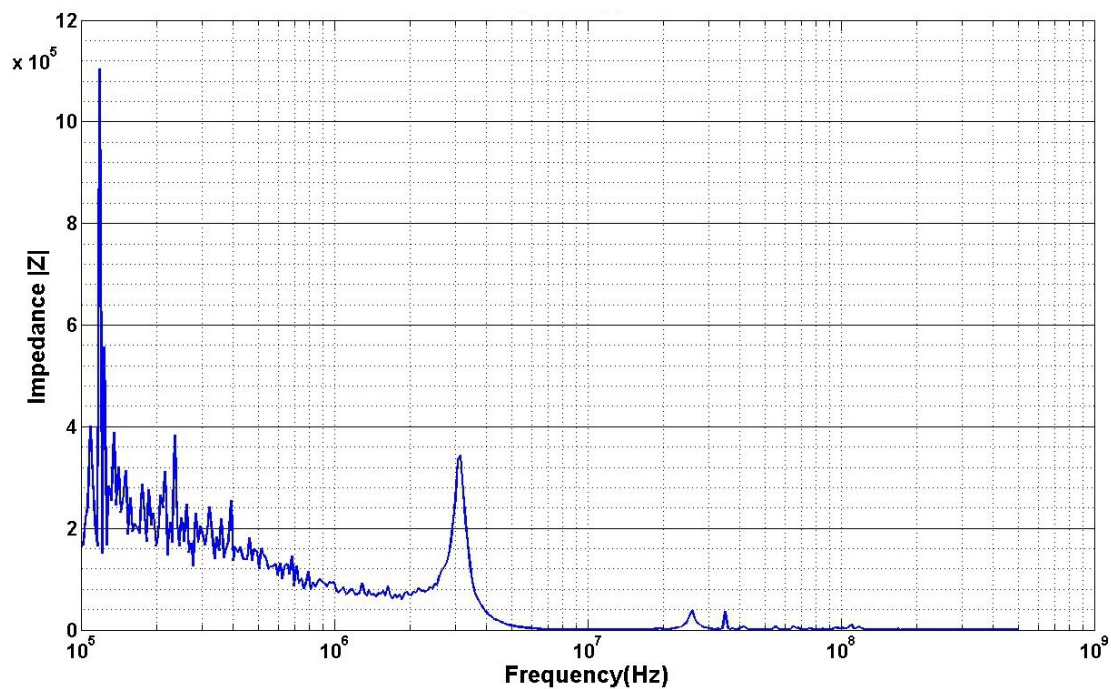
(a) Raw data of impedance |Z| measured between signal-in and signal-out lines in an SPST switch
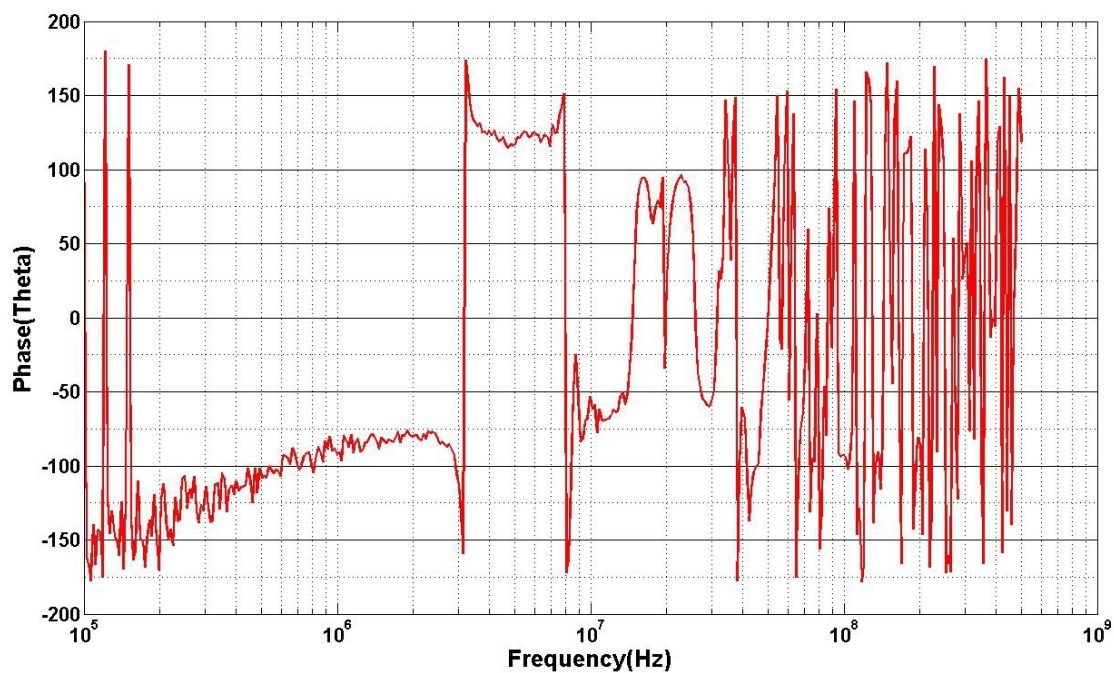
(b) Raw data of phase [θ] measured between signal-in and signal-out lines in an SPST switch

Figure 6.3.10.: Plot of raw data measured between signal-in and signal-out lines in an SPST switch

Parameter	$\mathbf{CA}[fF]$	$\mathbf{CB}[pF]$	$\mathbf{L}[\mu H]$	$\mathbf{R}[\Omega]$
Lower quartile, Q_1	71.395	1.3174	0.3003	0
Median, Q_2	113.74	2.4722	0.8845	0
Upper quartile, Q_3	274.12	7.6024	1.7091	6.8467
Interquartile range, IQR	202.73	6.2850	1.4088	6.8467

Table 6.7.: Box plot parameters for equivalent circuit in signal-in and signal-out line measurement

Software/ Analyser	CA $[fF]$	Error $[\%]$	CB $[fF]$	Error $[\%]$	L $[\mu H]$	Error $[\%]$	R $[\Omega]$	Error $[\%]$
HP4195A	9.3340	NA	7268.4	NA	10.877	NA	0	NA
EIS	20.000	0.8611	14.000	1.2341	6.300	43.308	9.0745μ	##
MEMS+ Model	5.9524	NA	1.6082^a	NA	NA	NA	0.4048^b	NA

---

[a]Manual calculation as shown in Appendix B

[b]Manual calculation as shown in Appendix A

Table 6.8.: Results for signal-in and signal-out equivalent model parameters using HP4195A, EIS Spectrum Analyser and Cadence simulation

6.3.2.3. Measurement Points: Capacitive Sensor A

Capacitive sensor A is a sensor for detecting the movement ability of mass. It is part of a self-monitoring feature of the MEMS switch. In order to quantify the capacitance value of this sensor, two needle measurements are used as shown in Figure 6.3.11. The measurement was performed during the off-state condition so as to obtain the original gap. A total of 6 samples were used for this measurement with 10 repetitions for each sample.

The box plot shown in Figure 6.3.12 was based on a total of 120 raw data measurements. Each of the raw datasets was processed by HP4195A using the equivalent

Element	Model 1	Error	Model 2	Error
$\mathbf{CA}[fF]$	20.000	0.8611%	5.000	1.1597%
$\mathbf{CB}[fF]$	14.000	1.2341%	1.890	0.2598%
$\mathbf{LA}[\mu H]$	6.300	43.308%	200.00	0.3928%
$\mathbf{LB}[\mu H]$	NA	NA	200.00	0.3928%
$\mathbf{RA}[\Omega]$	9.0745μ	##	19.901	##
$\mathbf{RB}[\Omega]$	NA	NA	18.978	##

Table 6.9.: Result of comparison for signal-in and signal-out equivalent models using EIS spectrum analyser

circuit model which is depicted in Figure 6.3.2b. The statistic distributions of the processed results are shown in Table 6.10. Similar to the previous measurement, the capacitor CA represents the value of the parallel plate of the contact where a median value of $1.3478pF$ was recorded. Capacitor CB represents a value of parasitic capacitance across two pads. Capacitor CB in this measurement represents the parasitic capacitance C_{SLA} in the proposed electrical model discussed in Section 5.1 on page 105. A relatively high median value of parasitic capacitance at $6pF$ was recorded. Inductance of the circuit had a median value of $1.5727\mu H$ and 0Ω for resistance value. The measurement again shows a similar pattern of greater variance for femto Farad range capacitance measurement. Some of the CA data was recorded at $30pF$ although the majority of the data was still in the femto Farad range as shown by the median value.

Further investigation was performed with results comparison analysis. A single raw dataset shown in Figure 6.3.13 was used for this analysis. Table 6.11 shows the difference between HP4195A, EIS and Cadence simulation results. For the contact area in capacitive sensor A represented by CA, the Cadence simulation gives a value of $5.9524fF$. A slightly higher value of $20fF$ was recorded by EIS software with 1.3152% fitting error. On the other hand, HP4195A gave a higher value of $2.2028pF$ with an unknown error percentage using the same raw dataset.

The parasitic capacitance represented by the CB value shows a similar trend. The manual calculation method presented in C showed an estimated value of $0.2299fF$ for the CB capacitor. The EIS software produced a value of $0.9fF$ with 1.7445% of error while the HP4195A produced $15.738pF$ for capacitance with unknown error.

The inductance values were obtained via EIS software and HP4195A data analysis. Both produced values in the micro Henry range and the former had $100\mu H$ with a 3.8215% error and the latter produced $16.539\mu H$. The resistance analysis showed a closer result between estimated calculation value of 0.4048Ω and 0.3795Ω obtained from HP4195A. The EIS software gave a relatively higher value of 19.677Ω.

The investigation of the same raw data was then extended to a comparison analysis between two different models depicted in Figure 6.3.2b for Model 1 and Figure 6.3.5b for Model 2. The results of the comparison are shown in Table 6.12. The CA value is recorded as $6.00fF$ with 1.0264% error using Model 2, compared to Model 1 which produced $2fF$ with 0.6014% of error. The results showed that Model 2 produced a fitting result that was closer to the simulation result at $5.9524fF$ even at a slightly higher percentage error. This is a better result when compared to the result for Model 1 that had a small error percentage with a smaller CA value when compared to the simulation result.

The CB value was $0.9fF$ with 1.7445% fitting error when using Model 1 and $2.98fF$ with 3.5728% error when using Model 2. Both models showed higher values when compared to the Cadence simulation result, with small error percentages.

The inductance components show a different pattern of results for the implementation of Model 1 and Model 2. In Model 1, an LA value of $100\mu H$ was recorded
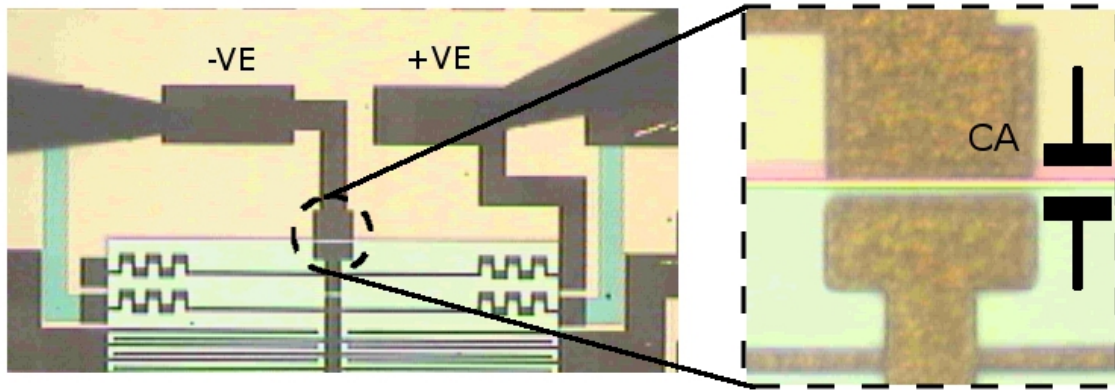
Figure 6.3.11.: A two-needle arrangement for measuring capacitive sensor A in the SPST switch

Parameter	$\mathbf{CA}[pF]$	$\mathbf{CB}[pF]$	$\mathbf{L}[\mu H]$	$\mathbf{R}[\Omega]$
Lower quartile, Q_1	0.4765	3.3595	0.5989	0
Median, Q_2	1.3478	6.1442	1.5727	0
Upper quartile, Q_3	12.153	17.898	16.668	0.3952
Interquartile range, IQR	11.676	14.539	16.069	0.3952

Table 6.10.: Box plot parameters for equivalent circuit data in measurement of capacitive sensor A in the SPST switch

with a 3.8215% fitting error. For Model 2, a closed value between LA and LB was recorded at $23.10\mu H$ and $24\mu H$. Both inductance values are smaller when compared to the result produced by Model 1.

The fitting errors in the resistance components in both models, were too large, with over than 1000%. Model 1 produced an RA value of 19.677Ω while Model 2 produced an RA value of 12.053Ω and RB value of $4.15\mu\Omega$. These results show that a reliable result for resistance can only be obtained using DC signal measurement.

To summarise, Model 2 is a better equivalent circuit model than Model 1 for capacitive sensor structure in an ISE-DC-MEMS switch. This is shown via better fitting results as discussed above with a smaller percentage of error.

6.3.2.4. Measurement Points: Capacitive Sensor B

Similarly to capacitive sensor A, capacitive sensor B is used to monitor the movement ability of Mass B. The sensor construction is similar to that of Sensor A with a slight difference in the routing in the pad area. The position of the pads was wider when compared to capacitive sensor A. Two needles measurements were used to measure the impedance value and the setup is shown in Figure 6.3.14. The measurement was performed in the off-state condition. Six samples were used to measure the high
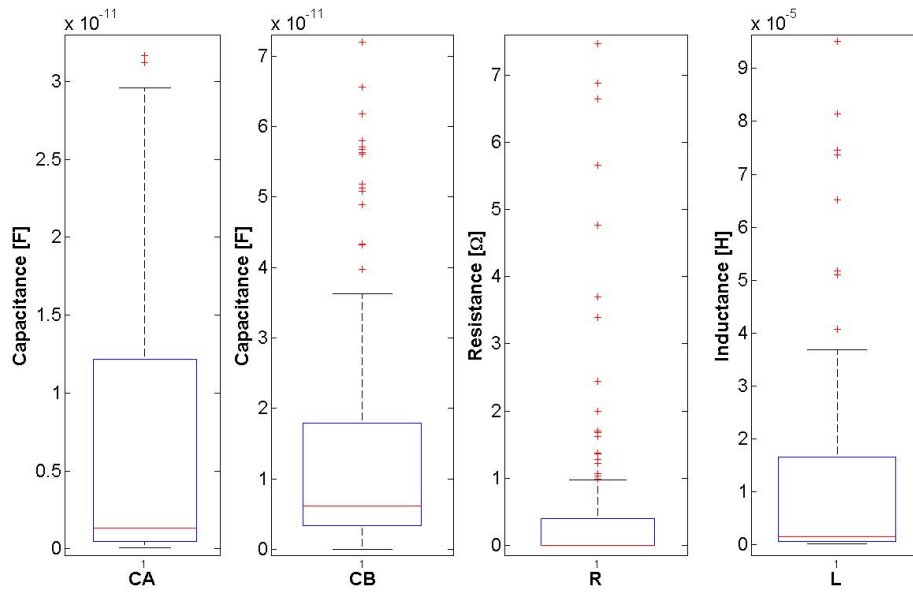
Figure 6.3.12.: Box-plot of SPST switch impedance measurement data for capacitive sensor A

Software/	CA	Error	CB	Error	L	Error	R	Error
Analyser	$[fF]$	$[\%]$	$[fF]$	$[\%]$	$[\mu H]$	$[\%]$	$[\Omega]$	$[\%]$
HP4195A	2202.8	NA	15738	NA	16.539	NA	0.3795	NA
EIS	2.000	0.6014	0.900	1.7445	100.00	3.8215	19.677	##
MEMS+ Model	5.9524	NA	0.2299^a	NA	NA	NA	0.4048^b	NA

^{a}Manual calculation as shown in Appendix C

^{b}Manual calculation as shown in Appendix A

Table 6.11.: Results for capacitive sensor A equivalent model parameters using HP4195A, EIS Spectrum Analyser and Cadence simulation

Element	Model 1	Error	Model 2	Error
CA$[fF]$	2.000	0.6014%	6.00	1.0264%
CB$[fF]$	0.900	1.7445%	2.98	3.5728%
LA$[\mu H]$	100.00	3.8215%	23.10	8.300%
LB$[\mu H]$	NA	NA	24.00	8.001%
RA$[\Omega]$	19.677	##	12.053	##
RB$[\Omega]$	NA	NA	4.15×10^{-6}	##

Table 6.12.: Result of comparison for capacitive sensor A equivalent models using EIS spectrum analyser
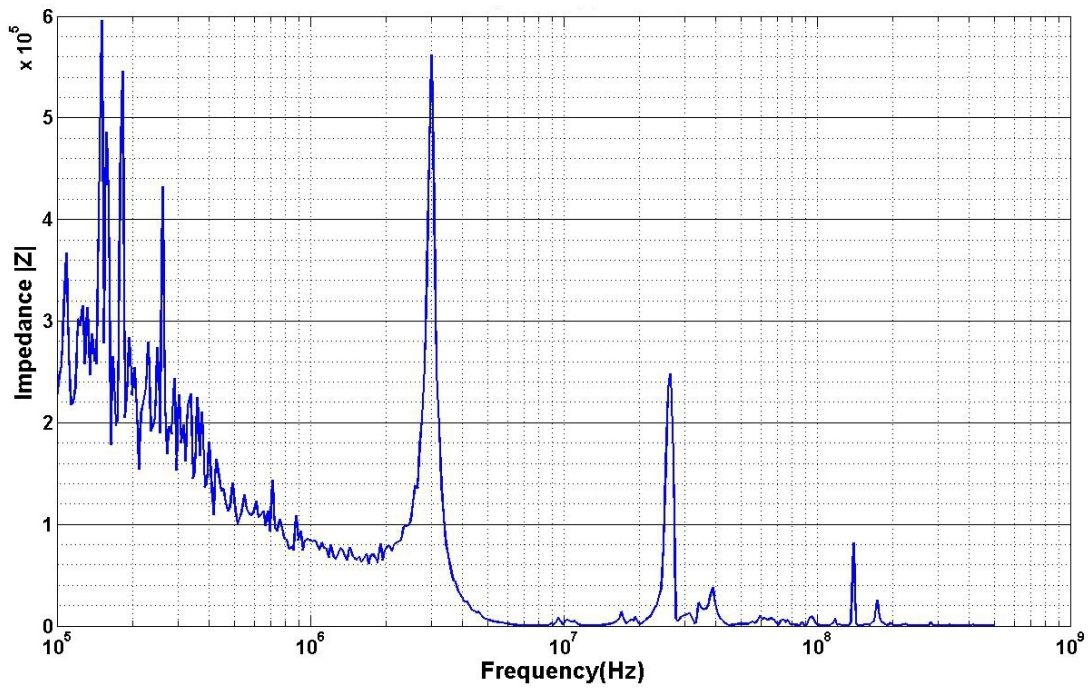
(a) Raw data of impedance |Z| measured at capacitive sensor A in an SPST switch
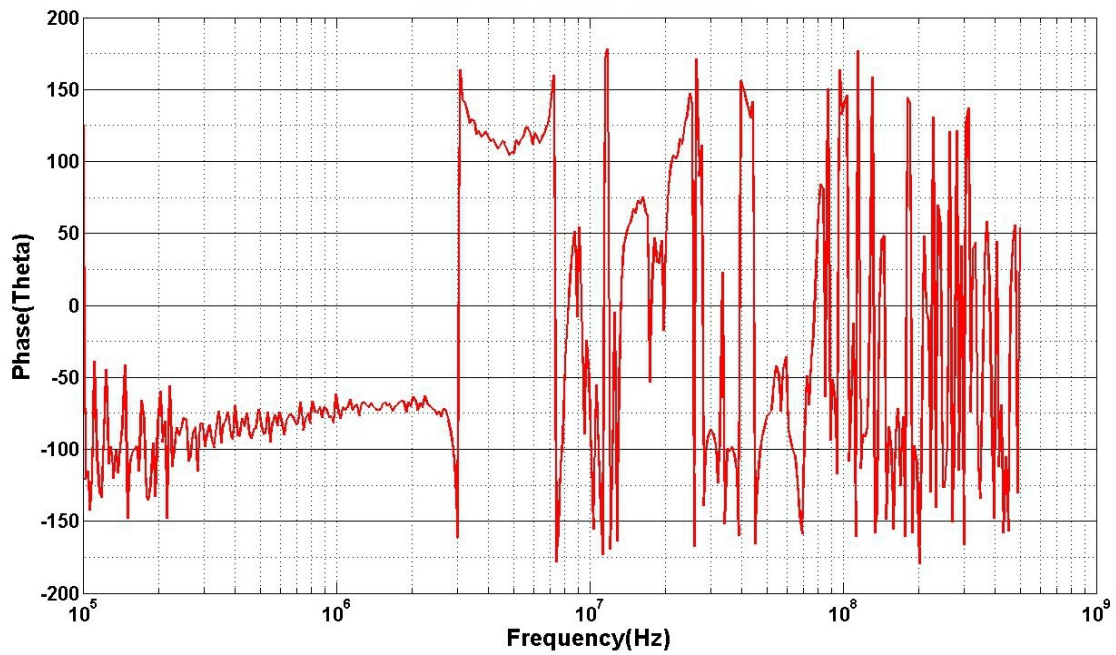
(b) Raw data of phase [θ] measured at capacitive sensor A in an SPST switch

Figure 6.3.13.: Plot of raw data measured at capacitive sensor A in an SPST switch

frequency response with 10 repetitions for each sample. A total of 120 raw data measurements were collected. This data was processed using the HP4195A network analyser with equivalent circuit as shown in Figure 6.3.2b.

The results of the processed data are presented in the box plot diagram shown in Figure 6.3.16. Table 6.13 provides the statistical distribution data obtained from the box plot. The median value of capacitor CA is recorded at $364fF$ and capacitor CB is $5.1276pF$. 50% of the CA data was populated between $200.2fF$ to $1.359pF$ and the median value is inclined towards the lower quartile Q_1. The CA value of sensor B was slightly higher than sensor A although they are still in the femto Farad range. The CB values for sensors A and B are both at a similar level, $6.1442pF$ and $5.1276pF$ respectively. Large variances of data for CA were recorded thus following similar patterns as previously, when the measurement result was in the femto Farad range.

The extended analysis for capacitive sensor B is not implemented due to similarities in the MEMS structures. The model and results obtained in the analysis of capacitive sensor A is applicable to capacitive sensor B.
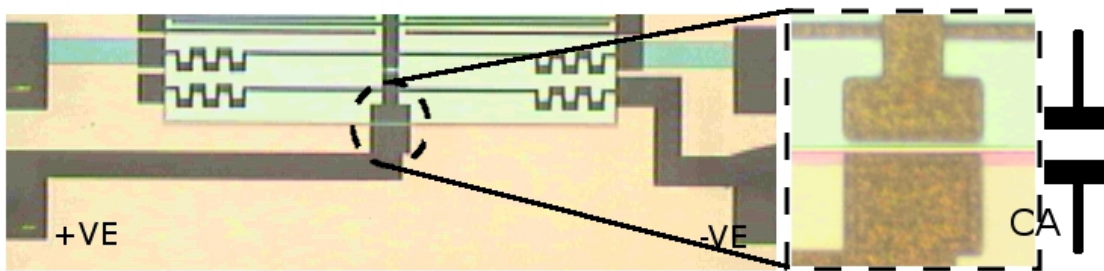
Figure 6.3.14.: A two-needle arrangement for capacitive sensor B measurement in an SPST switch

Parameter	$\mathbf{CA}[pF]$	$\mathbf{CB}[pF]$	$\mathbf{L}[\mu H]$	$\mathbf{R}[\Omega]$
Lower quartile, Q_1	0.2002	2.0908	0.3090	0
Median, Q_2	0.3640	5.1276	0.5974	0
Upper quartile, Q_3	1.3591	12.046	4.3175	1.9129
Interquartile range, IQR	1.1589	9.9552	4.0085	1.9129

Table 6.13.: Box plot parameters for equivalent circuit data in capacitive sensor B measurement in an SPST switch
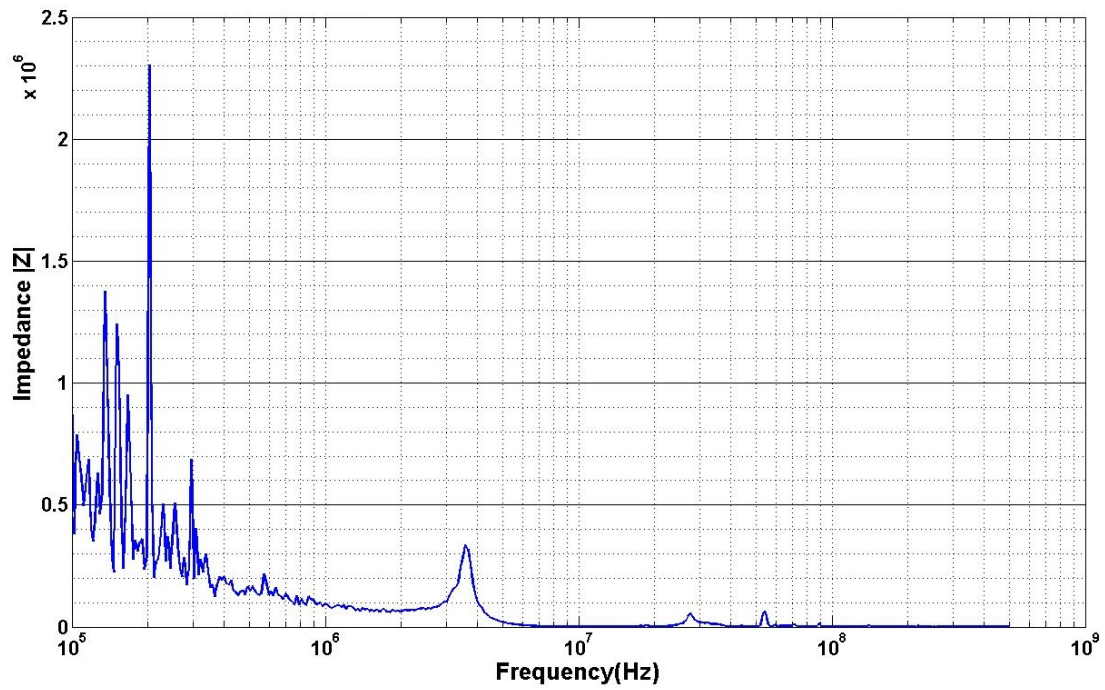
(a) Raw data of impedance |Z| measured at capacitive sensor B in an SPST switch
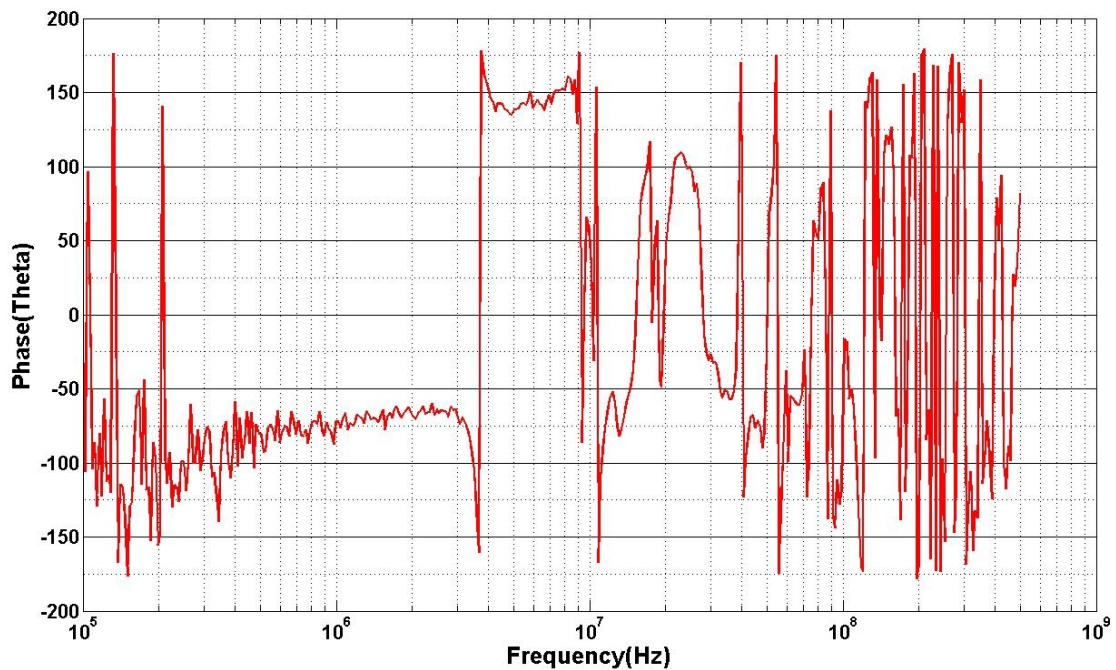
(b) Raw data of phase [θ] measured at capacitive sensor B in an SPST switch

Figure 6.3.15.: Plot of raw data measured at capacitive sensor B in an SPST switch
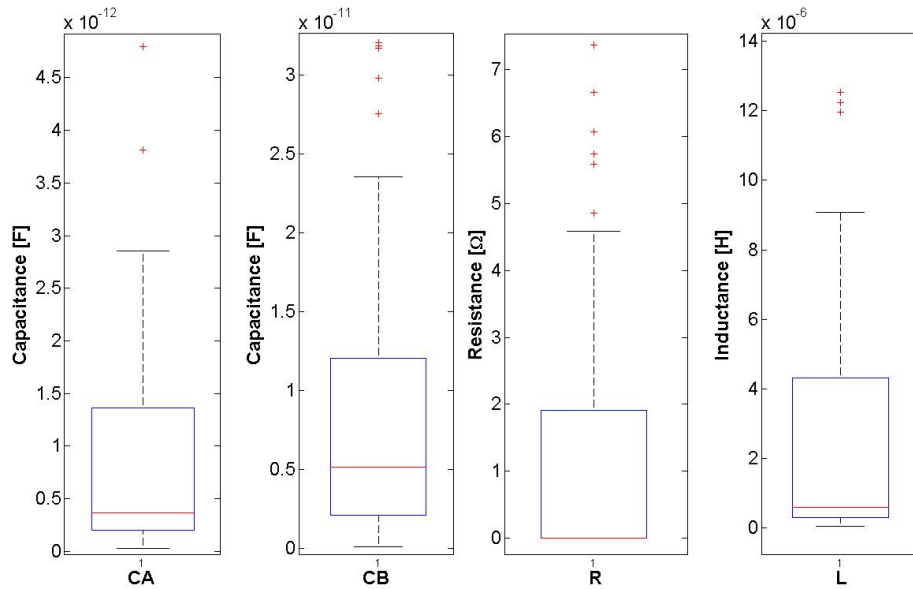
Figure 6.3.16.: Box-plot of SPST switch impedance measurement data for capacitive sensor B

6.3.2.5. Measurement Points: Signal-In/Out and Electrostatic Actuator

The next measurement point is set between the signal line and the electrostatic actuator. Each signal line shares the same moving structure with electrostatic actuator anchors. These two parts are electrically isolated from each other by a metal cut in the body mass. The impedance value between these two components is important for estimating the maximum working switching frequency of the switches with no clock feed through effect, which is similar to CMOS switches. Figure 6.3.17 shows the measurement setup and the construction of the involved parts.

Two sets of measurement were performed for this part. The first measurement point was performed between the signal-in and electrostatic actuator. The second measurement was performed between the signal-out and electrostatic actuator. Both measurements used 6 different samples with 10 repetitions of high frequency response measurements for each sample. In these measurement points, the equivalent circuit of the band-pass filter in Figure 6.3.2b was used. Four component values were extracted from the processed data using HP4195A. A box plot analysis is used to represent the processed data based on 120 raw data measurements. It can be seen in Figure 6.3.18 which has a similar pattern as discussed in the previous sections. The statistical distribution data from the box plot is presented in Table 6.14.

The capacitor CA value represents the capacitance in the body mass separated by the small gap induced by a metal cut shown in Figure 6.3.17. The capacitor CB is the parasitic capacitance measured between signal line and electrostatic actuator

beam. This summation of parasitic capacitance CA and CB is equivalent to the parasitic capacitance C_{PLE} that was mentioned in the discussion of electrical model improvement in Section 5.1. Table 6.14 shows the results of measurements between the signal-in and the actuator, where capacitor CA has a median capacitance value of $110.73fF$ and the median value of CB is recorded at $2.0145pF$. The signal-out and electrostatic actuator also records similar median data results as CA at $140.76fF$ and CB at $1.5111pF$ each. These values are about the same as the impedance measurement of the signal-in and signal-out lines since the structure is similar between these components.

The extended analysis was performed for the data obtained from measurement between the signal-in and the electrostatic actuator line. A single set of raw data plotted in Figure 6.3.20 was used for this analysis. Based on this data, HP4195A analysis gave $2.5363pF$ for the CA component. The manual calculation method estimated the value at less than $0.5313fF$ and the EIS software produced $0.900fF$ with 2.201% of fitting error. The CB components were roughly estimated at around $2.9139fF$ and the EIS software produced $3.00fF$ with 0.6588% of error. The HP4195A produced a CB value in the range of $18.944pF$ with unknown fitting error.

The inductance value was obtained only via the HP4195A and EIS software analysis. The EIS Powell algorithm produced a result of $55.9\mu H$ with 85.223% of error and the HP4195A produced $0.211\mu H$. The resistance R value was 0.4048Ω. The EIS software estimated a resistance value of 6.4408Ω with 19.998% error. The HP4195A produced 0Ω from the similar raw datasets.

A further analysis was performed with the same raw data but with two different equivalent circuit models in EIS Spectrum Analyser software. Model 1, as shown in Figure 6.3.2b, and Model 2, as shown in Figure 6.3.5b, were used in this analysis.

When Model 2 was implemented for the raw data, the fitting error was reduced in most of the elements. The fitting error for the CA value was reduced from 2.201% with $0.9fF$ to 1.319% with $5.00fF$. The results for the CB element show a similar trend to CA. Model 1 produced $3fF$ with 0.6588% error and Model 2 produced $2.00fF$ with 0.0958% fitting error.

The inductance components gave similar results as the other components. A reduction in fitting error for LA, from 85.223% to 1.241%, was recorded with a value of $55.9\mu H$ and $188\mu H$ respectively. The introduction of the LB element in Model 2 produced a value of $192.00\mu H$ with 1.219% error.

The fitting errors for resistance are the same for both models with more than 1000% errors. For RA resistor, Model 1 produced 5.7067Ω and Model 2 produced 19.605Ω. A very small value of RB was recorded at $1.21\mu\Omega$.

This comparison analysis showed that Model 2 is a better equivalent circuit than Model 1 in representing the component between signal line and electrostatic actuator beam.
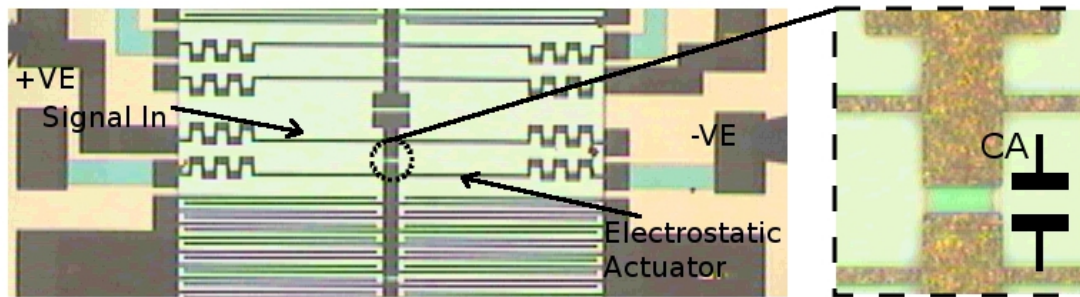
(a) Signal-in and electrostatic actuator
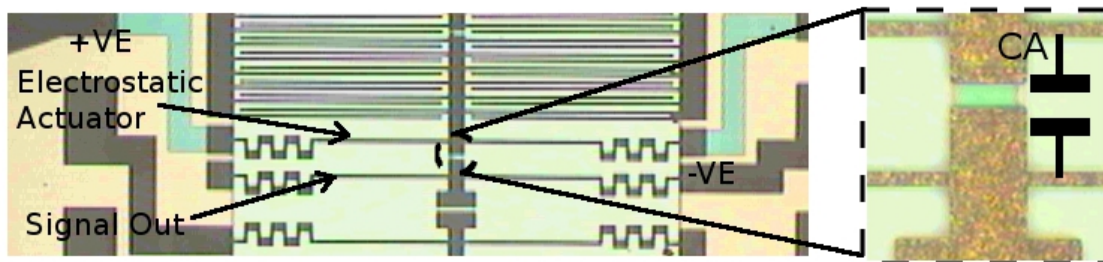
(b) Signal-out and electrostatic actuator

Figure 6.3.17.: A two-needle arrangement for measuring signal-in and electrostatic actuators in an SPST switch design
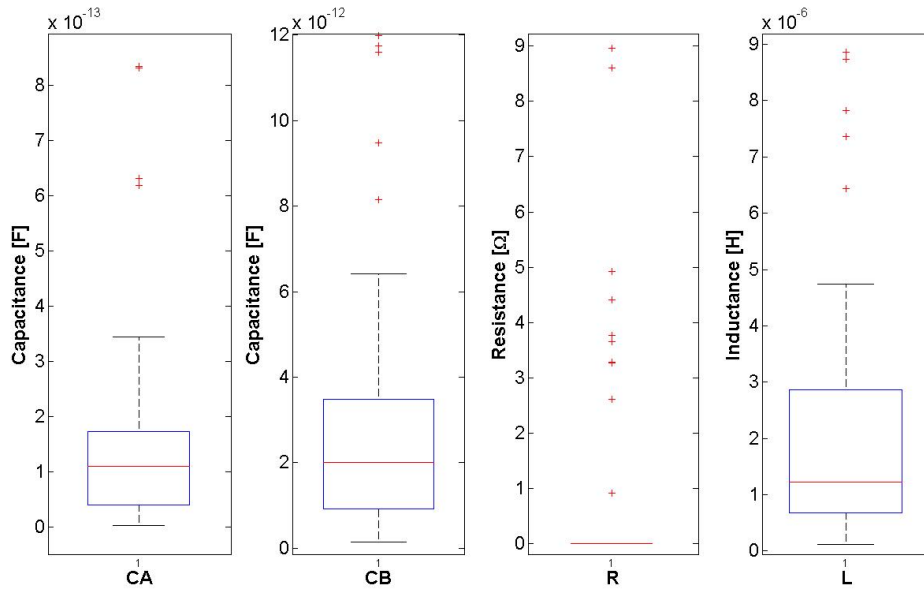
(a) Signal-in and electrostatic actuator
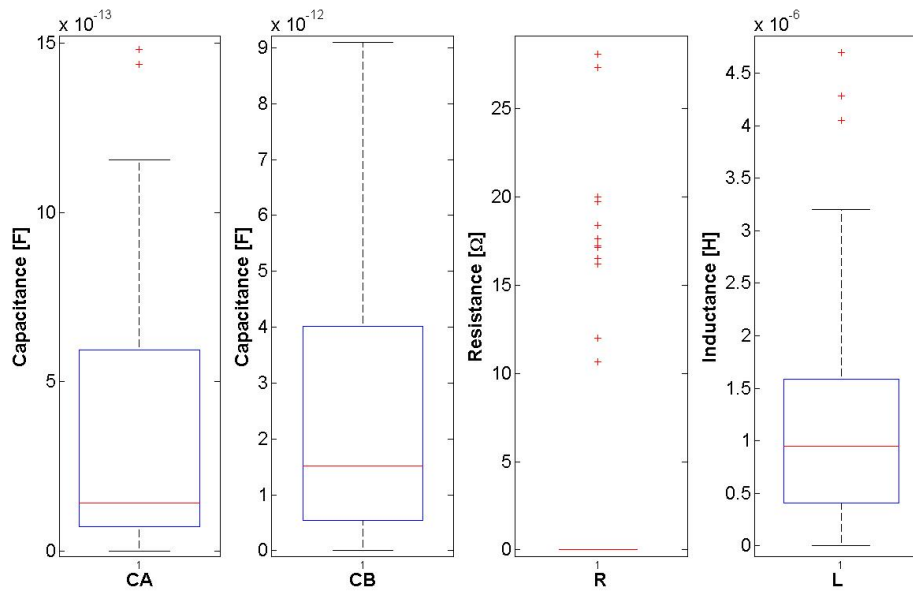
(b) Signal-out and electrostatic actuator

Figure 6.3.18.: Box plot of SPST switch impedance data for signal-in/out line and electrostatic actuator measurement

(a) Signal-in and electrostatic actuator measurement

Parameter	**CA**$[fF]$	**CB**$[pF]$	**L**$[\mu H]$	**R**$[\Omega]$
Lower quartile, Q_1	40.290	0.9254	0.6771	0
Median, Q_2	110.73	2.0145	1.2303	0
Upper quartile, Q_3	173.95	3.4820	2.8587	0
Interquartile range, IQR	133.66	2.5566	2.1816	0

(b) Signal-out and electrostatic actuator measurement

Parameter	**CA**$[fF]$	**CB**$[pF]$	**L**$[\mu H]$	**R**$[\Omega]$
Lower quartile, Q_1	72.196	0.5491	0.4074	0
Median, Q_2	140.76	1.5111	0.953	0
Upper quartile, Q_3	593.45	4.0206	1.5903	0
Interquartile range, IQR	521.25	3.4715	1.1830	0

Table 6.14.: Box plot parameters for equivalent circuit data in between signal-in/out lines and electrostatic actuator measurement for SPST switch design

Software/ Analyser	**CA** $[fF]$	**Err.** $[\%]$	**CB** $[fF]$	**Err.** $[\%]$	**L** $[\mu H]$	**Err.** $[\%]$	**R** $[\Omega]$	**Err.** $[\%]$
HP4195A	2536.3	NA	18944	NA	0.211	NA	0	NA
EIS	0.900	2.201	3.00	0.6588	55.9	85.223	5.7067	##
Calculation[a]	0.5313	NA	2.9139	NA	NA	NA	0.4048	NA

[a]Manual calculation as shown in Appendix B and A

Table 6.15.: Results for signal-in and electrostatic actuator equivalent model parameters using HP4195A, EIS Spectrum Analyser and calculations

Element	Model 1	Error	Model 2	Error
CA$[fF]$	0.900	2.201%	5.00	1.319%
CB$[fF]$	3.00	0.6588%	2.00	0.958%
LA$[\mu H]$	55.9	85.223%	188.00	1.241%
LB$[\mu H]$	NA	NA	192.00	1.219%
RA$[\Omega]$	5.7067	##	19.605	##
RB$[\Omega]$	NA	NA	1.21×10^{-6}	##

Table 6.16.: Results of comparison for signal-in and electrostatic actuator equivalent models using EIS Spectrum Analyser software
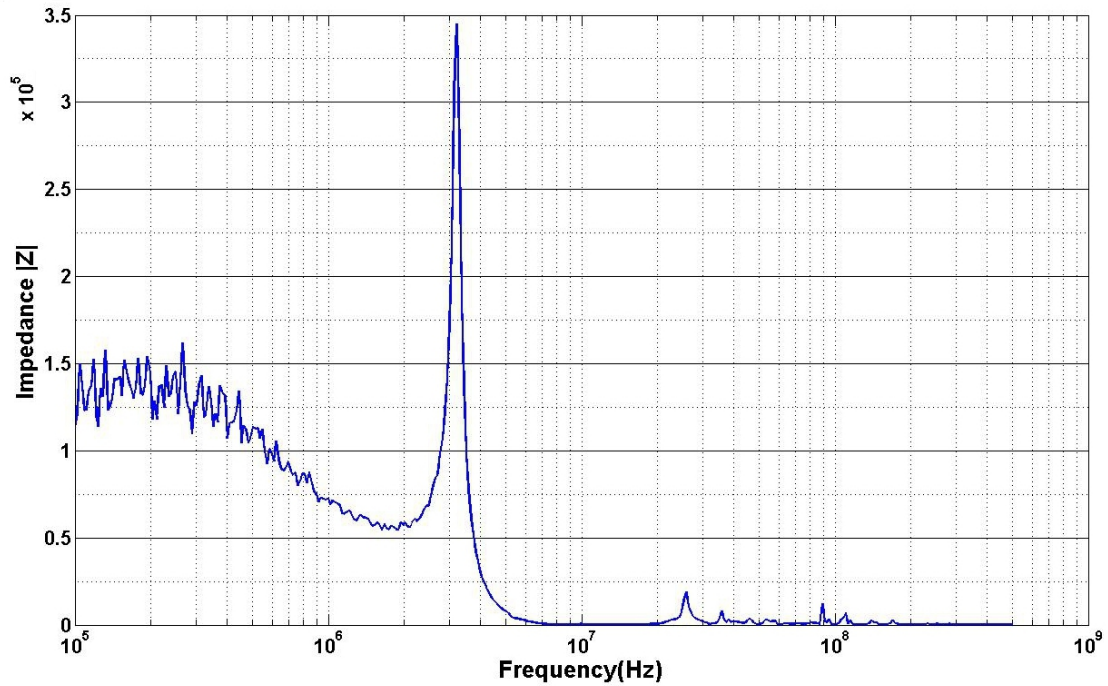
(a) Raw data of impedance |Z| measured between signal-in and electrostatic actuator in an SPST switch
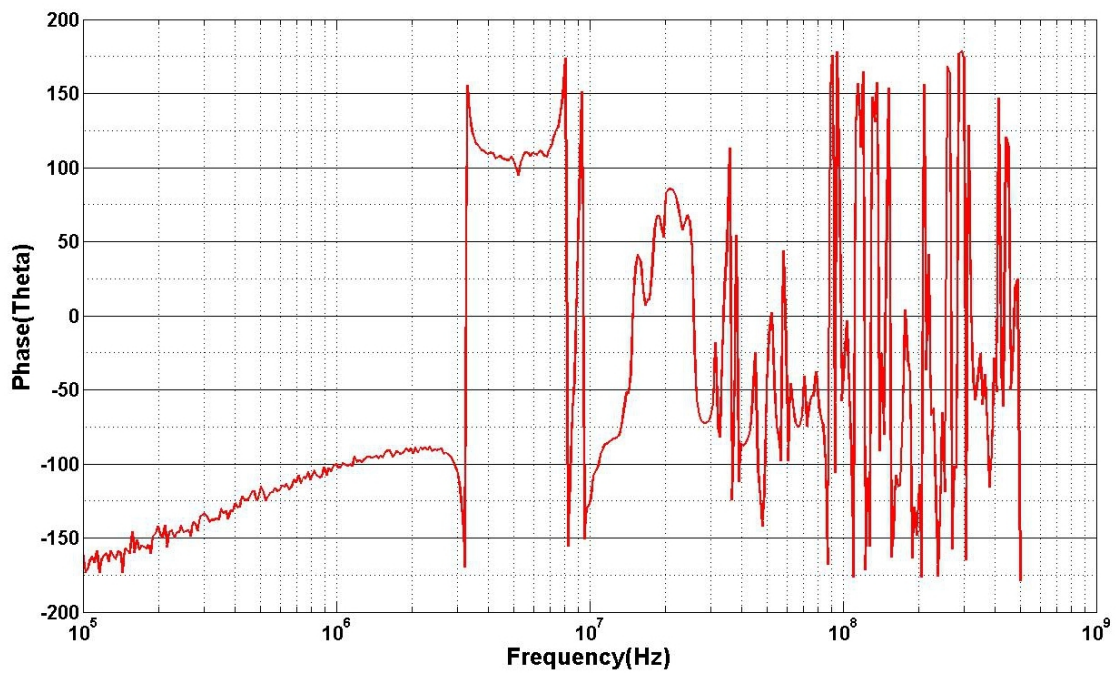

(b) Raw data of phase [θ] measured between signal-in and electrostatic actuator in an SPST switch

Figure 6.3.19.: Plot of raw data measured between signal-in line and electrostatic actuator in an SPST switch
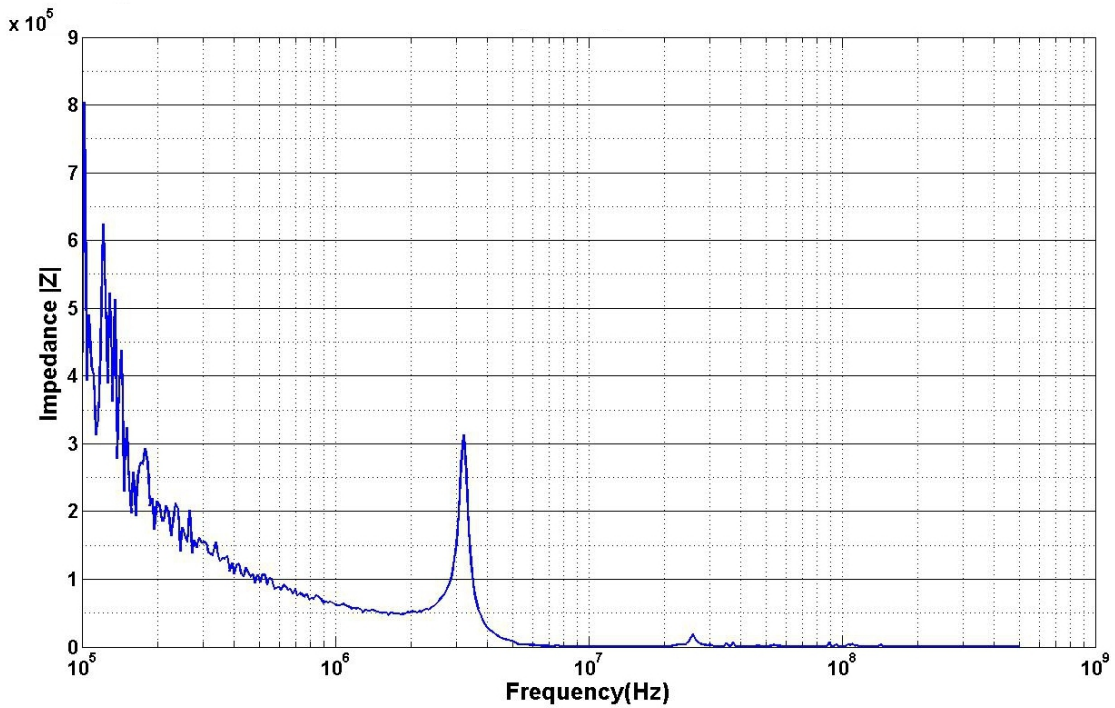
(a) Raw data of impedance |Z| measured between signal-out and electrostatic actuator in a SPST switch
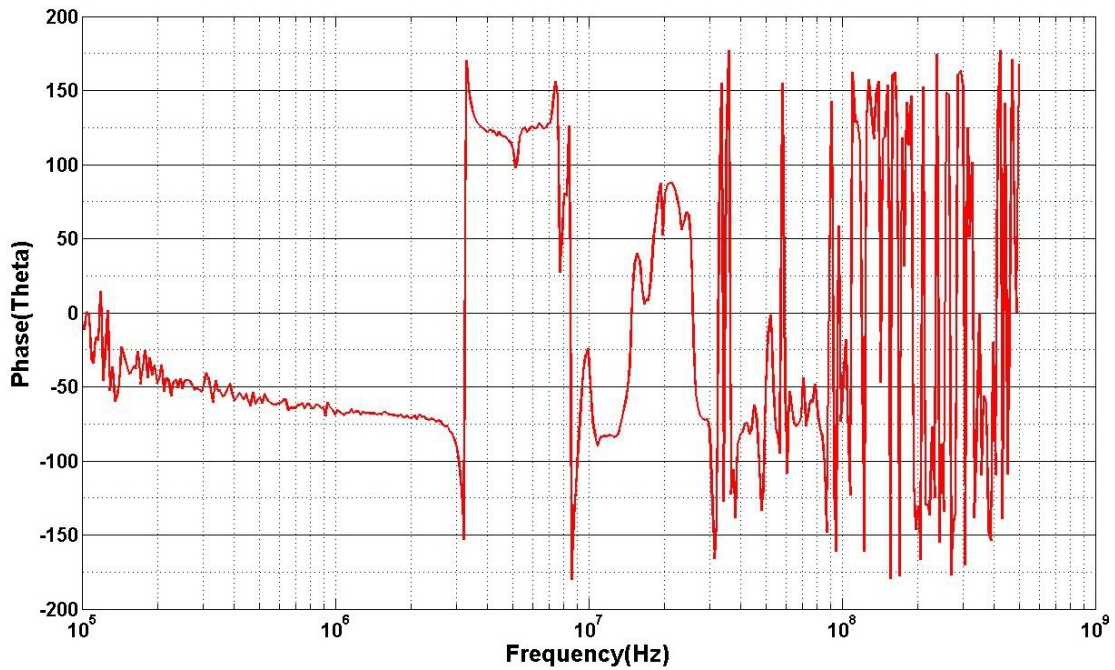
(b) Raw data of phase [θ] measured between signal-out and electrostatic actuator in a SPST switch

Figure 6.3.20.: Plot of raw data measured between the signal-out and the electrostatic actuator in an SPST switch

Sub-component	unit/sample
Signal-In/Out	2
Capacitive Sensors	2
Uni-directional Electrostatic Actuator	2
Bi-directional Actuator	1

Table 6.17.: Sub-components of SPDT switch

6.3.3. SPDT MEMS Switch Measurement Results

The evaluation of the SPDT MEMS switch requires a slightly different approach. There are only two SPDT switches in each die and that means fewer samples are available for testing, however the SPDT switch has an advantage in being identical in the sub-components design. Although smaller samples were used, the same amount of measurement data can be obtained for each sub-component. The sub-components of the switch and their respective units/samples can be broken down into four components, as shown in Table 6.17. The data presented below is based on 10 measurement repetitions and processed by the algorithm provided in the HP4195A network analyser. The median value of the measurement results are taken to show the trend of data population.

Since the structures in the SPDT switch are similar to those in the SPST switch, the extended analysis using EIS Spectrum Analyser software is not implemented for the dataset for the SPDT switch. This is because a similar outcome of the analysis is expected.

6.3.3.1. Measurement Point: Signal-In and Signal-Out

There are two identical signal-in and signal-out lines for each SPDT switch. The impedance measurement procedures are similar to those for SPST switches presented in previous sections. Similar equivalent circuits to those in Figure 6.3.2b are used in evaluating the impedance measurement. The measurements were performed on eight samples with ten repetitions on each sample. The SPDT switch samples were taken from chip dice C and E and labelled as CD1, CD2, ED1 and ED2. A total of 160 raw datasets were collected and processed by HP4195A network analyser using the equivalent circuit of the band-pass filter as in Figure 6.3.2b. Figure 6.3.22 shows a box plot of the data distribution for each component and Table 6.18 shows the distribution statistics. The median value contact capacitance CA is recorded as $242.49fF$ with Q_1 as $99.479fF$ and Q_2 as $547.68fF$. This shows a measurement consistency throughout the samples with small IQR value at $448.20fF$. For parasitic capacitance CB, the median data was recorded as $6.1942pF$ with Q_1 as $2.4826pF$ and Q_2 as $8.9951pF$. The median data for inductance was recorded as $1.1578\mu H$ with 0Ω in resistance.
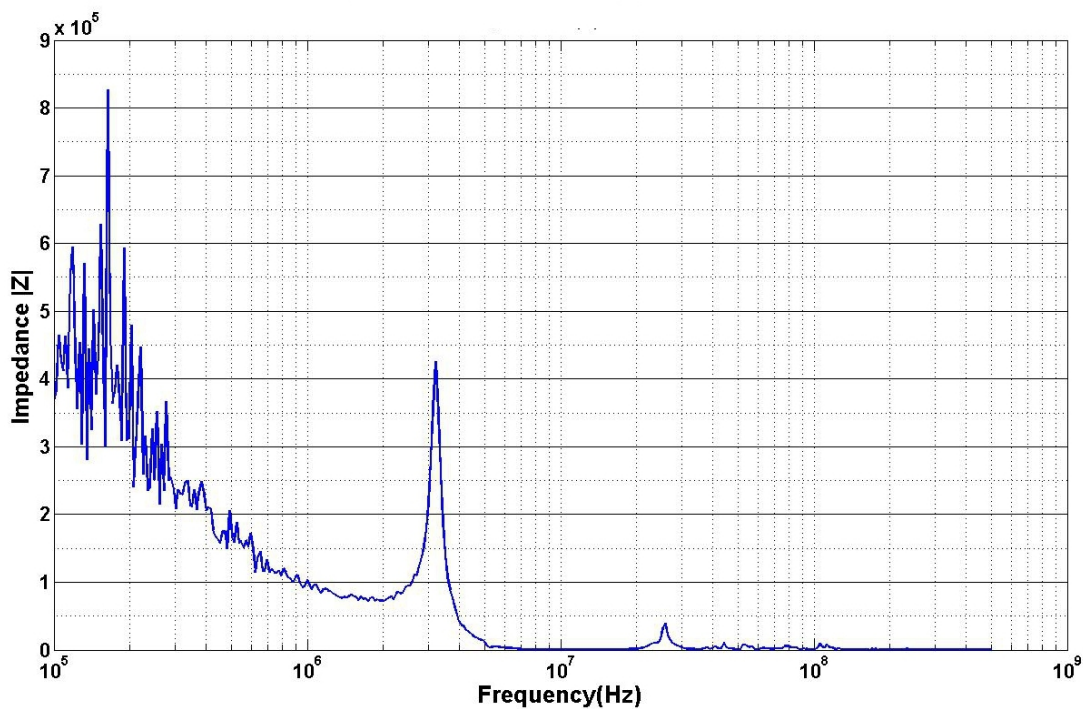
(a) Raw data of impedance |Z| measured between signal-in and signal-out lines in an SPDT switch
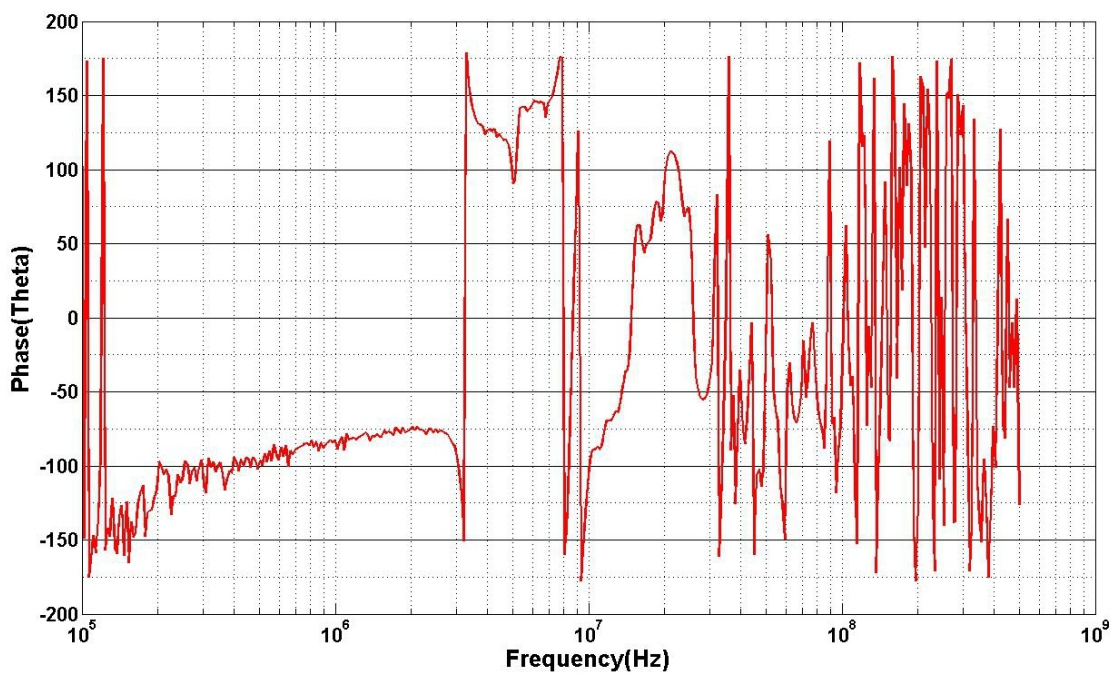
(b) Raw data of phase [θ] measured between signal-in and signal-out lines in an SPDT switch

Figure 6.3.21.: Plot of raw data measured between signal-in and signal-out lines in an SPDT switch

Parameter	$\mathbf{CA}[fF]$	$\mathbf{CB}[pF]$	$\mathbf{L}[\mu H]$	$\mathbf{R}[\Omega]$
Lower quartile, Q_1	99.479	2.4826	0.2671	0
Median, Q_2	242.49	6.1942	0.6979	0
Upper quartile, Q_3	547.68	8.9951	1.8124	0
Interquartile range, IQR	448.20	6.5125	1.5454	0

Table 6.18.: Box plot parameters for equivalent circuit data in between signal-in and signal-out lines in SPDT switches
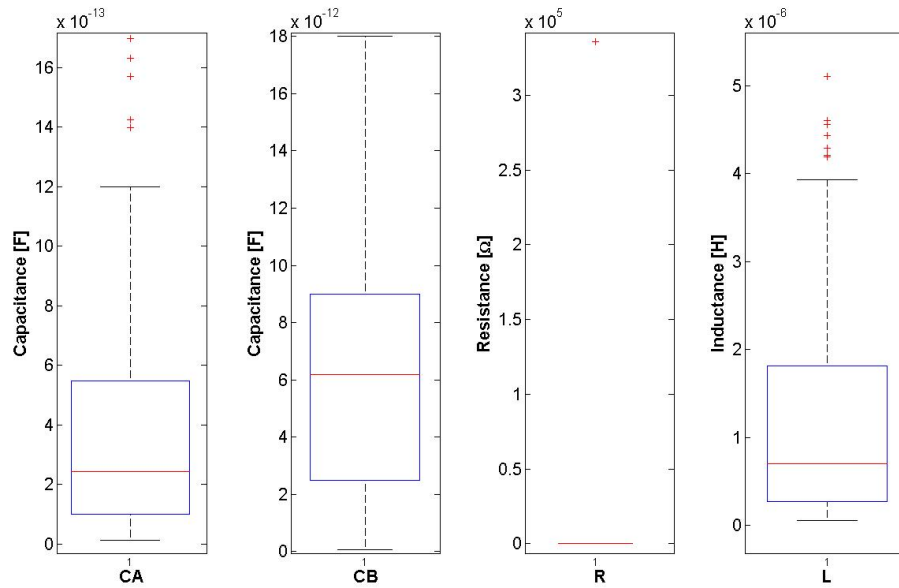
Figure 6.3.22.: Box-plot of impedance measurement data between signal-in and signal-out in SPDT switches

6.3.3.2. Measurement Points: Capacitive Sensors

Similarly to the SPST switch, the SPDT switch is also equipped with capacitive sensors in each body mass for self-monitoring the system. A similar measurement setup for capacitive sensors is applied here with usage of eight samples taken from chip dice C and E and labelled CD1, CD2, ED1 and ED2. A repetition of 10 times for each sample produced 160 raw data of measurement. The measurements were taken with the switch set to the off-state condition. The band-pass equivalent circuit as in Figure 6.3.2b was used to processed the raw data and extract the component values.

Figure 6.3.24 shows the box plot of the processed data and Table 6.19 gives the statistical distribution value. The median value of contact area CA was recorded as $384.36fF$ with Q_1 as $242.67fF$ and Q_3 as $689.59fF$. The median value of parasitic

Parameter	$\mathbf{CA}[fF]$	$\mathbf{CB}[pF]$	$\mathbf{L}[\mu H]$	$\mathbf{R}[\Omega]$
Lower quartile, Q_1	242.67	1.6893	0.3074	0
Median, Q_2	384.36	2.8527	1.1359	7.2904
Upper quartile, Q_3	689.59	6.2575	7.7541	6.2575
Interquartile Range, IQR	446.92	4.5682	7.4467	4.5682

Table 6.19.: Box plot parameters for equivalent circuit data in SPDT switch in capacitive sensors

capacitance, CB was recorded as $2.8527pF$ value. The median value of inductance, L was recorded as $1.5305\mu H$ and resistance, R as 7.2904Ω value. All components show consistent measurement results with small IQR values.
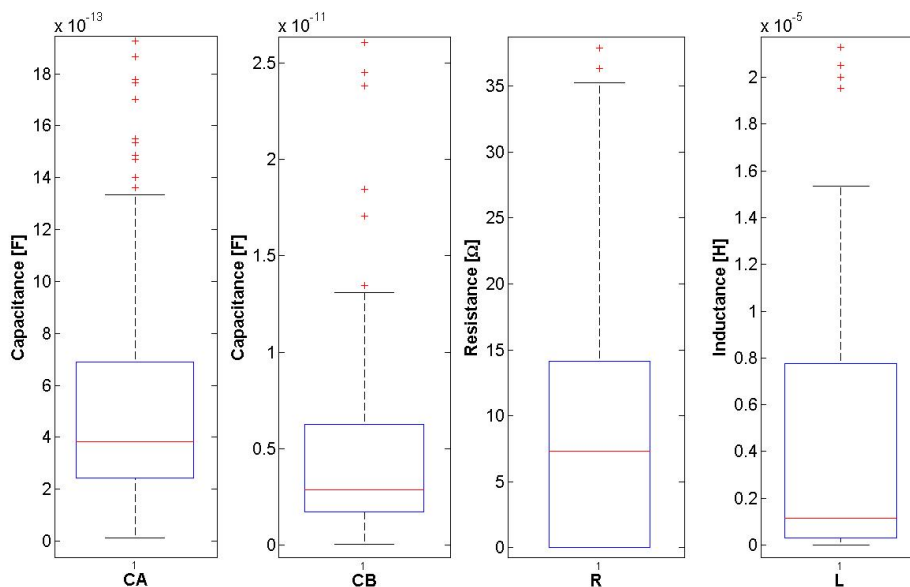
Figure 6.3.24.: Box-plot of SPDT switch impedance measurement data for capacitive sensor

6.3.3.3. Measurement Points: Signal-In/Out and Electrostatic Actuator

The next measurement point is the high frequency response between the signal lines and electrostatic actuators. Since there is no external routing path and the structure of the signal-in/out and electrostatic actuators are identical, it is possible to treat these measurement points as one. The same measurement setup is used, with eight samples labelled as CD1, CD2, ED1 and ED2. For each sample ten repetitions of measurement yielded 160 raw datasets. The data was processed using HP4195A with a band-pass equivalent circuit as in Figure 6.3.2b.
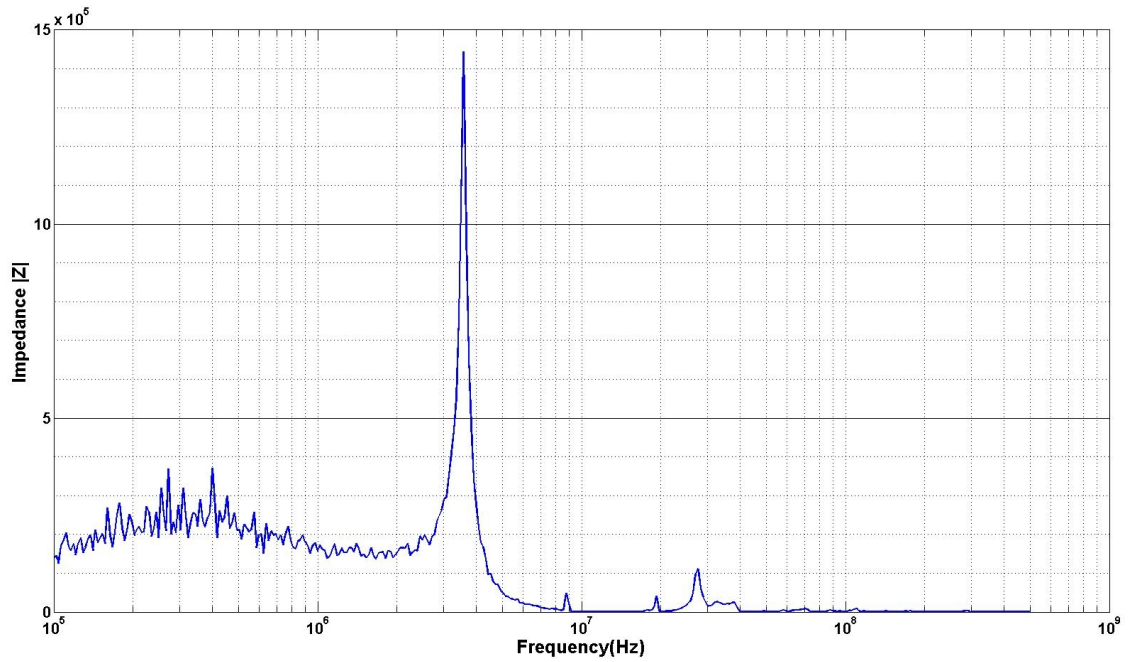
(a) Raw data of impedance |Z| measured in capacitive sensor of SPDT switch
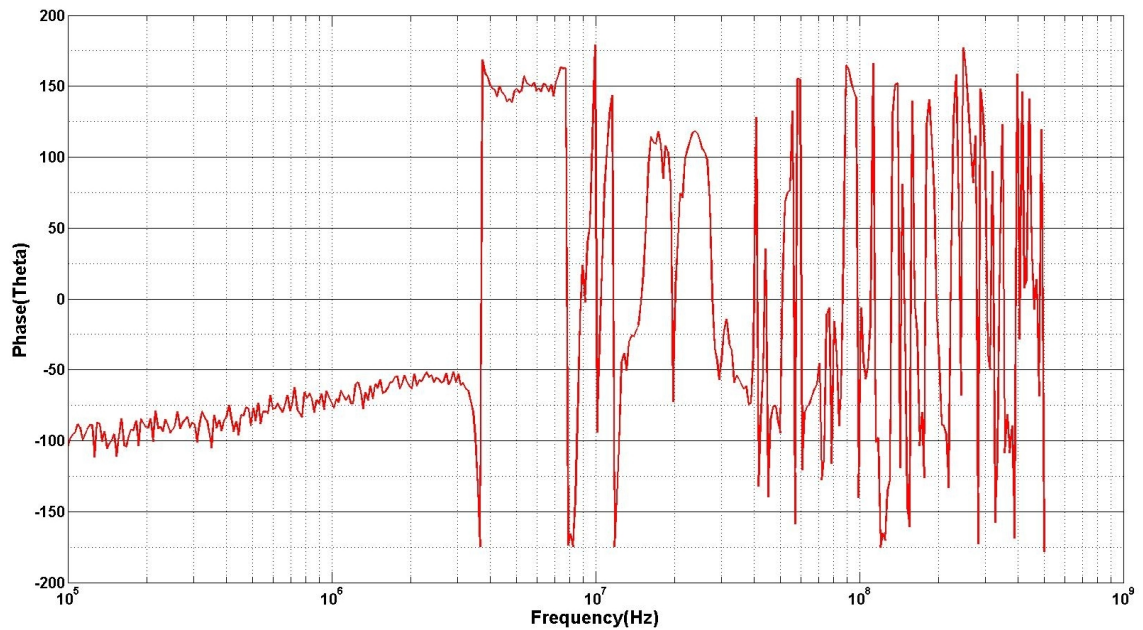
(b) Raw data of phase [θ] measured in capacitive sensor of SPDT switch

Figure 6.3.23.: Plot of raw data measured in the capacitive sensor area

Parameter	$\mathbf{CA}[fF]$	$\mathbf{CB}[pF]$	$\mathbf{L}[\mu H]$	$\mathbf{R}[\Omega]$
Lower quartile, Q_1	155.50	2.9200	0.5566	0
Median, Q_2	405.25	4.7938	1.5184	0
Upper quartile, Q_3	1287.2	9.1144	7.1261	4.2423
Interquartile range, IQR	1131.7	6.1944	6.5695	4.2423

Table 6.20.: Box plot parameters for equivalent circuit data in between signal-in/out lines and electrostatic actuator in an SPDT switch

Figure 6.3.26 shows the box plot diagram of the obtained data. The same size of data sample has resulted in the statistical distribution shown in Table 6.20. The capacitance CA recorded a median value of $405.25fF$ and parasitic capacitance CB was recorded as $4.7938pF$. The Q_1 of CA was recorded as $155.5fF$ and the Q_3 as $1287.7fF$ which made the IQR value at $1131.7fF$. The median value of inductance was $1.0279\mu H$ with 0Ω resistance. The impedance measurement results for the signal line and electrostatic actuator are shown here.
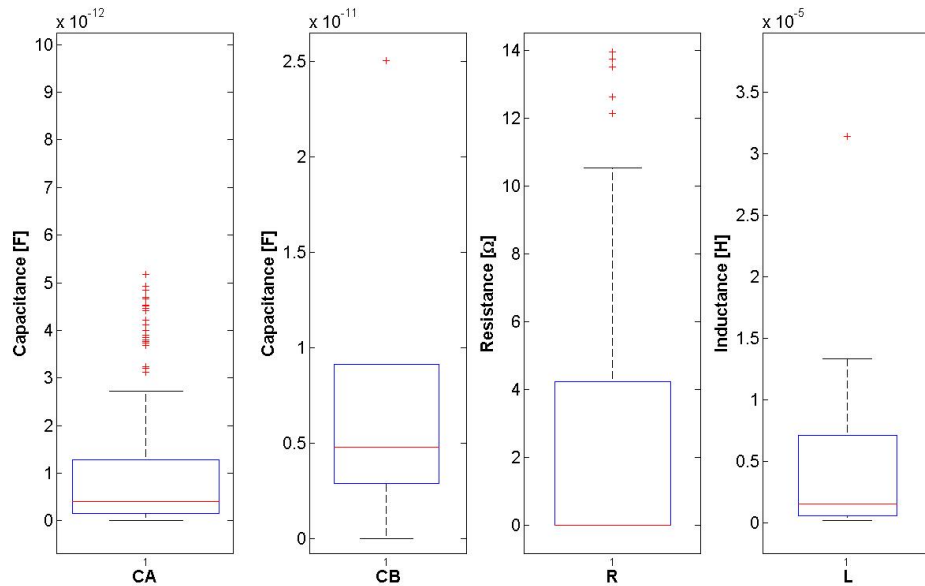
Figure 6.3.26.: Box-plot of SPDT switch impedance measurement data for signal-in/out and electrostatic actuator

6.3.3.4. Measurement Points: Uni-directional Electrostatic Actuators

The uni-directional electrostatic actuators provides movement for Mass A and Mass C in a SPDT switch. The impedance measurement at this point will provide information about the capacitance value of the structure. Similar to the SPST measure-
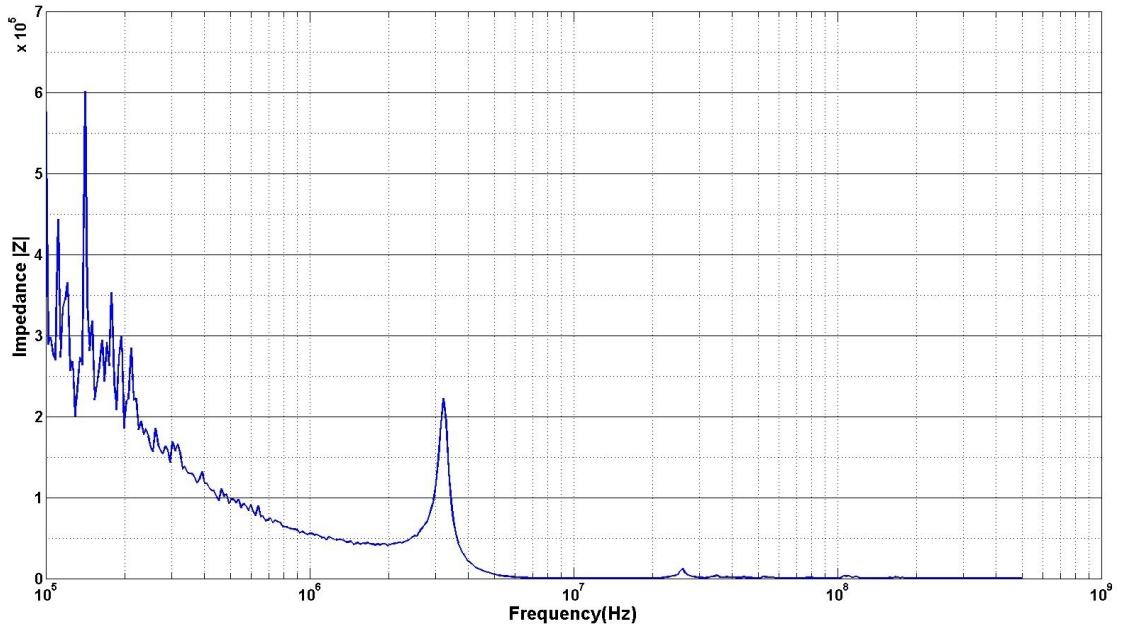
(a) Raw data of impedance |Z| measured between signal line and electrostatic actuator in an SPDT switch
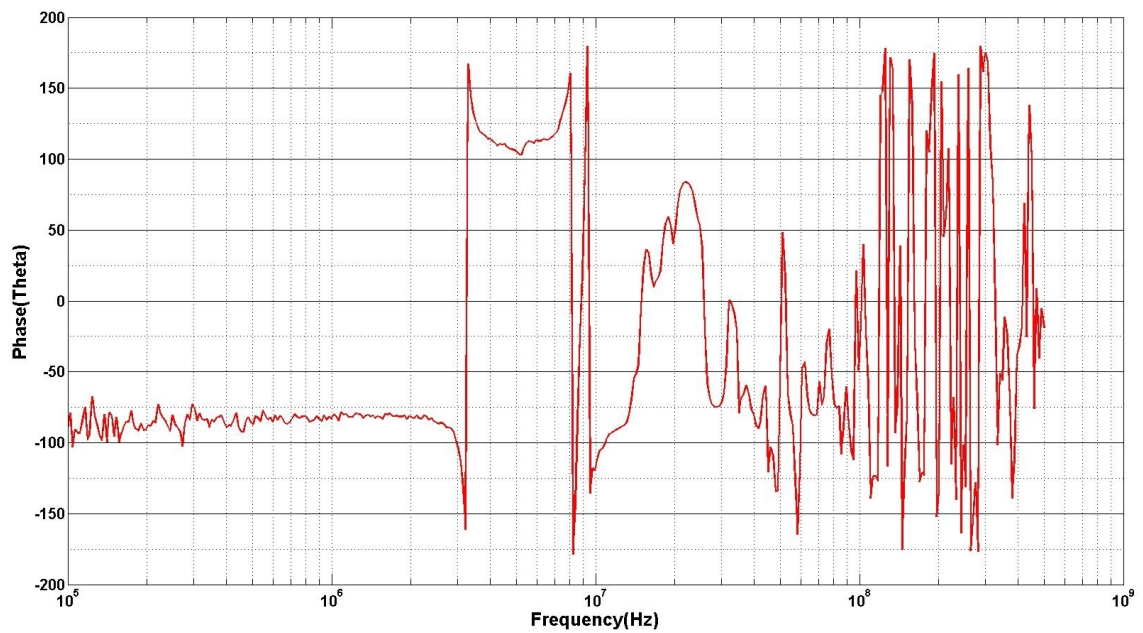
(b) Raw data of phase [θ] measured between signal line and electrostatic actuator in an SPDT switch

Figure 6.3.25.: Plot of raw data measured in the capacitive sensor area

Parameter	$\mathbf{CA}[pF]$	$\mathbf{L}[nH]$	$\mathbf{R}[\Omega]$
Lower quartile, Q_1	165.59	43.374	32.168
Median, Q_2	211.79	66.160	59.906
Upper quartile, Q_3	216.51	75.142	61.544
Interquartile range, IQR	50.920	31.768	29.375

Table 6.21.: Box plot parameters for equivalent circuit data in uni-directional electrostatic actuator in an SPDT switch

ment setup for the electrostatic actuator, eight samples were used for testing with ten repetitions for each sample which produced 160 raw datasets. The samples used for these measurements are labelled CD1, CD2, ED1 and ED2. The measurement was made with the switch set in the off-state condition.

The measurements were evaluated in HP4195A using the equivalent functions as for Figure 6.3.2a . Only three components exist in this model with a huge capacitance CA representing the total actuation capacitance of the actuator. The evaluated data is presented as a box plot diagram to show the statistical distribution. Figure 6.3.28 shows the box plot and Table 6.21 provides the relevant statistics. The median value of the capacitance measurements was recorded as $211.79pF$ with Q_1 as $165.59pF$ and Q_3 as $216.51pF$. The median data of inductance and resistance is recorded at $0.06894\mu H$ and 61.5995Ω respectively. The small IQR values for all components shows good consistency of the overall datasets.
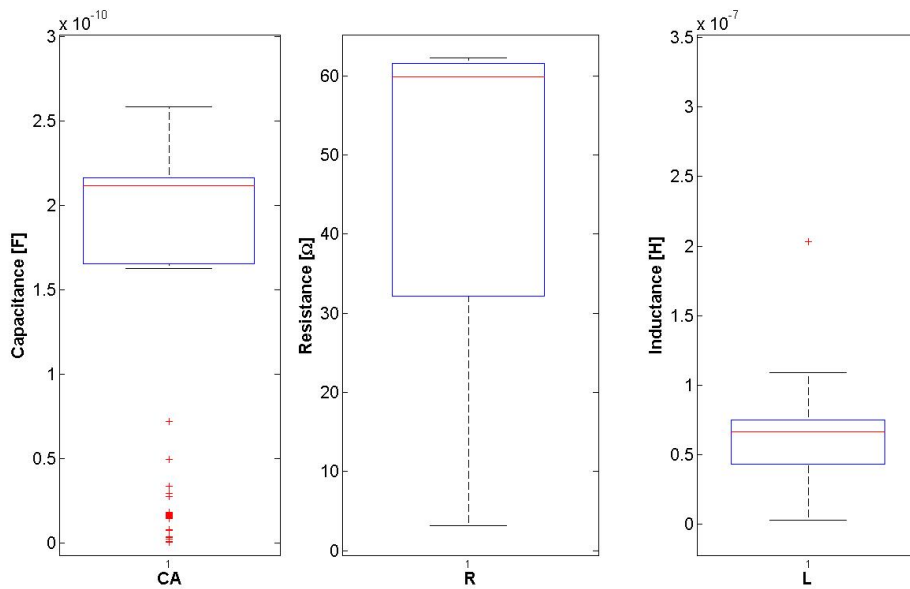
Figure 6.3.28.: Box-plot of SPDT switch impedance measurement data for uni-directional electrostatic actuator
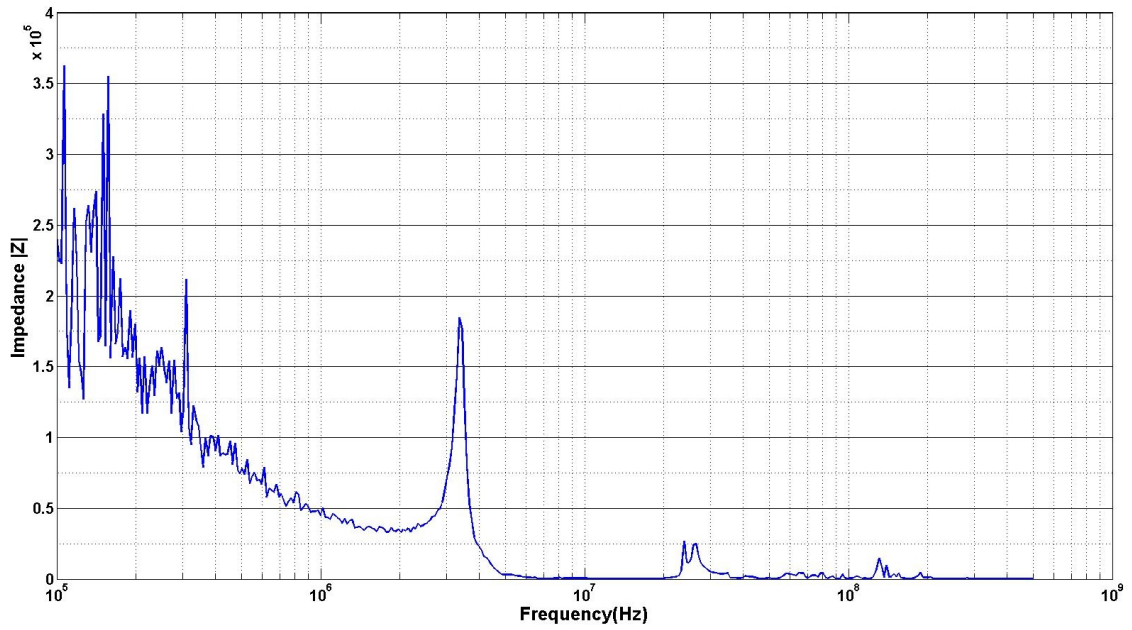
(a) Raw data of impedance |Z| measured at uni-directional electrostatic actuator in an SPDT switch
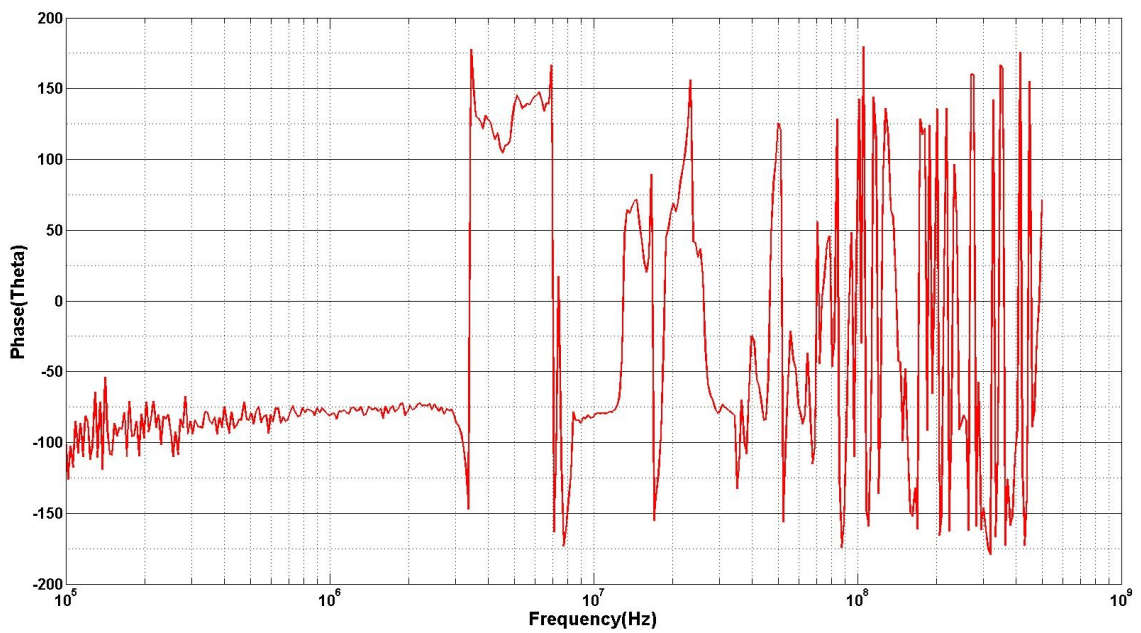
(b) Raw data of phase [θ] measured at uni-directional electrostatic actuator in an SPDT switch

Figure 6.3.27.: Plot of raw data measured in the uni-directional electrostatic actuator in an SPDT switch

Parameter	$\mathbf{CA}[pF]$	$\mathbf{L}[nH]$	$\mathbf{R}[\Omega]$
Lower quartile, Q_1	393.01	90.121	11.142
Median, Q_2	591.15	109.56	14.345
Upper quartile, Q_3	1398.1	200.38	22.853
Interquartile range, IQR	1005.1	110.26	11.710

Table 6.22.: Box plot parameters for equivalent circuit data in bi-directional electrostatic actuator in SPDT switch

6.3.3.5. Measurement Points: Bi-directional Electrostatic Actuator

The SPDT switch design has only one bi-directional electrostatic actuator which is represented by Mass B. The whole structure has almost double the capacitance of the uni-directional electrostatic actuators. The measurement setup is similar to that for the uni-directional electrostatic actuator, however, since there is no identical element in a single switch, eight different SPDT switches were used for data measurement. The samples were taken from dice C, E, F and G, labelled ID CD1, CD2, ED1, ED2, FD1, FD2, GD1 and GD2. A total of 160 raw datasets were obtained from eight samples with ten repetitions each. The switch was set to the off-state when the measurements were taken. Figure 6.3.29 shows an example of a frequency response from a single raw dataset.

The data was processed using the equivalent circuit to that in Figure 6.3.2a by HP4195A. The results of the three component values were then populated in a box plot diagram as shown in Figure 6.3.30. The respective statistics distribution values can be seen in Table 6.22. The measurement data recorded a median value of $591.15pF$ in CA value. The inductance value is recorded as $0.1295\mu H$ and 9.9133Ω for the resistance value.
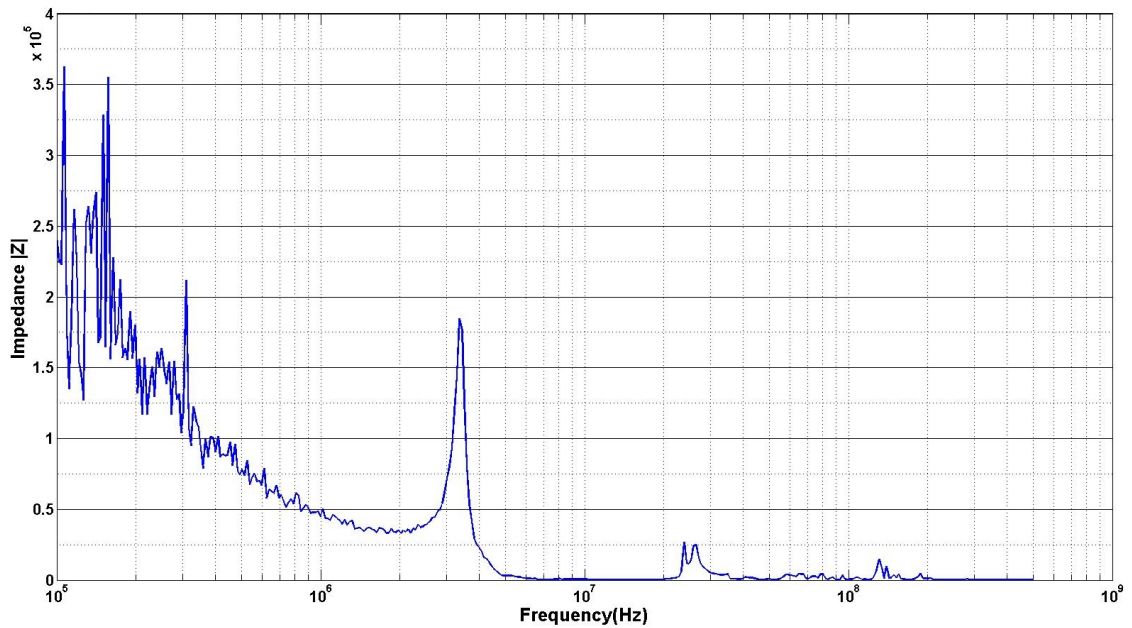
(a) Raw data of impedance |Z| measured at bi-directional electrostatic actuator in an SPDT switch
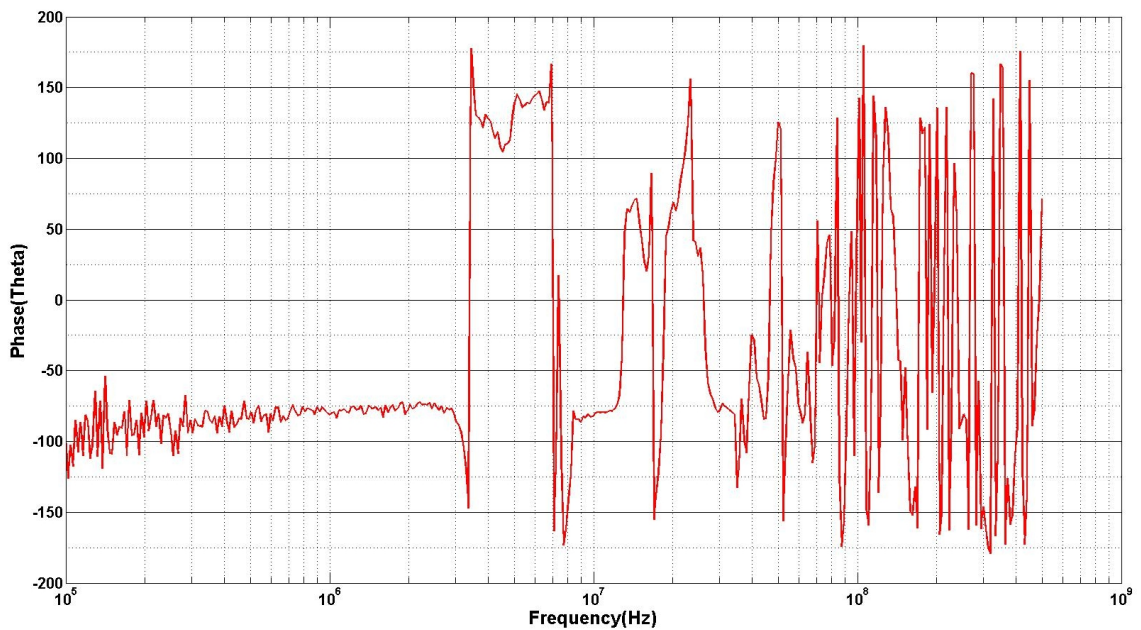
(b) Raw data of phase [θ] measured at bi-directional electrostatic actuator in an SPDT switch

Figure 6.3.29.: Plot of raw data measured in the bi-directional electrostatic actuator area in an SPDT switch
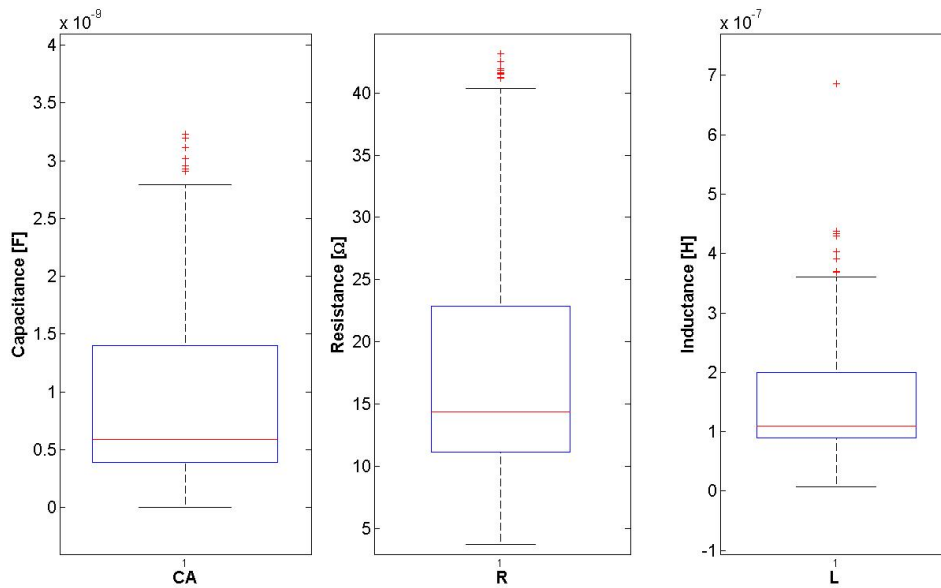
Figure 6.3.30.: Box-plot of SPDT switch impedance measurement data for in bidirectional electrostatic actuator

6.4. Mechanical Characteristics - Microactuators Functionalities

As explained in the design section in the Chapter 4, both ISE-DC-MEMS switches were equipped with two types of actuators. This section will elaborate further on the testing method and then discuss further observations and the test results.

6.4.1. Switching Action Using Electrostatic Actuators

Electrostatic actuators can be tested by providing a voltage source to the positive port and grounding to the negative port. The Keithley 236 and 238 were used as voltage sources. This equipment made it feasible to measure incremental input voltate precisely at DUT. In SPST switches the simulation results recorded a voltage pull-in at 84V. When evaluating the actual pull-in voltage of the actuator, a 10V increment for each step was implemented. The movement of the body mass was recorded via CCD camera to personal computer. Figure 6.4.1 shows the experimental setup for characterising the electrostatic actuator.

Six samples taken from die A were used to determine the functionality of the electrostatic actuators for the SPST switches. The samples are labelled with identification numbers AS1 to AS6. In the experiment, the body mass started visibly moving
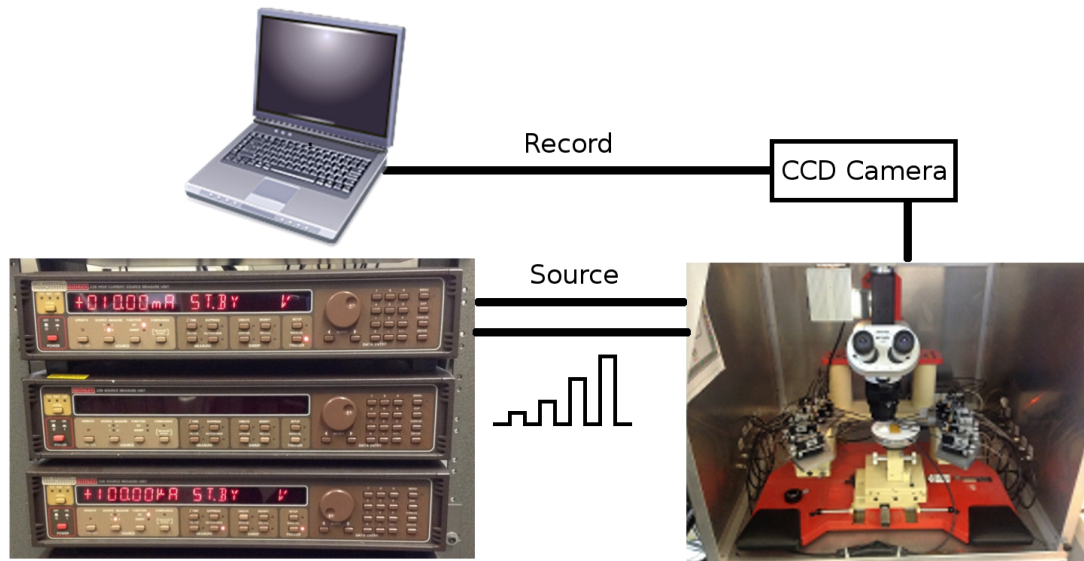
Figure 6.4.1.: Experiment setup for characterising electrostatic actuator behaviour

at around 60V. As the actuation voltage increased, on most occasions there was a failure between 70V and 80V. This failure took the form of stiction among the finger structures of the electrostatic actuator. Figure 6.4.2 shows one of the examples of the stiction in the electrostatic actuator after applying the voltage actuation.

The same problem occurred in the SPDT design. Four SPDT switches were tested from dice A and B, labelled AD1, AD2, BD1 and BD2. The electrostatic actuators were prone to stiction failure. Of the four samples that were tested, there was only one occasion on which the switch was able to make contact on the first attempt using electrostatic actuation. This switch later also suffered from a stiction problem when the experiment was repeated. The contact resistance recorded was in the range of 10Ω. This large contact resistance was due to the low contact force provided by electrostatic actuator.

6.4.2. Switching Action Using Heat Actuators

In the first prototype, there are two design variants of the heat actuator. The SPST switches are embedded with resistive layers of polysilicon and the SPDT switches have no additional resistive layer in the heat actuator structure. As the simulation results show in Section 4.6.2, the special arrangement of a serpentine structure alone can produce the required displacement to move the body mass.

The measurement setup consisted of a two channel power supply, multimeters and the DUTs. The power supply from Voltcraft is capable of producing 0-30V to up to 2.5A for every channel. For switching actions, the heat actuator from each body mass will need to be activated to produce a total of $10\mu m$ deflections. In the next
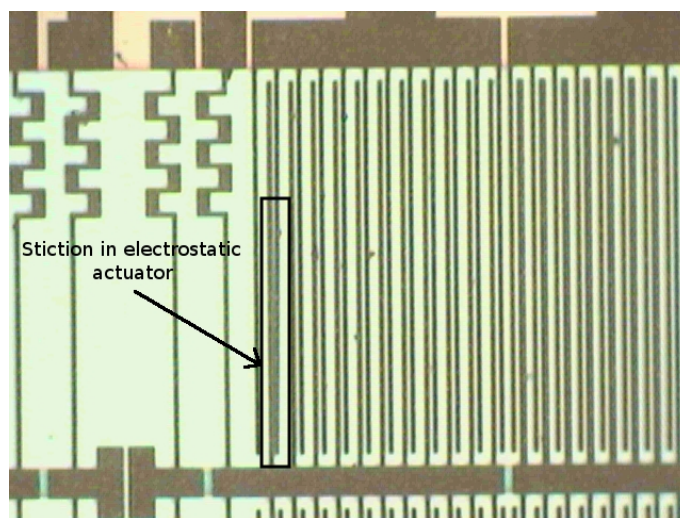
Figure 6.4.2.: Stiction failure in electrostatic actuator

sections, further details of experiment results for each type of MEMS switch will be presented.

6.4.2.1. SPST Heat Actuator

In the SPST MEMS switch, the pad to pad resistance varied from 227Ω to 430Ω. This is because of the difference in the poly layer construction in terms of width and length. Experiment results show that good actuation movements were produced. Several current levels, ranging from $50mA$ to $300mA$, were applied. First, the deflection direction of the heat actuator during actuation needs to be confirmed. The heat actuators were labelled as C,J and E,H and are shown in Figure 5.3.2a. Figure 6.4.4a shows the behaviour of heat actuators E and H with two different current levels at $0mA$ and $300mA$. These actuators produced a bigger gap at the switch contact in the presence of current, which is useful for self-repairing functions.

The actuators C and J in Figure 6.4.4b show the opposite behaviour as closing gap actions were produced when the current was applied. These actuators are suitable for switching actions. The actuator locations are intentionally further away from the signal line in order to prevent significant heat that may lead to any kind of noise in the signal.

The direction of the heat actuators depends on the design geometries. The difference in the heat actuator arrangement produced two opposite deflection directions. This was confirmed by the simulation result presented in Section 4.6.2. According to observation during the experiment, the displacement behaviour is dependent on the current supply across the heat actuator and does not increase over time. Even extended time with a continuous current supply at the same level will not produce further additional displacement in the heat actuator.
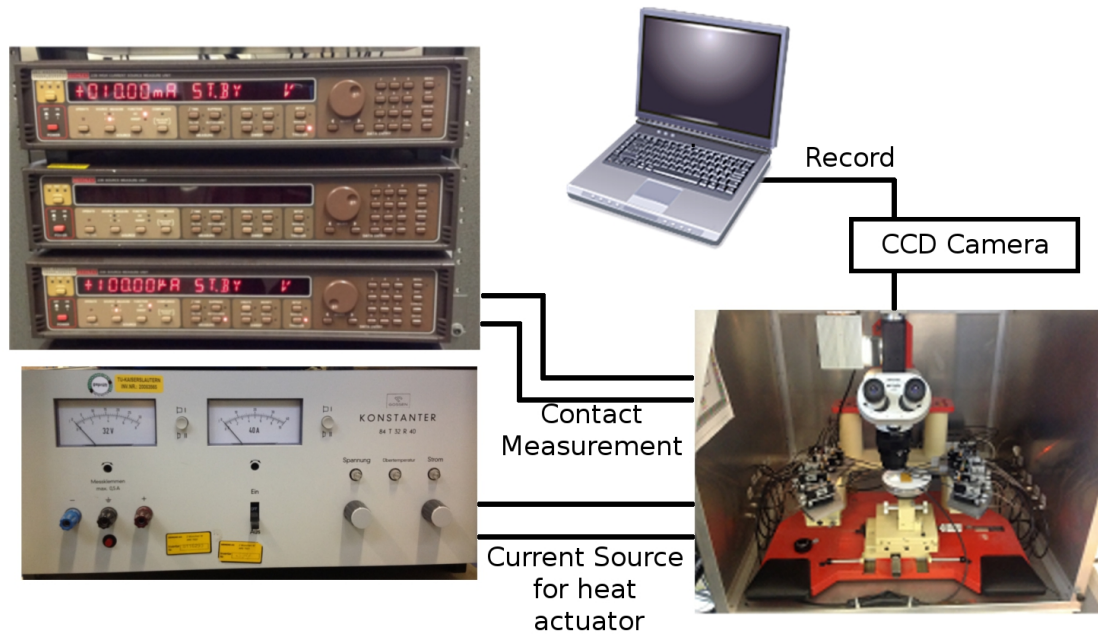
Figure 6.4.3.: Heat actuator measurement setup

(a) Heat actuators E & H direction movement **(b)** Heat actuator C & J direction movement
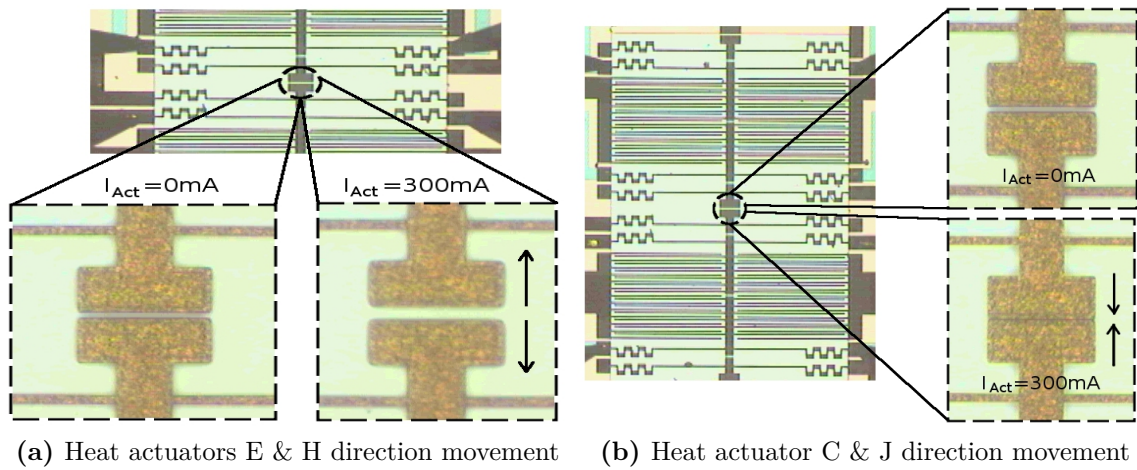
Figure 6.4.4.: Heat actuator actions
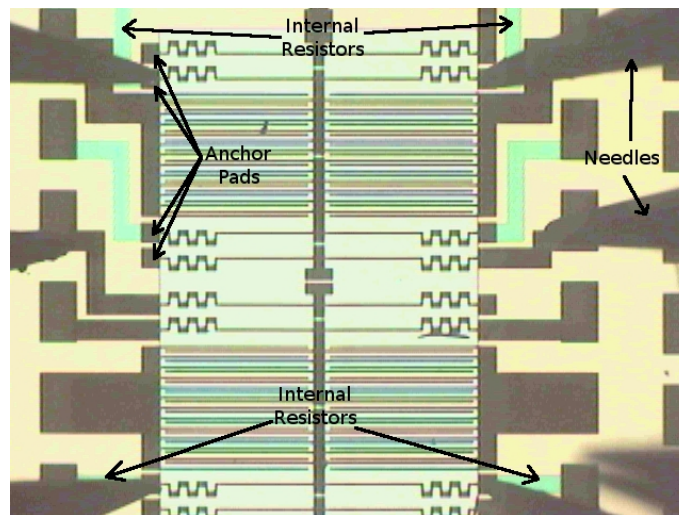
Figure 6.4.5.: The experiment setup of a single heat actuator without internal resistor

The heat actuators are evaluated under various conditions in the next sections. Four experimental setups were implemented for SPST switches. There were experiments involving a single heat actuator and a double heat actuator. These experiments were setup with and without internal resistors.

a) Single Heat Actuator without Internal Resistor

A single heat actuator arrangement involves a single actuator activated in each body mass. In the case of SPST switches, only heat actuators C and J were activated during the testing. Experiments were performed without using on-chip internal resistors. Three different samples were used for this experiment, BS1, BS3 and BS5. Figure 6.4.5 shows the needle of the micro-manipulator setup of the experiment. The needles bypassed the internal resistor and were in direct contact with the anchor pads of the heat actuators.

In this setup, the generated heat is produced by the resistance across the serpentine beam structure, which is around 5Ω. The difference in beam thickness will generate forces that create movement at the centre point of the beam structure. Several levels of electrical current were applied from $0mA$ to $300mA$ in $50mA$ steps. The results show that even at $300mA$ of current, the contacts of the signal line still did not make contact. Even if the gap was small there was no physical contact made. The switch is able to make physical contacts when the current at $310mA$ was applied, however at this point, the serpentine suffers a permanent deformation in the structure due to the excessive current and heat generated. The chronological gaps produced by each level of current are shown in Figure 6.4.6.

(a) $I_{Act} = 0mA$

(b) $I_{Act} = 0mA$

(c) $I_{Act} = 100mA$

(d) $I_{Act} = 100mA$

(e) $I_{Act} = 200mA$

(f) $I_{Act} = 200mA$

(g) $I_{Act} = 250mA$

(h) $I_{Act} = 250mA$

(i) $I_{Act} = 280mA$
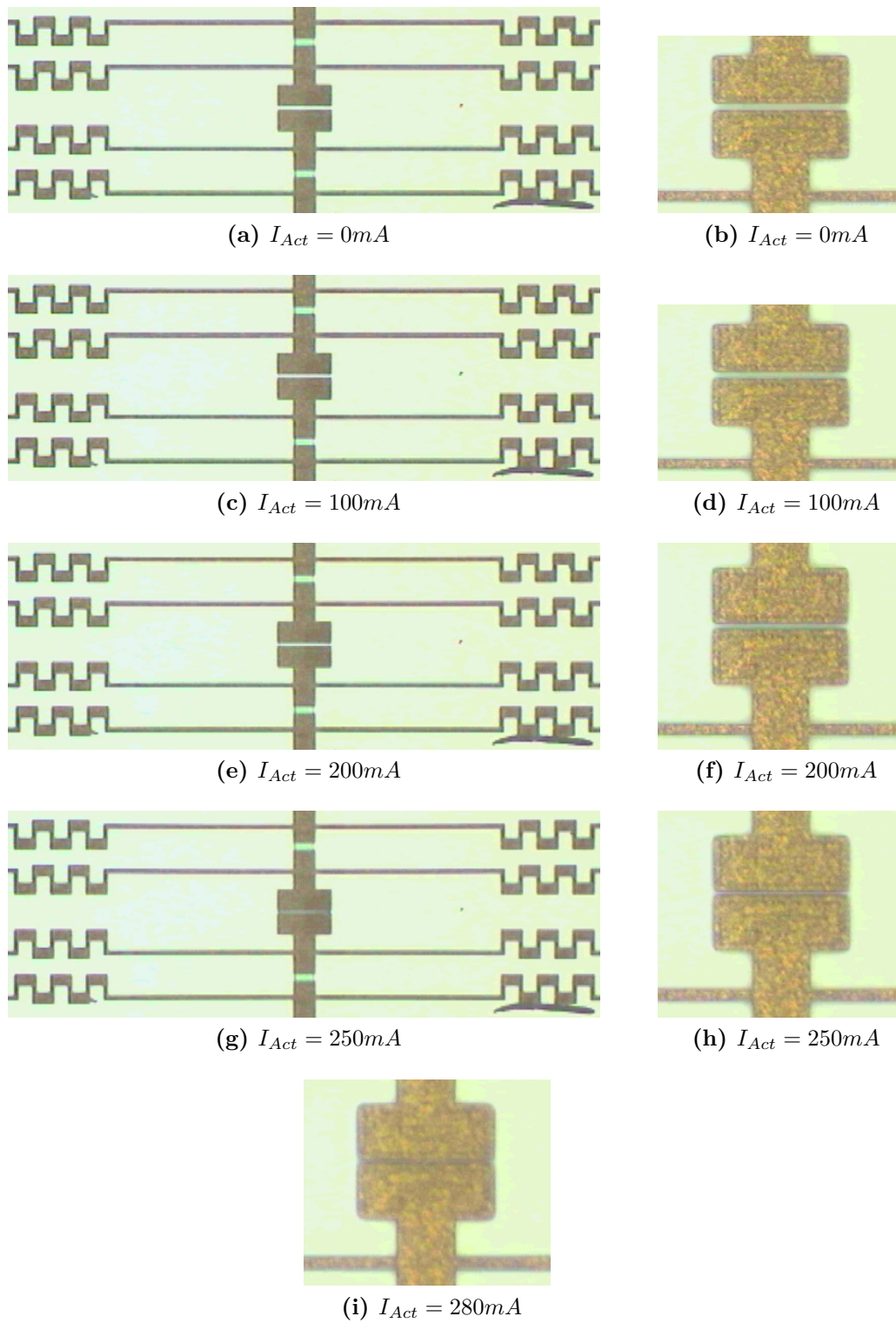
Figure 6.4.6.: Single heat actuator without internal resistance

b) Single Heat actuator with Internal Resistor

The second heat actuator arrangement was performed by applying the internal resistor to the chip. For a single heat actuator with internal resistor operations, the resistor will provide a local on-chip heat source for the heat actuator. In this experiment, samples with identification numbers BS2, BS4 and BS6 were used. The results show that the switch can be operated when current is applied at around $180mA$ and above. The local heat source has enhanced the ability of the heat actuator to produce higher deflection.

In this prototype, the internal resistors are built on each side of the heat actuators. Resistors R_{Int1} have a resistance of 150Ω each and R_{Int2} have a resistance of 230Ω each, however, only one resistor is used for each heat actuator during experiments. This is due to limitations of the power supply equipment, which restrict the maximum current at higher load resistance.

c) Double Heat Actuator without Internal Resistor

The third heat actuator arrangement is created using double heat actuator structures in a single body mass. SPST switch samples labelled DS1, DS3 and DS5 were used for this experiment. In the SPST switch, another serpentine structure with pads labelled B and K acted as the second heat actuator. The two heat actuators work simultaneously for each body mass. Heat actuators B and C generate movement for Mass One and actuator J and K for Mass Two.

In this arrangement the switching actions are produced at $250mA$. This is $60mA$ less than the actuator arrangement in a single heat actuator without internal resistor arrangement. The second heat actuator helps to generate more force so that less current is needed for switch actuation. The total resistance for both heat actuators was recorded at around 12Ω. The instantaneous power consumption for this setup was estimated at $0.75W$. Figure 6.4.7 shows the screenshots of the contact areas when various current levels were applied.

d) Double Heat Actuator with Internal Resistor

For this experiment setup, three SPST switch samples were used, labelled DS2, DS4 and DS6. The heat actuator operation using an internal resistor significantly improved the actuator's performance for switching purposes. When a switch is driven by double heat actuators with internal resistors, the switching current is reduced from $250mA$ to less than $150mA$. Similarly to the single heat actuator with the internal resistor arrangement, the obvious difference in actuator reactions is due to the presence of the internal resistor. This resistance generated more local heat in the actuator compared to the actuator without internal resistors. With a smaller current, more deflection can thus be produced.

(a) $I_{Act} = 0mA$

(b) $I_{Act} = 0mA$

(c) $I_{Act} = 100mA$

(d) $I_{Act} = 100mA$

(e) $I_{Act} = 150mA$

(f) $I_{Act} = 150mA$

(g) $I_{Act} = 200mA$

(h) $I_{Act} = 200mA$

(i) $I_{Act} = 250mA$

(j) $I_{Act} = 250mA$
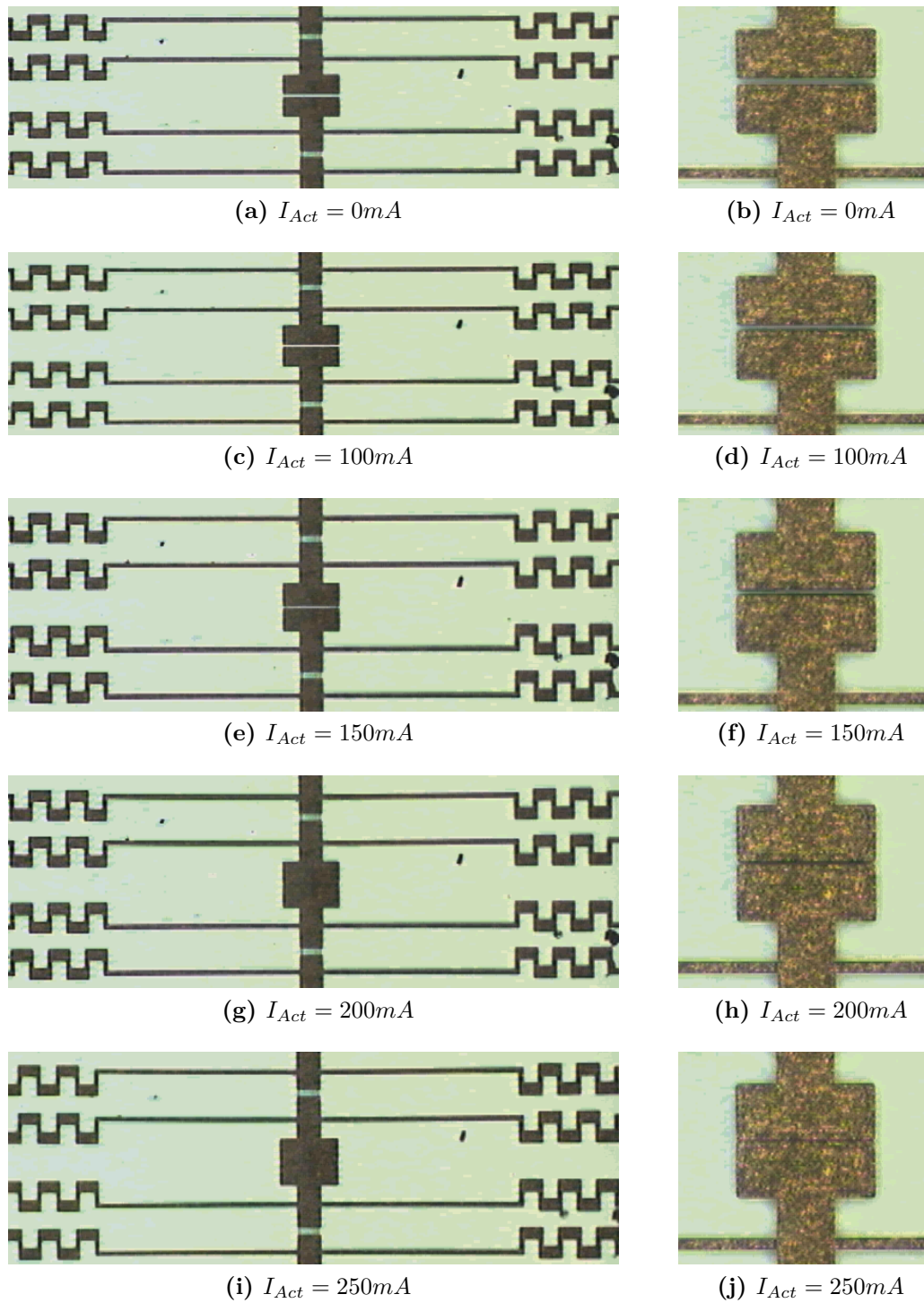
Figure 6.4.7.: Double heat actuator actions in various I_{Act} in an SPST switch of ISE-DC-MEMS

(a) $I_{Act} = 50mA$

(b) $I_{Act} = 50mA$

(c) $I_{Act} = 120mA$

(d) $I_{Act} = 120mA$

(e) $I_{Act} = 130mA$

(f) $I_{Act} = 130mA$

(g) $I_{Act} = 140mA$

(h) $I_{Act} = 140mA$

(i) $I_{Act} = 150mA$

(j) $I_{Act} = 160mA$
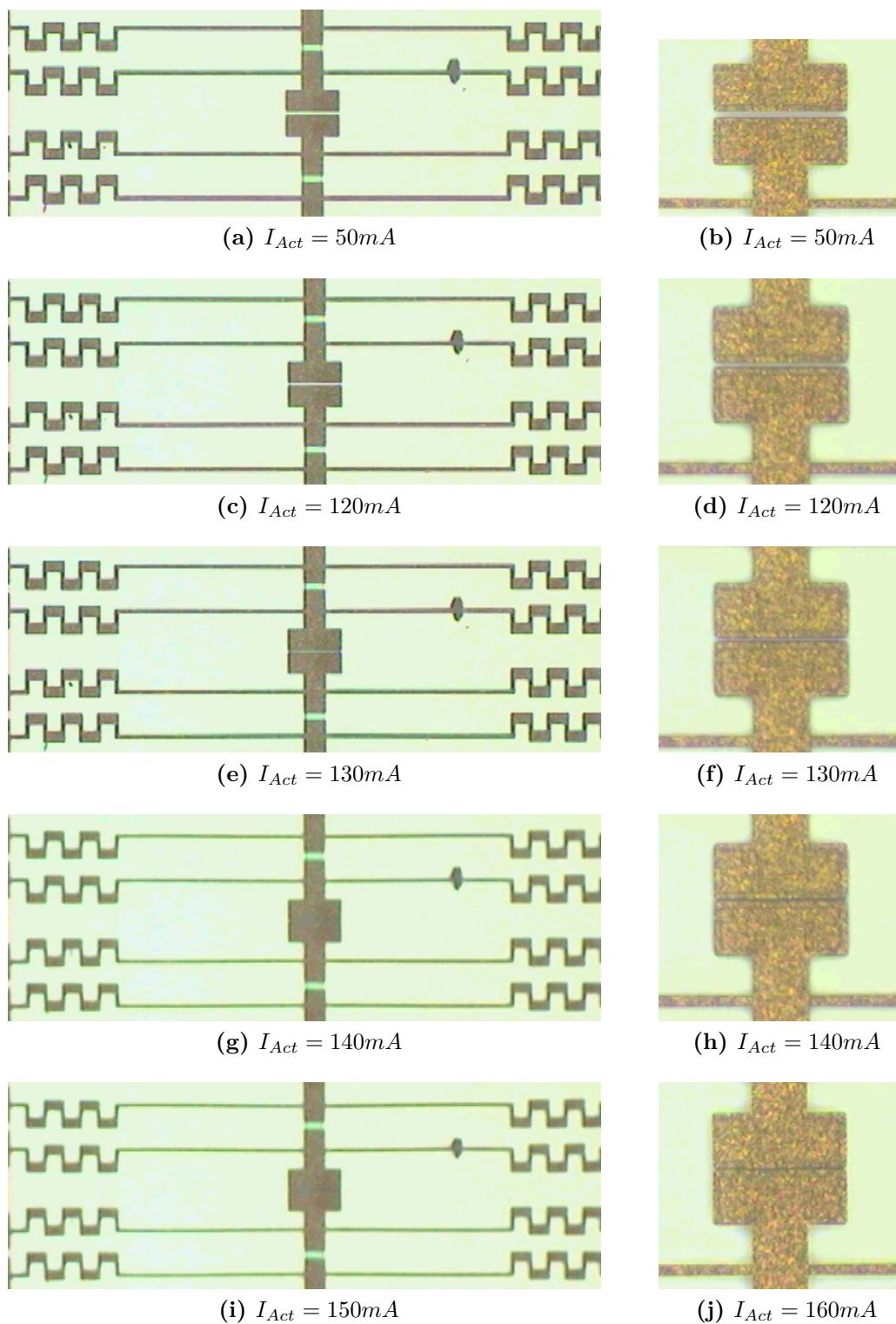
Figure 6.4.8.: Double heat actuator with internal resistance actions in various I_{Act} in an SPST switch of ISE-DC-MEMS

6.4.2.2. SPDT Heat Actuator

An SPDT MEMS switch has 6 heat actuator elements with two for each body mass. In contrast to the SPST design, the SPDT design does not include an integrated polysilicon layer for internal resistors. As shown in Table 6.2, the resistance value for each heat actuator is less than 6Ω. During the evaluation stage, an external resistor was connected in the series to increase the total resistance from the supply line. This is important in order to control the current and prevent burning the heat actuators. Resistor values in the range of 33Ω to 100Ω were used in the experiment.

Similarly to an SPST switch, the closing switch action for signal-in-out 1 can be controlled with heat actuators C and K and the self-repairing actions produced by actuators E and H. As for signal-in-out 2, heat actuators I and P were used for closing the switch action and actuators K and N produced movement in the opposite directions. The behaviours of all the heat actuators that were tested were consistent with the design geometry of heat actuators. This makes the design easily reusable in future MEMS design applications.

a) Single Heat Actuator

Based on experiment results using samples BD1 and BD2, physical contact takes place when $350mA$ current is applied. The actuators start to show the visible movement when $50mA$ current is applied. The permanent deformations in the structure begin at current greater than $300mA$. The instantaneous power, P, of the heat actuator during operation can be estimated at $0.61W$ with current value at $350mA$ and resistance at 5Ω.

Operation in this mode is not recommended since the current required for switching has reached the critical limit of the heat actuator. The permanent deformations in the heat actuators will shorten the switch lifetime.

b) Double Heat Actuator

In this experiment, SPDT switch samples taken from die D were used and labelled DD1 and DD2. When double heat actuators are applied, the contacts close when $220mA$ current is applied. The double heat actuation required $130mA$ less current to close the contacts compared to single heat actuation. The total resistance of both heat actuators was recorded at 12Ω and the instantaneous power was estimated at $0.58W$. This arrangement is better than the previous one, since it works below the critical current limit of the heat actuator. This will ensure a longer lifetime for the ISE-DC-MEMS switch.

ISE-DC-MEMS type	Heat actuator arrangement	On-board resistance resistance	Heat actuator current [mA]
SPST	Single	χ	310
	Single	$\checkmark$	180
	Double	χ	250
	Double	$\checkmark$	150
SPDT	Single	χ	350
	Double	χ	220

Table 6.23.: Summary of the heat actuator current required for turning on the switch from various heat actuator arrangements

Summary

The switching action of ISE-DC-MEMS switches using heat actuators is summarised in Table 6.23. This table gives information about the setup conditions of the ISE-DC-MEMS switches and heat actuator current at the point in which the on-state of the switch was achieved.

In the SPST switch driven by a single heat actuator, the on-state can be achieved at $310mA$. When a double heat actuator is applied, a lower current is needed at $250mA$ to turn the switch to the on-state. This is due to the greater force produced by the double heat actuator compared to a single heat actuator, which thus requires less current to turn the switch to the on-state.

The next observation in SPST switches was made in the heat actuator arrangement with and without on-chip resistance. The implementation of on-chip resistance generated more heat on the dice. This additional heat creates greater expansion at the lower current level. The switch that used a single heat actuator with on-chip resistance required $180mA$ to achieve on-state condition and the switch using double heat actuators with on-chip resistance required $150mA$. This data shows that the on-chip resistance helps to reduce the required heat actuator current, however, the heat produced by this on-chip resistance was distributed not only to the heat actuator but also all over the dice. A proper study of thermal management is required to reduce the thermal effect on the dice before this on-chip resistance can be implemented with the heat actuator.

In the SPDT switch for ISE-DC-MEMS, only the single and double heat actuation effects could be observed. When using a single heat actuator, the SPDT turns to the on-state when the heat actuator current is set to $350mA$. The required current is slightly higher compared to the SPST switch with the same configuration. This is because the SPDT mass is greater and thus requires more current to produce the same action. The same trend is shown in the double heat actuator arrangement which it required much lower heat actuation current than the single heat actuator arrangement in the SPDT switch.
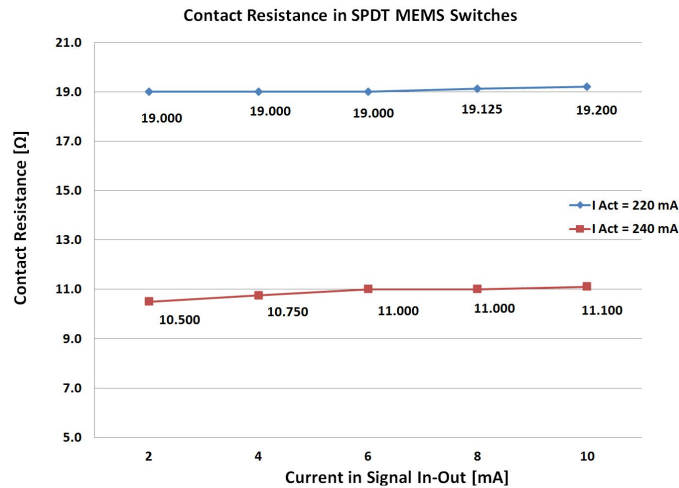
Figure 6.4.9.: Contact Resistance vs. I_{Act}

6.4.3. Contact Resistance in MEMS Switches

In DC MEMS switches the contact resistance is influenced by several factors. One of the main factors is the actuator force that is applied to the contact area. In the case of the heat actuator, the sum of the forces is determined by the electrical current applied in the actuator. This section will discuss the influence of current on the heat actuator and in the signal line towards contact resistance.

The current's influence on the heat actuator could be seen when several current levels were applied to it. In the SPDT switch with a double heat actuator arrangement using samples DD1 and DD2, the physical contact began at $I_{Act} = 220mA$. The contact resistance was recorded at around 19Ω. When $I_{Act} = 240mA$ is applied, the resistance dropped to the region of 10Ω. These measurements include offset resistance sourcing from wiring, equipment offset and contact resistance from micro-manipulator needles. Figure 6.4.9 shows the graph of contact resistance in the SPDT switch with various I_{Act}.

In the first prototype, the signal line structure shares the same geometry design as the heat actuator, however, the arrangement of these structures labelled G and F are similar to the heat actuators that are intended for self-repairing. In this condition, electrical current flow in the signal line during the on-state will have a negative impact on contact resistance. For a small current signal less than $10mA$, the negative effect is not really significant, as shown in Figure 6.4.9. Only an average 1% of resistance increase is recorded, however, experiment results show in the event that a bigger signal current (I_{Sig}) between $10mA$ to $50mA$ were applied, there would be significant increases in the contact resistance of the switch. Figure 6.4.10 shows the contact resistance of an SPDT MEMS switch with various I_{Sig} is applied. A 60% resistance increment was recorded between $10mA$ and $50mA$ for the actuator that supplied $220mA$. As for $I_{Act} = 240mA$, the contact resistance was increased to over 100% with similar I_{Sig}.
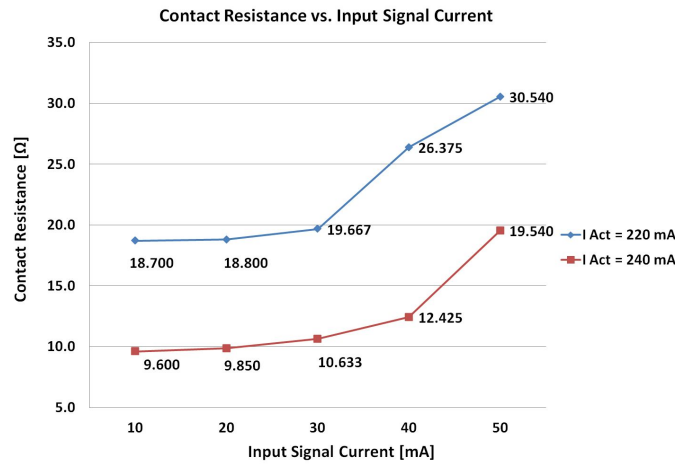
Figure 6.4.10.: SPDT-Contact resistance with higher I_{Sig} applied.

This negative effect can be turned to good use in the switch with a simple design fix. The arrangement of the signal line actuator follows the similar structure of the heat actuator for switching action. In a higher signal current, these active structures will bend towards closing the switch contact. This will add more forces to the switch contact and further help to reduce contact resistance.

6.4.4. Maximum Current for Heat Actuator and Signal-In-Out

The heat actuators and the signal lines share a similar design geometry. Based on several runs of experiments using SPDT switch samples taken from dice B and D labelled BD1, BD2, BD3 and BD4, the heat actuator worked well for current under $300mA$. Below this range, the serpentine structure exhibits similar elasticity and structure integrity in frequent switching actions. There was no sign of structural fatigue recorded during the experiment.

The serpentine structure shows permanent deformation when $300mA$ to $350mA$ current is applied. At this stage, the structures are still elastic and can make further switching repetition actions, but have lost their original shape. The gap in the capacitive sensors also changes due to this permanent deformation. Figure 6.4.11a shows permanent deformation in a heat actuator. It shows the gap in the contact which was changed, losing its original shape.

If excessive current is applied to the heat actuator structure, structure destruction may occur as shown in Figure 6.4.11b. The maximum current that can be applied in this actuator is from $350mA$ to $400mA$ before it is burned. In order to preserve the structure's integrity and to ensure higher reliability, the working current range is set at less than $300mA$.

The signal-in and out paths have identical structures and they are almost similar to the construction of the heat actuator. The difference between the signal paths
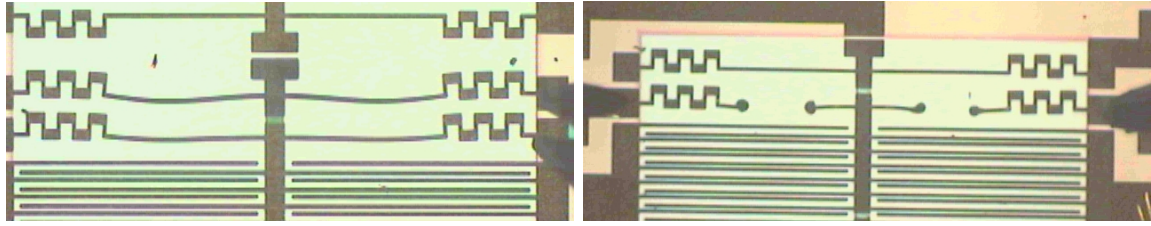
(a) An example of permanent deformation in the heat actuator when the applied current is over 310mA

(b) An example of heat actuator burned in case of excessive applied current

Figure 6.4.11.: Heat actuators in various conditions of excessive applied current

and the heat actuator is that the signal path has a contact structure attached to it. Based on the experiment, the switch can handle current of less than $50mA$ without any reliability problems. When the current applied is more than $50mA$, the possibility for stiction to occur is increased. Discussion of this matter can be found in Section 6.5.1.

6.5. Self-x Features in MEMS Switches

6.5.1. Self-repair Function

The self-repair function in MEMS switches is the ability of a switch to repair or recover from functionality errors. A typical MEMS device has a failure risk in the form of stiction. In these DC MEMS switches, two areas that can be described as high risk areas for stiction are the contact area and the electrostatic actuator area. The latter problem was addressed in detail in Section 6.4.1.

A stiction event in the contact area can be replicated by applying high current in signal lines. During several tests for measuring the effect of a high current signal on contact resistance, there are several symptoms of stiction in the contact. An SPDT switch labelled DD1 and DD2 was used. Two levels of stiction were encountered. The first type was a normal stiction which takes place when I_{Sig} is between $50mA$ to $100mA$. For this stiction type, a self-repairing action using heat actuators E & H in the SPST design are able to break the stiction force. In SPDT switches, the self-repairing function is provided by heat actuators in their respective body mass. In Body Mass 1, self-repair can be executed by heat actuator in Ports E and H. These actuators will produce movement in the opposite direction to closing the switch actions. In Body Mass 2, heat actuators K and N will do a similar job. In both designs, a single heat actuator is able to break a typical stiction force.

The second type of stiction in the contact area is called 'hard stiction'. It normally occurs when there is high I_{Sig} with more than $100mA$ applied. At this high current,
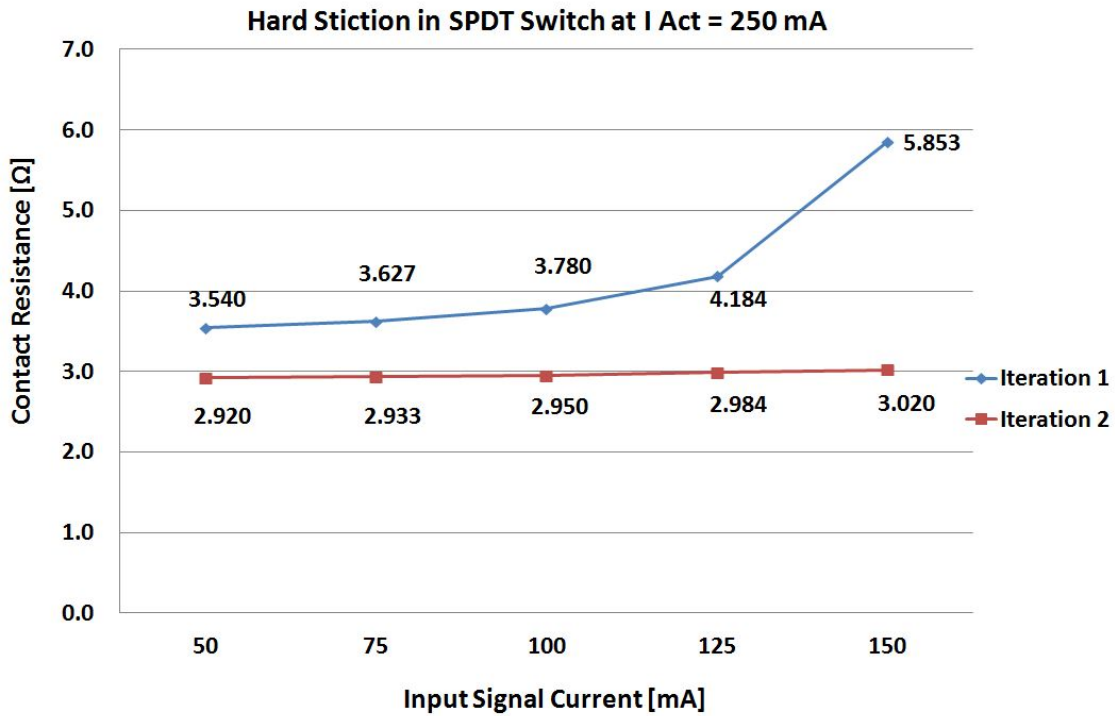
Figure 6.5.1.: Example of hard-stiction case during data measurement

the stiction force turns to a micro-welding state in the contact area. The phenomena can be shown in one series of iteration data in an SPDT MEMS switch in Figure 6.5.1. In this experiment, a linear sweep of I_{Sig} from $50mA$ to $150mA$ is applied to the contact with $25mA$ per step at 2 seconds interval. The I_{Act} is set at $250mA$. In the first iteration, the contact resistances were recorded between 3.5Ω and 5.8Ω. At this point the switch still shows the expected behaviour during increments of I_{Sig} as discussed in Section 6.4.3, however, during the second iteration, a much lower range of resistance was recorded, at less than 3Ω. The contact remains intact after the current signal sweep is finished. In this case, the force from the self-repairing actuator could not break the contact. The hard stiction was developed at the contact area with a micro-welding effect due to heat generated on the gold layer melting and creating a strong bond between them.

The stiction event which took place in the electrostatic actuator can be recovered using the self-repairing function. Stiction normally occurs on a single beam and a small movement of the mass will release the stiction. Based on the experiment observation, the activation of a single heat actuator using $150mA$ will release the stiction in the electrostatic actuator fingers.

CA$[fF]$	**CB**$[pF]$	**L**$[\mu H]$	**R**$[\Omega]$
153.94	1.1215	1.4563	10.7682

Table 6.24.: Median value of equivalent circuit in SPDT switch in capacitive sensor under stiction

6.5.2. Self-monitoring Function

The self-monitoring function in an ISE-DC-MEMS switch is enabled by the capacitive sensor structure in each of the body masses. In the rest state, the sensor's gap is set at $10\mu m$. This gap will be increased to a maximum value of $15\mu m$ when the switch contact is closed. Based on the sample with a hard stiction problem, sample DD1, measurement in a self-monitoring sensor is performed and compared with the measurement data in the rest state. The comparison is made between measurement results in Tables 6.13 and 6.24. Here the capacitance CA value is reduced from $364fF$ in the original state to $153.94fF$ in the stiction state. The difference in capacitance shows the ability to implement self-monitoring. The possible additional readout circuit technique can be seen in Appendix D.
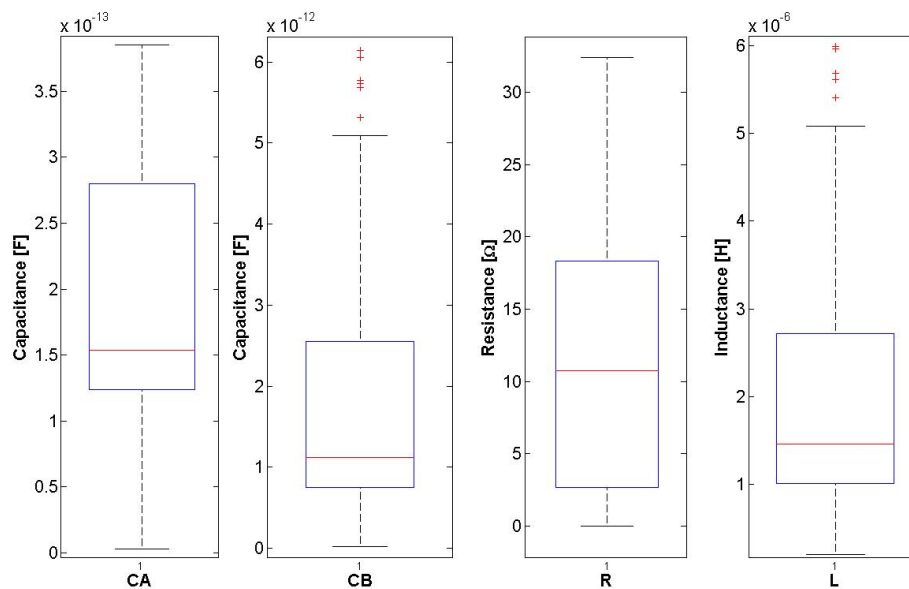
Figure 6.5.2.: Box-plot of SPST switch impedance measurement data for a capacitive sensor in the case of stiction
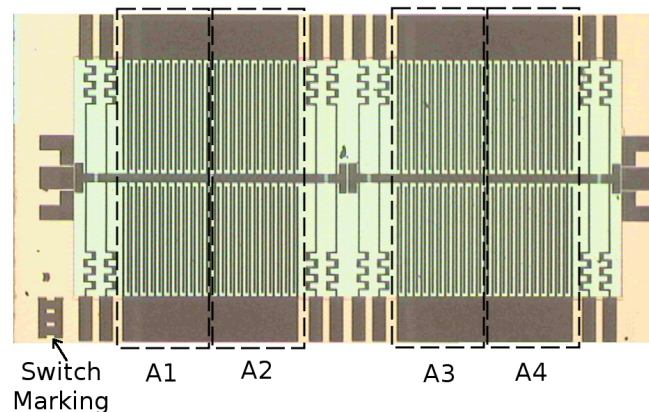
Figure 6.6.1.: Second generation of ISE-DC-MEMS switches layout and marking

6.6. Analysis of the 2nd Generation of ISE-DC-MEMS Switches

Submission of the second generation ISE-DC-MEMS switches mainly served two different purposes. Firstly, it was intended to provide switches that can be driven with lower voltage electrostatic actuation to at least 60V. This is to prepare these samples for chip on-board integration with a die from HV-CMOS technology for electrostatic actuation circuits. Three different switch designs with actuation voltage ranging from 20V to 80V were designed. Secondly, it was intended to determine the optimum design safety factor, S. The two S values of 1.5 and 2.0 were implemented in each of the designs. The initial characterisation activities were planned to verify these two properties.

The prototypes were received in the middle of November 2013. The dice were cut into smaller sub-dice and was specially marked with Roman numerals I, II and III. Each sub-dice contained two SPST switches with a different design safety factor, S. For easier identification, the switches were identified based on their positions on the chip. The switch that was closer to the mark was denoted as A and the other switch was denoted B. Each SPST switch had four separate electrostatic actuators and these structures were labelled 1-4 accordingly. Figure 6.6.1 provides a clear view of the identification of these structures. A total of 54 sub-dice were received, consisting of 108 switches, with every switch configuration having 18 switch samples.

6.6.1. Defect Analysis in ISE-DC-MEMS Switches

A quick optical scan using a microscope in the PM5 wafer probe revealed a major flaw in the outcome of the second prototypes. There were structural failures in most of the switch dice. Only 26 switches arrived in good condition from a total of 108 switches received. Figure 6.6.2 shows the pass and defect distribution of the
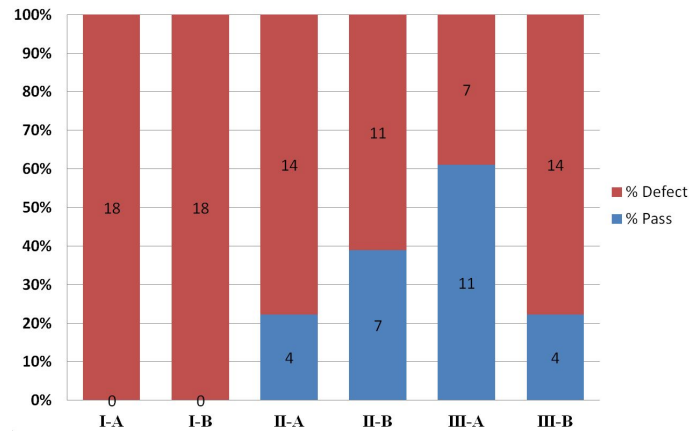
Figure 6.6.2.: Pass and defect percentage for second prototype ISE-DC-MEMS
switches

switches. A 100% failure rate was recorded for the Type I switches. Of the Type
II-A switches, only 22% were in good condition and 38.89% for type II-B. A higher
output yield was achieved in Type III-A switches with a more than 60% success
rate but Type III-B switches only yielded a 22% success rate. The low output yield
required an immediate investigation to identify the root cause of the problem.

The investigation continues by identifying the part of the switches that has failed.
According to an optical inspection, the structure failure happened in the area of the
electrostatic actuators. Most of the failed electrostatic actuator structure appeared
to be fused together in an unreleased condition. Figure 6.6.3 shows examples of
the mentioned failure conditions. Structural failure in MEMS can be the result
of three possible sources, design error, manufacturing process error and handling
error. A design error factor can be eliminated in this case since the design has
passed the simulation test, and most importantly the design-rule-check (DRC) of
the MetalMUMPs process. Further analysis of the MEMS will try to identify which
of the other two sources the problem fits.

After identifying the affected part of the MEMS switch, a statistical evaluation is
performed in order to understand the nature of the failure. In each failure switch,
there might be single, double or more electrostatic failures. The next analysis was
performed to determine which part of the electrostatic component is affected the
most. There are four electrostatic actuators in each mass labelled from 1 to 4.
Figure 6.6.4 shows the distribution of the electrostatic actuators in switch Type
I based on their locality. The Type I switches recorded a 100% failure rate and
the statistics show that in the TypeI-A switches, 90% of the failure happened in
actuators A1 and A4. Actuators A2 and A3 have a failure rate of less than 30%.
A similar trend was recorded for the Type I-B switches, with a failure rate of over
90% in the electrostatic actuators B1 and B4, and an approximately 80% success
rate in actuators B2 and B3.
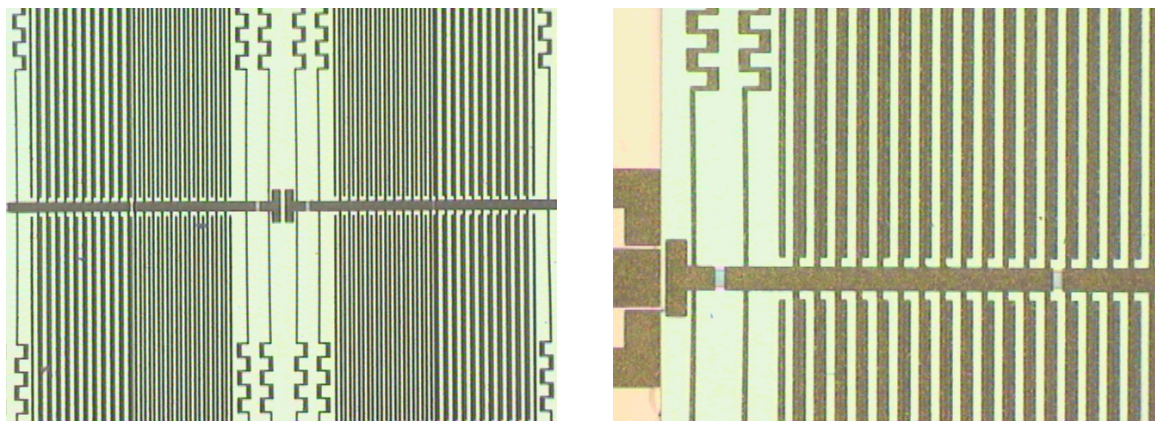
Figure 6.6.3.: Examples of failed electrostatic actuators in ISE-DC-MEMS switches

The same evaluations were also performed in the other types of switches. In Type II switches, the trend was similar, where electrostatic actuators 1 and 4 had a lower rate of success, as shown in Figure 6.6.5. In the A type switch, a better success rate was achieved in these two areas, of around 30%. Actuator A2 had a success rate over 90% and A3 had success rate over 70%. Type II-B showed a little improvement, with an approximately 50% success rate in actuators B1 and B4, and a higher success rate in B2 and B3 at around 70% to 80% success.

Figure 6.6.6 shows the failure distribution in Type III A and B switches. In the A1 actuator almost 80% of the switches were in good condition with 70% recorded in A4. For actuators A2 and A3, a success rate of about 90% was recorded. The same trend was observed in the III-B switches where actuators B1 and B4 had a lower success percentage compared to actuators B2 and B3. The B1 actuator had a 60% pass rate and B2 had 50%. In the B2 actuator, around 90% was in good condition and 80% in the B3 actuator.

Based on these results, the same trend in failure locality can be seen in all switches. A higher percentage of failure was recorded in actuators 1 and 4 than actuators 2 and 3. These structural defects were correlated with the size of the switch and the resonance frequency of the switch. This is because a higher resonance frequency in the switches resulted in lower structural failure rates.

After identifying the distribution of the failure localities, a closer look was taken to find any peculiar pattern in the structures. Special attention was paid to metal cuts in between the two electrostatic structures. Two types of imperfections were identified, based on the optical inspection. There was a completely missing metal cut between the two electrostatic actuators, as shown in Figure 6.6.7. This defect is related to manufacturing process error, for example during the process of etching the sacrificial layer.

Secondly, there appeared to be a larger metal cut than that originally intended. Figure 6.6.8(a) shows an example of these imperfections. The nitride and polysilicon layers were wider in the defective samples than in the normal samples. The initial

(a) I-A

(b) I-B
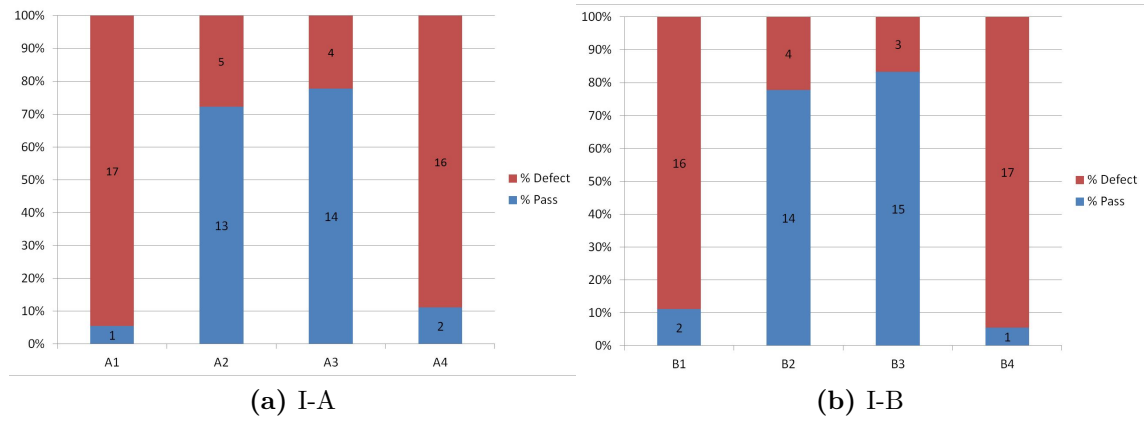
Figure 6.6.4.: Statistical distribution of electrostatic actuator failure in Type I switch

(a) II-A

(b) II-B
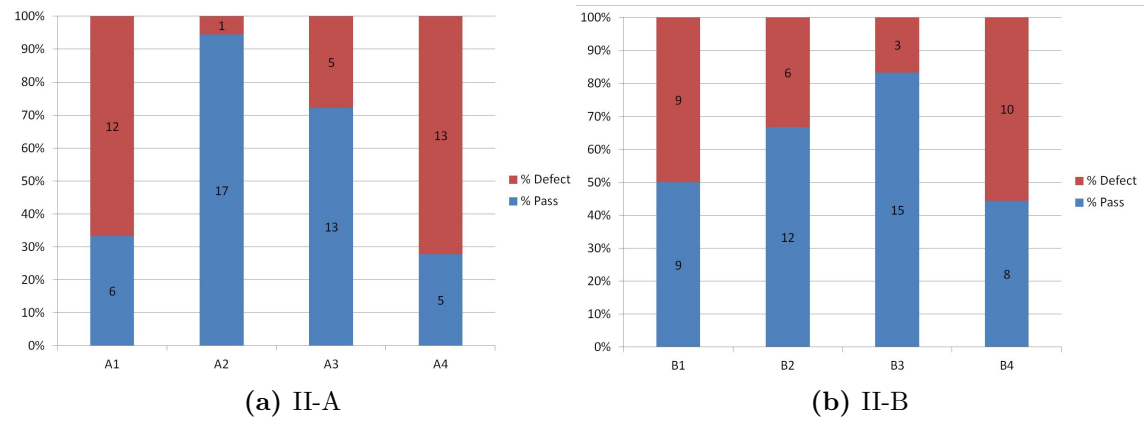
Figure 6.6.5.: Statistical distribution of electrostatic actuator failure in Type II switch

(a) III-A

(b) III-B
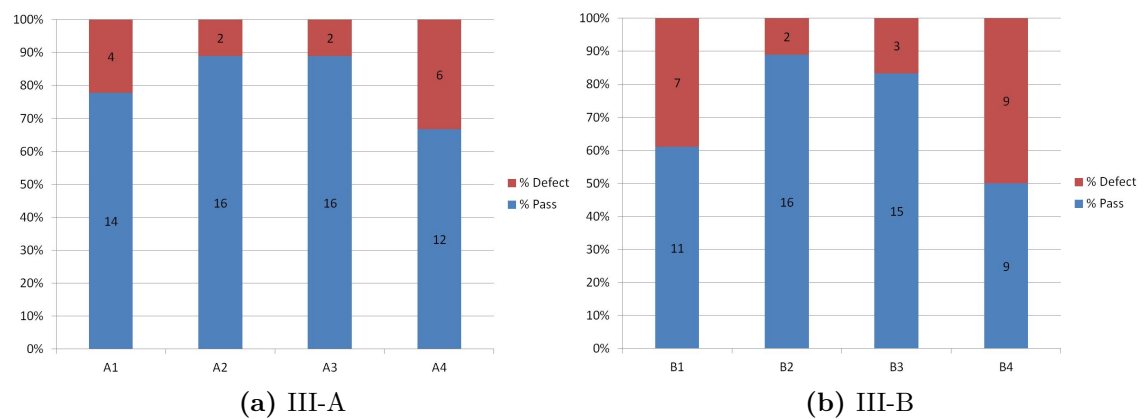
Figure 6.6.6.: Statistical distribution of electrostatic actuator failure in Type III switch
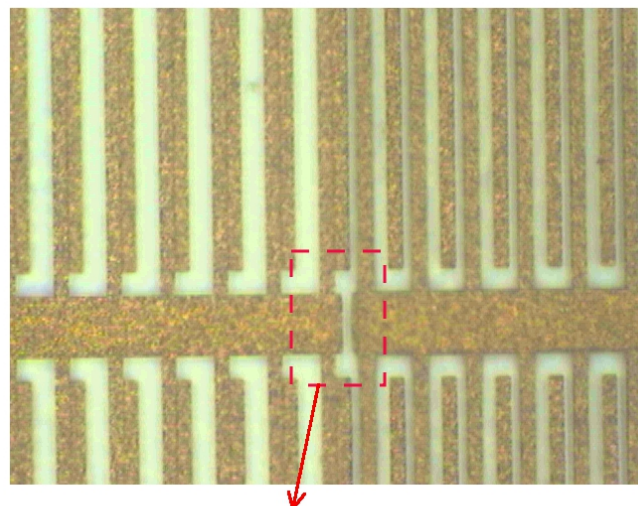
Figure 6.6.7.: A completely wash away metal cut in ISE-DC-MEMS switches

conclusion was that it might be due to manufacturing process error, however, in some of the samples, there was a wider metal cut but at the same time misalignment between the two masses that were supposed to connect. This misalignment suggested that the metal cut had broken in two. A structure can be broken during either the manufacturing process or the handling process. Figure 6.6.8(b) shows an example of misaligned structures.

There was one more peculiarity found in some of the samples. In the area of electrostatic actuator, gel-like residues from the process appeared to be sticking amongst the comb structure. Although the residue does not appears harmful to the structure, it may prevent its mobility during switching actions. Figure 6.6.9 shows an example of this finding.

An inquiry was made to Europractice for further investigation of the breakage. The response was that no other complaints had been received from other participants of the manufacturing run. This rules out manufacturing process error and leaves the handling process as the source of breakage. The investigation began by comparing the design parameters between the first and second generation ISE-DC-MEMS switches. The second generation has relatively larger movable structures than the SPST switch in the first generation. This was to achieve lower switch actuation voltage. At the same time the resonance frequency of the structures was also reduced. Table 6.25 shows a comparison of the area and resonance frequency for SPST switches by taking the first generation (V1) as the reference point. According to the table, the second generation has increased its size by a factor of 1.41 or more. The second generation has a lower resonance frequency with a factor 0.72 or less. In conclusion, the design of the second generation has become less robust than the first generation, thus make it susceptible to breakage in the handling process.

(a) Wider metal cut

(b) Misalignment between the masses
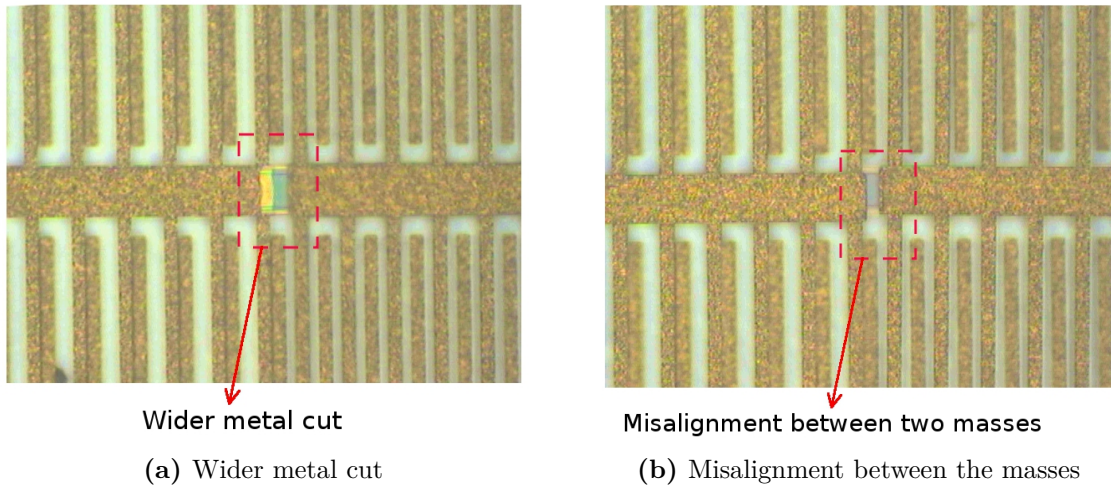
Figure 6.6.8.: Imperfect metal cut in ISE-DC-MEMS switches
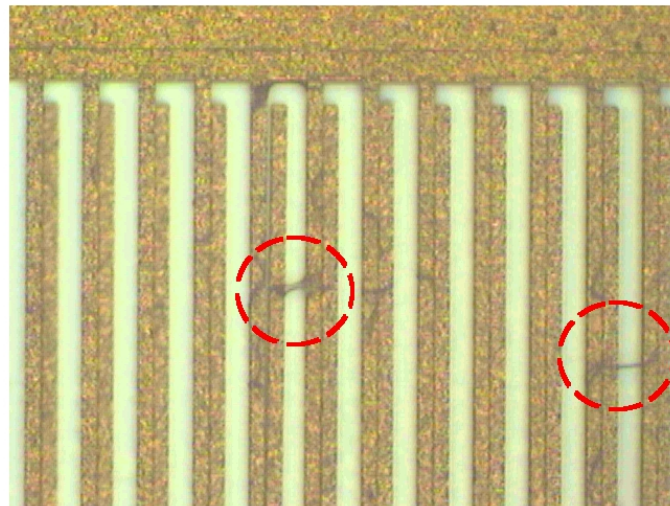
Figure 6.6.9.: Gel-like residue in electrostatic actuator form

	Area	Factor	Resonance Frequency	Factor
V1	5.11	1	6.4269	1.00
I-A	12.00	2.35	1.8584	0.29
II-A	9.25	1.81	2.7174	0.42
III-A	7.20	1.41	4.6393	0.72
I-B	12.00	2.35	1.8861	0.29
II-B	8.00	1.57	2.9800	0.46
III-B	8.10	1.59	4.1995	0.65

Table 6.25.: Comparison of area and resonance frequency factor between ISE-DC-MEMS switch of first and second generations

6.6.2. Evaluation of the S factor

Despite many failed samples in the second prototypes, S-factor determinations can still be characterised. Testing was undertaken using a similar setup as that in Figure 6.4.1. The first set of tests are called the 'stiction initiation experiment'. This was performed to determine the behaviour of the electrostatic actuator fingers under electrostatic force. The actuation voltage that moved the masses will be recorded until the stiction takes place in the structure. This should give the information about the minimum voltage that can initiate stiction in the structure, however, the experiment provided no information whether the switch made physical contact with the switch contacts since only one mass was activated.

The Keithley 238 is used as a programmable voltage source for electrostatic actuators. The voltage source was programmed to sweep from 0-110V or stop when stiction occurred. It has an equivalent length of T_{On} and T_{Off} at 2 seconds in 2V increments for each step. The behaviour of the switches is recorded on a personal computer using a SONY-CCD camera which is connected to the microscope. Since the testing is destructive in nature, switches with only one defect in four electrostatic actuators were considered for initial testing. In this kind of switch defect, only one body mass is affected and the other is considered well built.

6.6.2.1. Stiction Initiation Characterisation

Table 6.26 shows the results of this stiction initiation experiment and their respective offset values. The results show that in Design $I - A$, stiction occurred when $28V$ was applied and for Design $I - B$ stiction occurred at $30V$. These values were lower than expected since the simulation results suggested a maximum value of $30V$ in Design I-A and $35V$ for Design $I - B$.

A similar pattern of results was recorded for Design II and Design III. For Design $II - A$ the stiction occurred at $40V$ and the simulation results indicated $51V$. In Design II-B, the stiction occurred at $46V$ and the simulation result suggested $59V$ of actuation voltage. Design $III - A$ recorded stiction at $68V$ and the simulation result gave $79V$ of actuation voltage. Finally, Design $III - B$ recorded stiction at $76V$ and the simulation result proposed an actuation voltage at $80V$.

These results clearly showed the expected pattern between two design safety factors, S in Design A(1.5) and Design B(2.0). The switch Design A has an S value set at 1.5 and Design B has an S value set at 2.0. The results show higher values of actuation voltage for stiction occurrence in Design B compared to Design A.

The actuation voltages for stiction occurrences possessed significant offset values when compared to the simulation results, however the optimized value for the safety design factor, S, cannot be determined based on this experiment result only. Further investigation is required to identify the root cause of this problem.

Switch Behaviour	I-A	I-B	II-A	II-B	III-A	III-B
Maximum Allowable Voltage$[V]$	30	35	51	59	79	91
Stiction Occurence Voltage $[V]$	28	30	40	46	68	76
Offset Value $[V]$	2	5	11	13	11	15

Table 6.26.: Offset value for stiction initiation experiment results

6.6.2.2. Electrostatic Actuator Gap Characterisation

The investigation of the samples continued to determine the reason for offset value found in the previous results. An educated guess was made about this offset voltage phenomenon, as was due to the gap in the actual electrostatic actuators, which might be smaller when compared to the designed model.

In order to verify this guess, detailed observation was performed on the perfect switch samples. In a perfect switch sample, all gaps can be measured and compared to the actual design. When doing this, the measurement was performed only on four designs since there was no sample available for the switch I design as shown in the statistics in the Figure 6.6.2. Figure 6.6.10 and Figure 6.6.11 show the maximum zoom in the contact area for Design $II - A$, $II - B$, $III - A$ and $III - B$.

After careful examination of these photographs, an initial conclusion can be drawn that the contact gap $G3$ was bigger than the actuation gap $G1$. This contradicted the original design in which these two parameters were set equally at $10\mu m$. These two gaps need to be constructed precisely since they played a major role in electrostatic actuator performances. During design and simulation phases, the $G1$ gap is expected to move $5\mu m$ in each mass and produce $10\mu m$ total deflection. This total deflection was enough to close gap $G3$ at the switch contacts and the rest of $5\mu m$ in $G1$ gap was enough to avoid any stiction in the electrostatic actuators. Since the manufacturing imperfection occurred in these critical areas, further investigation will be undertaken to verify this problem.

Since there is no scanning electron microscope or SEM equipment available in the ISE department, the measurements of the switch parameters must to be taken using simpler methods. Pictures were taken with the CCD camera, and then measured using pixel to pixel ratio. This method might not give the highest accuracy of measurement but good assumptions can be made.

Figure 6.6.12 shows the measurement points to determine the switch parameters. An educated assumption was made that the manufacturing variation most affected the condensed and high aspect ratio areas, such as the electrostatic actuator rather than the less condensed areas such single beams. Based on this assumption, the number of pixels that represent the width of beam $B1$ were taken as equivalent to the original design value. The other parameters were then determined using this reference ratio.
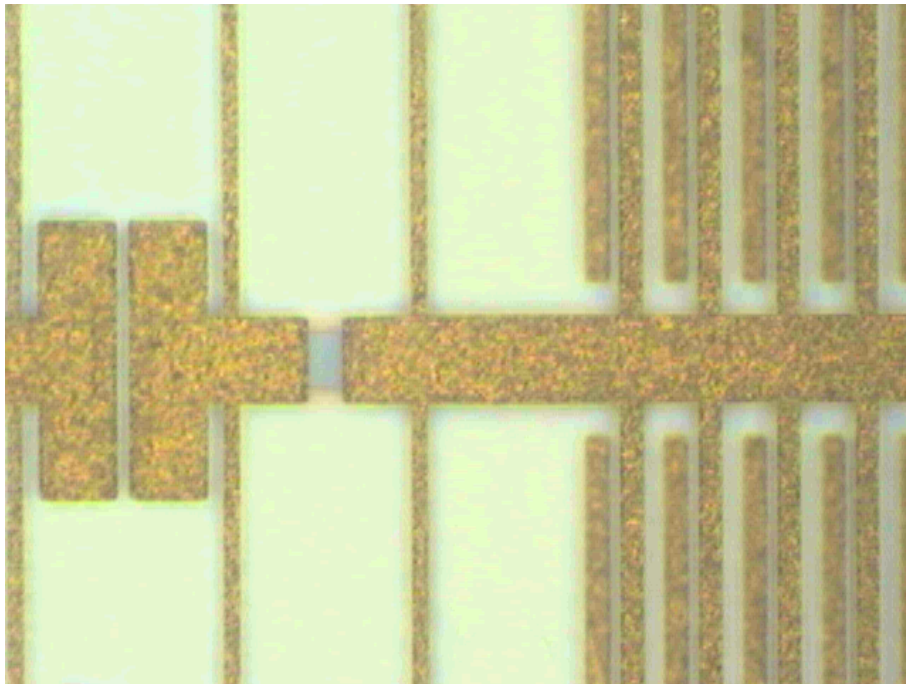
(a) Design II-A
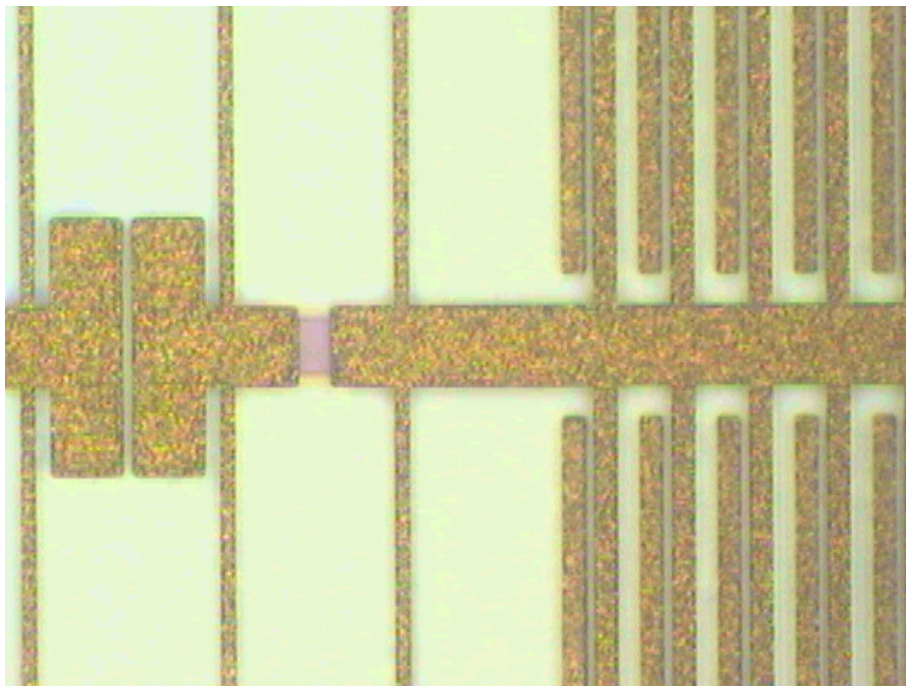
(b) Design II-B

Figure 6.6.10.: Zoom picture of Design II
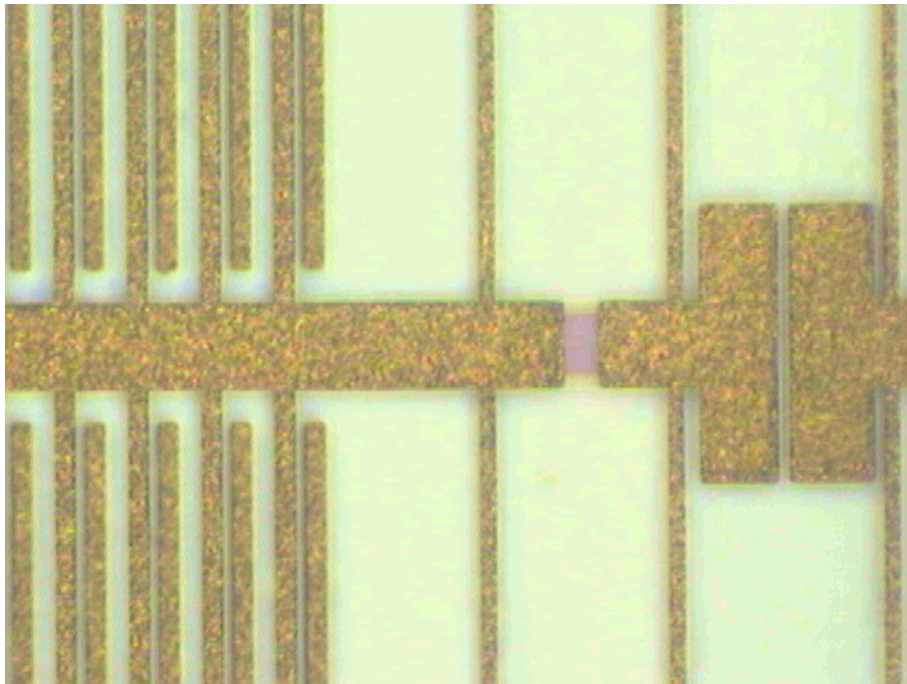
(a) Design III-A
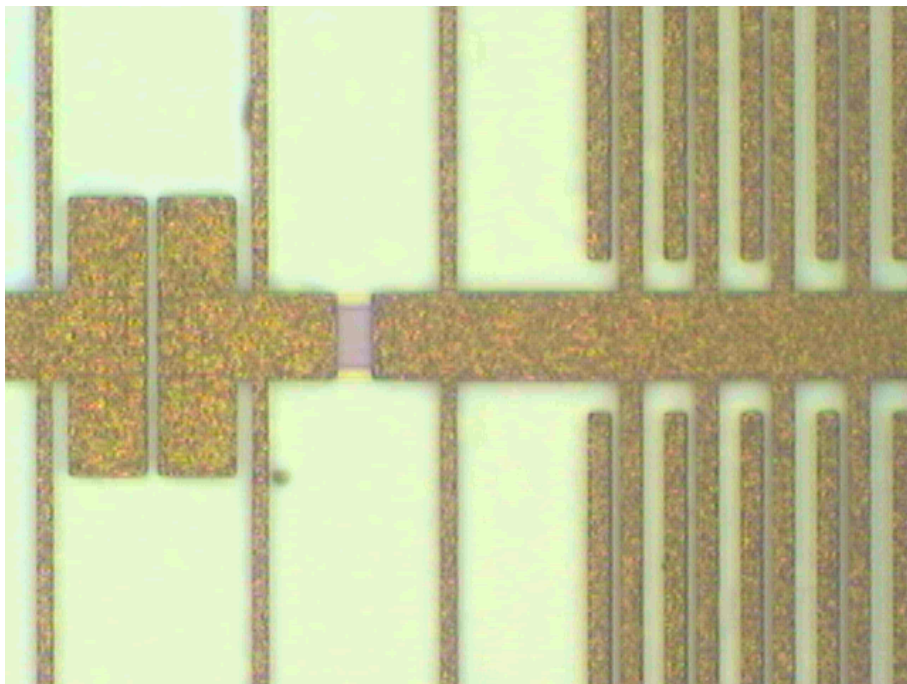
(b) Design III-B

Figure 6.6.11.: Zoom picture of Design III
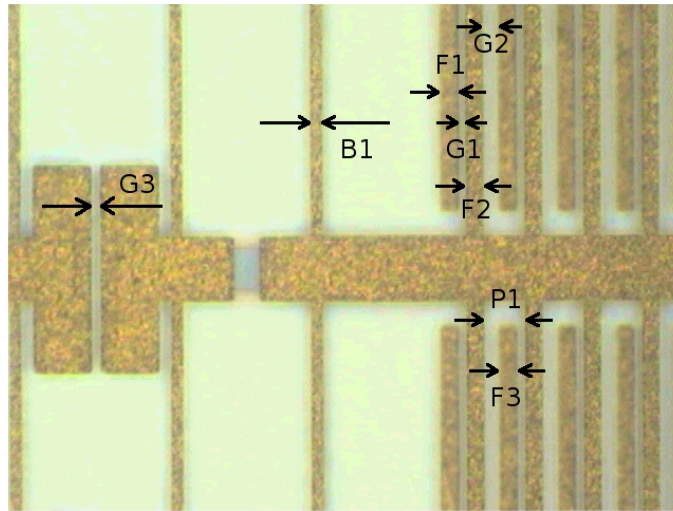
Figure 6.6.12.: Measurement points for pixel analysis

Switch Design	II-A		II-B		III-A		III-B	
Parameter	Est.	Des.	Est.	Des.	Est.	Des.	Est.	Des.
Beam, B1$[\mu m]$	10	10	10	10	10	10	10	10
Finger 1, F1$[\mu m]$	14.55	16	17	18	13.64	14	13.33	15
Finger 2, F2$[\mu m]$	15.45	16	18	18	13.64	14	15	15
Finger 3, F3$[\mu m]$	15.45	16	17	18	14.54	14	14.17	15
Gap 1, G1$[\mu m]$	6.36	10	5	10	4.55	10	4.17	10
Gap 2, G2$[\mu m]$	13.63	20	15	20	14.54	20	11.67	20
Gap 3, G3$[\mu m]$	8.18	10	7	10	6.36	10	5.83	10

Table 6.27.: Results of estimation switch parameter values

After carefully examining the pictures in Figure 6.6.10 and Figure 6.6.11, the results of estimation switch parameters values were populated and compared with the original values shown in Table 6.27. According to the estimation results, the gaps in the electrostatic actuators were smaller than the originally intended gap. Most of the $G1$ electrostatic gaps were reduced to almost 50% of the original value. In Design II-A, the estimated gap $G1$ was at $6.36\mu m$ which is almost half the original design value.

The manufacturing variations in the gap reported in Table 6.27 are the reason for the offset measurement in stiction occurrences as reported in Table 6.26. The gap G1 of 10um is used in simulations which contributed to the higher allowable actuation voltage. On the other hand, stiction occurrence measurements were performed with the smaller gap in the actual MEMS switch device which explains the lower voltage of stiction occurrences.

6.6.2.3. Effective Stiction Force Characterisation

Based on the data obtained earlier, analysis of the stiction point was extended with regard to the electrostatic force generated by the voltage. Since the gaps between the actual MEMS devices are not same as the simulation model, the only way to investigate and compare them is via characterising the electrostatic force during stiction.

During design and simulation stages, the S-factor was implemented to provide a withstanding allowance of maximum forces that can initiate stiction in a single finger of an electrostatic actuator. In this section, a comparison of effective output force is made between the simulation results and the measurements from the actual device for MEMS switch type $III - B$. Table 6.28 shows the comparison data for these two conditions.

In those comparisons, it was assumed that the simulation model and the actual prototype had the same length and width values. In the MEMS simulation model, the actuation voltage was set to $65V$, which produced a closed switching action. The $G1$ and $G2$ gap values were in the closed-switched position. The output forces for MEMS+ model was the final value after multiplication with safety factor S. In theory, no stiction will take place if the force applied to the finger is less than $20.7\mu N$.

The electrostatic gap characterisation presented in Section 6.6.2.2 gave valuable information in order to characterise the stiction phenomenon. Using the $G1$ and $G2$ gap obtained previously, the effective force during stiction can be calculated. In the experiment, stiction occurred at $72V$ in the actuator. The initial condition of the $G1$ gap is $4.17\mu m$ and the $G2$ gap is $11.67\mu m$. In this condition, the effective force applied in a single finger is $18.5\mu N$ which almost reaches to the maximum allowable value of $20.7\mu N$. In a dynamic state of the electrostatic actuator under $72V$, an assumption is made that the gap is reduced by $1\mu m$. In this case the $G1$ gap will become $3.17\mu m$ and the $G2$ value will become $12.67\mu m$. The effective output force in this condition will become $34.3\mu N$ and this is higher that the allowable force set by the design. This condition contributed to the occurrence of stiction.

This analysis has shown that in the actual MEMS device, finger structures were able to withstand the applied force and match the simulation results of MEMS model with a design safety factor S equivalent to 2.

6.6.2.4. Electrostatic Actuator Characterisation

The second prototype of MEMS switch design using MetalMUMPs once again turned out to be a failure. In the first prototype, the switch faced stiction failure due to a lack of structure stiffness. The second prototypes revealed manufacturing variations in producing required gap which is a critical factor in the lateral structure of electrostatic actuators. This problem was not observed during first prototype

| Switch | Parameter | | | | | | | Output |
	Length	Width	ε	S	Voltage	G1	G2	Force
	$[\mu m]$	$[\mu m]$			$[V]$	$[\mu m]$	$[\mu m]$	$[\mu N]$
MEMS+ Model*	720	20	8.85×10^{-12}	2.0	65	5.00	25.00	20.7
Actual Prototype	720	20	8.85×10^{-12}	2.0	76	4.17	11.67	18.5
	720	20	8.85×10^{-12}	2.0	76	3.17	12.67	34.3

* Worst case scenario

Table 6.28.: Comparison table of output force applied on a pair of electrostatic finger in switch III-B

investigation since it had always the same thickness and width in the electrostatic actuator. Furthermore, the beam structure is much smaller than in the second prototype.

Based on the results reported in Table 6.27, the MetalMUMPs technology could not produce the same gap values in the contact area and in between electrostatic actuators as intended in the original design. It is suggested that a larger gap was produced in the contact area than in the electrostatic actuator. These low precision results might be related to the aspect ratio between the width and length of the intended structure. As the gaps in the electrostatic actuators are smaller than the gaps in contact areas, it is impossible to close the gaps in contacts without causing a short circuit in the electrostatic actuator.

In conclusion, the lateral electrostatic actuator is not feasible in MetalMUMPs technology due to the inability to produce the gap between structures precisely. Many factors influence the precision output of the MEMS structures and that requires further investigation.

6.7. Discussion

Evaluation of the ISE-DC-MEMS switch was carried out with satisfactory results. Although the findings indicated that the electrostatic actuators failed to function properly, intensive study identified the root cause of the problem.

The high frequency measurement activities were improved with the implementation of external mathematical tools in evaluating the raw data. Originally, the impedance measurement results presented here were solely dependent on the circuit model and algorithm provided by the network analysers in HP4195A. The preferred switch model as proposed in Figure 4.9.6a on page 97 cannot be implemented, and instead the equivalent model as shown in Figure 6.3.2b on page 134 was used.

The models provided by HP4195A are limited with no potential to add more elements or values for improved results. For example, the datasets to determine the

R-L-C values where the resistance value that has been estimated via calculation and also DC measurement and it does not change over the course of the sweeping frequency. However, the process results from the raw datasets show that sometimes the resistance values were estimated at rather high values in the range of hundreds and thousands Ohms. An incorrect estimation in resistance does not reflect the actual resistance of the structure and impacts the results of other impedance elements in L and C. It would better to have the ability to feed in the certain impedance values in resistance prior to processing the rest of impedance values. This flexibility is currently lacking in the HP4195A network analyser.

The EIS Spectrum Analyser software provides an alternative way to further evaluate the electrical model of MEMS switches. The flexibility of adding our own electrical model in the fitting analysis opened the ability to establish the characterisation of parasitic elements in the MEMS switch. Based on the initial investigation presented above, the original electrical model for the electrostatic actuator component, consisting of CA, LA and RA as depicted in Figure 6.3.2a is accurate enough to represent the structure. A better electrical model was established for the signal-in and signal-out structure, which consists of six elements as shown in Figure 6.3.5b. The parasitic capacitance which is not modelled in the MEMS+ and Cadence simulation was identified and quantified. A similar model was implemented in the capacitive sensor structure and a better result was obtained in return. These results can be introduced back into the switch model and a comparison in performance can be demonstrated as reported in Chapter 5.

The new heat actuator structure has promising features with additional functionality. The special geometries applied in the design have produced the required deflections with minimal out of plane effect. Based on the experiment results, the on-chip resistance in the heat actuator can be eliminated since there is no significant contribution when these resistors were used during switching operations. The use of these resistors only leads to higher power consumption during switching actions and produces excessive heat on the MEMS dice. The excessive heat may hamper the performance of the switch in the long term.

The elimination of the on-chip resistance will provide two significant advantages. The low resistance across the structure, which is less than 3Ω will produce lower power consumption in the heat actuator device. The second advantage of this heat actuator is that no excessive heat is produced on the chip and thus eliminating the need for temperature management in the device. Further study of geometric optimisation of the heat actuator is required in order to reduce the current level required for switching. In order to classify as a low consumption device, this aspect requires immediate attention.

The investigation of the second prototype produced several new findings. The ISE-DC-MEMS switches with parameters of different values have demonstrated manufacturing variations in the actual prototype. This output deviation has correlation with the geometry of the intended structures. It appeared that the structure width

and length ratio has significant repercussions in the actual prototype. This output deviation meant that the electrostatic actuators did not function properly.

On a positive note, the safety design factor, S, as implemented in the second design, has effectively increased the stiffness of the finger structure in the electrostatic actuator. This was proven by the investigation reported above, which shows the ability of the finger to withstand the electrostatic forces until its maximum value. In conclusion, the proposed stiffness conformity test in the MEMS structure is useful and should be integrated in the design flow process of the MEMS device. This will improve the design and simulation result of MEMS devices which will help to reduce the overall R&D cost of for new MEMS products.

7. System Simulation of ISE-DC-MEMS Switches in Different Applications

7.1. Potential Applications of ISE-DC-MEMS Switches

Explorative research on the DC MEMS switch by the ISE research group is driven by the need for better solutions for switching applications in several specific areas. The DC MEMS switch exhibits the superior properties of low on-resistance and no leakage current when compared to transmission gates. In this chapter, four interesting applications that can benefit from these properties in their operations will be discussed.

7.2. Power Management Control for Digital Circuit

The ISE-DC-MEMS switch can be used in the power management of digital block circuits to achieve low power operation. It can be used to turn on and off entire digital circuits for better power management. The ability to handle high current and low power loss is due to low on resistance across the switch, make it suitable for this application, since, there is no leakage current in ISE-DC MEMS switch during off-state which avoids any consumption of power.

An inverter circuit is used as a simulation vehicle to demonstrate this potential. In this simulation the inverter consists of one NMOS transistor and one PMOS transistor. Both transistors are identical in size at $0.35\mu m$ in length and $10\mu m$ in width. Figure 7.2.1 shows a simulation circuit for this example. The inverter is controlled in three different ways using, an ideal voltage source, ISE-DC-MEMS-switch and transmission gate. In this simulation, the digital circuit is modelled as a capacitive load. The output inverter and the input voltage used to bias the inverter will be observed.

Figure 7.2.1 shows a comparison of inverter output changing from the off to on-states. Three different switch mechanisms were used in this simulation, namely ideal source,
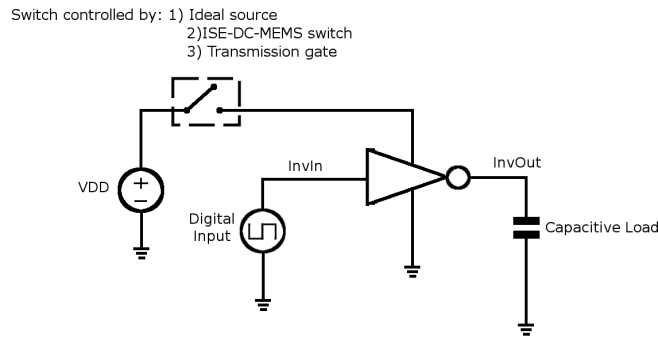
Figure 7.2.1.: A simulation circuit to demonstrate an inverter circuit controlled by different switch solutions

the transmission gate and DC-MEMS switch. The time taken to change the voltage from 0 to $2.97V$ was measured. When using the ideal source, the time required was recorded as $1.2251028ms$. The inverter response when using the DC MEMS switch is slightly longer when compared to the ideal source with a difference of $1.09ns$. Switching with the transmission gate recorded the worst performance, which it took $0.1801ms$ when compared to the ideal source performance.

A total DC isolation and minimal parasitic capacitance in DC MEMS switch provided better switching performances when compared to the transmission gate switch. This system simulation shows the ISE-DC-MEMS switch as a viable choice for the power control application in digital circuits.

7.3. Impedance Spectroscopy Measurement in Lab-on-Spoon

In the ISE research group, there is on-going research into the design and development of an autonomous data logger denoted Lab-on-Spoon for life assistance and food safety applications[96][1]. A network analyser chip, AD5933 [97], that is capable of producing an excitation voltage to a maximum frequency of $100kHz$ has been used for impedance spectroscopy measurement. The ISE-DC-MEMS switches can be used in the calibration of impedance spectroscopy measurements. Figure 7.3.1 shows the block diagram of the calibration and measurement circuit in a lab-on-spoon device.

In this setup, two SPDT switches can be used to switch the functions between measurement mode and calibration mode. In measurement mode, two of the switches will connect to the measurement electrodes. In calibration mode the switch will connect to the reference resistance. In this application, a low on-resistance switch is desired in order to ensure precise measurement.

---

[1]www.eit.uni-kl.de/koenig/gemeinsame_seiten/projects/LabonSpoon.html
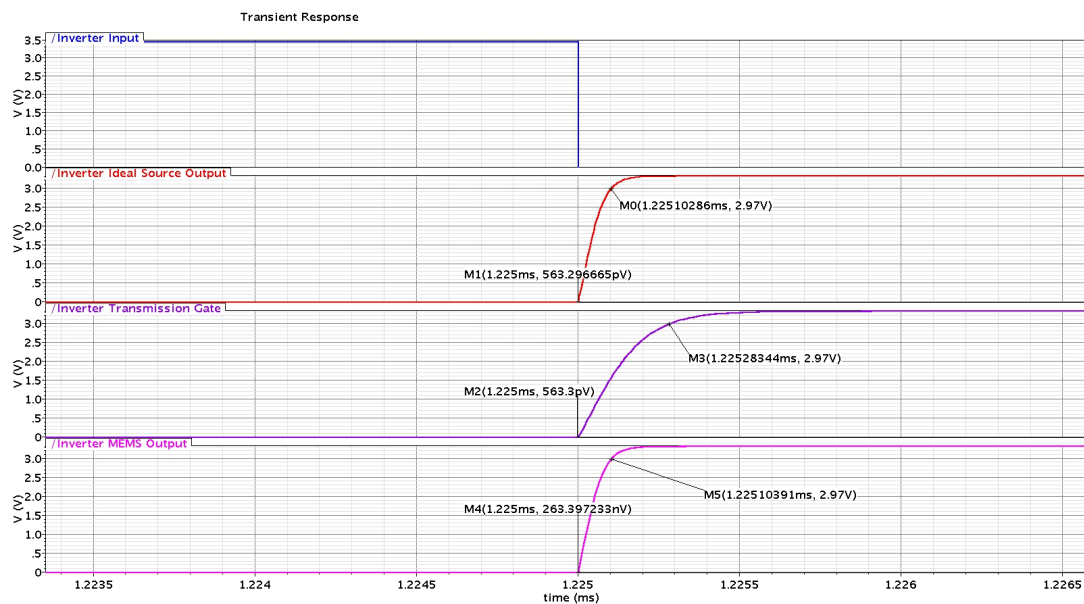
Figure 7.2.2.: Comparison of inverter output with capacitive load driven by ideal source, transmission gate or DC MEMS switch during the on-state

A system simulation has been performed to study the feasibility of using this application scenario with four ISE-DC-MEMS model SPST switches. The output of the two SPST switches is connected to become one SPDT switch. A transient analysis for a period of $150ms$ is set to show both cycles of measurement and calibration. The input sine wave with frequency set to $100Hz$ and amplitude at $3.3Vp-p$. The reference load is set to $1k\Omega$ while the measurement load is a resistor with a $10k\Omega$ value.

Figures 7.3.2 to 7.3.4 show the results of the system simulation. In this transient analysis, the simulation starts with the calibration cycle for the first $50ms$. In this period, the S2 and S3 switches are activated and connect the AC input signal with the reference load. After $50ms$, all four switches are turned to off-state for $20ms$. The measurement cycle for $50ms$ then starts where switches S1 and S4 turn to the on-state.

The voltage drop across the reference load during the calibration cycle can be seen in Figure 7.3.3 with the plot label 'Voltage Drop Across Reference'. 'No voltage drop' can be seen in the same figure with plot label 'Voltage Drop Across Load'. The peak-to-peak voltage is recorded at $3.28V$ with very small loss from the original $3.3V$. A similar response can be obtained during the measurement. Here the load is set to $10k\Omega$ which produced a smaller current as shown in Figure 7.3.4. In this figure, the current plots show the current response for every circuit condition in the off-state, calibration and measurement cycles. In this system simulation, the low R_{On} properties of the ISE-DC-MEMS switch have a significant advantage in high precision measurement circuits.
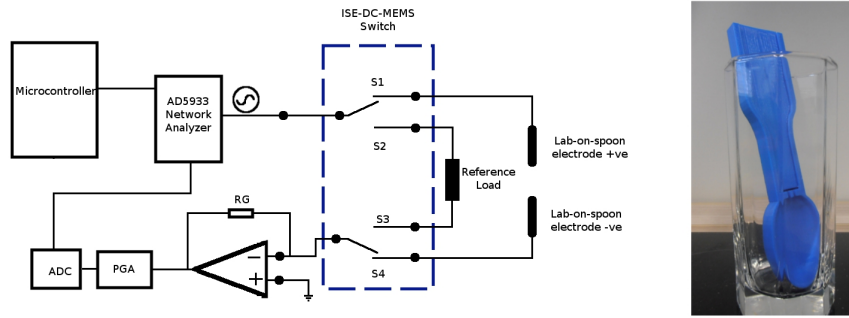
Figure 7.3.1.: Lab-on-spoon for impedance spectroscopy measurement using MEMS switches
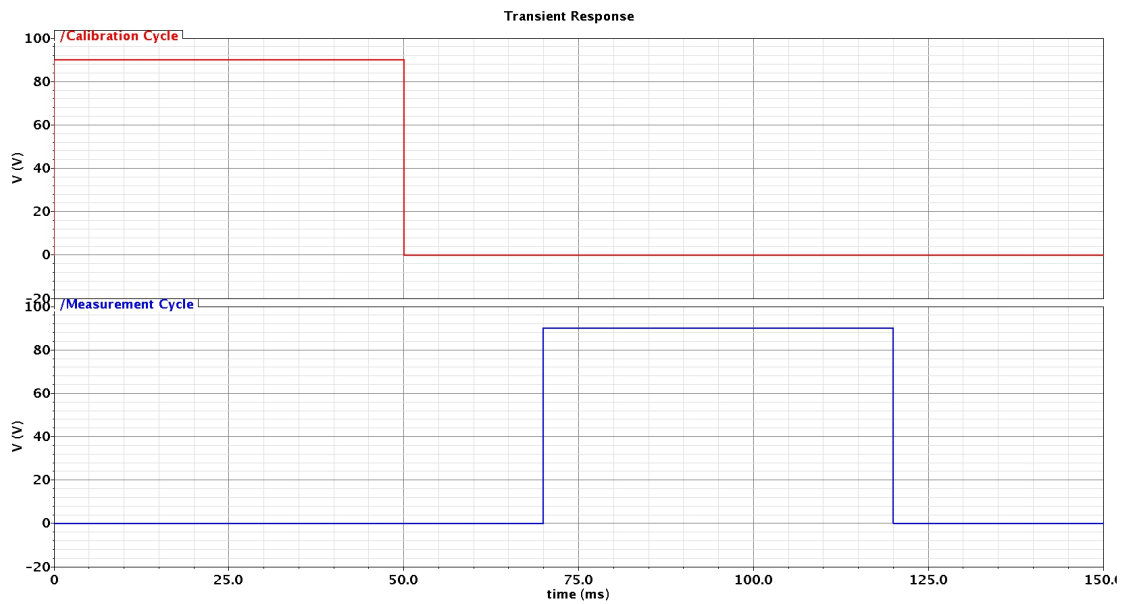
Figure 7.3.2.: Input plot for transient analysis of lab-on-spoon applications

The application of ISE-DC-MEMS switches in the lab-on-spoon device can be extended by switching to different reference load values. A different value is required for the reference load for different frequency ranges. Here the ISE-DC-MEMS switch can provide a switching solution without adding additional resistance to it.

7.4. Magnetic Localisation of Autonomous Sensor Node

ISE has been active in a BMBF funded research project on distributed measurement systems based on a swarm of autonomous integrated sensory nodes (PAC4PT-
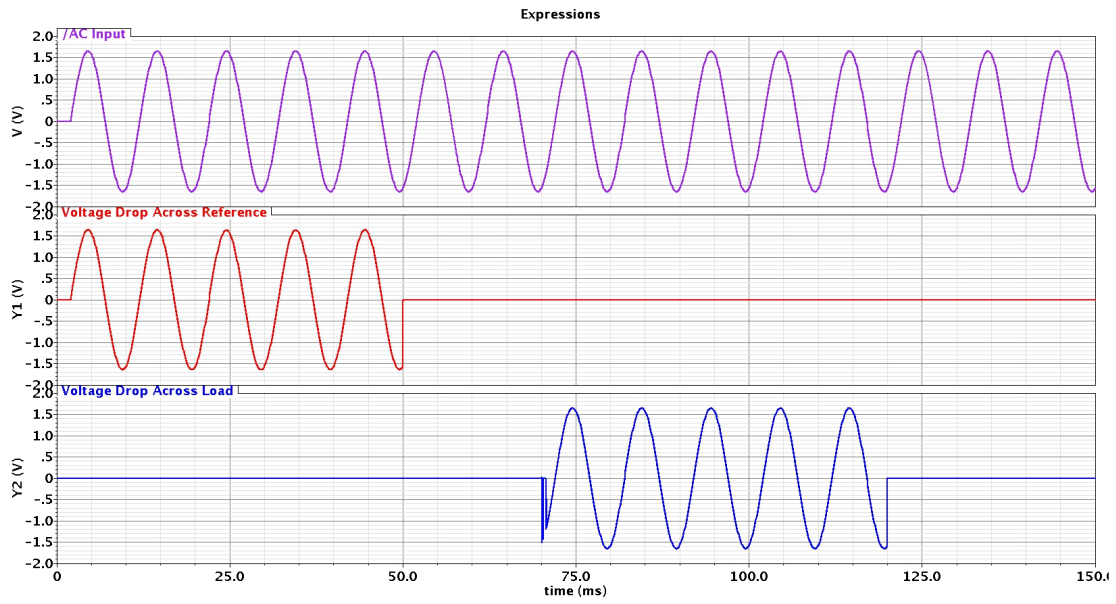
Figure 7.3.3.: Input plot for transient analysis of lab-on-spoon applications
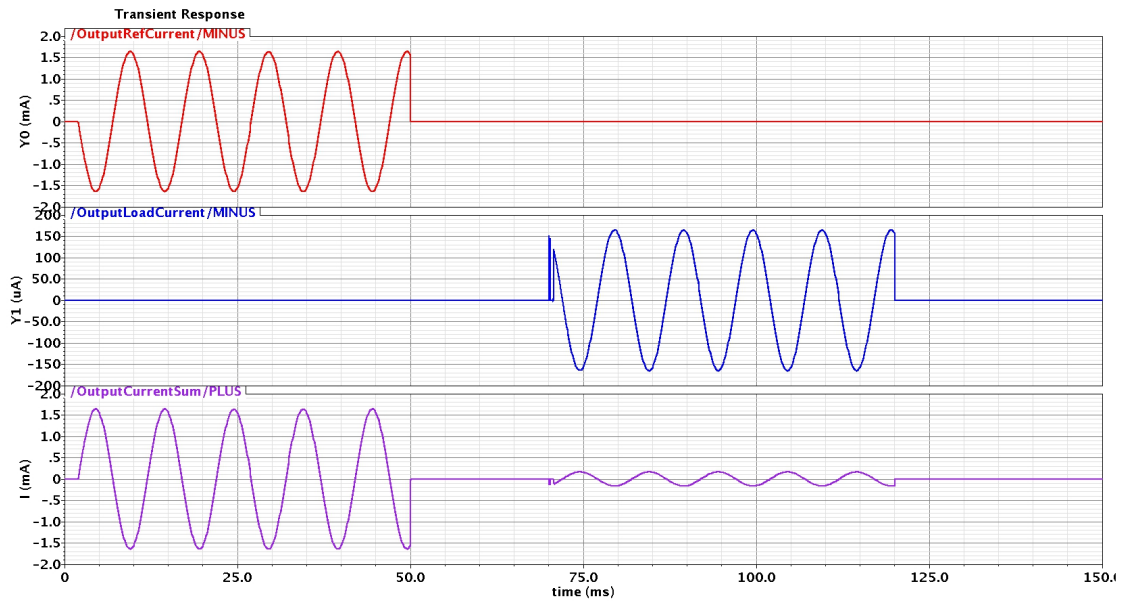
Figure 7.3.4.: Input plot for transient analysis of lab-on-spoon applications
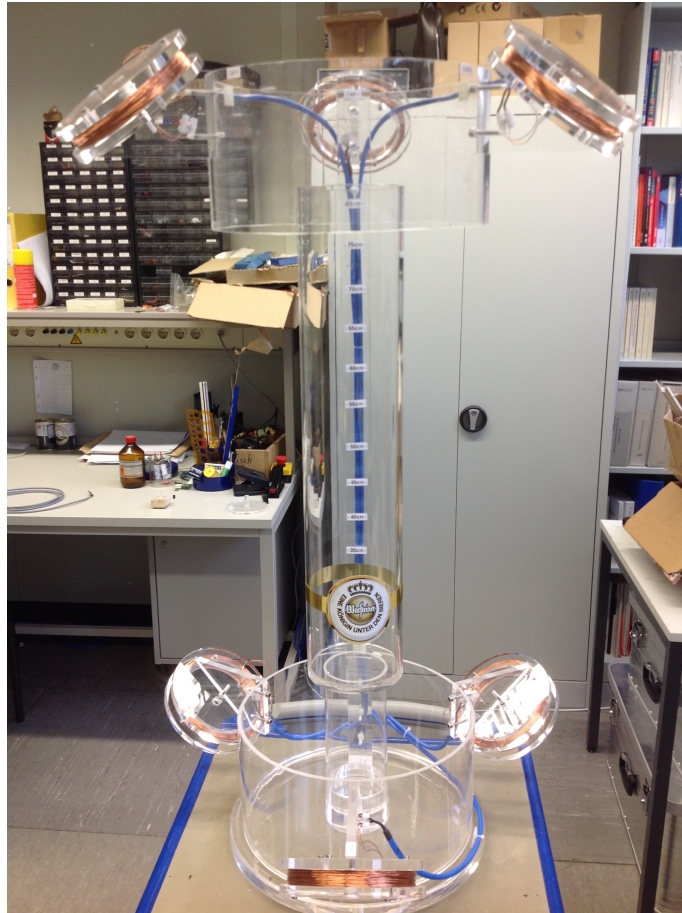
Figure 7.4.1.: Laboratory scale industrial water tank for localisation research

ROSIG) [2]. The various parameters of the manufacturing process in a fermentation tank in the brewing industry should be measured along with the time and location context. A dedicated localisation system has been conceived for the required localisation of the sensory nodes, based on the principle of the changes in the electromagnetic field in the Anisotropic Magneto-Resistive (AMR) sensor. AFF755B AMR sensors from Sensitec [98] were used in this research.

In order to properly map sensor positions, three axes of AMR sensors are required, representing X,Y and Z axes in a single sensor node. An industrial tank is then equipped with several coils with specific positions as magnetic sources. The locality of the sensor nodes are then determined with an algorithm that is calculated based on the strength of the magnetic field from the sources [29, 30]. Figure 7.4.1 shows the laboratory size industrial tank model conceived for Hannover Messe 2013 by D. Groben et al., with magnetic coils for sensor node localisation research. The optimum algorithms to determine sensor node positions were studied using this laboratory model.

---

[2]http://www.eit.uni-kl.de/koenig/gemeinsame_seiten/projects/ROSIG.html

(a) Circuit block diagram   **(b)**   AMR Sensor node
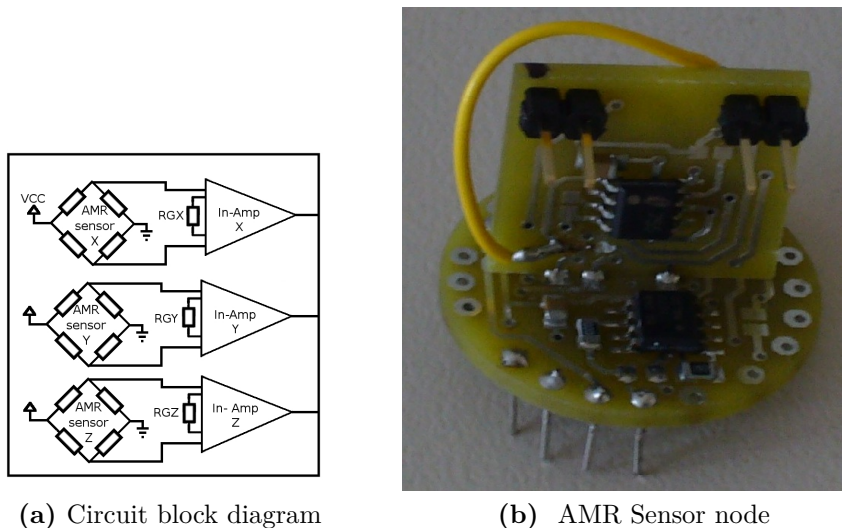
Figure 7.4.2.: Block diagram and actual 3D-AMR sensor node

7.4.1. The AMR Sensor Node Design

For localisation research purposes, a 3-axes AMR sensor node without self-x features was designed and developed in ISE[99] . The block diagram of the sensor node consists of three axis AMR sensors, a signal amplifying circuit and the DAQ or Arduino controller as shown in Figure 7.4.2. The sensor node used AFF755B AMR sensors from Sensitec and an INA122 instrumentation amplifier for sensor signal amplification. This instrumentation amplifier allows an easy output gain setup via a single external resistor. The first generation of sensor nodes has a fixed value of gain that is initially set to 100.

An AMR sensor shows degradation and deviation behaviour in the output voltage after long runs of repetitive measurements. The symptoms will be more obvious if the near saturated magnetic field is applied to the sensor. The reason for this phenomenon involves the permalloy microstructure. The uneven size in the permalloy crystal produces different magnitudes of magnetisation vector. In smaller crystals, the easy-magnetisation axis can easily change under influence of a magnetic field that is rated smaller than maximum.

In the event of repetitive measurements at various levels of magnetic field, these small magnetisation vectors change their direction and retained it. This will lead to an overall resistance value that is not the same as before, and will cause an offset in measurement. The error was reported and documented in the first case study of this research [99]. Figure 7.4.3 shows the difference between the normal state and degradation state of an AMR sensor. A square wave test signal is used for visual clarity. The normal state measurement (Figure 7.4.3(a)) was taken directly after resetting the AMR sensor. The measurement of the degradation state was taken using an aging AMR sensor after runs of magnetic measurements. (Figure 7.4.3(a)).

(a) AMR sensor in normal state　　　　**(b)** AMR sensor in degraded state
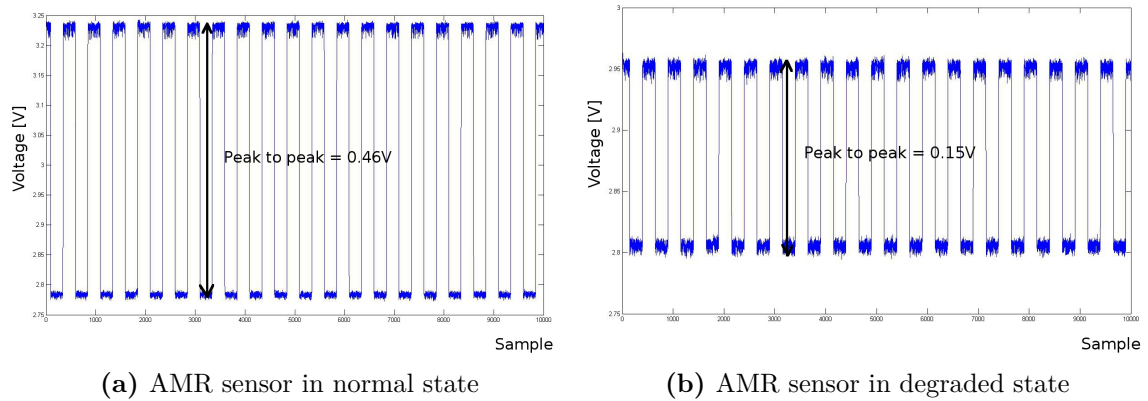
Figure 7.4.3.: Degradation effects in AMR sensor

(a) Normal output measure-　**(b)** Induced high magnetic　**(c)** In the saturation state
ment　　　　　　　　　　　field
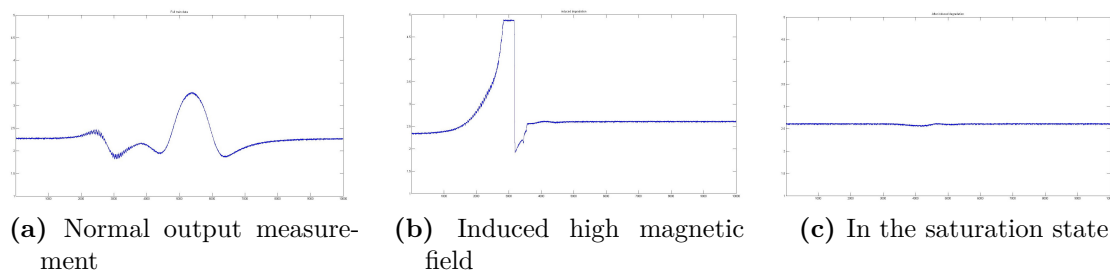
Figure 7.4.4.: Example of various states of AMR sensor output measurement

These two measurements show a huge difference in peak to peak voltage output which clearly demonstrates the effect of degradation.

The ability of the AMR sensor to sense magnetic change is also limited. When the sensor is exposed to more than the maximum limit of magnetic field, it will become saturated. This is also known a sensor's blind state where it cannot measure any magnetic changes surrounding it. It happens when the orientation of the magnetic material is changed following the direction of an external field.

In order to rectify this problem, the sensor has to be reset to the original condition. The resetting process can be performed by applying a strong magnetic field in the same direction as the factory setting so that it can rearrange the magnetisation to the original position. Figure 7.4.4 shows the saturation phenomenon in the AMR sensor. In this experiment, the sensor detects a moving metal object that passes in front of it. A typical measurement is recorded as shown in Figure 7.4.4(a). The inducement of saturation is performed by adding a strong permanent magnet to the moving object as shown in Figure 7.4.4(b). As the object approaches the sensor node, the output increases until it reaches the maximum point and then enters a blind state. In the next round in Figure 7.4.4(c), no more sensor output is registered because the sensor has reached the saturation state.
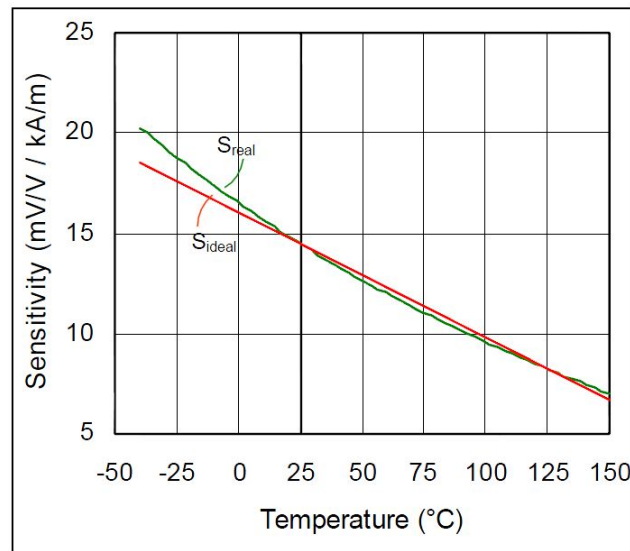
Figure 7.4.5.: Graph temperature dependency of AMR Sensor AFF755B, Sensitec

Another precaution that needs to be taken when using AMR sensor in one application involves the working temperature. The sensor also shows temperature dependency with resulting deviations in output measurements. Figure 7.4.5 shows the sensor sensitivity to temperature. There is an almost linear behaviour of sensitivity reduction as the temperature increases. A feedback system is required in the measurement system to ensure the offset in the data is compensated accordingly towards the ambient temperature.

These three points that require attention when the sensors are used in any application. The next section presents further discussion on how to rectify or minimise these effects in order to obtain good measurement results.

7.4.2. Proposals for Improvement in the AMR Sensor Node

The first two deficiencies of the AMR sensor can be rectified via the introduction of self-x features for self-monitoring and self-repairing. This requires tools in the form of coils as actuators.

The self-monitoring feature is an important function in an AMR sensor since the device gives continuous output that can be recorded as no change in the magnetic field during saturation state. This wrong information is dangerous if not addressed properly as the system cannot differentiate whether the measurement is correct or not.

The application of an embedded coil in AFF755B AMR sensor which provides a test magnetic field is one solution. This coil is positioned in such a way that it can produce a magnetic field in a specific direction. The test signal is generated when
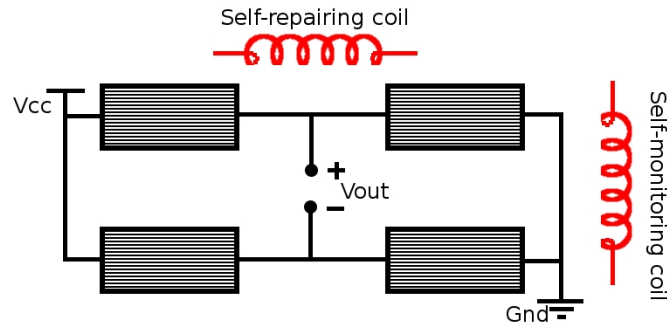
Figure 7.4.6.: Embedded coils act as actuator for self-x features in AMR sensors

a short pulse of maximum $200mA$ current flows through the coil which produces the magnetic field. When using a pre-determined magnetic field test, the sensor condition can be always be monitored to ensure correct functionality.

The remedy for the saturation problem during sensor operation can be implemented via the self-repairing capability. Another coil integrated in the AMR chip is employed for this purpose. This coil produces a magnetic field that can realign the magnetisation vector back onto the original axis. A short pulse current of $150mA$ for $1\mu s$ is adequate. The self-repair function will recover the sensor to its original working state. Figure 7.4.6 shows both coils embedded in AMR sensor.

The dependence of sensor sensitivity on temperature requires another self-monitoring feature. A system that can provide information about ambient temperature is required. A typical solution is to add another sensor specifically to measure the temperature, however in this research, an alternative method of temperature measurement was proposed and introduced [100].

Instead of using an additional temperature sensor, the proposed technique reuses the same AMR sensor bridge to measure the temperature. This smart technique made used of the permalloy material temperature properties and thus eliminate the need for an additional temperature sensor. In this solution, the same component can be switched between magnetic change detection and temperature measurement to perform these two functions. The derivation of temperature calculation using AMR sensor bridge is as follows.

The AMR sensor sensitivity (S) can be written as:

$$S = \frac{\frac{V_{Out}}{V_{Supply}}}{H} \tag{7.4.1}$$

The relationship between sensor sensitivity (S) and temperature (T)can be written

as:

$$S\left(T\right) = -0.061 \left[\frac{\left(\frac{\text{mV/V}}{\text{kA/m}} \right)}{^{\circ}C} \right] T + 16.1 \left[\frac{\text{mV/V}}{\text{kA/m}} \right] \tag{7.4.2}$$

Equation 7.4.1 and Equation 7.4.2 are then rearranged to become:

$$\frac{V_{Out}}{S\left(T\right)} = H \cdot V_{Supply} \tag{7.4.3}$$

The representation of $V_{Out}/S(T)$ is still proportional to the measured magnetic field and thus still serves the purpose of the AMR sensor but with the advantage of eliminating the temperature dependency. A better measurement of magnetic field strength can be obtained with this equation:

$$H = \frac{\left(\frac{V_{Out}}{V_{Supply}} \right)}{S\left(T\right)} \tag{7.4.4}$$

Based on the results reported in [100], the relationship between temperature,(T) and permalloy resistance, R_B can be written based on their bridge power supply,V_{Supply}.

- For $V_{Supply} = 3.3V$:

$$R_B\left(T\right) = 6.16 \left[\frac{\Omega}{^{\circ}C} \right] \cdot T + 2338\left[\Omega \right] \tag{7.4.5}$$

- For $V_{Supply} = 5.0V$:

$$R_B\left(T\right) = 6.11 \left[\frac{\Omega}{^{\circ}C} \right] \cdot T + 2343\left[\Omega \right] \tag{7.4.6}$$

To quantify the ambience temperature, T, using the AMR sensor bridge, Equations 7.4.5 and 7.4.6 need to be rearranged to become:

- For $V_{Supply} = 3.3V$:

$$T = \frac{R_B - 2338\left[\Omega \right]}{6.16 \left[\frac{\Omega}{^{\circ}C} \right]} \tag{7.4.7}$$

- For $V_{Supply} = 5.0V$:

$$T = \frac{R_B - 2343\,[\Omega]}{6.16\left[\frac{\Omega}{^\circ C}\right]} \tag{7.4.8}$$

By knowing the ambient temperature, the sensor's sensitivity point $S\left(T\right)$ can be determined using Equation 7.4.2. Finally the magnetic field strength H, can be measured using Equation 7.4.4.

The variance in sensor sensitivity with respect to temperature shows the need for output gain signal adjustment. A suitable instrumentation amplifier with output gain reconfigurability is therefore required. An INA-122 is a feasible instrumentation amplifier, that requires one external resistor for gain adjustment. The gain setting resistance is easily calculated using Equation 7.4.9.

$$R_G = \frac{200k\Omega}{G-5} \tag{7.4.9}$$

In order to enable dynamic changes in the output gain, a reconfigurable circuit built from various resistor values for different sets of output gain is activated by a switching device. The DC MEMS switch was selected as the switching element since it provides high isolation and low contact resistance during switching operations.

7.4.3. Self-x Feature Implementation in AMR Sensor Nodes

Self-x implementations in AMR sensor node can be on both, the system and component levels. Figure 7.4.7 illustrates the overall implementation proposal. At system level, two types of self-x feature are implemented. Self-monitoring is performed to monitor the ambient temperature using the technique explained in Section 7.4.2. This is important in order to adjust sensor sensitivity. Self-calibrating is then activated in case gain adjustment is needed based on the temperature information.

In this study, the self-calibration function was enabled using DC MEMS switches. Two switches were used to provide various combinations of gain resistance for the instrumentation amplifier. Table 7.1 shows the function table of possible gain combinations that can be achieved from two SPDT switches. The R_G can be adjusted depending on the suitability of the applications.

The self-x features are also implemented at the component level. At this level, the selected components were added with additional features apart from their original functions. These functions were enabled by specific actuation schemes that were embedded in the components.

Two components involved in this case study are the AMR sensor and the ISE-DC-MEMS switch. Both have two implemented self-x features. The first implementation is self-monitoring of the AMR sensor state. The embedded coil that provides a test
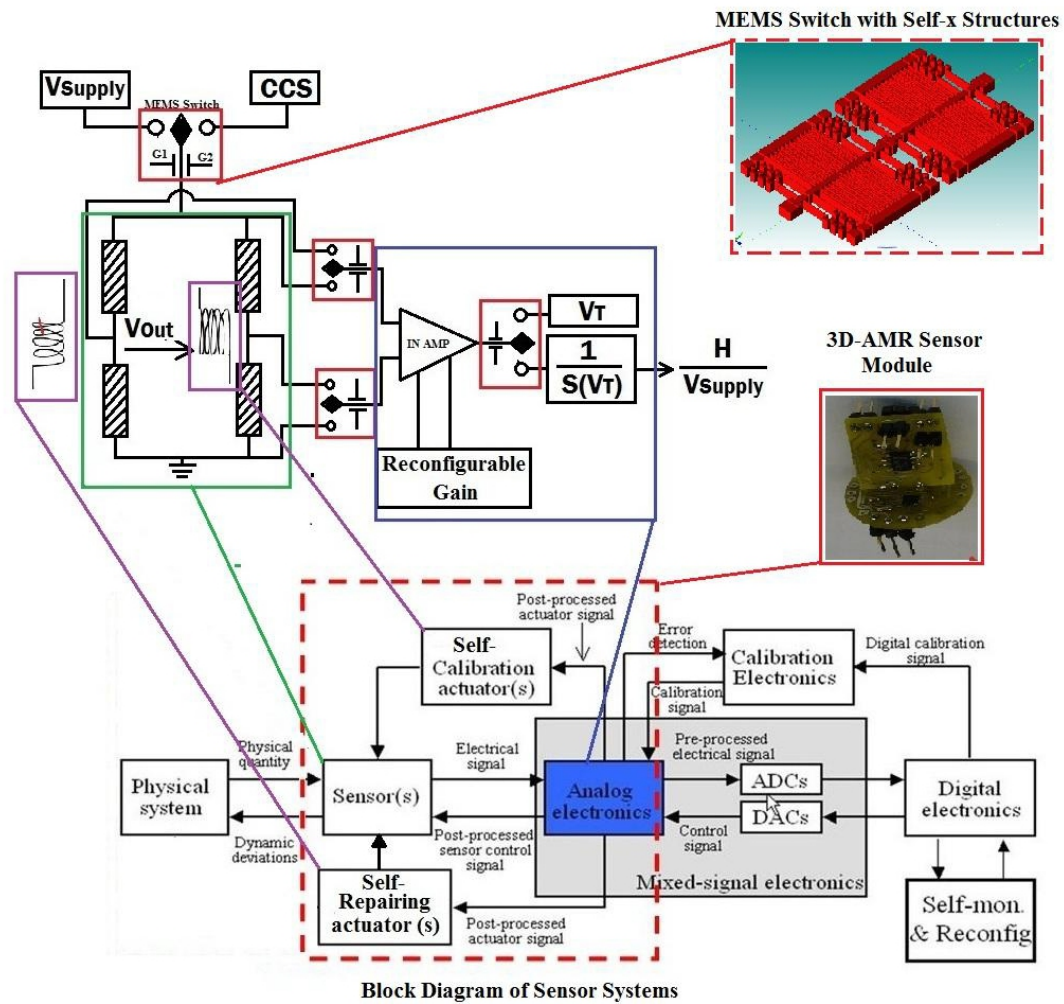
Figure 7.4.7.: Block diagram of AMR sensor node with self-x features implementation

SPDT 1		SPDT 2		Output
$R_{G1} = 2.1k\Omega$	$R_{G2} = 4.4k\Omega$	$R_{G3} = 13.3k\Omega$	$R_{G4} = 40k\Omega$	Gain
0	0	0	0	5
0	0	0	1	10
0	0	1	0	20
0	1	0	0	50
0	1	0	1	
0	1	1	0	51
1	0	0	0	100
1	0	0	1	72
1	0	1	0	76

Table 7.1.: Function table of SPDT switch and gain that can be achieved

magnetic field signal is responsible for realising this function. The second implementation is self-repair of the AMR sensor. A second coil is embedded in the AMR sensor to enable this feature and recover the sensor's function from the saturated state. In both self-x features, the coils act as actuators with a pulse current as source signal.

The second component equipped with self-x features is the ISE-DC MEMS switch. The self-x features in the ISE-DC-MEMS switch were discussed in detail in Chapter 4 and 6.

A sensor node to demonstrate these self-x concepts in the AMR sensor was built as shown in Figure 7.4.9. In this demonstrator, commercial MEMS switches were used to demonstrate the switching benefits and capability of the sensor front-end circuits.

The ISE-DC-MEMS switch is still not applied in the demonstrator due to the problem noted in Chapter 6, however, the self-x concepts at the component level of ISE-DC-MEMS switch were explained and demonstrated in Chapter 4 and 6.

7.5. ISE-DC-MEMS Switch as Multiplexer

A multiplexer built using an ISE-DC-MEMS switch or MEMS-Mux is another potential application. In parallel with this research, the ISE research group is also working on designing a generic and dynamic sensor signal conditioner with self-x features[101]. Figure 7.5.1 shows the first version of the aspired generic sensor signal conditioner which is equipped with transmission gate multiplexers.

A MEMS-Mux multiplexer can be used to complement the transmission gate multiplexer or TG-Mux. Section 5.2.3 has discussed the feasibility of using ISE-DC-MEMS switches as multiplexers. Table 7.2 shows the performance comparison between TG-Mux and MEMS-Mux. This table provides guidelines to help select the
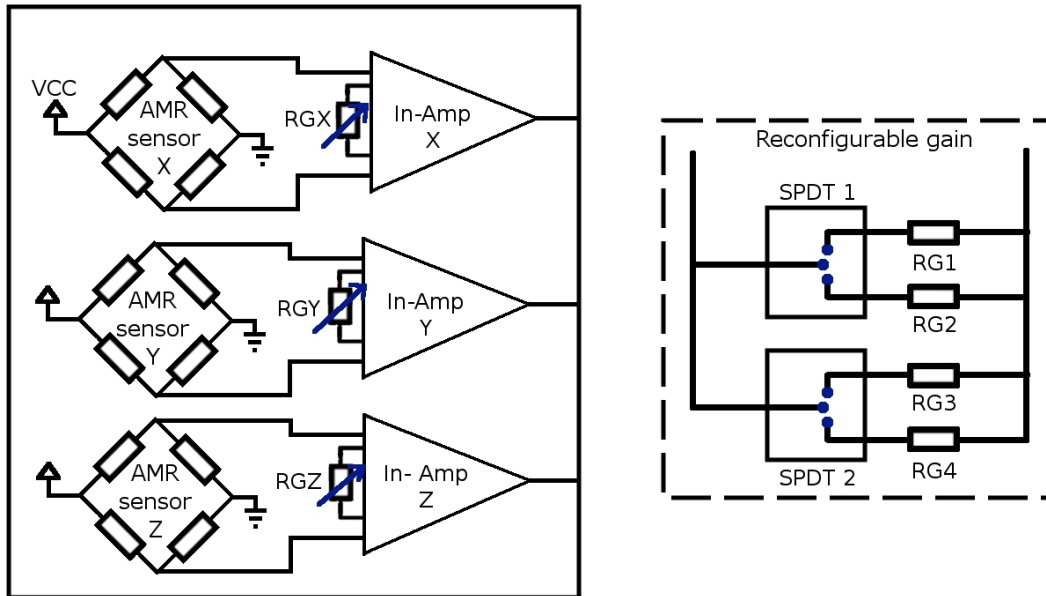
Figure 7.4.8.: Block diagram of AMR sensor node demonstrator

(a) Side View

(b) Top View
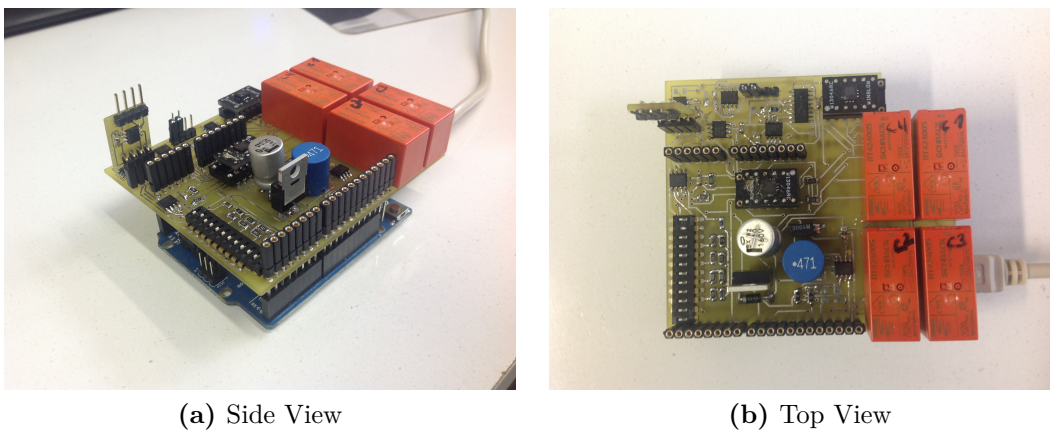
Figure 7.4.9.: A 3D-Axis AMR sensor with MEMS Switch integration
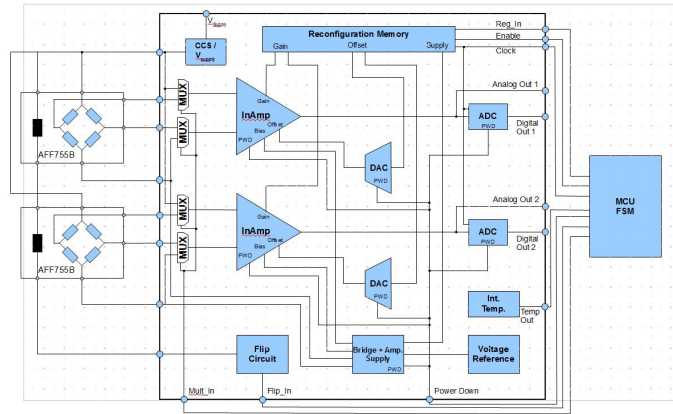
Figure 7.5.1.: A block diagram of a generic sensor signal conditioner

	VDD 3.3V	VRef 1.65V	VPLL:3.3V 4MHz clock	Cross-talk at 40kHz	Switching time
TG-Mux	AMR supply: 1.81V AMR output: 10.89mV	AMR supply: 1.12V AMR output: 6.72mV	No visible distortion	V_{p-p} equal to 2.68nV	~ 0.5μs
MEMS-Mux	AMR supply: 3.29V AMR output: 19.76mV	AMR supply: 1.647V AMR output: 9.88mV	No visible distortion	V_{p-p} equal to 15.7nV	~ 600μs

Table 7.2.: Performance comparison between TG-Mux and MEMS-Mux switch

best multiplexer with respect to applications. For an application that requires low on resistance and sourcing applications, the MEMS-Mux is a better choice than a TG-Mux. In order to sink and source a bridge, two TG-Muxs must be replaced by two MEMS-Muxs. The chip in Figure 7.5.1 must be rewired, taking control signals and source signals to the pad frame. A high voltage driving block must also be added, preferably based on HV-CMOS.

The ISE-DC-MEMS switch has a lower voltage drop for controlling supply voltage, due to low R_{On} when compared to a transmission gate multiplexer. When handling AC signals, the transmission gate produces a lower crosstalk value when compared to ISE-DC-MEMS. For high frequency switching applications, the transmission gate is more suitable due to its fast switching rate.

Integration of a generic sensor signal conditioner which consists of several dice from different technologies in a single package can be developed. Figure 7.5.2 shows a block diagram of the generic sensor signal conditioner. This integration includes two different dice, the generic sensor signal conditioner chip and MEMS-Mux. The generic sensor conditioner could be built using HV-CMOS technology with an addi-
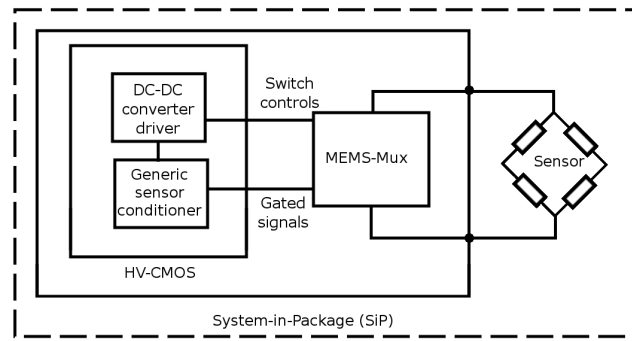
Figure 7.5.2.: Generic sensor signal conditioner with MEMS-Mux multiplexer

tional DC-DC converter circuit for driving the ISE-DC-MEMS switch. The MEMS-Mux is included to complement the TG-Mux of the generic sensor conditioner.

8. Conclusions and Future Work

8.1. Conclusions

The integration of multi-sensor elements, sensor electronics and sophisticated signal processing algorithms resulted in intelligent sensor systems with significant level of complexity. This complexity leads to higher vulnerability in performing their respective functions in dynamic environments. The dependability of systems can be improved via the implementation of self-x features in reconfigurable systems. Reconfiguration capability requires switching elements typically in the form of a CMOS switch or miniaturised electromagnetic relay. These switching options have both advantages and disadvantages. The emerging DC-MEMS switch has the potential to complement the CMOS switch in System-in-Package as well as in integrated circuits solutions.

The main goal of this research was to study the feasibility of DC-MEMS switches in enabling self-x features for reconfigurable integrated sensory systems. A survey was undertaken to understand and identify self-x concepts and their general applications. Another survey was focused on self-x applications in MEMS devices. This has helped in collecting and adapting new ideas for the intended target application of DC MEMS switches. A summary table has been provided to give an overview of the survey results.

A study of general MEMS technology and its availability was carried out to identify the most feasible technology for DC-MEMS switches. This study includes the latest software tool for MEMS CAD and as a result the MEMS+ software from Coventor was acquired. This software complements the Cadence design tools to allow a complete design and simulation tool for MEMS and mixed analogue signal electronics.

ISE-DC-MEMS switches embedded with self-monitoring and self-repairing functions were designed and optimised. The electrical and mechanical properties of the SPST and SPDT switches were characterised. The original MEMS model of MEMS+ for the electrical and mechanical domains was not complete. Characterisation results of the actual prototype were used to configure and validate the proposed additional model. The improved electrical models for the SPST switch were used for system application simulation. In the mechanical model, the assumption of rigid body in the electrostatic actuator structure resulted in inaccurate simulation results which led to a stiction problem in the actual prototype. A stiction conformity test was

proposed, implemented, and successfully validated to compensate for the inaccurate mechanical model.

Four different system simulations of representative applications were carried out to analyse the aptness and performance of the ISE-DC-MEMS switch in sensitive reconfiguration tasks in the application, and to compare it with the transmission gates. These simulation results were used to build a comparison matrix to help users select the best reconfiguration device solutions. A hybrid system-in-package consisting of multiplexers built either from transmission gates or MEMS switches is an attractive combination in terms of performance and cost for analogue mixed signal electronics.

8.2. Contributions of the Thesis

A list of achievements and innovations of this research is as follows:

- Comprehensive survey of self-x concepts and its implementation in the MEMS device
- Survey and analysis of DC-MEMS switches with regard to manufacturing technology, design tools and design variations
- The ISE-DC-MEMS switches consist of self-monitoring and self-repairing functionalities embedded in the hardware of the MEMS switch itself
- A different approach to the self-repairing concept, which does not use subsystem redundancy but active structures in the form of heat actuators
- A special design structure for heat actuators that provides actuation movement at the centre point of the beam with minimum out of plane deflections
- A procedure for design conformity tests for designing electrostatic actuators to compensate for the MEMS+ mechanical model in ISE-DC-MEMS structure. This procedure can be used to design electrostatic actuators with comb structures in MEMS+ software
- The self-x implementation at component level in the form of self-monitoring and self-repairing has been shown in AMR sensors and ISE-DC-MEMS switches.
- Self-x implementation at the system level of the AMR sensor to monitor ambient temperature utilising the AMR sensor bridge
- A demonstrator was built as a proof-of-principle in implementing self-x features at system and component level

8.3. Future work

The ISE-DC-MEMS switch is a feasible switching solution, but requires further optimisation and scaling to allow a robust design with HV-CMOS compatibility.

The current ISE-DC-MEMS switches are of average performance when compared to commercial DC-MEMS switches but with additional functionality in self-x features. A revisiting process for evaluating the different technology and switch configurations is required. Vertical movement is worth considering in order to produce a small device with a robust design. The bi-stability concept of switch design should also be revisited for static power saving.

The latest information from MEMSCAP Inc. was that starting from 2014, a new MEMS technology will be offered with piezoelectric material under PiezoMUMPs technology. Piezoelectric material based on aluminium nitride (AlN) is another potential material that can be used either for microactuators or sensors. This is one of the promising future directions in DC MEMS switches using piezoelectric material which requires low voltage and current actuation during operations.

The basic design of the current heat actuator also requires further optimisation. The heat actuator presented in this research can be considered a new category of heat actuators. It requires further investigation in scaling parameters for further size optimisations. The absence of a heating element as normal practice in heat actuators gives a significant advantage, especially in the thermal management of heat actuators in MEMS devices. Simulation and experiment results also show the minimal off-the-plane deflection by this kind of structure. This results in actuator behaviour that is easy to control and predict.

A. Calculation of Signal Line Resistance

Another interesting part that requires investigation is the signal line resistance. This is an important value in evaluating the switch performance in handling information signals. In the MEMS+ model the resistance model is not included and there is only an ideal assumption. In order to obtain the resistance value for various switch models, manual calculations have been done.

The resistance in the MEMS structure can be calculated using Equation A.0.1.

$$Resistance\,(R) = \frac{length(l) * Resistivity\,of\,material\,(\rho)}{width\,(w) * thickness\,(T)} \tag{A.0.1}$$

In a given fixed layer, the resistance R can be calculated by:

$$R = \rho' * \frac{l}{w} \tag{A.0.2}$$

where w is the width of the resistor; l is the length of the resistor and ρ' is resistance per square area.

Calculation of the resistances is done by evaluating the structural geometry of the MEMS structure. In determining the R_{Line} value in one signal line, the structure is divided into several sections and the evaluation is done individually using Equation A.0.2. The sections of a signal line are defined as shown in Figure A.0.1. The corresponding resistance values for the SPST V1 model are shown in Table A.1. Special consideration has been given to meander structures in the area labelled with C1 and D1. In this area, a multiplier with a value of 0.6 has been implemented in the calculation due to the difference in current density in such structures [102].

The MEMS switch signal line can be connected in several ways. Users can choose either a simple connection that produces higher resistance or a complex connection that produces lower resistance. The R_{Line} value depends on the connection that has been chosen.

In a simple configuration, connections with floating points are used. Only one anchor is connected to each signal line, which leads to easy integration at chip level. The
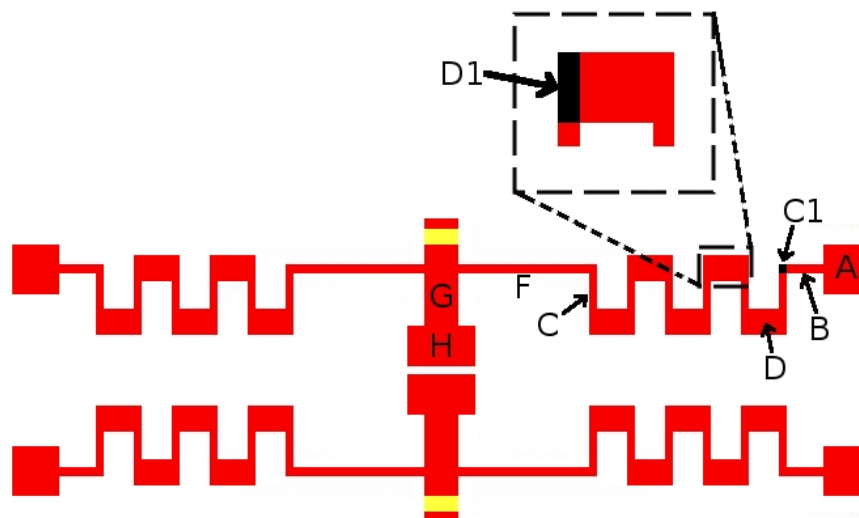
Figure A.0.1.: Contact zoom with labels

Area	Qty	Multiplier	Length	Width	$\frac{l}{w}$	$\frac{\rho}{T}$	R
			$[\mu m]$	$[\mu m]$		$\frac{\Omega}{\mu m}$	$[\Omega]$
A	1	1	100	100	1.00	4.00×10^{-3}	4.00×10^{-3}
B	1	1	45	10	4.50	4.00×10^{-3}	1.80×10^{-2}
C1	2	0.6	10	10	1.00	4.00×10^{-3}	2.88×10^{-3}
C	2	1	30	10	3.00	4.00×10^{-3}	2.40×10^{-2}
D	5	1	40	30	1.33	4.00×10^{-3}	2.67×10^{-2}
D1	10	0.6	20	30	0.67	4.00×10^{-3}	9.60×10^{-3}
E	4	1	20	10	2.00	4.00×10^{-3}	3.20×10^{-2}
F	1	1	515	10	51.50	4.00×10^{-3}	2.06×10^{-1}
G	1	1	110	60	1.83	4.00×10^{-3}	7.33×10^{-3}
H	1	1	150	60	2.50	4.00×10^{-3}	1.00×10^{-2}

Table A.1.: Example of subsection resistance calculations for SPST V1

(a) Total resistance with floating point configuration, R_{LFl}

Resistor	Resistance [Ω]
R_{AF}	3.2315×10^{-1}
R_G	7.333×10^{-3}
R_H	1.000×10^{-2}
R_{LFl}	3.405×10^{-1}

(b) Total resistance with no floating point configuration, R_{LNF}

Resistor	Resistance [Ω]
R_{AFP}	1.616×10^{-1}
R_G	7.333×10^{-3}
R_H	1.000×10^{-2}
R_{LNF}	1.789×10^{-1}

Table A.2.: Calculation of signal line resistance elements for SPST V1 DC MEMS switch

Model	SPST							SPDT
	V1	I-A	II-A	III-A	I-B	II-B	III-B	
R_{LFl}	0.4048	0.5227	0.3367	0.4390	0.5143	0.4390	0.3376	0.3370
R_{LNF}	0.2111	0.2685	0.1755	0.2267	0.2643	0.2267	0.1760	0.1763

Table A.3.: R_{Line} values for each MEMS switch design based on connection

R_{Line} will be equivalent to R_{LFl} to represent the floating effect. The R_{LFl} is a summation of R_{AF}, R_G and R_H.

On the other hand, a lower resistance value can be achieved by connecting both anchors to the signal lines. This will increase the complexity of the chip level integration but as a reward a lower resistance can be achieved. The lower resistance can be achieved due to the parallel effect in most of the resistance geometry across the signal line. Based on Table A.1, the geometry elements from A to F are in a parallel condition and thus reduce the resistance, R_{AF} to half, which is denoted as R_{AFP}. In this connection, the resistance of the non-floating connection, R_{LNF} is comprised of R_{AFP}, R_G and R_H.

Table A.2 shows a calculation example for the SPST V1 MEMS model in determining the R_{LFl} and R_{LNF} values. The R_{Line} values for all MEMS designs are shown in Table A.3.

228

B. Parasitic Capacitance in Signal Lines

The MEMS+ model has provided a good mechanical behavioural model. Since there is no parasitic capacitance model that can be extracted, the electrical behavioural model needs to be improved. This information is important to understand the electrical performance of the MEMS behaviour. In an effort to improve the electrical model from the given MEMS structure, the calculation of the parasitic capacitances surrounding the signal lines in the MEMS switch is presented.

In this section, the parasitic capacitance calculations surrounding the signal lines in the MEMS switch for all design models are presented. The calculations were done based on the gaps during the switch off-state. The capacitance is calculated using a parallel plate capacitor equation:

$$C = \frac{\varepsilon_0 A}{d} \tag{B.0.1}$$

where $\varepsilon_0 = 8.854 \times 10^{-12} F/m$, A is the area of the parallel plate and d is the separation between the two plates. In order to simplify the calculation, the fringing capacitances in these calculations are neglected.

There are two different sources in determining parasitic capacitance:

- Source from lateral structure
- Source from horizontal structure

Lateral Parasitic Signal Line Capacitor

The lateral parasitic capacitances are accumulated in between the signal path and the MEMS structures that are in a lateral relation with it. These structures are separated by air. Figure B.0.1 shows the parasitic capacitance contributed by the lateral structures.

For lateral parasitic capacitances along a signal line, there are two parasitic elements involved. First, C_{PLE} is a parasitic capacitance between the signal paths and the closest beam in electrostatic actuators, depicted as A to F in Figure B.0.1. Table B.1
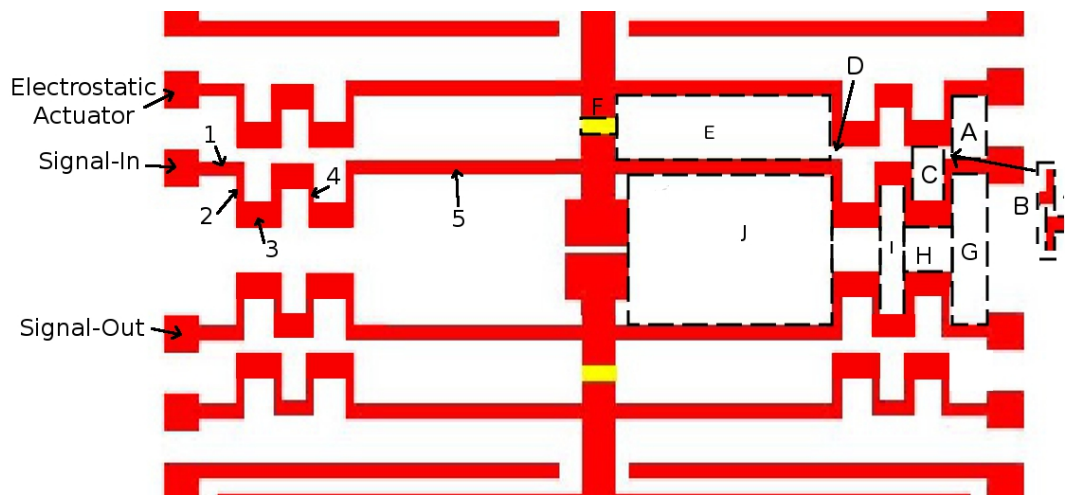
Figure B.0.1.: Parasitic capacitance elements along signal line path

Area	Thickness [μm]	Length [μm]	Gap [μm]	Multiplier	Capacitance [fF]
A	20	45	115	4	0.2772
B	20	10	55	8	0.2576
C	20	40	95	20	1.4912
D	20	10	45	16	0.6296
E	20	515	115	4	3.1721
F	20	60	20	1	0.5313
Total lateral parasitic capacitance (C_{PLE})					6.3590

Table B.1.: Calculation of lateral structure capacitance between signal line and electrostatic actuator of SPST V1

shows the numerical calculation of this parasitic capacitance value with the C_{PLE} value at $6.3590\,fF$.

Second, C_{PLL} is the parasitic capacitance between the structures of the signal-in and signal-out lines labelled as G to J. These capacitance areas are then calculated as shown in Table B.2, where the parameters are based on the SPST V1 model. A small C_{PLL} value of $1.6082\,fF$ is calculated due to the large gap between the signal-in and signal-out lines.

Horizontal Parasitic Signal Line Capacitor, C_{PH}

The horizontal parasitic capacitance is found in between MEMS structures and the substrate layer with an air gap. The gap between these two layers is determined by the trench cut of the substrate which is set at $25\mu m$. In this case, only the signal paths were considered in contributing the parasitic capacitance, as depicted

Area	Thickness [μm]	Length [μm]	Gap [μm]	Multiplier	Capacitance [fF]
G	20	45	220	2	0.0724
H	20	60	100	6	0.6375
I	20	40	200	4	0.1417
J	20	470	220	2	0.7566
Total lateral parasitic capacitance (C_{PLL})					1.6082

Table B.2.: Calculation of lateral structure capacitance between two signal lines of SPST V1

Area	Thickness [μm]	Length [μm]	Gap [μm]	Multiplier	Capacitance [fF]
1	10	55	25	4	0.7792
2	10	30	25	4	0.4250
3	30	60	25	20	12.7500
4	10	20	25	20	1.4167
5	10	515	25	4	7.2959
6	60	110	25	2	4.6750
7	150	60	25	2	6.3750
Total horizontal parasitic capacitance (C_{PH})					33.7167

Table B.3.: Example of C_{VC} calculation for SPST V1 model

in Figure B.0.1 with labels 1-7.

Summary

Table B.4 shows the parasitic values for all MEMS switch models presented in this thesis. The MEMS model SPSTV1 and SPDT have similar parasitic values because they share the same width and heat actuator design. For the second MEMS prototype, similar parasitic values were recorded for models that share the same design.

The parasitic capacitance only influenced the switch operation in specific circumstances. For example, in the case of signal isolation between signal-in and signal-out, the C_{PLL} capacitance will add to the contact capacitance. The sum of these capacitances will determine the cut-off frequency that determines the signal isolation.

As for the C_{PLE} the capacitance will only influence the signal line in the case of a clock-feed-through phenomenon from high frequency switching action of the electrostatic actuator. Since the capacitance is really low at femto Farad range and the cut-off frequency is in Giga *Hertz*, the parasitic capacitance is unlikely to cause

Model	SPST						
	V1	**I-A**	**II-A**	**III-A**	**I-B**	**II-B**	**III-B**
$C_{PLE}[fF]$	6.3590	7.6905	6.4931	4.7897	7.6905	6.4931	4.7897
$C_{PLL}[fF]$	1.6082	2.7569	2.1662	1.5211	2.7569	2.1662	1.5211
$C_{PH}[fF]$	33.7167	45.2166	39.8970	32.955	45.2166	39.8970	32.955

Table B.4.: The parasitic capacitance values for each ISE-SPST MEMS switch design

Model	SPDT
$C_{PLE}[fF]$	6.3590
$C_{PLL}[fF]$	1.6082
$C_{PH}[fF]$	33.7167

Table B.5.: The parasitic capacitance values for ISE-SPDT MEMS switch design

any noise problem to the signal line. This is because the switching frequency of the electrostatic actuator will not reach such a high frequency.

C. Parasitics in the Capacitive Sensor

Capacitive sensors in the ISE DC-MEMS switch are another important element to investigate. In the first prototype ISE-DC-MEMS switches, each SPST switch has two capacitive sensors called sensor A and B. Since the dice were not cut into smaller dice, additional metal routing was required for easy accessibility during the characterization process. Similar to the parasitic capacitance for the signal line, two different capacitances from the lateral surface and horizontal surface were considered. The calculation presented in this section is done for the switch off-state.

Lateral Parasitic Capacitance

The parasitic capacitances in the capacitive sensors were contributed by this additional metal routing. Both sensors have a different geometry in the routing because of limited space on the die. This makes the parasitic capacitance in the two sensors non-identical.

This parasitic capacitance contributed to the overall sensing capacitance. In this section, both parasitic capacitances will be calculated in order to estimate the value. Two parasitic elements will be calculated. Firstly, C_{SLE} is the parasitic contributed by structures between the sensor signal path and electrostatic actuator. This parasitic does not contribute towards the total capacitive sensor and the value is identical for both sensor A and B.

Secondly, a parasitic capacitance is contributed by structures between the two signal paths of the sensor. This parasitic capacitance will add to the total capacitive sensing and is not identical between sensor A and B. This is because they have different routing structures. C_{SLA} is the parasitic capacitive sensor A and C_{SLB} is the parasitic capacitive sensor B.

Parasitic Capacitance C_{SLE}

Figure C.0.1 shows determination of the parasitic element in sensor A. The parasitic capacitance C_{SLE} is determined by the capacitance labelled as A to F with a total of $2.9139fF$.
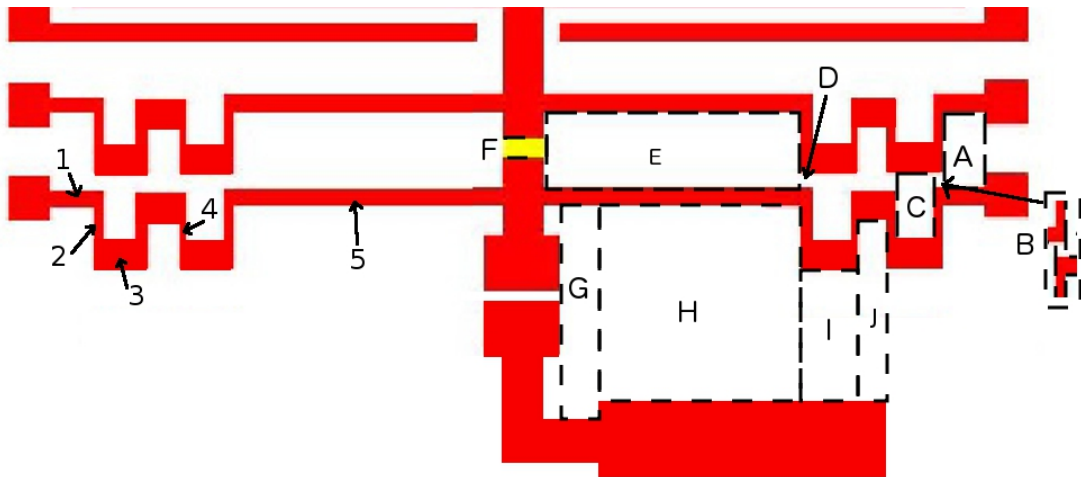
Figure C.0.1.: Parasitic capacitance elements along sensor A of SPST V1 switch
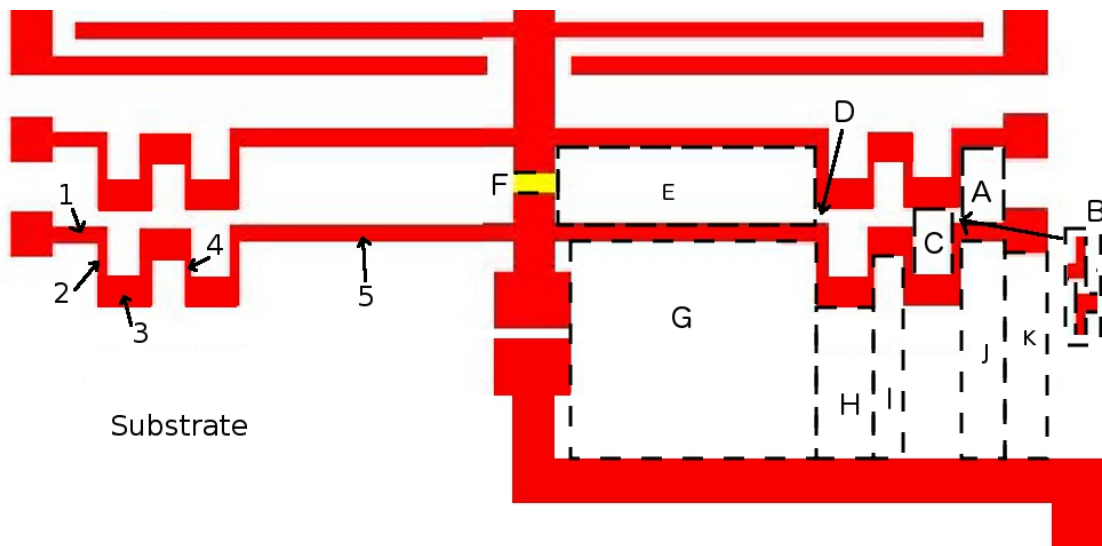
Figure C.0.2.: Parasitic capacitance elements along sensor B of SPST V1 switch

Area	Thickness	Length	Gap	Multiplier	Capacitance
	$[\mu m]$	$[\mu m]$	$[\mu m]$		$[fF]$
A	20	45	115	2	0.1386
B	20	10	55	4	0.1288
C	20	40	95	10	0.7456
D	20	10	45	8	0.3148
E	20	515	115	2	1.5861
F	20	60	20	1	0.5313
Parasitic Capacitance, C_{SLE}					3.4451

Table C.1.: Calculation of C_{SLE} value for sensor A in SPST V1 design

Area	Thickness [μm]	Length [μm]	Gap [μm]	Multiplier	Capacitance [fF]
G	20	75	495	1	0.0268
H	20	400	445	1	0.1592
I	20	60	385	1	0.0276
J	20	40	435	1	0.0163
Parasitic capacitance, C_{SLA}					0.2299

Table C.2.: Calculation of C_{SLA} value for sensor A in SPST V1 design

Area	Thickness [μm]	Length [μm]	Gap [μm]	Multiplier	Capacitance [fF]
G	20	452	215	1	0.3723
H	20	60	155	3	0.2056
I	20	40	205	2	0.0691
J	20	45	215	1	0.0371
K	20	100	170	1	0.1042
L	20	80	92	1	0.1540
Parasitic capacitance, C_{SLB}					0.9423

Table C.3.: Calculation of C_{SLB} value for sensor B in SPST V1 design

Parasitic Capacitance C_{SLA}

The parasitic capacitance between two signal paths in sensor A is shown in Figure C.0.1 labelled from G to J. Table C.2 shows the value of the elements involved in the parasitic capacitance C_{SLA}. Based on this calculation the total value of C_{SLA} is $0.2299 fF$.

Parasitic Capacitance C_{SLB}

For sensor B, the parasitic elements involved were labelled from G to L as shown in Figure C.0.2. Based on the results presented in Table C.3, the parasitic capacitance CSLB is recorded at $0.2299 fF$.

Horizontal Parasitic Capacitance, C_{SH}

The horizontal parasitic capacitor, C_{SH} can be defined as the capacitance value between the signal path of the sensor and the substrate. The C_{SH} value is half the value of C_{PH} because only one movable structure is considered in the capacitive sensor. Table C.4 shows that the total value of C_{SH} is $16.86 fF$.

Area	Thickness	Length	Gap	Multiplier	Capacitance
	$[\mu m]$	$[\mu m]$	$[\mu m]$		$[fF]$
1	10	55	25	2	0.389
2	10	30	25	2	0.213
3	30	60	25	10	6.375
4	10	20	25	10	0.708
5	10	515	25	2	3.648
6	60	110	25	1	2.338
7	150	60	25	1	3.188
Horizontal Parasitic Capacitance,C_{SH}					16.86

Table C.4.: Calculation of horizontal parasitic capacitor, C_{SH}
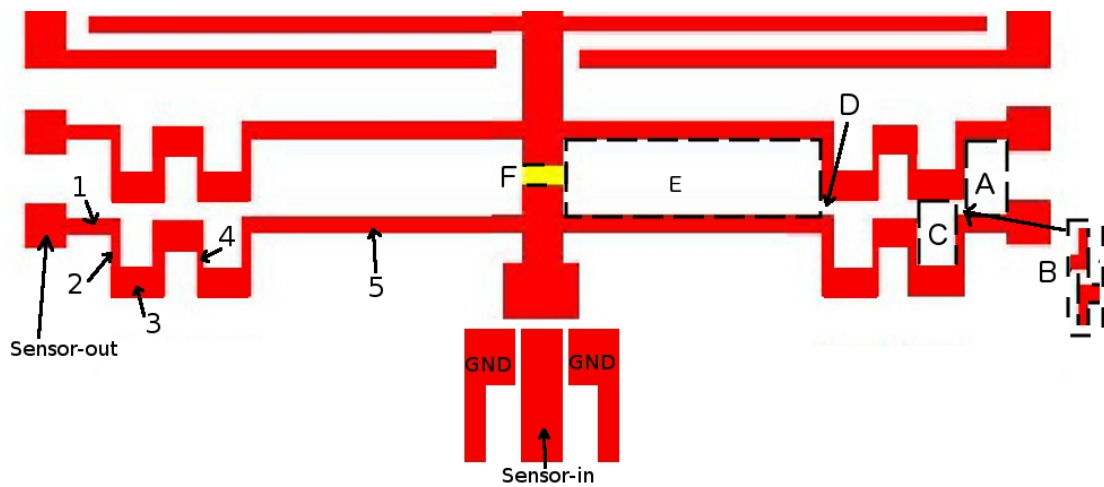
Figure C.0.3.: Parasitic capacitance elements along capacitive sensor for all second prototype switches

Summary

The parasitic capacitance of the capacitive sensor in ISE-DC-MEMS switches for all prototype designs are presented in the Table C.5. In the first prototype in SPSTV1 and SPDT switches, the parasitic capacitance values for sensors A and B differ because of the differences in metal path towards the pads. This is not the case for the second protoypes because the sub-dicing process cuts the dice into specific switch types. This allows identical metal routing for both sensor A and sensor B. This metal routing does not contribute to additional parasitic capacitance and as a result a higher precision sensor can be produced. This is part of the improvement in the second prototype designs of ISE-DC-MEMS switches. Figure C.0.3 shows the metal pads routing for the capacitive sensors in the second prototype switches.

Model	SPST							SPDT
	V1	**I-A**	**II-A**	**III-A**	**I-B**	**II-B**	**III-B**	
$C_{SLE}[fF]$	3.4451	4.0198	3.4594	2.6099	4.0198	3.4594	2.6099	3.4451
$C_{SLA}[fF]$	0.2299	0	0	0	0	0	0	1.1853
$C_{SLB}[fF]$	0.9423	0	0	0	0	0	0	1.6271
$C_{SH}[fF]$	16.8584	22.7659	20.0459	16.5750	22.7659	20.0459	16.5750	16.86

Table C.5.: The parasitic capacitance values of capacitive sensor A for each MEMS switch design

238

D. Electrical Simulation of Self-Monitoring Structure

The capacitive sensor for self-monitoring features had a very small capacitance value in the range of less than $10fF$. The challenge lies in measuring such a small level of difference. Recent research on a universal signal interface for capacitive sensors [103] has reported the capability to measure in the pico Farad range of capacitance values.

However, a simple sub-femto Farad measurement technique has been suggested by McGauby et al. [104]. In our research we propose to adopt the same technique to measure the sensing parameter. The measurement technique can be implemented in CMOS technology and it can be combined with other analog instrumentation technology for higher level integration. The measurement simulation presented here was done using C35B4 CMOS technology.

The advantages of this measurement technique are:

- Implementation can be integrated with other analog circuitry in CMOS technology.
- Charging and discharging of capacitance are done simultaneously without any additional effort of switching.
- The technique is valid for a wide range of frequency measurements.
- It is easy to implement as only two wire connections are required to the MEMS sensor.

The technique proposed uses an on-board measurement circuit comprising two pairs of PMOS and NMOS transistors connected in the pseudo-inverter form, each having their own gate input, as shown in Figure D.0.1.

Both of the pseudo-inverters are similar in size. The first pseudo-inverter is considered as a reference point. The second pseudo-inverter is connected to the MEMS capacitive sensor (C_{ST}) as its capacitive loading. The input signal V_1 is to control the NMOS transistor while V_2 is for the PMOS transistor. The V_1 and V_2 signals are non-overlapping signals, as shown in Figure D.0.2 (a) and (b). The non-overlapping signals are used to ensure that only one of the two transistors conducts the current at any given time. This can avoid any short circuit event from V_{DD} to ground.

A complete measurement cycle consists of two phases, namely charging and discharging. In the charging phase, the PMOS transistor is turned on while the NMOS

Switch State	Gap[μm]	C_{SL} [fF]	C_{Sense}[fF]	C_{ST} [fF]
Off (Open)	10	0.9423	6.089	7.0313
On (Closed)	15	0.9423	4.107	5.0493

Table D.1.: C_{ST} value at various states

is turned off. The V_{DD} will charge up the parasitic capacitance in the transistor and the capacitance load from the ISE-DC-MEMS capacitive sensor.

During the discharging phase, the PMOS transistors are turned off so that there is no more current flow from the V_{DD}. The NMOS transistors are turned on, which discharges all the accumulated charges in the capacitance load to the ground.

The current consumed by both pseudo-inverter pairs can be measured and labelled as I_1 and I_2 respectively. Since both PMOS transistors are similar in size, the current I_1 represents the charge consumed by the parasitic capacitor in the transistor. The current I_2 is the combination of the parasitic capacitance and the capacitance load. Thus the current consumed by the MEMS capacitive sensor can be calculated by:

$$I_{Sense} = I_2 - I_1 \qquad \text{(D.0.1)}$$

As suggested in [104], the capacitance (C_{ST}) is the slope function of I_{Sense}, V_{DD} and frequency(f) with the following equation:

$$I_{Sense} = C_{ST} \cdot V_{DD} \cdot f \qquad \text{(D.0.2)}$$

Based on both equations above, a simulation was done to extract the information from during the measurement cycle. Table D.2 shows the I_{Sense} measurement with various values of C_{ST} obtained from Table D.1. Two types of information can be extracted from the simulations:

- I_{Sense} (Int) is the integration value measured at the specific charging time.
- I_{Sense} ($Peak$)is the peak value recorded during the charging time.

In this self-monitoring application, the sensor linearity is not important since it only monitors the state of movable structures in the MEMS body switch which produces two different gaps. The mismatch and parasitic effect of the transistors can be eliminated via calibration after complete integration. The calibration process will include these imperfection factors in the reference data that will be stored in the main controller.
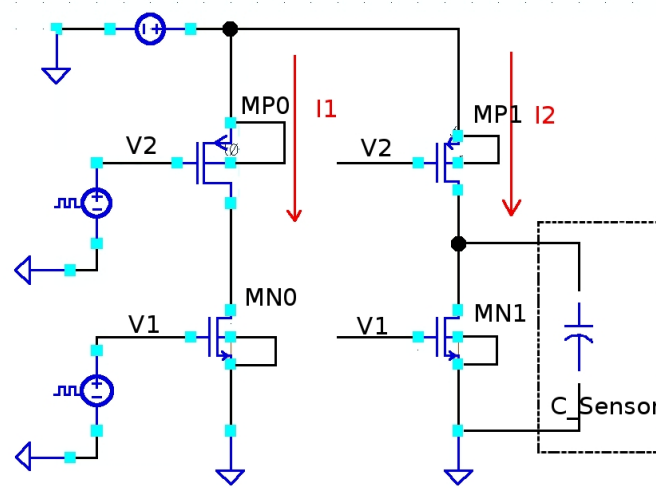
Figure D.0.1.: Circuit for sub-femto Farad range measurement

(a) Current integration measurement

Parameter	$C_{ST}[fF]$	
	7.0313	5.0493
$I_1\,(Int)[fA]$	172.2	175.2
$I_2\,(Int)[fA]$	262.8	256.3
$I_{Sense}\,(Int)[fA]$	87.65	81.12

(b) Peak current measurement

Parameter	$C_{ST}[fF]$	
	7.0313	5.0493
$I_1\,(Peak)[\mu A]$	214.11	214.3
$I_2\,(Peak)[\mu A]$	295.74	290.12
$I_{Sense}\,(Peak)[\mu A]$	81.63	75.82

Table D.2.: Output measurement with various C_{ST} values
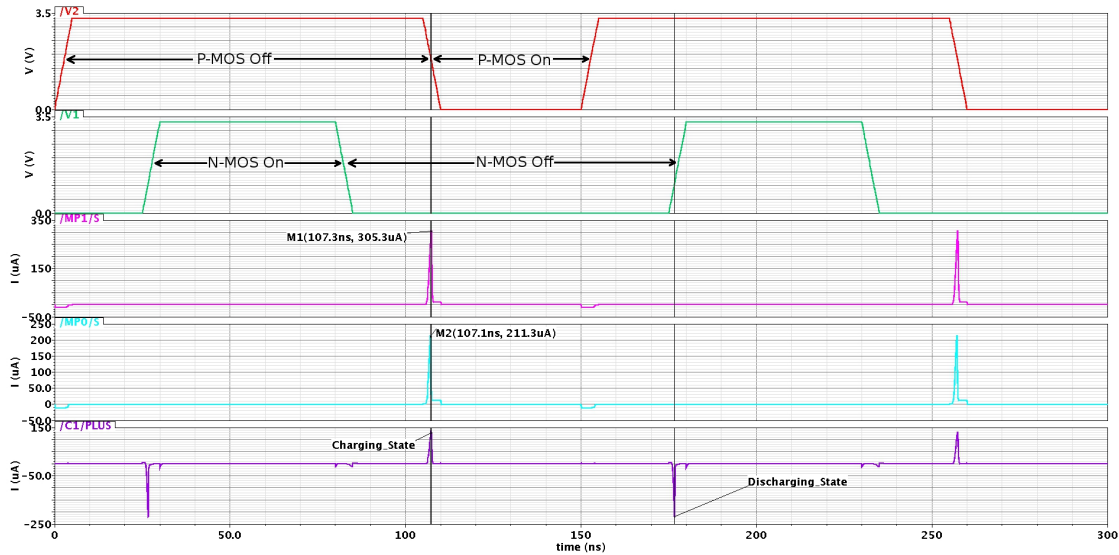
Figure D.0.2.: Measurement cycle of proposed self-monitoring features in ISE-DC-MEMS switch

E. MEMS+ Model Netlist

This appendix shows an example of a netlist generated for Spectre by MEMS+ software when a MEMS+ design is imported to a Cadence simulation system. The netlist shown here is taken from SPST-V1 of the ISE-DC-MEMS switch.

Algorithm E.1 Netlist of SPST ISE-DC MEMS switch

```
1  //Netlist automatically generated for spectre by MEMS+ //Please
   to not edit. //Generated on: Tue Dec 17 09:54:03 2013 // subckt
   SPSTPara2 ( Act1R Act2L Contact1A Contact1B GndL GndR MonA1
   MonAGnd MonB1 MonBGnD  )
2     parameters NicThic=20 T=293.15 AdhesionSoftening=0.01
       AnchorWidth=50 AnchorLength=150 AnchorBCtrY=100 AnchorBleng
       =1000 AnchorBWid=10 AnchorOffWid=0 AnchorOffWidY=20
       MassCombLength=670 MassCombWidth=60 MassCombFngerLeng=800
       MassCombDelY=20 StatorOffset=5 StatorAnchWidth=100 StatorGap
       =25 ContGap=5 ContY=600 ContTX=150 ContTY=60 HeatActColdW=10
        HeatActHotW=20 HeatActBL1=220 HeatActBL2=10 SerpAncAngel=10
        SerpAncBeamLength=300 SerpAncAxisY=100 SerpAncWidPar=10
       SerpAncWidPer=10 SerpAncAmpL=100 SerpAncAmpR=75 SerpAncPitch
       =30 LX1=50 LX2=100 LY1=125 LY2=0 LX3=150 ContSoftening=0.05
       Scene3DfileBasename="./scene3d" SuggestScaling=no
3     I0_schematic_manager_0 _schematic_managerV1 schematic_name="/
       home/akmal/003SPST/SPSTPar.3dsch" search=no global_values00=
       NicThic global_values01=T global_values02=AdhesionSoftening
       global_values03=AnchorWidth global_values04=AnchorLength
       global_values05=AnchorBCtrY global_values06=AnchorBleng
       global_values07=AnchorBWid global_values08=AnchorOffWid
       global_values09=AnchorOffWidY global_values10=MassCombLength
        global_values11=MassCombWidth global_values12=
       MassCombFngerLeng global_values13=MassCombDelY
       global_values14=StatorOffset global_values15=StatorAnchWidth
        global_values16=StatorGap global_values17=ContGap
       global_values18=ContY global_values19=ContTX global_values20
       =ContTY global_values21=HeatActColdW global_values22=
       HeatActHotW global_values23=HeatActBL1 global_values24=
       HeatActBL2 global_values25=SerpAncAngel global_values26=
       SerpAncBeamLength global_values27=SerpAncAxisY
       global_values28=SerpAncWidPar global_values29=SerpAncWidPer
       global_values30=SerpAncAmpL global_values31=SerpAncAmpR
       global_values32=SerpAncPitch global_values33=LX1
       global_values34=LX2 global_values35=LY1 global_values36=LY2
```

```
          global_values37=LX3 global_values38=ContSoftening
          global_names00="NicThic" global_names01="T" global_names02="
          AdhesionSoftening" global_names03="AnchorWidth"
          global_names04="AnchorLength" global_names05="AnchorBCtrY"
          global_names06="AnchorBleng" global_names07="AnchorBWid"
          global_names08="AnchorOffWid" global_names09="AnchorOffWidY"
           global_names10="MassCombLength" global_names11="
          MassCombWidth" global_names12="MassCombFngerLeng"
          global_names13="MassCombDelY" global_names14="StatorOffset"
          global_names15="StatorAnchWidth" global_names16="StatorGap"
          global_names17="ContGap" global_names18="ContY"
          global_names19="ContTX" global_names20="ContTY"
          global_names21="HeatActColdW" global_names22="HeatActHotW"
          global_names23="HeatActBL1" global_names24="HeatActBL2"
          global_names25="SerpAncAngel" global_names26="
          SerpAncBeamLength" global_names27="SerpAncAxisY"
          global_names28="SerpAncWidPar" global_names29="SerpAncWidPer
          " global_names30="SerpAncAmpL" global_names31="SerpAncAmpR"
          global_names32="SerpAncPitch" global_names33="LX1"
          global_names34="LX2" global_names35="LY1" global_names36="
          LY2" global_names37="LX3" global_names38="ContSoftening"
          version=2.1 result_file_basename=Scene3DfileBasename
          suggest_scaling=SuggestScaling
4    I1_LocalFrame_SPST2A_RigidPlate_MassComb ( M189x M189y M189z
          M189rx M189ry M189rz M189vx M189vy M189vz M189vrx M189vry
          M189vrz M189ax M189ay M189az M189arx M189ary M189arz 0 0 0 0
           0 0 0 0 ) NonlinearRigidPlate name="/LocalFrame.SPST2A/
          RigidPlate.MassComb"
5    I1_LocalFrame_SPST2A_RigidPlate_MassComb_StraightCombSegment_
          CombD_StraightCombStator_StraightCombStator1 ( M189x M189y
          M189z M189rx M189ry M189rz GndL Act2L 0 0 )
          StraightCombSingleStator name="/LocalFrame.SPST2A/RigidPlate
          .MassComb/StraightCombSegment.CombD/StraightCombStator.
          StraightCombStator1"
6    I1_LocalFrame_SPST2A_RigidPlate_MassComb_StraightCombSegment_
          CombU_StraightCombStator_StraightCombStator1 ( M189x M189y
          M189z M189rx M189ry M189rz GndL Act2L 0 0 )
          StraightCombSingleStator name="/LocalFrame.SPST2A/RigidPlate
          .MassComb/StraightCombSegment.CombU/StraightCombStator.
          StraightCombStator1"
7    I1_LocalFrame_SPST2A_RigidPlate_MassComb_RectangularSegment_
          ContactR1_RectangularSegmentSideElectrode_SideElectrodeContact2
           ( M189x M189y M189z M189rx M189ry M189rz Contact1A
          Contact1B ) RigidPlateSideElectrode name="/LocalFrame.SPST2A
          /RigidPlate.MassComb/RectangularSegment.ContactR1/
          RectangularSegmentSideElectrode.SideElectrodeContact2"
8    I1_LocalFrame_SPST2A_RigidPlate_MassComb_RectangularSegment_
          ContactL1_RectangularSegmentSideElectrode_SideElectrodeContact2
           ( M189x M189y M189z M189rx M189ry M189rz MonAGnd MonA1 )
          RigidPlateSideElectrode name="/LocalFrame.SPST2A/RigidPlate.
          MassComb/RectangularSegment.ContactL1/
          RectangularSegmentSideElectrode.SideElectrodeContact2"
```

```
 9    I1_LocalFrame_SPST2A_LocalFrame_SigLine2_RectangularPlate_AncB11
         ( M2x M2y M2z M2rx M2ry M2rz M189x M189y M189z M189rx
      M189ry M189rz M31x M31y M31z M31rx M31ry M31rz M2x M2y M2z
      M2rx M2ry M2rz M189x M189y M189z M189rx M189ry M189rz M31x
      M31y M31z M31rx M31ry M31rz M2vx M2vy M2vz M2vrx M2vry M2vrz
       M189vx M189vy M189vz M189vrx M189vry M189vrz M31vx M31vy
      M31vz M31vrx M31vry M31vrz M2vx M2vy M2vz M2vrx M2vry M2vrz
      M189vx M189vy M189vz M189vrx M189vry M189vrz M31vx M31vy
      M31vz M31vrx M31vry M31vrz 0 0 0 0 0 0 )
      LinearFlexiblePlateOrderR2S1 name="/LocalFrame.SPST2A/
      LocalFrame.SigLine2/RectangularPlate.AncB11"
10    I1_LocalFrame_SPST2A_LocalFrame_SigLine2_RectangularPlate_AncB13
         ( M7x M7y M7z M7rx M7ry M7rz M189x M189y M189z M189rx
      M189ry M189rz M5x M5y M5z M5rx M5ry M5rz M7x M7y M7z M7rx
      M7ry M7rz M189x M189y M189z M189rx M189ry M189rz M5x M5y M5z
       M5rx M5ry M5rz M7vx M7vy M7vz M7vrx M7vry M7vrz M189vx
      M189vy M189vz M189vrx M189vry M189vrz M5vx M5vy M5vz M5vrx
      M5vry M5vrz M7vx M7vy M7vz M7vrx M7vry M7vrz M189vx M189vy
      M189vz M189vrx M189vry M189vrz M5vx M5vy M5vz M5vrx M5vry
      M5vrz 0 0 0 0 0 0 ) LinearFlexiblePlateOrderR2S1 name="/
      LocalFrame.SPST2A/LocalFrame.SigLine2/RectangularPlate.
      AncB13"
11    I1_LocalFrame_SPST2A_LocalFrame_SigLine2_ByPointsBeam_BeamPath11
         ( M31x M31y M31z M31rx M31ry M31rz 0 0 0 0 0 0 M31vx M31vy
      M31vz M31vrx M31vry M31vrz 0 0 0 0 0 0 M31ax M31ay M31az
      M31arx M31ary M31arz 0 0 0 0 0 0 0 0 0 0 0 0 )
      NonlinearSuspension2Node name="/LocalFrame.SPST2A/LocalFrame
      .SigLine2/ByPointsBeam.BeamPath11"
12    I1_LocalFrame_SPST2A_LocalFrame_SigLine2_ByPointsBeam_BeamPath12
         ( M2x M2y M2z M2rx M2ry M2rz 0 0 0 0 0 0 M2vx M2vy M2vz
      M2vrx M2vry M2vrz 0 0 0 0 0 0 M2ax M2ay M2az M2arx M2ary
      M2arz 0 0 0 0 0 0 0 0 0 0 0 0 )
      NonlinearSuspension2Node name="/LocalFrame.SPST2A/LocalFrame
      .SigLine2/ByPointsBeam.BeamPath12"
13    I1_LocalFrame_SPST2A_LocalFrame_SigLine2_ByPointsBeam_BeamPath21
         ( M5x M5y M5z M5rx M5ry M5rz 0 0 0 0 0 0 M5vx M5vy M5vz
      M5vrx M5vry M5vrz 0 0 0 0 0 0 M5ax M5ay M5az M5arx M5ary
      M5arz 0 0 0 0 0 0 0 0 0 0 0 0 )
      NonlinearSuspension2Node name="/LocalFrame.SPST2A/LocalFrame
      .SigLine2/ByPointsBeam.BeamPath21"
14    I1_LocalFrame_SPST2A_LocalFrame_SigLine2_ByPointsBeam_BeamPath22
         ( M7x M7y M7z M7rx M7ry M7rz 0 0 0 0 0 0 M7vx M7vy M7vz
      M7vrx M7vry M7vrz 0 0 0 0 0 0 M7ax M7ay M7az M7arx M7ary
      M7arz 0 0 0 0 0 0 0 0 0 0 0 0 )
      NonlinearSuspension2Node name="/LocalFrame.SPST2A/LocalFrame
      .SigLine2/ByPointsBeam.BeamPath22"
15    I1_LocalFrame_SPST2A_LocalFrame_SigLine1_RectangularPlate_AncB11
         ( M23x M23y M23z M23rx M23ry M23rz M189x M189y M189z M189rx
       M189ry M189rz M21x M21y M21z M21rx M21ry M21rz M23x M23y
      M23z M23rx M23ry M23rz M189x M189y M189z M189rx M189ry
      M189rz M21x M21y M21z M21rx M21ry M21rz M23vx M23vy M23vz
      M23vrx M23vry M23vrz M189vx M189vy M189vz M189vrx M189vry
```

```
         M189vrz M21vx M21vy M21vz M21vrx M21vry M21vrz M23vx M23vy
         M23vz M23vrx M23vry M23vrz M189vx M189vy M189vz M189vrx
         M189vry M189vrz M21vx M21vy M21vz M21vrx M21vry M21vrz 0 0 0
         0 0 0 ) LinearFlexiblePlateOrderR2S1 name="/LocalFrame.
         SPST2A/LocalFrame.SigLine1/RectangularPlate.AncB11"
16    I1_LocalFrame_SPST2A_LocalFrame_SigLine1_RectangularPlate_AncB13
         ( M27x M27y M27z M27rx M27ry M27rz M189x M189y M189z M189rx
          M189ry M189rz M25x M25y M25z M25rx M25ry M25rz M27x M27y
         M27z M27rx M27ry M27rz M189x M189y M189z M189rx M189ry
         M189rz M25x M25y M25z M25rx M25ry M25rz M27vx M27vy M27vz
         M27vrx M27vry M27vrz M189vx M189vy M189vz M189vrx M189vry
         M189vrz M25vx M25vy M25vz M25vrx M25vry M25vrz M27vx M27vy
         M27vz M27vrx M27vry M27vrz M189vx M189vy M189vz M189vrx
         M189vry M189vrz M25vx M25vy M25vz M25vrx M25vry M25vrz 0 0 0
         0 0 0 ) LinearFlexiblePlateOrderR2S1 name="/LocalFrame.
         SPST2A/LocalFrame.SigLine1/RectangularPlate.AncB13"
17    I1_LocalFrame_SPST2A_LocalFrame_SigLine1_ByPointsBeam_BeamPath11
         ( M21x M21y M21z M21rx M21ry M21rz 0 0 0 0 0 0 M21vx M21vy
         M21vz M21vrx M21vry M21vrz 0 0 0 0 0 0 M21ax M21ay M21az
         M21arx M21ary M21arz 0 0 0 0 0 0 0 0 0 0 0 0 0 0 0 )
         NonlinearSuspension2Node name="/LocalFrame.SPST2A/LocalFrame
         .SigLine1/ByPointsBeam.BeamPath11"
18    I1_LocalFrame_SPST2A_LocalFrame_SigLine1_ByPointsBeam_BeamPath12
         ( M23x M23y M23z M23rx M23ry M23rz 0 0 0 0 0 0 M23vx M23vy
         M23vz M23vrx M23vry M23vrz 0 0 0 0 0 0 M23ax M23ay M23az
         M23arx M23ary M23arz 0 0 0 0 0 0 0 0 0 0 0 0 0 0 0 )
         NonlinearSuspension2Node name="/LocalFrame.SPST2A/LocalFrame
         .SigLine1/ByPointsBeam.BeamPath12"
19    I1_LocalFrame_SPST2A_LocalFrame_SigLine1_ByPointsBeam_BeamPath21
         ( M25x M25y M25z M25rx M25ry M25rz 0 0 0 0 0 0 M25vx M25vy
         M25vz M25vrx M25vry M25vrz 0 0 0 0 0 0 M25ax M25ay M25az
         M25arx M25ary M25arz 0 0 0 0 0 0 0 0 0 0 0 0 0 0 0 )
         NonlinearSuspension2Node name="/LocalFrame.SPST2A/LocalFrame
         .SigLine1/ByPointsBeam.BeamPath21"
20    I1_LocalFrame_SPST2A_LocalFrame_SigLine1_ByPointsBeam_BeamPath22
         ( M27x M27y M27z M27rx M27ry M27rz 0 0 0 0 0 0 M27vx M27vy
         M27vz M27vrx M27vry M27vrz 0 0 0 0 0 0 M27ax M27ay M27az
         M27arx M27ary M27arz 0 0 0 0 0 0 0 0 0 0 0 0 0 0 0 )
         NonlinearSuspension2Node name="/LocalFrame.SPST2A/LocalFrame
         .SigLine1/ByPointsBeam.BeamPath22"
21    I1_LocalFrame_SPST2B_RigidPlate_MassComb ( M1x M1y M1z M1rx
         M1ry M1rz M1vx M1vy M1vz M1vrx M1vry M1vrz M1ax M1ay M1az
         M1arx M1ary M1arz 0 0 0 0 0 0 0 0 ) NonlinearRigidPlate
         name="/LocalFrame.SPST2B/RigidPlate.MassComb"
22    I1_LocalFrame_SPST2B_RigidPlate_MassComb_StraightCombSegment_
         CombD_StraightCombStator_StraightCombStator1 ( M1x M1y M1z
         M1rx M1ry M1rz GndR Act1R 0 0 ) StraightCombSingleStator
         name="/LocalFrame.SPST2B/RigidPlate.MassComb/
         StraightCombSegment.CombD/StraightCombStator.
         StraightCombStator1"
23    I1_LocalFrame_SPST2B_RigidPlate_MassComb_StraightCombSegment_
         CombU_StraightCombStator_StraightCombStator1 ( M1x M1y M1z
```

```
        M1rx M1ry M1rz GndR Act1R 0 0 ) StraightCombSingleStator
        name="/LocalFrame.SPST2B/RigidPlate.MassComb/
        StraightCombSegment.CombU/StraightCombStator.
        StraightCombStator1"
24      I1_LocalFrame_SPST2B_RigidPlate_MassComb_RectangularSegment_
        ContactR1_RectangularSegmentSideElectrode_SideElectrodeContact2
        ( M1x M1y M1z M1rx M1ry M1rz 0  0  )
        RigidPlateSideElectrode name="/LocalFrame.SPST2B/RigidPlate.
        MassComb/RectangularSegment.ContactR1/
        RectangularSegmentSideElectrode.SideElectrodeContact2"
25      I1_LocalFrame_SPST2B_RigidPlate_MassComb_RectangularSegment_
        ContactL1_RectangularSegmentSideElectrode_SideElectrodeContact2
        ( M1x M1y M1z M1rx M1ry M1rz MonBGnD MonB1 )
        RigidPlateSideElectrode name="/LocalFrame.SPST2B/RigidPlate.
        MassComb/RectangularSegment.ContactL1/
        RectangularSegmentSideElectrode.SideElectrodeContact2"
26      I1_LocalFrame_SPST2B_LocalFrame_SigLine2_RectangularPlate_AncB11
        ( M33x M33y M33z M33rx M33ry M33rz M1x M1y M1z M1rx M1ry
        M1rz M20x M20y M20z M20rx M20ry M20rz M33x M33y M33z M33rx
        M33ry M33rz M1x M1y M1z M1rx M1ry M1rz M20x M20y M20z M20rx
        M20ry M20rz M33vx M33vy M33vz M33vrx M33vry M33vrz M1vx M1vy
        M1vz M1vrx M1vry M1vrz M20vx M20vy M20vz M20vrx M20vry
        M20vrz M33vx M33vy M33vz M33vrx M33vry M33vrz M1vx M1vy M1vz
        M1vrx M1vry M1vrz M20vx M20vy M20vz M20vrx M20vry M20vrz 0
        0 0 0 0 0 ) LinearFlexiblePlateOrderR2S1 name="/LocalFrame.
        SPST2B/LocalFrame.SigLine2/RectangularPlate.AncB11"
27      I1_LocalFrame_SPST2B_LocalFrame_SigLine2_RectangularPlate_AncB13
        ( M37x M37y M37z M37rx M37ry M37rz M1x M1y M1z M1rx M1ry
        M1rz M35x M35y M35z M35rx M35ry M35rz M37x M37y M37z M37rx
        M37ry M37rz M1x M1y M1z M1rx M1ry M1rz M35x M35y M35z M35rx
        M35ry M35rz M37vx M37vy M37vz M37vrx M37vry M37vrz M1vx M1vy
        M1vz M1vrx M1vry M1vrz M35vx M35vy M35vz M35vrx M35vry
        M35vrz M37vx M37vy M37vz M37vrx M37vry M37vrz M1vx M1vy M1vz
        M1vrx M1vry M1vrz M35vx M35vy M35vz M35vrx M35vry M35vrz 0
        0 0 0 0 0 ) LinearFlexiblePlateOrderR2S1 name="/LocalFrame.
        SPST2B/LocalFrame.SigLine2/RectangularPlate.AncB13"
28      I1_LocalFrame_SPST2B_LocalFrame_SigLine2_ByPointsBeam_BeamPath11
        ( M20x M20y M20z M20rx M20ry M20rz 0 0 0 0 0 0 M20vx M20vy
        M20vz M20vrx M20vry M20vrz 0 0 0 0 0 0 M20ax M20ay M20az
        M20arx M20ary M20arz 0 0 0 0 0 0 0 0 0 0 0 0 )
        NonlinearSuspension2Node name="/LocalFrame.SPST2B/LocalFrame
        .SigLine2/ByPointsBeam.BeamPath11"
29      I1_LocalFrame_SPST2B_LocalFrame_SigLine2_ByPointsBeam_BeamPath12
        ( M33x M33y M33z M33rx M33ry M33rz 0 0 0 0 0 0 M33vx M33vy
        M33vz M33vrx M33vry M33vrz 0 0 0 0 0 0 M33ax M33ay M33az
        M33arx M33ary M33arz 0 0 0 0 0 0 0 0 0 0 0 0 )
        NonlinearSuspension2Node name="/LocalFrame.SPST2B/LocalFrame
        .SigLine2/ByPointsBeam.BeamPath12"
30      I1_LocalFrame_SPST2B_LocalFrame_SigLine2_ByPointsBeam_BeamPath21
        ( M35x M35y M35z M35rx M35ry M35rz 0 0 0 0 0 0 M35vx M35vy
        M35vz M35vrx M35vry M35vrz 0 0 0 0 0 0 M35ax M35ay M35az
        M35arx M35ary M35arz 0 0 0 0 0 0 0 0 0 0 0 0 )
```

```
        NonlinearSuspension2Node name="/LocalFrame.SPST2B/LocalFrame
        .SigLine2/ByPointsBeam.BeamPath21"
31   I1_LocalFrame_SPST2B_LocalFrame_SigLine2_ByPointsBeam_BeamPath22
        ( M37x M37y M37z M37rx M37ry M37rz 0 0 0 0 0 0 M37vx M37vy
        M37vz M37vrx M37vry M37vrz 0 0 0 0 0 0 M37ax M37ay M37az
        M37arx M37ary M37arz 0 0 0 0 0 0 0 0 0 0 0 0 0 0 0 )
        NonlinearSuspension2Node name="/LocalFrame.SPST2B/LocalFrame
        .SigLine2/ByPointsBeam.BeamPath22"
32   I1_LocalFrame_SPST2B_LocalFrame_SigLine1_RectangularPlate_AncB11
        ( M61x M61y M61z M61rx M61ry M61rz M1x M1y M1z M1rx M1ry
        M1rz M59x M59y M59z M59rx M59ry M59rz M61x M61y M61z M61rx
        M61ry M61rz M1x M1y M1z M1rx M1ry M1rz M59x M59y M59z M59rx
        M59ry M59rz M61vx M61vy M61vz M61vrx M61vry M61vrz M1vx M1vy
         M1vz M1vrx M1vry M1vrz M59vx M59vy M59vz M59vrx M59vry
        M59vrz M61vx M61vy M61vz M61vrx M61vry M61vrz M1vx M1vy M1vz
         M1vrx M1vry M1vrz M59vx M59vy M59vz M59vrx M59vry M59vrz 0
        0 0 0 0 0 ) LinearFlexiblePlateOrderR2S1 name="/LocalFrame.
        SPST2B/LocalFrame.SigLine1/RectangularPlate.AncB11"
33   I1_LocalFrame_SPST2B_LocalFrame_SigLine1_RectangularPlate_AncB13
        ( M65x M65y M65z M65rx M65ry M65rz M1x M1y M1z M1rx M1ry
        M1rz M63x M63y M63z M63rx M63ry M63rz M65x M65y M65z M65rx
        M65ry M65rz M1x M1y M1z M1rx M1ry M1rz M63x M63y M63z M63rx
        M63ry M63rz M65vx M65vy M65vz M65vrx M65vry M65vrz M1vx M1vy
         M1vz M1vrx M1vry M1vrz M63vx M63vy M63vz M63vrx M63vry
        M63vrz M65vx M65vy M65vz M65vrx M65vry M65vrz M1vx M1vy M1vz
         M1vrx M1vry M1vrz M63vx M63vy M63vz M63vrx M63vry M63vrz 0
        0 0 0 0 0 ) LinearFlexiblePlateOrderR2S1 name="/LocalFrame.
        SPST2B/LocalFrame.SigLine1/RectangularPlate.AncB13"
34   I1_LocalFrame_SPST2B_LocalFrame_SigLine1_ByPointsBeam_BeamPath11
        ( M59x M59y M59z M59rx M59ry M59rz 0 0 0 0 0 0 M59vx M59vy
        M59vz M59vrx M59vry M59vrz 0 0 0 0 0 0 M59ax M59ay M59az
        M59arx M59ary M59arz 0 0 0 0 0 0 0 0 0 0 0 0 0 0 0 )
        NonlinearSuspension2Node name="/LocalFrame.SPST2B/LocalFrame
        .SigLine1/ByPointsBeam.BeamPath11"
35   I1_LocalFrame_SPST2B_LocalFrame_SigLine1_ByPointsBeam_BeamPath12
        ( M61x M61y M61z M61rx M61ry M61rz 0 0 0 0 0 0 M61vx M61vy
        M61vz M61vrx M61vry M61vrz 0 0 0 0 0 0 M61ax M61ay M61az
        M61arx M61ary M61arz 0 0 0 0 0 0 0 0 0 0 0 0 0 0 0 )
        NonlinearSuspension2Node name="/LocalFrame.SPST2B/LocalFrame
        .SigLine1/ByPointsBeam.BeamPath12"
36   I1_LocalFrame_SPST2B_LocalFrame_SigLine1_ByPointsBeam_BeamPath21
        ( M63x M63y M63z M63rx M63ry M63rz 0 0 0 0 0 0 M63vx M63vy
        M63vz M63vrx M63vry M63vrz 0 0 0 0 0 0 M63ax M63ay M63az
        M63arx M63ary M63arz 0 0 0 0 0 0 0 0 0 0 0 0 0 0 0 )
        NonlinearSuspension2Node name="/LocalFrame.SPST2B/LocalFrame
        .SigLine1/ByPointsBeam.BeamPath21"
37   I1_LocalFrame_SPST2B_LocalFrame_SigLine1_ByPointsBeam_BeamPath22
        ( M65x M65y M65z M65rx M65ry M65rz 0 0 0 0 0 0 M65vx M65vy
        M65vz M65vrx M65vry M65vrz 0 0 0 0 0 0 M65ax M65ay M65az
        M65arx M65ary M65arz 0 0 0 0 0 0 0 0 0 0 0 0 0 0 0 )
        NonlinearSuspension2Node name="/LocalFrame.SPST2B/LocalFrame
        .SigLine1/ByPointsBeam.BeamPath22"
```

```
38    I1_M1_x ( 0 M1x M1vx M1ax ) NonlinearMechanicalDOF name="/M1x
      "  I1_M1_y ( 0 M1y M1vy M1ay ) NonlinearMechanicalDOF name
      ="/M1y"  I1_M1_z ( 0 M1z M1vz M1az ) NonlinearMechanicalDOF
      name="/M1z"  I1_M1_rx ( 0 M1rx M1vrx M1arx )
      NonlinearMechanicalDOF name="/M1rx"    I1_M1_ry ( 0 M1ry
      M1vry M1ary ) NonlinearMechanicalDOF name="/M1ry"
      I1_M1_rz ( 0 M1rz M1vrz M1arz ) NonlinearMechanicalDOF name
      ="/M1rz"
39    I1_M2_x ( 0 M2x M2vx M2ax ) NonlinearMechanicalDOF name="/M2x
      "  I1_M2_y ( 0 M2y M2vy M2ay ) NonlinearMechanicalDOF name
      ="/M2y"  I1_M2_z ( 0 M2z M2vz M2az ) NonlinearMechanicalDOF
      name="/M2z"  I1_M2_rx ( 0 M2rx M2vrx M2arx )
      NonlinearMechanicalDOF name="/M2rx"    I1_M2_ry ( 0 M2ry
      M2vry M2ary ) NonlinearMechanicalDOF name="/M2ry"
      I1_M2_rz ( 0 M2rz M2vrz M2arz ) NonlinearMechanicalDOF name
      ="/M2rz"
40    I1_M5_x ( 0 M5x M5vx M5ax ) NonlinearMechanicalDOF name="/M5x
      "  I1_M5_y ( 0 M5y M5vy M5ay ) NonlinearMechanicalDOF name
      ="/M5y"  I1_M5_z ( 0 M5z M5vz M5az ) NonlinearMechanicalDOF
      name="/M5z"  I1_M5_rx ( 0 M5rx M5vrx M5arx )
      NonlinearMechanicalDOF name="/M5rx"    I1_M5_ry ( 0 M5ry
      M5vry M5ary ) NonlinearMechanicalDOF name="/M5ry"
      I1_M5_rz ( 0 M5rz M5vrz M5arz ) NonlinearMechanicalDOF name
      ="/M5rz"
41    I1_M7_x ( 0 M7x M7vx M7ax ) NonlinearMechanicalDOF name="/M7x
      "  I1_M7_y ( 0 M7y M7vy M7ay ) NonlinearMechanicalDOF name
      ="/M7y"  I1_M7_z ( 0 M7z M7vz M7az ) NonlinearMechanicalDOF
      name="/M7z"  I1_M7_rx ( 0 M7rx M7vrx M7arx )
      NonlinearMechanicalDOF name="/M7rx"    I1_M7_ry ( 0 M7ry
      M7vry M7ary ) NonlinearMechanicalDOF name="/M7ry"
      I1_M7_rz ( 0 M7rz M7vrz M7arz ) NonlinearMechanicalDOF name
      ="/M7rz"
42    I1_M20_x ( 0 M20x M20vx M20ax ) NonlinearMechanicalDOF name
      ="/M20x"    I1_M20_y ( 0 M20y M20vy M20ay )
      NonlinearMechanicalDOF name="/M20y"    I1_M20_z ( 0 M20z
      M20vz M20az ) NonlinearMechanicalDOF name="/M20z"
      I1_M20_rx ( 0 M20rx M20vrx M20arx ) NonlinearMechanicalDOF
      name="/M20rx"    I1_M20_ry ( 0 M20ry M20vry M20ary )
      NonlinearMechanicalDOF name="/M20ry"    I1_M20_rz ( 0 M20rz
      M20vrz M20arz ) NonlinearMechanicalDOF name="/M20rz"
43    I1_M21_x ( 0 M21x M21vx M21ax ) NonlinearMechanicalDOF name
      ="/M21x"    I1_M21_y ( 0 M21y M21vy M21ay )
      NonlinearMechanicalDOF name="/M21y"    I1_M21_z ( 0 M21z
      M21vz M21az ) NonlinearMechanicalDOF name="/M21z"
      I1_M21_rx ( 0 M21rx M21vrx M21arx ) NonlinearMechanicalDOF
      name="/M21rx"    I1_M21_ry ( 0 M21ry M21vry M21ary )
      NonlinearMechanicalDOF name="/M21ry"    I1_M21_rz ( 0 M21rz
      M21vrz M21arz ) NonlinearMechanicalDOF name="/M21rz"
44    I1_M23_x ( 0 M23x M23vx M23ax ) NonlinearMechanicalDOF name
      ="/M23x"    I1_M23_y ( 0 M23y M23vy M23ay )
      NonlinearMechanicalDOF name="/M23y"    I1_M23_z ( 0 M23z
      M23vz M23az ) NonlinearMechanicalDOF name="/M23z"
```

```
       I1_M23_rx ( 0 M23rx M23vrx M23arx ) NonlinearMechanicalDOF
          name="/M23rx"    I1_M23_ry ( 0 M23ry M23vry M23ary )
          NonlinearMechanicalDOF name="/M23ry"    I1_M23_rz ( 0 M23rz
          M23vrz M23arz ) NonlinearMechanicalDOF name="/M23rz"
45     I1_M25_x ( 0 M25x M25vx M25ax ) NonlinearMechanicalDOF name
          ="/M25x"     I1_M25_y ( 0 M25y M25vy M25ay )
          NonlinearMechanicalDOF name="/M25y"    I1_M25_z ( 0 M25z
          M25vz M25az ) NonlinearMechanicalDOF name="/M25z"
          I1_M25_rx ( 0 M25rx M25vrx M25arx ) NonlinearMechanicalDOF
          name="/M25rx"    I1_M25_ry ( 0 M25ry M25vry M25ary )
          NonlinearMechanicalDOF name="/M25ry"    I1_M25_rz ( 0 M25rz
          M25vrz M25arz ) NonlinearMechanicalDOF name="/M25rz"
46     I1_M27_x ( 0 M27x M27vx M27ax ) NonlinearMechanicalDOF name
          ="/M27x"     I1_M27_y ( 0 M27y M27vy M27ay )
          NonlinearMechanicalDOF name="/M27y"    I1_M27_z ( 0 M27z
          M27vz M27az ) NonlinearMechanicalDOF name="/M27z"
          I1_M27_rx ( 0 M27rx M27vrx M27arx ) NonlinearMechanicalDOF
          name="/M27rx"    I1_M27_ry ( 0 M27ry M27vry M27ary )
          NonlinearMechanicalDOF name="/M27ry"    I1_M27_rz ( 0 M27rz
          M27vrz M27arz ) NonlinearMechanicalDOF name="/M27rz"
47     I1_M31_x ( 0 M31x M31vx M31ax ) NonlinearMechanicalDOF name
          ="/M31x"     I1_M31_y ( 0 M31y M31vy M31ay )
          NonlinearMechanicalDOF name="/M31y"    I1_M31_z ( 0 M31z
          M31vz M31az ) NonlinearMechanicalDOF name="/M31z"
          I1_M31_rx ( 0 M31rx M31vrx M31arx ) NonlinearMechanicalDOF
          name="/M31rx"    I1_M31_ry ( 0 M31ry M31vry M31ary )
          NonlinearMechanicalDOF name="/M31ry"    I1_M31_rz ( 0 M31rz
          M31vrz M31arz ) NonlinearMechanicalDOF name="/M31rz"
48     I1_M33_x ( 0 M33x M33vx M33ax ) NonlinearMechanicalDOF name
          ="/M33x"     I1_M33_y ( 0 M33y M33vy M33ay )
          NonlinearMechanicalDOF name="/M33y"    I1_M33_z ( 0 M33z
          M33vz M33az ) NonlinearMechanicalDOF name="/M33z"
          I1_M33_rx ( 0 M33rx M33vrx M33arx ) NonlinearMechanicalDOF
          name="/M33rx"    I1_M33_ry ( 0 M33ry M33vry M33ary )
          NonlinearMechanicalDOF name="/M33ry"    I1_M33_rz ( 0 M33rz
          M33vrz M33arz ) NonlinearMechanicalDOF name="/M33rz"
49     I1_M35_x ( 0 M35x M35vx M35ax ) NonlinearMechanicalDOF name
          ="/M35x"     I1_M35_y ( 0 M35y M35vy M35ay )
          NonlinearMechanicalDOF name="/M35y"    I1_M35_z ( 0 M35z
          M35vz M35az ) NonlinearMechanicalDOF name="/M35z"
          I1_M35_rx ( 0 M35rx M35vrx M35arx ) NonlinearMechanicalDOF
          name="/M35rx"    I1_M35_ry ( 0 M35ry M35vry M35ary )
          NonlinearMechanicalDOF name="/M35ry"    I1_M35_rz ( 0 M35rz
          M35vrz M35arz ) NonlinearMechanicalDOF name="/M35rz"
50     I1_M37_x ( 0 M37x M37vx M37ax ) NonlinearMechanicalDOF name
          ="/M37x"     I1_M37_y ( 0 M37y M37vy M37ay )
          NonlinearMechanicalDOF name="/M37y"    I1_M37_z ( 0 M37z
          M37vz M37az ) NonlinearMechanicalDOF name="/M37z"
          I1_M37_rx ( 0 M37rx M37vrx M37arx ) NonlinearMechanicalDOF
          name="/M37rx"    I1_M37_ry ( 0 M37ry M37vry M37ary )
          NonlinearMechanicalDOF name="/M37ry"    I1_M37_rz ( 0 M37rz
          M37vrz M37arz ) NonlinearMechanicalDOF name="/M37rz"
```

```
51    I1_M59_x ( 0 M59x M59vx M59ax ) NonlinearMechanicalDOF name
        ="/M59x"      I1_M59_y ( 0 M59y M59vy M59ay )
      NonlinearMechanicalDOF name="/M59y"      I1_M59_z ( 0 M59z
      M59vz M59az ) NonlinearMechanicalDOF name="/M59z"
      I1_M59_rx ( 0 M59rx M59vrx M59arx ) NonlinearMechanicalDOF
      name="/M59rx"      I1_M59_ry ( 0 M59ry M59vry M59ary )
      NonlinearMechanicalDOF name="/M59ry"      I1_M59_rz ( 0 M59rz
      M59vrz M59arz ) NonlinearMechanicalDOF name="/M59rz"
52    I1_M61_x ( 0 M61x M61vx M61ax ) NonlinearMechanicalDOF name
        ="/M61x"      I1_M61_y ( 0 M61y M61vy M61ay )
      NonlinearMechanicalDOF name="/M61y"      I1_M61_z ( 0 M61z
      M61vz M61az ) NonlinearMechanicalDOF name="/M61z"
      I1_M61_rx ( 0 M61rx M61vrx M61arx ) NonlinearMechanicalDOF
      name="/M61rx"      I1_M61_ry ( 0 M61ry M61vry M61ary )
      NonlinearMechanicalDOF name="/M61ry"      I1_M61_rz ( 0 M61rz
      M61vrz M61arz ) NonlinearMechanicalDOF name="/M61rz"
53    I1_M63_x ( 0 M63x M63vx M63ax ) NonlinearMechanicalDOF name
        ="/M63x"      I1_M63_y ( 0 M63y M63vy M63ay )
      NonlinearMechanicalDOF name="/M63y"      I1_M63_z ( 0 M63z
      M63vz M63az ) NonlinearMechanicalDOF name="/M63z"
      I1_M63_rx ( 0 M63rx M63vrx M63arx ) NonlinearMechanicalDOF
      name="/M63rx"      I1_M63_ry ( 0 M63ry M63vry M63ary )
      NonlinearMechanicalDOF name="/M63ry"      I1_M63_rz ( 0 M63rz
      M63vrz M63arz ) NonlinearMechanicalDOF name="/M63rz"
54    I1_M65_x ( 0 M65x M65vx M65ax ) NonlinearMechanicalDOF name
        ="/M65x"      I1_M65_y ( 0 M65y M65vy M65ay )
      NonlinearMechanicalDOF name="/M65y"      I1_M65_z ( 0 M65z
      M65vz M65az ) NonlinearMechanicalDOF name="/M65z"
      I1_M65_rx ( 0 M65rx M65vrx M65arx ) NonlinearMechanicalDOF
      name="/M65rx"      I1_M65_ry ( 0 M65ry M65vry M65ary )
      NonlinearMechanicalDOF name="/M65ry"      I1_M65_rz ( 0 M65rz
      M65vrz M65arz ) NonlinearMechanicalDOF name="/M65rz"
55    I1_M189_x ( 0 M189x M189vx M189ax ) NonlinearMechanicalDOF
        name="/M189x"      I1_M189_y ( 0 M189y M189vy M189ay )
      NonlinearMechanicalDOF name="/M189y"      I1_M189_z ( 0 M189z
      M189vz M189az ) NonlinearMechanicalDOF name="/M189z"
      I1_M189_rx ( 0 M189rx M189vrx M189arx )
      NonlinearMechanicalDOF name="/M189rx"    I1_M189_ry ( 0
      M189ry M189vry M189ary ) NonlinearMechanicalDOF name="/
      M189ry"    I1_M189_rz ( 0 M189rz M189vrz M189arz )
      NonlinearMechanicalDOF name="/M189rz"
56  ends
```

Bibliography

[1] C. von der Malsburg. Self organization of orientation sensitive cells in the striate cortex. *Kybernetik*, (14):85–100, 1973. Springer Verlag.

[2] Organic computing: Computer und system architektur im jahr 2010. *VDE/ITG/GI-Position Paper*, page 6, 2003.

[3] A. D. King. Inertial navigation-forty years of evolution. *GEC review*, 13(3):140–149, 1998.

[4] M. Perlmutter and L. Robin. High-performance, low cost inertial $MEMS$: A market in motion! In *Position Location and Navigation Symposium (PLANS), 2012 IEEE/ION*, pages 225–229, 2012.

[5] N. Barbour and G. Schmidt. Inertial sensor technology trends. *Sensors Journal, IEEE*, 1(4):332–339, 2001.

[6] M. Pourhomayoun, M. Fowler, and Zhanpeng Jin. A novel method for medical implant in-body localization. In *Engineering in Medicine and Biology Society (EMBC), 2012 Annual International Conference of the IEEE*, pages 5757–5760, 2012.

[7] H. Schmeck. Organic computing - a new vision for distributed embedded systems. In *Eighth IEEE International Symposium on Object-Oriented Real-Time Distributed Computing, 2005. ISORC 2005.*, pages 201–203, 2005.

[8] C. Muller-Schloer. Organic computing - on the feasibility of controlled emergence. In *International Conference on Hardware/Software Codesign and System Synthesis, 2004. CODES + ISSS 2004.*, pages 2–5, 2004.

[9] H. Seebach, F. Ortmeier, and W. Reif. Design and construction of organic computing systems. In *IEEE Congress on Evolutionary Computation, 2007. CEC 2007.*, pages 4215–4221, 2007.

[10] J. Branke, M. Mnif, C. Muller-Schloer, and H. Prothmann. Organic computing no.150; addressing complexity by controlled self-organization. In *Second International Symposium on Leveraging Applications of Formal Methods, Verification and Validation, 2006. ISoLA 2006.*, pages 185–191, 2006.

[11] M. Gudemann, F. Nafz, F. Ortmeier, H. Seebach, and W. Reif. A specification and construction paradigm for organic computing systems. In *Second IEEE International Conference on Self-Adaptive and Self-Organizing Systems, 2008. SASO '08.*, pages 233–242, 2008.

[12] F. Nafz, F. Ortmeier, H. Seebach, J.P. Steghoefer, and W. Reif. A generic software framework for role-based organic computing systems. In *ICSE Workshop on Software Engineering for Adaptive and Self-Managing Systems, 2009. SEAMS '09.*, pages 96–105, 2009.

[13] A. Bouajila, J. Zeppenfeld, W. Stechele, A. Herkersdorf, A. Bernauer, O. Bringmann, and W. Rosenstiel. Organic computing at the system on chip level. In *Very Large Scale Integration, 2006 IFIP International Conference on*, pages 338–341, 2006.

[14] M. Komann and D. Fey. Marching pixels - using organic computing principles in embedded parallel hardware. In *Parallel Computing in Electrical Engineering, 2006. PAR ELEC 2006. International Symposium on*, pages 369–373, 2006.

[15] C. Puig and L. Sheynblat. Sensors system integrations challenges. In *Semiconductor Sensors innovating Mobile Devices & User Experiences*, WCA Mobile SIG & Futures SIG. Wireless Communication Alliance, April April 2012.

[16] Department of Transportation USA. Federal motor vehicle safety standards: Tire pressure monitoring systems ($TPMS$):controls and displays, 2003.

[17] Final report:$APOLLO - IST - 2001 - 34372$ intelligent tyre for accident-free traffic. Technical report, Technical Reasearch Centre of Findland, 2005.

[18] E. Guizzo. How google's self-driving car works. IEEE Spectrum, October 2011.

[19] E. A. Lee. Cyber physical systems: Design challenges. Technical Report UCB/EECS-2008-8, EECS Department, University of California, Berkeley, Jan 2008.

[20] Foresight Vehicle. Foresight vehicle technology roadmap. *Society of Motor Manufacturers and Traders: London*, 2004.

[21] K. Iswandy and A. Koenig. Methodology, algorithms, and emerging tool for automated design of intelligent integrated multi-sensor systems. *Algorithms*, 2(4):1368–1409, 2009.

[22] S. K. Lakshmanan. *Towards Dynamically Reconfigurable Mixed-Signal Electronics For Embedded and Intelligent Sensor Systems*. PhD thesis, A. Koenig, Hrsg., Technical University of Kaiserslautern, Germany, 2008.

[23] P. Tawdross. *Bio-Inspired Circuit Sizing and Trimming Methods for Dynamically Reconfigurable Sensor Electronics in Industrial Embedded Systems*. PhD thesis, A. Koenig, Hrsg., Technical University of Kaiserslautern, Germany, 2007.

[24] J. Teichmann, K. Burger, W. Hasche, J. Herrfurth, and G. Taschner. One time programming (OTP) with zener diodes in $CMOS$ processes. In *European Solid-State Device Research, 2003. ESSDERC '03. 33rd Conference on*, pages 433–436, 2003.

[25] S. Laville, S. Pontarollo, C. Dufaza, and D. Auvergne. Integrated offset trimming technique. In *Solid-State Circuits Conference, 2001. ESSCIRC 2001. Proceedings of the 27th European*, pages 89–92, 2001.

[26] B. Male. Non-volatile memory cell for linear mos integrated circuits utilizing fused mosfet gate oxide, May 8 2001. US Patent 6,229,733.

[27] International technology roadmap for semiconductors 2012 update overview, 2012.

[28] W. Arden, M. Brillouet, P. Cogez, M. Graef, B.Huizing, and R. Mahnkopf. $More - than - Moore$ white paper. *International Technology Roadmap for Semiconductors (ITRS)*, page 31, 2010.

[29] S. Carrella, K. Iswandy, and A. Lutz, K.; Koenig. $3D$-localization of low-power wireless sensor nodes based on AMR-sensors in industrial and AmI applications. In *Sensoren und Messsysteme 2010*, volume 15, page 828. AMA (Hrsg.), Mei 2010.

[30] K. Iswandy, S. Carrella, and A. Koenig. Intelligent magnetic sensing system for low power WSN localization immersed in liquid-filled industrial containers. In *Proceedings of the 14th international conference on Knowledge-based and intelligent information and engineering systems: Part II*, KES'10, pages 361–370, Berlin, Heidelberg, 2010. Springer-Verlag.

[31] C. P. O. Treutler. Magnetic sensors for automotive applications. *Sensors and Actuators A: Physical*, 91(1-2):2–6, 2001.

[32] AMA Fachverband fuer Sensorik e.V Redaktionsteam. Sensor-trends 2014: Trends in zukunfsorientierten sensortechnologien. page 85, 2013.

[33] R. Mueller, M. Nuber, and R. Werthschuetzky. Selbstueberwachender durchflusssensor mit diversitaerer redundanz (self monitoring flowmeter with diversity). *TM-Technisches Messen*, 72(4/2005):198–204, 2005.

[34] MEMSIC. $MXA2050A$ data sheets, 2007.

[35] STMicroelectronics. $LYPR540H$ data sheets, 2009.

[36] X. Xiong, Y. L. Wu, and W. B. Jone. Design and analysis of self-repairable $MEMS$ accelerometer. pages 21–29, 2005. Design and analysis of self-repairable MEMS accelerometer.

[37] M. van der Meulen. On the use of smart sensors, common cause failure and the need for diversity. Report M 2749 X 04, WIB Internation Instrument Users' Association, May 2004.

[38] C. von der Malsburg. *The Handbook of the Brain Theory and Neural Networks*. The MIT Press, 2002. English.

[39] F. Bernd. Growing cell structures: a self-organizing network for unsupervised and supervised learning. *Neural Netw.*, 7(9):1441–1460, 1994. 195912.

[40] S. Marsland, J. Shapiro, and U. Nehmzow. A self-organising network that grows when required. *Neural Networks*, 15(8-9):1041–1058.

[41] B. Charlot, S. Mir, F. Parrain, and B. Courtois. Electrically induced stimuli for $MEMS$ self-test. In *VLSI Test Symposium, 19th IEEE Proceedings on. VTS 2001*, pages 210 –215, 2001.

[42] H. V. Allen, S. C. Terry, and D. W. De Bruin. Accelerometer systems with built-in testing. *Sensors and Actuators A: Physical*, 21:381 – 386, 1990. Proceedings of the 5th International Conference on Solid-State Sensors and Actuators and Eurosensors III.

[43] H. V. Allen, S. C. Terry, and D. W. De Bruin. Accelerometer systems with self-testable features. *Sensors and Actuators*, 20:153–161, 1989. A Special Issue Devoted to Micromechanics.

[44] N. Deb and R.D. Blanton. Built-in self-test of $MEMS$ accelerometers. *Microelectromechanical Systems, Journal of*, 15(1):52 – 68, feb. 2006.

[45] N. Deb and R.D. Blanton. Built-in self test of $CMOS - MEMS$ accelerometers. In *Test Conference, 2002. Proceedings. International*, pages 1075 – 1084, 2002.

[46] W. Chen, X. Chen, G. Zheng, X. Liu, and H. Zhang. Analysis of the self-test characteristics of a micromachined accelerometer. In *Nano/Micro Engineered and Molecular Systems, 2009. NEMS 2009. 4th IEEE International Conference on*, pages 396 –399, jan. 2009.

[47] F. Pourahmadi, L. Christel, and K. Petersen. Silicon accelerometer with new thermal self-test mechanism. In *Solid-State Sensor and Actuator Workshop, 1992. 5th Technical Digest., IEEE*, pages 122 –125, June 1992.

[48] A. Fruehling, M. Abu Khater, B. Jung, and D. Peroulis. $CMOS$-based monitoring of contact events up to 4 MHz in ohmic $RF - MEMS$ switches. In *Microwave Symposium Digest (MTT), 2010 IEEE MTT-S International*, pages 300 –303, May 2010.

[49] J.H.-L. Lu, M. Inerowicz, S. Joo, J. K. Kwon, and B. Jung. A low-power, wide-dynamic-range semi-digital universal sensor readout circuit using pulsewidth modulation. *Sensors Journal, IEEE*, 11(5):1134–1144, May 2011.

[50] X. Xiong, Y. L. Wu, and W. B. Jone. Reliability analysis of self-repairable $MEMS$ accelerometer. pages 236–244, 2006. 1550-5774.

[51] X. Xiong, Y. L. Wu, and W. B. Jone. Yield analysis for self-repairable $MEMS$ devices. *Analog Integrated Circuits and Signal Processing*, 56(1):71–81, 2008. http://dx.doi.org/10.1007/s10470-007-9111-3.

[52] X. Xiong, Y. L. Wu, and W. B. Jone. A dual-mode built-in self-test technique for capacitive $MEMS$ devices. In *VLSI Test Symposium, 2004. Proceedings. 22nd IEEE*, pages 148–153, 2004.

[53] X. Xiong, Y. L. Wu, and W. B. Jone. A dual-mode built-in self-test technique for capacitive $MEMS$ devices. *Instrumentation and Measurement, IEEE Transactions on*, 54(5):1739–1750, 2005.

[54] M. Eigen and P. Schuster. A principle of natural self-organization. *Naturwissenschaften*, 64(11):541–565, 1977.

[55] M. Kawahara. Self-monitoring system, January 27 1990. US Patent 4,896,321.

[56] H. Zhang and A. Arora. GS3: scalable self-configuration and self-healing in wireless sensor networks. *Computer Networks*, 43(4):459–480, 2003.

[57] K. Isamoto, T. Makino, A. Moroswa, C. Chong, H. Fujita, and H. Toshiyoshi. Self-assembly technique for $MEMS$ vertical comb electrostatic actuator. *IEICE Electronics Express*, 2(9):311–315, 2005.

[58] J. A. Carlson, J. M. English, and D. J. Coe. A flexible, self-healing sensor skin. *Smart Materials and Structures*, 15(5):N129–N135, 2006. 0964-1726.

[59] D. Ghosh, R. Sharman, H. Raghav Rao, and S. Upadhyaya. Self-healing systems – survey and synthesis. *Decision Support Systems*, 42(4):2164–2185, 2007.

[60] N. Mohamed and J. Al-Jaroodi. Self-configured multiple-network-interface socket. *Journal of Network and Computer Applications*, 33:35–42, 2010.

[61] D. Marinakis and G. Dudek. Self-calibration of a vision-based sensor network. *Image and Vision Computing*, 27(1-2):116–130, 2009.

[62] A. D. Derrick and N. Hobson. Electromechanical relays, February 18 1997. US Patent 5,604,656.

[63] C. K. Moore. Electromechanical relay monitoring system with status clocking, September 19 1995. US Patent 5,451,879.

[64] S. Akiyama. Solid state relay, February 14 1989. US Patent 4,804,866.

[65] D. M. Brown, M. Garfinkel, and J. A. Laurent. Solid state relay, October 7 1980. US Patent 4,227,098.

[66] R. G. Gilbertson and J. D. Busch. A survey of micro-actuator technologies for future spacecraft missions. *Journal of the British Interplanetary Society*, 49(4):129–138, 1996.

[67] X. Jia-shan, G. Tao, S. Hong-ming, and G. Hang. Analysis of a piezoelectric micro-pump by using $ANSYS$. In *Symposium on Piezoelectricity, Acoustic Waves, and Device Applications, 2008. SPAWDA 2008.*, pages 370–373, Dec 2008.

[68] P. Woias. Micropumps–past, progress and future prospects. *Sensors and Actuators B: Chemical*, 105(1):28–38, 2005.

[69] V. Srinivasan, V. Pamula, M. Pollack, and R. Fair. A digital microfluidic biosensor for multianalyte detection. pages 327–330, 2003. 1084-6999.

[70] M. R. Douglass. Lifetime estimates and unique failure mechanisms of the digital micromirror device (DMD). In *Reliability Physics Symposium Proceedings, 1998. 36th Annual. 1998 IEEE International*, pages 9–16. IEEE, 1998.

[71] C. K. Malhi, P. Rudra, and B. Navakanta. Design of a high sensitivity fet integrated mems microphone. *Procedia Chemistry*, 1(1):875–878, 2009.

[72] Y. Iguchi, M. Goto, M. Iwaki, A. Ando, K. Tanioka, T. Tajima, F. Takeshi, S. Matsunaga, and Y. Yasuno. Silicon microphone with wide frequency range and high linearity. *Sensors and Actuators A: Physical*, 135(2):420–425, 2007.

[73] Wenbin Ding. Press release: Emerging consume applications are boosting the $MEMS$ pressure sensor market- taken from $MEMS$ pressure sensor, a report from $Yole\ Development$, March 2013.

[74] B. Roussel. Press release:the biomems market will almost triple in size over the next five years, announces $Yole\ Development$, January 2013.

[75] D. M. Tanner. $MEMS$ reliability: Where are we now? *Microelectronics Reliability*, 49(9-11):937–940.

[76] J. Grafe. Future challenges in assembly and packaging. Technical report, Frauhofer IZM-ASSID, 2010.

[77] C. Maxfield. $2D$ vs.$2.5D$ vs.$3D\ ICs$, August 2012. extracted from website $http\ :\ //www.eetimes.com/document.asp?doc_id\ =\ 1279540$ on 13 January 2013.

[78] P. Pieters, D. Qi, and A. Witvrouw. Integration and packaging mems directly above active $CMOS$. In *International Symposium on High Density packaging and Microsystem Integration, 2007. HDP '07.*, page 1, June 2007.

[79] J.J. Khazaai and H. Qu. Electro-thermal $MEMS$ switch with latching mechanism: Design and characterization. *Sensors Journal, IEEE*, 12(9):2830–2838, 2012.

[80] V. Agrawal. *A latching $MEMS$ relay for DC and RF applications*. In *Electrical Contacts, 2004. Proceedings of the 50th IEEE Holm Conference on Electrical Contacts and the 22nd International Conference on Electrical Contacts*, pages 222 – 225, 2004.

[81] M. Staab and H.F. Schlaak. Novel electrothermally actuated magnetostatic bistable microrelay for telecommunication applications. *Conference on Micro Electro Mechanical Systems (MEMS), 2011 IEEE 24th International*, pages 1261–1264, 2011.

[82] Jaeseok Jeon, V. Pott, Hei Kam, R. Nathanael, E. Alon, and Tsu-Jae King Liu. Seesaw relay logic and memory circuits. *Microelectromechanical Systems, Journal of*, 19(4):1012–1014, 2010.

[83] R. Nathanael, V. Pott, H. Kam, J. Jeon, and T. K. Liu. 4-terminal relay technology for complementary logic. In *Electron Devices Meeting (IEDM), 2009 IEEE International*, pages 1 –4, Dec. 2009.

[84] H. Kam, T. K. Liu, V. Stojanovic and, D. Markovic and, and E. Alon. Design, optimization, and scaling of MEM relays for ultra-low-power digital logic. *Electron Devices, IEEE Transactions on*, 58(1):236 –250, Jan. 2011.

[85] H. Kam, V. Pott, R. Nathanael, J. Jeon, E. Alon, and T. K. Liu. Design and reliability of a micro-relay technology for zero-standby-power digital logic applications. In *Electron Devices Meeting (IEDM), 2009 IEEE International*, pages 1–4, 2009.

[86] G. M. Rebeiz. *RF MEMS: Theory, Design, and Technology*. John Wiley & Sons, Inc., Hoboken, New Jersey, 1st edition, 2003.

[87] R. Wood, R. Mahadevan, V. Dhuler, B. Dudley, A. Cowen, E. Hill, and K. Markus. $MEMS$ microrelays. *Mechatronics*, 8(5):535–547, 1998.

[88] L. Leijie, X. Yu, L. Xiuhan, L. Yu, F. Dongming, and Z. Haixia. Fabrication and characteristics of tunable band pass filter using $MetalMUMPs$ technology. In *IEEE International Conference on Nano/Micro Engineered and Molecular Systems (NEMS)*, pages 249–253, 2011.

[89] J. Pal, Y. Zhu, J. Lu, and D. V. Dao. A novel electrothermally actuated $RF-MEMS$ switch for wireless applications. In *8th IEEE Conference on Industrial Electronics and Applications (ICIEA), 2013*, pages 1594–1598, 2013.

[90] E. Kohn, W. Menzel, F. J. Hernandez-Guillen, R. Muller, A. Munding, P. Schmid, D. Grobe, and J. Kusterer. Evaluation of CVD diamond for heavy duty microwave switches. In *Microwave Symposium Digest, 2003 IEEE MTT-S International*, volume 3, pages 1625–1628 vol.3, 2003.

[91] M.J. Sinclair. A high force low area $MEMS$ thermal actuator. In *The Seventh Intersociety Conference on Thermal and Thermomechanical Phenomena in Electronic Systems, ITHERM.*, volume 1, pages –132, 2000.

[92] M. A. Johar and A. Koenig. Stiction conformity test for electrostatic $MEMS$ device in design and simulation process. In *Proceedings of Sensors and Measuring Systems 2014; 17. ITG/GMA Symposium;*, pages 1–6. VDE, 2014.

[93] J.K. Luo, A.J. Flewitt, S.M. Spearing, N.A. Fleck, and W.I. Milne. Young's modulus of electroplated nickel thin film for $MEMS$ applications. *Materials Letters*, 58(17-18):2306–2309, 2004.

[94] D. Hyman and M. Mehregany. Contact physics of gold microcontacts for $MEMS$ switches. In *Electrical Contacts, 1998. Proceedings of the Forty-Fourth IEEE Holm Conference on*, pages 133–140, 1998.

[95] A. S. Bondarenko and G. A. Ragoisha. EIS spectrum analyser. In *Progress in Chemometrics Research*, pages 89–102, 2005.

[96] A. Koenig and K. Thongpull. Lab-on-spoon a 3-d integrated hand-held multi-sensor system for low-cost food quality, safety, and processing monitoring in assisted-living systems. *Journal of Sensors and Sensor Systems*, 4:63–75, 2015.

[97] Analog Device. *AD5933, 1MSPS, 12-Bit Impedance Converter, Network Analyser*, 2013.

[98] Sensitec GmbH. *'AFF755 Magnetoresistive Field Sensor'*, 2011.

[99] M. A. Johar and A. Koenig. Case study of an intelligent AMR sensor system with self-x properties. In A. G. Cunha, R. Takahashi, G. Schaefer, and L. Costa, editors, *Soft Computing in Industrial Applications*, volume 96 of *Advances in Intelligent and Soft Computing*, pages 337–346. Springer Berlin Heidelberg, 2011.

[100] M. A. Johar, R. Freier, and A. Koenig. Adding self-x capabilities to AMR sensors as a first step towards dependable embedded systems. In *Proceedings of the Ninth Workshop on Intelligent Solutions in Embedded Systems (WISES)*, pages 41–46, 2011.

[101] R. Freier. *Ein universelles und dynamisch rekonfigurierbares Interface fuer eingebettete und intelligente Multi-Sensor-Systeme mit Self-x Eigenschaften*. PhD thesis, A. Koenig, Hrsg., Technical University of Kaiserslautern, Germany, 2015.

[102] P.E. Allen and D.R. Holberg. *CMOS Analog Circuit Design*. Oxford series in electrical and computer engineering. Oxford University Press, 2002.

[103] A. Heidary. *A low-cost universal integrated interface for capacitive sensors*. PhD thesis, Delft University of Technology, Delft, the Netherlands, 2010.

[104] B.W. McGaughy, J.C. Chen, D. Sylvester, and Chenming H. A simple method for on-chip, sub-femto farad interconnect capacitance measurement. *Electron Device Letters, IEEE*, 18(1):21–23, 1997.

List of Figures

List of Tables

Nomenclature

ABW Anchor beam width

AD Anchor distance between contact edge to the edge of anchor beam

AMR Anisotropic Magneto-Resistive Sensor

b_c Thickness of nickel layer in comb structure

C_{Cont} Capacitance value in contact area during open state of the MEMS switch

C_{PH} Horizontal parasitic capacitance across the signal line

C_{PLE} Parasitic capacitance between signal line and electrostatic actuator

C_{PLL} Parasitic capacitance between signal-in and signal-out

C_{Sens} The capacitance value of capacitive sensor for self-monitoring feature

C_{SLA} Parasitic capacitance between two signal path in sensor A

C_{SLB} Parasitic capacitance between two signal path in sensor B

C_{SLE} Parasitic capacitance between sensor path and electrostatic actuator

Cb_{Off} Offset value from the middle point of pitch value in comb structure

Cb_P Pitch value of comb structure measured between two fingers.

CbW The width of the centre mass body structure.

CdL Length of the cold arm in heat actuator

CdW Width of cold arm in heat actuator

CL Contact length

$CntW$	Width of the contact area
CS	Capacitive sensor
CW	The width of metal layer cut in the centre mass body structure.
DUT	Device under test
E	Young's Modulus
EA	Electrostatic actuator
EI	Stiffness factor of the structure.
$F1$	Electrostatic force created with $g1$ gap
$F2$	Electrostatic force created with $g2$ gap
F_{BMin}	Force required to deflect a single comb finger structure
F_{BNew}	Optimized value of F_{BMin} with consideration of S value
F_{Eff}	Sum of electrostatic force created by a pair of comb structure
FL	Finger length of electrostatic actuator
FP	Finger pitch of electrostatic actuator
FW	Finger width of electrostatic actuator
G	Gap between contact or capacitive sensor
$g1$	Small gap between movable comb structure
$g2$	Big gap between movable comb structure
h_{cNew}	Optimized value of h_c with consideration of I_{New} value
h_c	Beam width of a single comb structure
HA	Heat actuator
HaL	Length of the hot arm of heat actuator
HaW	Width of the hot arm of heat actuator
HCL	The length of the center beam in heat actuator
HtL	The overall length of heat actuator

I	Moment of inertia
I_{New}	Optimized value of I with consideration of F_{BNew} value
l_c	Beam length of a single comb structure
MW	The width of centre mass body
R_{Cont}	Resistance value of across contact area of a MEMS switch during on-state.
R_{LFl}	Line resistance value with one floating connection configuration
R_{Line}	Resistance value along the signal line inside the MEMS switch
R_{LNF}	Line resistance value with no floating connection configuration
S	Safety design factor
SAW	The width of the anchor stator of the electrostatic actuators
SG	The gap value from the edge of the electrostatic fingers to the edge of centre mass or to the edge of stator anchor
SL	The overall length of electrostatic actuator
SL_M	The length of a single mass switch
$SPDT$	Single Pole-Double Throw
$SPST$	Single Pole-Single Throw
SW	The width of a single mass switch
T_{Nic}	Thickness of nickel layer in MetalMUMPs technology
w_c	Deflection of a comb finger under electrostatic force

Lebenslauf

Persönliche Daten

Name: Muhammad Akmal Johar
Staatangehörigkeit: Malayisch
Familienstand: Verheiratet

Bildungsgang

1985-1990:   Primary School of Peserai, Batu Pahat

1991-1993:   High School of Batu Pahat

1994-1995:   Science School of Muar

1996-2000:   University Technology of Malaysia

                (B. Eng. in Mechatronics Engineering)

2000-2004:   R&D Engineer in Panasonic AVC Networks Pasir Gudang,

                Johor

2004-2005:   Tutor in Faculty of Mechanical and Manufacturing

                Engineering in University Tun Hussein Onn Malaysia

2005-2007:   University of Applied Science Ravensburg-Weingarten,

                Germany (MSc. in Mechatronics Engineering)

2007-2009:   Lecturer in Faculty of Mechanical and Manufacturing

                Engineering in University Tun Hussein Onn Malaysia

2009-2014:   Study leave for pursuing PhD. in Technical University of

                Kaiserslautern, Germany